THE NON-NEWTONIAN MICRORHEOLOGY OF HYDRODYNAMICALLY INTERACTING COLLOIDS: TOWARD A NON-EQUILIBRIUM STOKES-EINSTEIN RELATION

A Dissertation

Presented to the Faculty of the Graduate School

of Cornell University

in Partial Fulfillment of the Requirements for the Degree of

Doctor of Philosophy

by

Henry Chi Wah Chu

August 2017

THE NON-NEWTONIAN MICRORHEOLOGY OF HYDRODYNAMICALLY INTERACTING COLLOIDS: TOWARD A NON-EQUILIBRIUM STOKES-EINSTEIN RELATION

Henry Chi Wah Chu, Ph.D.

Cornell University 2017

The understanding of the flow properties of complex fluids is central to the development of materials and technology as diverse as paint, polymer solutions, biofluids, foodstuffs, and many other industrial compounds, and was made possible by advances in theoretical and experimental methods in the second half of the 20^{th} century. Development of nonequilibrium statistical mechanics theory, computational methods, microscopy, and bulk rheometry produced detailed understanding of structure-property relationships in these ubiquitous materials. Complex fluid rheology typically focuses on suspensions subjected to bulk shearing or extensional flow. However, ever-increasing need to understand microscopically small samples of fluid, especially biofluids, has demanded development of techniques that can interrogate tiny volumes of fluid and detect heterogeneity over the micron length scale — far outside the capability of bulk techniques that smear out such detail. Active microrheology has emerged as the premiere technique to fill this need.

In active microrheology, a microscopic probe, or set of probes, is driven by an external force through a complex fluid. As the probe moves through the suspension, it drives its configuration out of equilibrium; meanwhile Brownian motion of the suspended particles acts to recover their equilibrium configuration. These distortions and relaxations of the microstructure alter probe motion,

and this interplay evolves with flow strength and with microscopic suspension forces. Changes in mean and fluctuating probe motion can be related constitutively to suspension and flow properties, in direct analogy to such approaches in macroscopic rheology of single and complex fluids and solids.

The focus of this dissertation work has been to expand the existing theory of microrheology to predict one of the most central flow properties, the suspension stress. Because the particles are small enough to give a vanishingly small Reynolds number, inertia is negligible and Stokes' equations govern fluid motion. We consider particles small enough to undergo Brownian diffusion, which acts to restore flow-induced distortions of the spatial arrangement of particles. The shape of the distorted microstructure is set by the strength of the external force relative to the entropic restoring force of the suspension, and by the balance of microscopic forces between the constituent particles. The former is given by the Péclet number, Pe, whereas the latter comprise the external, Brownian, and interparticle forces, and the sensitivity of each to flow strength Pe is set by the dimensionless repulsion range, κ. To analyze the influence of these forces on the structure and suspension stress as they evolve with flow strength, we formulate and solve a Smoluchowski equation — an advection-diffusion equation governing the stochastic distribution of particles, systematically tuning the relative strength of hydrodynamic and entropic forces. The resulting distribution is employed as a weighting function in a statistical mechanics framework to compute the suspension stress averaged over the probe particle phase, the primary contribution to the nonequilibrium stress. A colloidal dispersion of hard spheres serves as the model system.

To understand the fundamental influence of hydrodynamic and entropic forces on the structure and suspension stress as they evolve with flow strength,

we first solve the Smoluchowski equation analytically in the dual limits of weak and strong external force and hydrodynamic interactions, and then numerically for arbitrary values of Pe and κ. Nonequilibrium statistical mechanics are then utilized to compute elements of the stress tensor. Because geometry of the microstructure about the line of the external force is axisymmetric, only the diagonal elements are nonzero. When hydrodynamic interactions are negligibly weak, only the hard-sphere interparticle force matters regardless of the flow strength, where the normal stresses scale quadratically and linearly in the external force strength in the limits of weak and strong forcing, respectively. As the repulsion range κ shrinks, hydrodynamic interactions begin to play a role: when forcing is weak, Brownian disturbance flows provide the dominant contribution to the suspension stress, but as Pe increases, the external force-induced stress takes over to dominate the total stress. Interestingly, the total suspension stress decreases as the strength of hydrodynamic interactions increases, regardless of the value of Pe. That is, hydrodynamic interactions suppress suspension stress. Owing to the dependence of hydrodynamic interactions on particle configuration, this stress suppression varies with flow strength: At low Pe, the stress scales as Pe^2 and the suppression is quantitative, whereas at high Pe the stress scales as Pe^δ, where $1 \geq \delta \geq 0.799$ for hydrodynamic interactions spanning from weak to strong. We identify the origin of stress suppression via an analysis of pair trajectories: While entropic forces — interparticle repulsion and Brownian motion — destroy reversible trajectories, hydrodynamic interactions suppress structural asymmetry and this underlies the suppression of the nonequilibrium stress. We relate the stress to the energy density: Hydrodynamic interactions shield particles from direct collisions and promote fore-aft and structural symmetry, resulting in reduced storage.

The detailed discussion of the individual normal stresses offers a fundamental understanding of the role played by hydrodynamic and entropic forces in energy density in a suspension. Non-Newtonian rheology is, however, more commonly characterized by the combined effect of the normal stresses — the normal stress differences and particle osmotic pressure; and the rich phenomena that they exhibit warrant a separate examination. In Chapter 3, the micromechanical theory developed in Chapter 2 is utilized to compute and analyze the first and the second normal stress difference, N_1 and N_2, and the particle osmotic pressure Π . As hydrodynamic interactions grow from weak to strong, the influence of couplings between the stress and the entrained motion on N_1 changes with the strength of flow. When flow is strong, hydrodynamic interactions suppress magnitude of N_1, owing to collision shielding that preserves structural symmetry. In contrast, when flow is weak, hydrodynamic interactions enhance disparity in normal stresses and, in turn, increase the magnitude of N_1. The first normal stress difference changes sign as flow strength increases from weak to strong, due strictly to the influence of elastic interparticle forces. Regardless of the strength of flow and hydrodynamic interactions, the second normal stress difference is identically zero owing to the axisymmetry of the microstructure around the probe. Hydrodynamic forces act to suppress the osmotic pressure for any strength of flow; when forcing is strong, this effect is qualitative, reducing the flow-strength dependence from linear to sublinear as hydrodynamic interactions grow from weak to strong. Non-Newtonian rheology persists as long as entropic forces play a role, *i.e.* in the presence of particle roughness or even very weak Brownian motion, but vanishes entirely in the pure-hydrodynamic limit.

The micromechanical theory presented in Chapter 2 and 3 predicts the

non-Newtonian response of a dilute suspension, provided that its particle microstructure is known. Nevertheless, measuring particle distribution is tedious in practice. In the second part of this dissertation, Chapter 4, we derive a non-equilibrium Stokes-Einstein relation for predicting suspension stress following the original model of Zia and Brady [154], now for a dispersion of hydrodynamically interacting colloids simply by tracking probe motion. The theory is an expansion of Einstein's equilibrium fluctuation-dissipation theory, where Cauchy's equation of motion, rather than an equation of state, serves as the fundamental conservation framework. We construct an anisotropic effective resistance tensor comprising microviscosity and flow-induced diffusivity to model the hydrodynamically coupled particle motion which, when coupled with particle flux, constitutes the advective and diffusive components of Cauchy's momentum balance. The resultant phenomenological relation between suspension stress, viscosity and diffusivity is a generalized non-equilibrium Stokes-Einstein relation which enables a full rheological characterization of a hydrodynamically interacting suspension by simply tracking the mean and mean-square motion of a single probe. The predictions by the new theory are compared with the results obtained from the micromechanical theory for dilute suspensions via the normal stresses, normal stress differences and the particle osmotic pressure, where we find excellent agreement between the two sets of results in all quantities for any strength of flow and hydrodynamic interactions.

The micromechanical theory and phenomenological model presented in previous chapters give accurate prediction to non-Newtonian rheology in a dilute suspension. In the third part of this dissertation, Chapter 5, we extend the scope of the present research by investigating the influence of particle concentration and the associated many-body interactions on suspension rheology. Analogous

to the unbound monodisperse colloidal system studied in Chapter 2 to 4, we conduct active microrheology simulations via the Accelerated Stokesian Dynamics framework for suspensions with various particle concentrations, ranging from dilute $\phi = 0.05$ to $\phi = 0.40$. We showed that the influence of particle concentration on the particle structure and rheology is qualitative. When flow is strong, a high particle concentration alters the fore-aft asymmetry of the microstructure around the probe by enhancing the particle accumulation inside the boundary layer and shortening the wake due to stronger Brownian drift. At equilibrium, the ring-like structure is recovered for a concentrated suspension, and it is attenuated as the suspension becomes dilute. The suspension rheology is studied via the microviscosity and the suspension stress, and they are both enhanced with increasing particle concentration. As concentration increases, microstructure is more closely-spaced, leading to stronger hydrodynamic dissipation and thus viscosity. The more compact structure also suggests that a probe moving in a concentrated suspension pushes through more bath particles and causes more configuration distortion as compared to one driven by the same force in a dilute suspension, giving rise to higher energy density in a suspension, or equivalently a higher suspension stress. To bridge the results of dilute and concentrated suspensions, we further utilize concentrated mobility functions to construct scaling theories to collapse the microviscosity and particle stress of suspensions of different particle concentrations, offering a robust predictive model for concentrated suspension rheology.

Overall, in this work the major accomplishments are a micromechanical theory and a generalized nonequilibrium Stokes-Einstein relation for obtaining the stress, diffusivity and viscosity from the motion of a single particle, and a scaling theory connecting the response of dilute and concentrated suspensions.

BIOGRAPHICAL SKETCH

The author was born in the United States, and grew up in British Hong Kong. Intrigued by fluid dynamics and applied mathematics, he embarked on his journey of scientific research in the final year of his undergraduate study in The University of Hong Kong, after he returned from The University of Aberdeen, Scotland as an exchange student. He investigated the coupling effect of electrokinetics and hydrophobicity in channel fluid flows, and graduated with a Bachelor of Engineering and Master of Philosophy in Mechanical Engineering from The University of Hong Kong in 2010 and 2012. He moved to Ithaca in 2012 to pursue the research presented in this dissertation. Next, he will undertake postdoctoral research in the Department of Chemical Engineering at Carnegie Mellon University, studying transport of particles at liquid-liquid interfaces in the presence of Marangoni stress.

To those who were, and have been in my life.

Especially to my parents.

May and James.

ACKNOWLEDGEMENTS

This dissertation arose in part out of five years of research that has been conducted since September 2012. In this period, I have worked with people whose contribution in assorted ways has fostered this research and brought me great experience. It is a pleasure to convey my gratitude to them all in my humble acknowledgement.

In the first place, I would like to record my gratitude to my advisor Prof. Roseanna N. Zia for her genuine interest in science and my development as a scholar. I remember the moments that we discovered new science in Olin 344 and in Africana Library; I remember the encouragement that Roseanna gave me before my first talk in the Society of Rheology Annual Meeting in Philadelphia in 2014; and I remember the joyful group Christmas party every year in her house. In these five years, the advice and guidance from Roseanna as well as the extraordinary experience that she shared have profoundly refined my work, which have also inspired and enriched my growth as a researcher. It is truly my honor to be a student of her.

I gratefully acknowledge Prof. Donald L. Koch and Prof. Brian J. Kirby for being my research committee members. Their advice and comments during various occasions have revealed some technical details that I had not fully considered. I am pleased to have this chance to perfect my understanding of the subject matter.

My academic development has been fostered by the vibrant learning environment in Cornell and the following faculty: Prof. Jane Z. Wang from MAE6010, Prof. Richard H. Rand from TAM6110 and MAE6840, Prof. Stuart L. Phoenix from MAE6810, Prof. Fernando A. Escobedo from CHEME 7110, and Prof. Saul A. Teukolsky from PHYS7680.

I am pleased to be friends with my fellow groupmates and colleagues, who contributed so much to making it a memorable experience to work in Cornell: Christian Aponte-Rivera, Benjamin E. Dolata, Emma Gonzalez Gonzalez, Nicholas J. Hoh, Hung-lun Hsu, Chelsea Hu, Derek E. Huang, Lilian C. Johnson, Benjamin J. Landrum, Tianshu Liu, Ritesh P. Mohanty, Gaddiel Quaknin, Poornima Padmanabhan, Joshua Roybal, Jialun Wang, Wei Shuya, Pankaj Singh, Yu Su, Steven Zhizhen Zhao, Zerui Sophie Zhu and Xiaolu Zheng. In particular, I would like to thank Nicholas J. Hoh and Yu Su, with whom I had many fruitful discussions.

Friendship outside Olin Hall completes my life in Ithaca. Thank you my flatmates, Jiun-Ruey Chen, Po-Cheng Chen, and Chinglin Hsieh for creating a warm atmosphere and living together in the past four years. Thank you my neighbors Wei-Liang Chen, Ding-Yuan Kuo and Shih-Hao Tseng, and especially to those living in Apartment 2, Julia T. Chen, Wanda I-Tzu Chen, Joyce Fang, Yu-Ting Kao and Xinhe Lian, for always being here through my ups and downs, and for being here as if we were living together.

Thanks also goes to my academic mentors Prof. Chiu-On Ng and Prof. Kwok-Wing Chow at my alma mater who, during the earliest stage of my research journey, shared with me their valuable experience and provided me with continuous encouragement.

Finally, thank you Mum and Dad for your unconditional love and support, and bringing me to this world to experience so many wonderful things in life.

TABLE OF CONTENTS

LIST OF FIGURES

CHAPTER 1

INTRODUCTION

1.1 Historical background

Rheology is the study of the flow and deformation of matter. The historical origin of the term rheology is the Greek word $\pi\alpha\nu\tau\alpha\ \rho\epsilon\iota$, "everything flows", put forth by the Greek philosopher Heraclitus, an idea made more specific as "everything flows if one waits long enough" [117]. This highlights a central aspect of the study of material flow: the timescale over which flow occurs, compared to timescales familiar in daily life, permits the broad classification of materials as solids or liquids. In fact, many everyday materials display both solid-like or liquid-like behavior: toothpaste is a solid in its container but it yields and flows like a liquid when it is squeezed; corn starch behaves like a liquid when flow is weak but it hardens when it is shaken vigorously. These are all examples of so-called complex fluids, where their internal, multiphase microscale structures evolve over observable timescales. While the details of the microstructures can vary widely — from immiscible droplets in an emulsion to bubbles in a foam — they share a remarkably rich commonality in macroscopic behavior: when subject to external forcing or flow, distortions in the microstructure give rise to shear-rate dependent non-Newtonian phenomena, including shear-thinning, thickening, viscoelastic or memory effects. The workhorse model system utilized to study complex fluids is the hard-sphere colloidal dispersion, a collection of microscopic particles suspended in a Newtonian solvent. There are many useful approaches to the study of complex fluids: empirical models devised from fitting experimental data to give postdictions simultaneously ac-

counting for normal experimental uncertainty; at the other end of the spectrum, the micromechanical approach connecting the evolution of the microstructure and rheology via statistical mechanics theory offers first-principles insights into the interplay between microscopic forces and the microstructural origin of rheological phenomena. Between these two approaches is the phenomenological model, in which part or all of the theoretical foundation is built constitutively rather than from first principles for the sake of robust simplicity. We adopt the micromechanical approach to study the non-Newtonian rheology in hydrodynamically interacting colloidal suspensions, with the goal of developing a phenomenological model for predicting dilute and concentrated suspension rheology.

1.1.1 Macroscale observations : Non-Newtonian rheology

In a Newtonian material, shear stress is linearly proportional to the shear rate via a proportionality constant, the viscosity; and the shear stress is identically zero in the absence of bulk flow. In contrast, in a non-Newtonian material, shear stress can be nonzero even if there is no imposed shear, and the shear stress may grow nonlinearly with shear rate (Fig. 1.1). One major thrust propelling continued research in rheology is a lack of a comprehensive description of non-Newtonian response via the classical Newtonian framework. A famous example was Weissenberg's [140] discovery of rod climbing: when a rod is rotated in a bath of polymer solution, the free surface of the solution climbs up the rotating rod, in contrast to rod dipping exhibited by a Newtonian fluid in which the free surface is depressed near the rod by inertial effects. Another well-known example of non-Newtonian rheology is the reduced viscosity of blood at

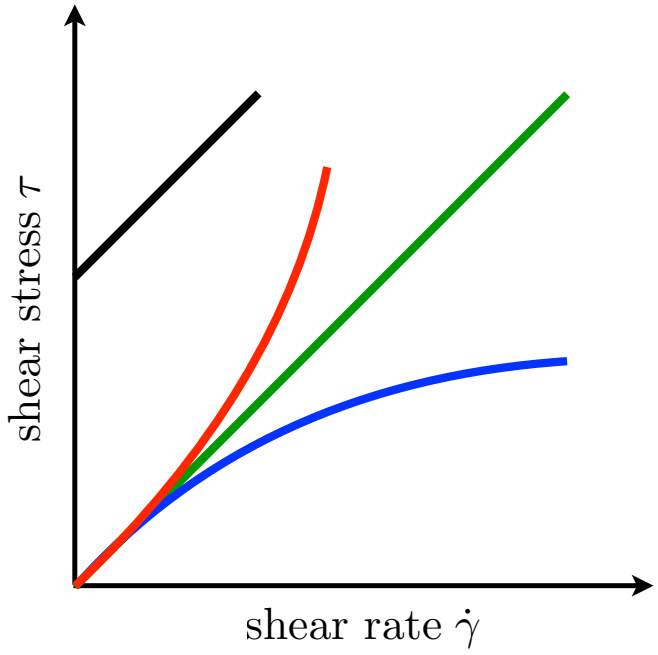

Figure 1.1: Shear stress τ plotted against shear rate $\dot{\gamma}$ for Newtonian and different non-Newtonian materials. Red line: shear-thickening material, green line: Newtonian material, blue line: shear-thinning material, black line: Bingham plastic.

high shear rates, a shear-thinning phenomenon established in the community of hemorheology. These phenomena have been thoroughly investigated: the Weissenberg effect has been successfully explained as a buildup of anisotropic normal stresses, and shear-thinning, as the weakening of Brownian dissipation as flow strength increases. Approaches to model this behavior theoretically include modification of the stress tensor in the Navier-Stokes equation, for instance the Ostwald-de Waele power law fluid model [110] and the Oldroyd-B model [109]. Other approaches include empirical modeling by fitting experimental data, such as the Krieger-Dougherty equation [82]. However, the regime of validity of these models for predicting non-Newtonian behaviors is confined to limited regimes. For instance, the Krieger-Dougherty equation is restricted to evaluation of suspension viscosities at equilibrium. This leaves open the need

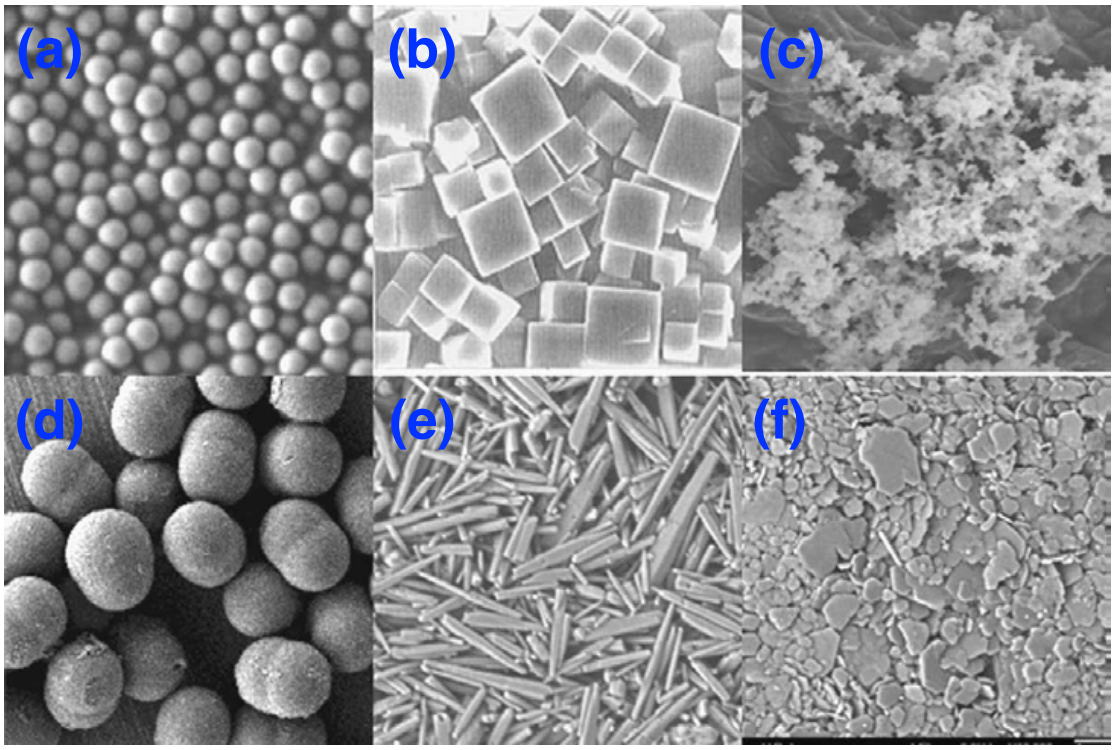

Figure 1.2: Typical colloidal particles. (a) Silica spheres, (b) lead sulfite crystals, (c) fumed silica aerogel, (d) polymer dumbbells, (e) calcium carbonate rods, and (f) kaolin clay. From [101], with permission.

for the development of a generalized predictive model. Naturally, this points to examination not just the macroscopic response of a material, but its underlying microscale constituents.

1.1.2 Microscopic origin of non-Newtonian flow : Colloids and microstructure

Colloidal dispersions serve as a workhorse model system for complex fluids, a two-phase medium comprising microscopic particles, called colloids, dis-

persed in a Newtonian solvent (Fig. 1.2). The size of colloids ranges from 10nm to a few microns, where the lower size limit is required to model surrounding fluid as a continuum, and the upper size limit ensures that they are susceptible to Brownian motion. The use of colloids dates back to the crafting of a Roman art piece, the Lycurgus cup [9]; Graham [59] first defined colloids with reference to their size as "substances that would not diffuse through a membrane separating water from an aqueous solution". The definition of colloids evolved with time, and not until the work by Brown [29], Einstein [44] and Perrin [113] did the definition of colloids firmly relate their size to Brownian motion. Utilizing a contemporaneously novel ultramicroscope, Brown observed "spontaneous" motion of pollen grains, coal dust, arsenic and other microscopic particles [65]. To test his hypothesis that the spontaneous motion owes its origin to some living constituents of the particles, he attempted to kill them by treating the particles in severe chemical and thermodynamic conditions. Yet, no matter how harshly treated, the spontaneous motion prevailed which, on one hand, disputed his hypothesis that the particles were living objects and, on the other hand, left open a question of the origin of the motion of the particles.

After three-quarters of a century, a study by Einstein [44] shed light on the origin of the spontaneous motion of microscale particles. Einstein set up a theoretical model for sedimentation of a dilute suspension of non-interacting hard-spheres, in which, at equilibrium, the downward advective flux owing to sedimentation is balanced precisely by an upward Fickian diffusive flux arising from the emergent spatial concentration gradient. The result is the famous Stokes-Einstein relation for spherical particles,

$$\boldsymbol{D} = \frac{kT}{6\pi\eta a}\boldsymbol{I}, \tag{1.1}$$

where $\boldsymbol{D}$ is the diffusivity of an isolated particle, k is the Boltzmann's constant, T

is the absolute temperature, η is the Newtonian solvent viscosity, a is the radius of the colloid, and $\boldsymbol{I}$ is the identity tensor. Physically, the Stokes-Einstein relation states that a microscale particle of size a immersed in a solvent with viscosity η will fluctuate due to random impacts from solvent molecules of magnitude kT. Since diffusivity of a particle relates to its mean-square displacement, and Boltzmann's constant relates to Avogadro's number, Avogadro's number was determined conclusively by Einstein. The Stokes-Einstein relation thus provides offers strong support for the existence of atoms by linking quantitatively a microscopic quantity to experimentally accessible macroscopic quantities. Perrin [113] tested the relation by tracing the mean-square displacements of an ensemble of isolated colloidal particles. His discovery that the mean-square displacement grew linearly with time confirmed Einstein's hypothesis that passive motion of colloidal particles indeed originates from their collisions with background solvent molecules. With credit goes to Brown [29] who first observed the phenomenon, the passive motion of microscopic particles arising from thermal fluctuations of solvent molecules is nowadays called Brownian motion. An ancillary result from Einstein's work, required for determination of Avogadro's number, in the same work Einstein [44] also derived a relation between the particle volume fraction $\phi = 4\pi n a^3/3$ (where n is the number density of particles) and the effective viscosity of the solvent plus a particle η_{eff},

$$\eta_{eff} = \eta(1 + 2.5\phi), \tag{1.2}$$

giving the well-known Einstein $O(\phi)$ correction to the suspension viscosity. Readers are referred to Zia and coworkers [151, 154] for a detailed presentation of the historical context of the work.

While Einstein's work demonstrated the connection between rheology and the underlying microstructure, it applies only to a very dilute suspension in

which the "structure" is formed by a single particle, *i.e.,* it is uniform. In the same year, independent of Einstein, Smoluchowski [123] presented a more general model for a many-body system, describing the time evolution of the probability density function of particle positions under the influence of microscopic forces,

$$\frac{\partial P_N(\boldsymbol{r}_n, t)}{\partial t} + \sum_{i=1}^{N} \nabla_i \cdot \boldsymbol{j}_i = 0, \tag{1.3}$$

where $P_N(\boldsymbol{r}_n, t)$ is the probability distribution function of N particle configuration vector $\boldsymbol{r}_N$, and $\boldsymbol{j}$ is the flux of particle i which comprises contributions from non-conservative (hydrodynamic) and conservative (thermodynamic) forces. Later, instead of taking on a probability approach, Langevin [87] constructed a stochastic differential equation of motion for Brownian particles based on conservation of momentum,

$$m\frac{d^2\boldsymbol{x}}{dt^2} = -6\pi\eta a\frac{d\boldsymbol{x}}{dt} + \boldsymbol{X}, \tag{1.4}$$

where m and $\boldsymbol{x}$ are the mass and position vector of a particle, respectively, t is time, and $\boldsymbol{X}$ is the stochastic Brownian force (originally termed as a "complementary" force in [87]) representing the effect of collisions between the particle and molecules of the solvent. Although the Langevin equation (1.4) delineates the motion of a single particle and is seemingly irrelevant to describing a microstructure normally comprising many particles, this momentum-based approach can in fact recover the same particle distribution and the same rheological result as the probability-based approach upon taking appropriate averages of many realizations of a single-particle trajectory. An example was shown in [87] that in fact the average Langevin equation can recover the particle diffusion as derived by Einstein [44]. Indeed, the Langevin equation serves as the backbone of a large class of modern particle dynamics simulation frameworks such as Brownian dynamics [45, 47] and Stokesian Dynamics simulations [22].

The key idea of particle dynamics simulations is to determine the change in particle position caused by microscopic forces in the system such as Brownian and interparticle forces and, from which, obtain the time evolution of particle position and rheological properties upon appropriate averaging. Overall, these work opened a new avenue for investigating rheology by not just taking the approach of making macroscale observations, but also highlighting the role of microstructure and its connection to rheology.

1.1.3 Micromechanics to connect particle configuration to rheology

We introduced in Sec. 1.1.2 that a pioneering micromechanical model is the Smoluchowski equation (1.3) which describes a conservation of probability flux arising from advection and diffusion due to interactions of microscopic forces. Despite the generality of the Smoluchowski theory to account for interactions in a N-body system, the link connecting the microstructure to macroscopic properties of a suspension was still missing. One would ask how could macroscopic properties of a suspension be defined if Brownian motion is random and is constantly altering the particle configuration? This points to the need for some averaging process to properly account for all possible particle configurations, and the method of averaging must be specified. A leap forward in nonequilibrium statistical mechanics was required.

Batchelor and co-workers [11, 12, 17, 16, 14] addressed the issue of averaging as the first step to build a micromechanical framework for computing the nonequilibrium stress in a suspension. In his first work [11], he posted the fol-

lowing problem statement: "How could we know what stress is generated in a suspension when a prescribed bulk motion is imposed on it?" He noted that this seemingly elementary question in fact demands an in-depth understanding of the averaging process: Brownian force yields random particle configurations, and the velocity and pressure inducing suspension stress both vary statistically with position. Suspension properties are thus determinate only in a statistical sense. One may straightforwardly resort to ensemble average — a large number of particle configurations (realizations) with the same macroscopic boundary conditions constitute an ensemble, but he pointed out that ensemble averages can neither be calculated directly nor observed conveniently, and it necessitates building a connection between ensemble averages and some calculable averages that are observable in common experiments. He made a careful analysis of the statistical homogeneity of a suspension and its ergodicity property, leading to his heroic proposition (and proof) of the equivalence between an ensemble average and the calculable volume average. This underpins the computation of average quantities in later work, which is an essential step in connecting statistically-varying microstructure of a suspension to its macroscopic rheological properties for practical use.

Upon defining the averaging process, Batchelor delineated a framework that separates the total (bulk) suspension stress into fluid and particle contributions but still, no significant analytical progress could be made until he narrowed his scope to a dilute suspension of hard spheres. Distinct from a concentrated suspension, pair interactions dominate the behavior in a dilute suspension [12], and this enabled Batchelor and Green [17, 16] to develop a nonequilibrium Smoluchowski equation by expressing the relative velocity of a particle pair in terms of hydrodynamic functions coupling the imposed straining flow to the induced

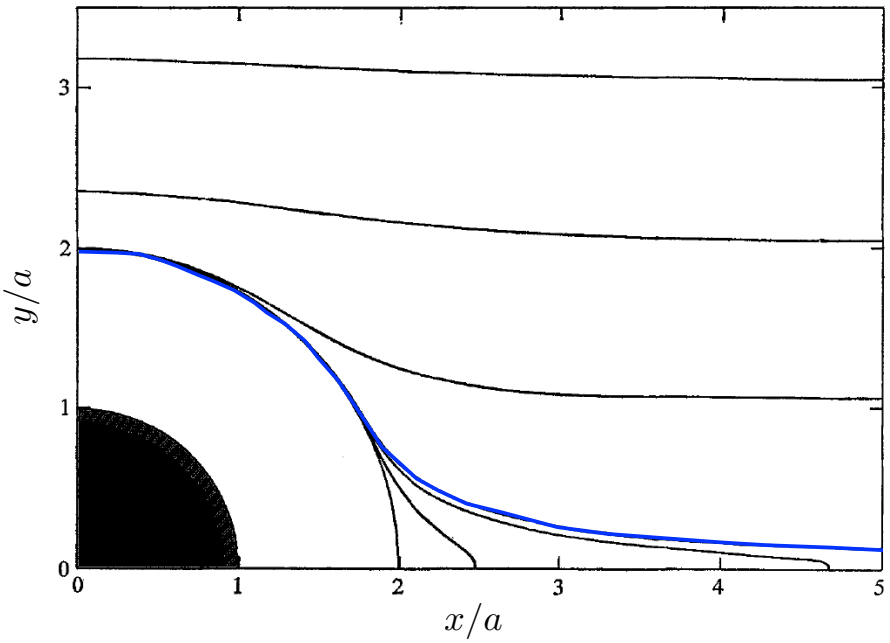

Figure 1.3: The trajectories of a noncolloidal, smooth, hard-sphere flowing around another identical reference sphere (black region) in a quadrant of a steady simple shear flow. Both spheres are on the same flow/flow-gradient plane. The limiting trajectory is colored in blue, within which trajectories are closed. All trajectories are symmetric about both the x and y axes. From [17], with permission.

particle motion. They solved the microstructure and particle stress analytically in the asymptotic limit of strong advection. In this limit, where Brownian motion is absent, they showed that the microstructure around any given particle is spherically symmetric, which forbids the development of nonequilibrium stress, suggesting that structural *asymmetry*, not just distortion, is essential to produce non-Newtonian rheology. The structure was then utilized to compute the suspension viscosity. The $O(\phi^2)$ correction to the viscosity was found to be $\eta^{eff,\infty}(\phi) = 7.6\eta\phi^2$ for a straining flow and $\eta^{eff,\infty}(\phi) = 5.2\eta\phi^2$ a simple shear flow, respectively. Here, $\eta^{eff,\infty}$ is the effective high-frequency shear viscosity of the suspension, that is the equilibrium viscosity of the suspension accounting for

just the equilibrium microstructure without the influence of Brownian motion. The correction for a simple shear flow was confirmed by Wagner and Woutersen [137], in which a more accurate value of $5.0\eta\phi^2$ was obtained via statistical mechanics theory, where more accurate values for the hydrodynamic functions were achieved via advances in numerical techniques. A subtle point to note here is that in these calculations the suspensions studied were noncolloidal and, in the case of a simple shear flow, there is a region of closed trajectories in which a particle will orbit a reference particle (Fig. 1.3). In consequence, inside this region the distribution of particles is indeterminate around any given particle, and it intrinsically bars the determination of the suspension viscosity. To make analytical progress, Batchelor and Green, and Wagner and Woutersen assumed a random initial configuration, and this structure maintains during flow.

Batchelor [14] subsequently generalized his nonequilibrium Smoluchowski equation for a colloidal suspension by incorporating the effect of Brownian and interparticle forces,

$$\frac{\partial g(\boldsymbol{r})}{\partial t} + \nabla_r \cdot (\boldsymbol{U}_r g(\boldsymbol{r})) = \nabla_r \cdot \boldsymbol{D}_r \cdot \nabla_r g(\boldsymbol{r}), \tag{1.5}$$

where $g(\boldsymbol{r})$ is the pair distribution function, $\boldsymbol{U}_r$ and $\boldsymbol{D}_r$ is the relative velocity and diffusivity between individual particle in a pair, and derivatives are taken with respect to the relative separation $\boldsymbol{r}$. The presence of thermodynamic forces drives particles across trajectories, breaking the reversibility of Stokes flow, negating the need for an assumed initial particle configuration to determine macroscopic suspension response. He further derived expressions for the stresses arising from hydrodynamic, Brownian and interparticle forces. In the limit of weak flow, he solved the Smoluchowski equation via a regular perturbation and showed that, to $O(Pe)$, a colloidal suspension is Newtonian with no normal stresses or normal stress differences owing to fore-aft symmetry of

the microstructure. He conjectured that non-Newtonian behavior would arise at $O(Pe^2)$ structure . Here, the Péclet number, Pe, is a measure of the strength of advection, which distorts the suspension, relative to the strength of diffusion that acts to recover the equilibrium microstructure. In the same weak flow limit, he presented the $O(\phi^2)$ correction to the equilibrium viscosity as $6.2\eta\phi^2$ for a straining flow which, when compared to his aforementioned finding in the strong flow limit (a correction equals $7.6\eta\phi^2$), suggested a shear-thickening response. Batchelor's conjecture for non-Newtonian rheology was confirmed by Brady and Vicic [27] who extended the perturbation analysis to $O(Pe^2)$ structure, and that for shear-thickening was validated and reproduced in later models by solving the Smoluchowski equation numerically for the full range of flow strength [19]. The importance of Batchelor's work is apparent, and his generalized nonequilibrium Smoluchowski equation forms the basis of future micromechanical theories, such as models concerning effect of particle concentration [119, 136, 24, 93, 92], particle roughness [39, 116, 142, 143, 41, 141], particle shape [127, 36, 37, 38, 32, 33, 96, 129, 130, 98], and external electromagnetic fields [120, 28, 4, 5, 6, 98].

All the models discussed above are developed for macrorheology, in which a bulk motion is imposed to a tested suspension due in part to the community of such flows in practice, and in part due to the requirement of statistically homogeneous structure in volume averaging. Indeed most theories and experiments in the literature are pertinent to macrorheology owing to the ease of performing bulk examination. However, the use of macrorheology in fact abandons the most fundamental and groundbreaking premise of the original Einstein fluctuation-dissipation theory and the associated technique that rheological response can be connected to the motion of a single particle in the sus-

pension. In view of this, a new wave of research emerges in recent years to revisit this powerful rheometric technique — microrheology.

1.1.4 Characterizing rheology : The renaissance of microrheology

As discussed in previous sections, microrheology was invented in the early 20^{th} century by Einstein [44], in which the mean-square displacement of an isolated particle in a suspension, the probe, was tracked to infer the viscosity of the solvent. This technique is now known as passive microrheology, since the motion of the probe particle arises strictly from thermal fluctuations — no applied or external force is required. Passive microrheology has the advantages over traditional rheometry that rheological response of a solvent can be inferred from the motion of a single, embedded particle without applying a bulk (shear or extensional) motion. Because of that, it requires much less amount of sample for investigation, and can be potentially utilized to probe confined systems and local heterogeneity of a material. Nowadays, particle-tracking has become more accessible thanks to development of techniques such as dynamic light scattering, video particle-tracking microscopy, and diffusing wave spectroscopy; and thus passive microrheology has been widely utilized to study various biophysical systems, for instance mechanical moduli of cytoskeleton of animal cells [2] and entangled actin-filament networks [97, 58], the directional anisotropy of Deoxyribonucleic acid (DNA) solutions [64], and the *in situ* gelation of hectorite clay [71] (see reviews [57, 138, 139, 145, 125]). Much effort has been placed to generalize the original Stokes-Einstein relation, and one prominently successful

attempt was by Mason and Weitz [100] who treated complex fluids as a continuum and derived a time-dependent relation,

$$D(\omega) = \frac{kT}{6\pi\eta^*(\omega)a}, \tag{1.6}$$

where ω is the frequency of the probe motion, $D(\omega)$ and $\eta^*(\omega)$ is the frequency-dependent diffusivity and complex viscosity of the suspending medium, respectively. The value of this generalization is not just enabling passive microrheology to examine temporal variant response as well as the response from a wide range of frequencies simultaneously, it also allows determination of the linear viscoelasticity of a material via the relation $i\omega\eta^*(\omega) = G'(\omega)+iG''(\omega)$, where $G'(\omega)$ and $G''(\omega)$ are the storage and loss moduli, respectively. Despite this advancement, connections between mean-square displacement of tracers (diffusion) and bulk moduli are still inexact [152], and are restricted to the linear regime. To obtain a nonlinear view of a suspension, the material itself must be driven out of equilibrium, and this motivates the development of active microrheology.

In active, nonlinear microrheology, a probe particle (or set of probes) is driven through a suspension by magnetic tweezers [61], or by trapping the probe with optical tweezers and dragging the bath past it [61, 51, 102, 126, 144]. The probe motion distorts the equilibrium microstructure but, at the same time, Brownian motion of bath particles acts to recover the equilibrium configuration. Nonequilibrium dynamic response of a material, such as viscosity, can then be inferred from the motion of a single probe particle via application of the Stokes' drag law,

$$F^{ext} = 6\pi\eta_{eff}a\langle U\rangle, \tag{1.7}$$

where F^{ext} is the magnitude of the constant external force and $\langle U\rangle$ is the resultant average velocity of the probe over many realizations. Batchelor and Wen

[15, 18] employed their nonequilibrium Smoluchowski equation to construct the first active microrheology framework in the context of sedimentation of polydisperse particles. Their model were general to consider the effect of Brownian diffusion and interparticle forces and, in the presence of gravity, they derived formulae for the average sedimentation velocity of particles of each species to $O(\phi)$ in the limits of asymptotically small and large Pe, and particle size ratio of the two species. Yet, no connection had been made between the probe's motion to the suspension viscosity until the work by Miliken *et al.* [103] and Davis and Hill [40], who proposed the relation Eq. (1.7), connecting the constant external (gravitational) force to the resultant sedimentation velocity via the effective viscosity of a noncolloidal suspension — falling-ball rheometry as we know today (see parallel discussions by Hoh and Zia [68, 69]). Davis and Hill also calculated the variance (fluctuations) of the sedimentation velocity, and concluded that hydrodynamic diffusivity varies significantly with the relative size of the two species. In addition to the effect of particle size, Almog and Brenner [3] studied another interesting facet of active microrheology: instead of imposing a constant external force on the probe particle and allowing its instantaneous velocity to fluctuate — the constant-force mode, he applied a fixed velocity on a non-rotating probe and allowed the resultant force to vary — the constant-velocity mode. Regarding the latter of the two modes, $\langle U \rangle$ becomes U, and F^{ext} becomes $\langle F^{ext} \rangle$ in Eq. (1.7). While the effective suspension viscosity in the two modes were shown to be the same as the solvent viscosity plus the Einstein correction $2.5\eta\phi$ when the probe is much larger than bath particles (as expected), they found that, when the size of the particles are comparable, η_{eff} in the constant-velocity mode is substantially higher due to the inability of the probe to fluctuate and travel around bath particles along its trajectory, leading

to a larger drag and thus higher viscosity. Despite these significant accomplishments, all of these models neglected Brownian motion.

Squires and Brady [124] generalized the models in prior work to the colloidal regime successfully, merging passive microrheology with Batchelor's study on polydisperse sedimentation [15, 18]. In particular, they coined the term "microviscosity", η^{micro}, to denote the pair-level correction to the effective viscosity in Eq. (1.7), and showed its qualitative resemblance to the $O(\phi^2)$ correction in shear macrorheology for the full range of flow strength for a non-hydrodynamically interacting suspension, recovering the low- and high-*Pe* Newtonian plateaus and force-thinning. Most suspensions in practice comprise hydrodynamically interacting colloids however, where the range of particle thermodynamic screening is not infinitely long. Such thermodynamic screening can arise in the presence of repulsive charges, particle surface asperities, or other features employed to sterically stabilize a suspension, which can be represented simplistically by a thermodynamic (effective) size of particles larger than their actual hydrodynamic size — the notion of the excluded-annulus model devised by Russel [118]. Employing this model, Khair and Brady [78] examined the influence of hydrodynamic interactions on microrheology by systematically tuning the thermodynamic size relative to the hydrodynamic size of particles, revealing that hydrodynamic interactions qualitatively alter the structure deformation and thus the rheology. For example, as the strength of hydrodynamic interactions increases in the strong-flow regime, the separation point of the particle-rich boundary layer moves to the rear side of the probe and the particle-deficit wake behind the probe becomes narrower; the evolution of the microviscosity transitions from force-thinning to force-thickening. Later studies of microviscosity further investigated the effect of the probe-to-bath particles size ratio [67],

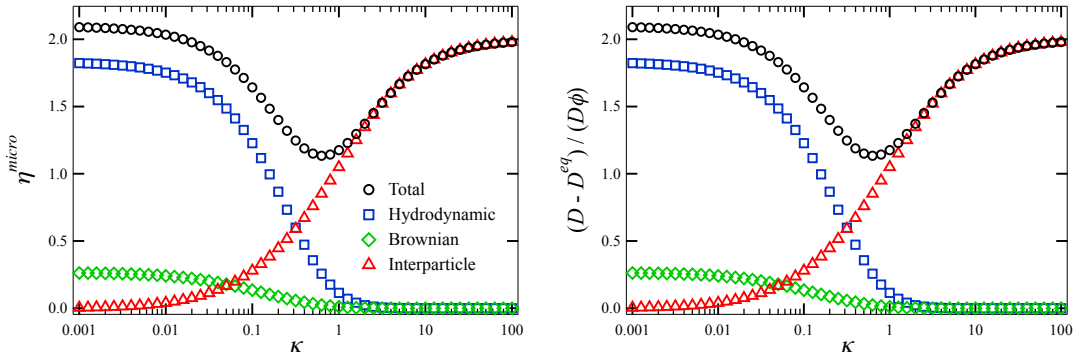

Figure 1.4: (a) Equilibrium diffusivity $\boldsymbol{D}^{eq} = (D + D^{eq,H} + D^{eq,B} + D^{eq,P})\boldsymbol{I}$ and (b) equilibrium microviscosity $\eta^{micro} = \eta^{micro,H} + \eta^{micro,B} + \eta^{micro,P}$ as a function of the strength of hydrodynamic interactions κ. Superscripts H, B and P denote contributions from hydrodynamic (blue squares), Brownian (green diamonds), and interparticle (red triangles) forces. The total quantity is denoted by black circles. From [69], with permission.

the difference between constant-force versus constant-velocity mode [131], and transient response during start-up and cessation flow [155].

The presence of microstructure not only hinders the mean motion of a probe particle, but it also deflects the probe from its mean trajectory. This net diffusive motion owes its origin to the preferential kicks of surrounding particles, and underlies many interesting biological and industrial applications, for instance particle margination in a pipe [132, 114, 150, 84] and resuspension [88, 90, 89, 1]. In the colloidal regime, Zia and Brady [153] defined flow-induced diffusivity (microdiffusivity) to characterize such behavior in a non-hydrodynamically interacting suspension, and a series of studies followed to examine flow-induced diffusivity in the dual limit of strong flow and no Brownian motion [68], in the presence of hydrodynamic interactions [69], and the effect of particle size [70]. Akin to the microviscosity, hydrodynamic interactions were shown to be influential to the evolution of the flow-induced diffusivity, in particular they en-

hance the anisotropy of diffusion drastically in the strongly nonlinear regime, again owing to a qualitative change in microstructural asymmetry [69]. In the same work, Hoh and Zia [69] also demonstrated the applicability of the Stokes-Einstein relation in a suspension, but not just in a continuum Newtonian solvent,

$$\boldsymbol{D}^{eq} = \frac{kT}{6\pi\eta(1+\eta^{micro}\phi)a}\boldsymbol{I} + O(\phi^2), \tag{1.8}$$

where $\boldsymbol{D}^{eq}$ is the isotropic equilibrium diffusivity, and the evolution of the equilibrium diffusivity for the full range of hydrodynamic interactions was shown to be identical as that of the microviscosity (Fig. 1.4). Physically, this is a manifestation of the equilibrium fluctuation-dissipation principle — the energy imparted from background fluctuations to trigger probe motion is dissipated precisely in the microstructure. Equilibrium fluctuation-dissipation principle could not be recovered otherwise using traditional shear macrorheology, and results here motivated extension of such principle to a more general system.

Zia and Brady [154] recognized the potential of forming a nonequilibrium fluctuation-dissipation relation from active microrheology. As the first step, they computed the nonequilibrium stresses using both micromechanics theory and Brownian dynamics simulations. They compared their results with those evaluated from an equilibrium relation, $\partial\boldsymbol{\Sigma}/\partial n \propto \boldsymbol{D}$, revealing a significant deviations between two sets of data. These findings motivated them to revisit the equilibrium relation, and identify its negligence of advective flux — while the equilibrium relation is governed by an equation of state and diffusive flux alone suffices to account for particle transport, a nonequilibrium relation must be derived from an equation of motion to address the advective flux arising from the mean flow. Taking into account the effect of advective flux, they derived a phenomenological theory delineating the nonequilibrium balance between fluc-

tuation and dissipation that produces stress — an equation linking suspension stress, microviscosity and flow-induced diffusivity — a nonequilibrium Stokes-Einstein relation,

$$-\frac{\boldsymbol{\Sigma}^{neq}}{n_a kT} = (2-\eta^{micro})\frac{\boldsymbol{D}^{flow}}{D} + \frac{1}{3}tr\left(\frac{\boldsymbol{D}^{flow}}{D}\right)\boldsymbol{I}. \tag{1.9}$$

The importance of this nonequilibrium relation not only lies in its fundamental, scientific understanding of nonequilibrium fluctuation and dissipation, highlighting how a change in the timescale at which fluctuations are dissipated produces sustained microstructural asymmetry that in turn generates stress, but also it broadens the scope of active microrheology so that one can obtain the suspension stress tensor, which gives a full rheological description of a suspension, from the mean and mean-square displacement of a single, embedded probe. Distinct from statistical mechanics theory and dynamics simulations, this novel theory requires no information of the microstructure, which can be tedious to measure in practice, and requires no intensive computational simulations.

1.2 Roadmap for this body of work

The original nonequilibrium Stokes-Einstein relation [154] provides new insights into energy fluctuation and dissipation in matter in the nonlinear regime, and it extends the applicability of the active microrheology technique such that the stress in a suspension can be inferred when its microviscosity and flow-diffusivity are known. In this initial work, both the micromechanical theory for the stress and the phenomenological model were developed for suspensions comprising non-hydrodynamically interacting colloids. These theories will no longer hold, however, in the general case of a hydrodynamically interacting sus-

pension since hydrodynamic interactions qualitatively alter the evolution of the particle microstructure and thus rheology, as discussed in Sec. 1.1. This motivates a reexamination of the balance between stress, viscosity and diffusivity — a generalized nonequilibrium Stokes-Einstein relation for a hydrodynamically interacting suspension. Furthermore, previous work in active microrheology theory has been restricted entirely to dilute suspensions. This left open questions of how suspension rheology depends on particle volume fraction and, in order to predict concentrated suspension rheology efficiently, the development of a theory unifying dilute and concentrated suspension response.

In the present research, we address three main topics. First, we develop a micromechanical theory to study the influence of hydrodynamic interactions on the evolution of the suspension stress and non-Newtonian rheology in a hard-sphere colloidal suspension via an active microrheology framework. Relevant theories and the model system are presented in the following section 1.3 of this chapter, followed by analyses of the normal stresses and the associated non-Newtonian rheology presented in Chapters 2 and 3, respectively. Second, in Chapter 4, we generalize the current nonequilibrium Stokes-Einstein relation to one that applies to a hydrodynamically interacting, hard-sphere suspension. Third, in Chapter 5, we examine the effect of particle concentration on suspension response, from which we develop a scaling theory connecting dilute and concentrated suspension rheology. Lastly, in Chapter 6, a conclusion is given to summarize key findings of the present work. Some future research directions are presented.

1.3 Continuum and statistical mechanics approaches

The goal of the present research is to understand the origin and evolution of the non-Newtonian rheology of a colloidal suspension through examining its connection to the underlying particle microstructure. Further to that, how the microstructure of a suspension evolves depends on the interacting forces between the constitutive particles, and the coupling between the particles and the suspending Newtonian solvent. In this section, we will present the scientific background of three elements that describe the evolution of suspension dynamics — fluid dynamics, microscopic forces, micromechanical model for microstructural evolution. We start by introducing the equations that govern the fluid flow.

1.3.1 Fluid dynamics

The flow of the intervening Newtonian solvent in a suspension is governed by the continuity equation and the Navier-Stokes equation. The continuity equation for an incompressible fluid is given by

$$\nabla \cdot \boldsymbol{u} = 0, \tag{1.10}$$

where $\boldsymbol{u}$ is the flow velocity. The Navier-Stokes equation can be derived from Cauchy's equation of motion, giving point-wise momentum balance

$$\rho \left[\frac{\partial \boldsymbol{u}}{\partial t} + (\boldsymbol{u} \cdot \nabla)\boldsymbol{u} \right] = \nabla \cdot \boldsymbol{\sigma} + \boldsymbol{f}, \tag{1.11}$$

where ρ is the density and $\boldsymbol{f}$ is the external body force per unity volume arising from, for instance gravity. The total fluid stress tensor $\boldsymbol{\sigma}$ comprises an isotropic

mechanical pressure field $p^a \boldsymbol{I}$ and a deviatoric stress tensor $\boldsymbol{\tau}$

$$\boldsymbol{\sigma} = -p^a \boldsymbol{I} + \boldsymbol{\tau}, \tag{1.12}$$

where, for an incompressible Newtonian fluid, the latter can be written constitutively as the product of the dynamic viscosity η and the strain rate tenor $\boldsymbol{E}$ as

$$\boldsymbol{\tau} = 2\eta \boldsymbol{E} = 2\eta \left\{ \frac{1}{2} \left[\nabla \boldsymbol{u} + (\nabla \boldsymbol{u})^T \right] \right\}, \tag{1.13}$$

where $(\nabla \boldsymbol{u})^T$ is the transpose of the velocity gradient. Inserting Eqs. (1.12) and (1.13) into Eq. (1.11), and absorbing the body force into the dynamic pressure p via the relation $p = p^a - \boldsymbol{f}$, the Navier-Stokes equation for an incompressible, Newtonian fluid is written as

$$\rho \left[\frac{\partial \boldsymbol{u}}{\partial t} + (\boldsymbol{u} \cdot \nabla) \boldsymbol{u} \right] = -\nabla p + \eta \nabla^2 \boldsymbol{u}. \tag{1.14}$$

Physically, the first term on the left-hand side represents a time-dependent acceleration, the second term represents an inertial acceleration of the flow with respect to space, also known as the advective acceleration. The first term on the right-hand side represents a dynamic pressure gradient, and the last term represents viscous stress.

For simplification of analysis, we nondimensionalize the Navier-Stokes equation with the following scheme,

$$t^* = \frac{t}{a/U}, \quad \boldsymbol{x}^* = \frac{\boldsymbol{x}}{a}, \quad \nabla^* = \frac{\nabla}{1/a}, \quad \boldsymbol{u}^* = \frac{\boldsymbol{u}}{U}, \quad p^* = \frac{p}{\eta U/a}, \tag{1.15}$$

where symbols with asterisk are nondimensionalized, and a and U are the characteristic length and velocity of the flow, respectively which, in this study, are the hydrodynamic radius and velocity of a colloidal particle. The viscously-scaled Navier-Stokes equation reads

$$Re \left[\frac{\partial \boldsymbol{u}^*}{\partial t^*} + (\boldsymbol{u}^* \cdot \nabla^*) \boldsymbol{u}^* \right] = -\nabla^* p^* + \nabla^{*2} \boldsymbol{u}^*, \tag{1.16}$$

where the Reynolds number $Re = \rho U a/\eta$ emerges from the scaling. In the present study, we consider microscopically small particles, where $Re \ll 1$. This yields the famous Stokes equation,

$$\nabla^{*2}\boldsymbol{u}^* = \nabla^* p^*. \tag{1.17}$$

In a suspension, the interface between fluid and particles, along with far-field flow conditions, give two boundary conditions and thus a well-posed problem that can be solved to obtain the fluid velocity and pressure field around the particles, and subsequently the fluid stress tensor itself and moments of the stress tensor such as hydrodynamic force, torque and stresslet. In the following, we will introduce three key characteristics of the Stokes equation, then give examples of formulating fluid-particle couplings.

Stokes equation is a Poisson equation of the flow velocity with the pressure gradient being the forcing terms, and it bears three key features of an elliptic equation, namely linearity, instantaneity, and time-reversibility. Linearity stems from elimination of the nonlinear advection in the Navier-Stokes equation. As a result, fluid motion and hence hydrodynamic traction moments are linear in the boundary data; for a no-slip hard sphere of radius a traveling alone in a solvent of viscosity η at a fixed velocity $\boldsymbol{U}^P$, the hydrodynamic force is $\boldsymbol{F}^H = -6\pi\eta a\boldsymbol{U}^P$ [Eq. (1.7)], the familiar Stokes drag law. Linearity also permits superposition of solutions. Instantaneity suggests that the only time-dependence of Stokes flow is via time-dependent boundary conditions, meaning that at a given time, Stokes flow entails no information of flows at another time. Thus, if boundary condition $\mathcal{A}$ gives flow field $\mathcal{A}$ and boundary condition $\mathcal{B}$ gives flow field $\mathcal{B}$, then if we apply boundary condition $\mathcal{A}$ to flow field $\mathcal{B}$, flow field $\mathcal{B}$ will change immediately to be identical to flow field $\mathcal{A}$ — time reversibility. We will take advantage of these properties when we formulate fluid-particle coupling below.

We begin with the motion involving a single spherical particle, then extend it to two-body and many-body interactions.

Let us consider a spherical particle fixed in a translating solvent with a constant free-stream velocity $\boldsymbol{U}^{\infty}$, and our goal is to determine the hydrodynamic force induced by the fluid on the sphere. To this end, we solve for the disturbance velocity $\boldsymbol{u}$ and pressure fields p around the sphere, defined as

$$\boldsymbol{u} = \boldsymbol{u}^{tot} - \boldsymbol{u}^{\infty}, \tag{1.18}$$

and

$$p = p^{tot} - p^{\infty}, \tag{1.19}$$

where the superscript ∞ denotes the fields in the absence of any disturbance due to the sphere, and the superscript *tot* denotes the total fields. The presence of the sphere and its motion provide information to fully determine the governing continuity equation and Stokes equation, Eqs. (1.10) and (1.17), via the boundary conditions,

$$\boldsymbol{u} = -\boldsymbol{U}^{\infty} \qquad \text{at} \qquad r = a, \tag{1.20}$$

$$\boldsymbol{u}, p \to 0 \qquad \text{as} \qquad r = \infty, \tag{1.21}$$

where r is the radial coordinate centered at the origin of the sphere of radius a. The pressure field can be solved by recognizing its harmonicity and the linearity of Stokes flow. For the former, the pressure is governed by a Laplace equation, where its general solution comprises a sum of spherical harmonics, and here decaying harmonics are chosen because the pressure must decay to zero as prescribed by the second boundary condition Eq. (1.21). For the latter, the pressure must be linear in the imposed filed $-\boldsymbol{U}^{\infty}$. Together these give the general solution for the disturbance pressure and velocity as

$$p = C_1 \frac{\boldsymbol{U}^{\infty} \cdot \boldsymbol{x}}{r^3}, \tag{1.22}$$

$$\boldsymbol{u} = \frac{p}{2\eta}\boldsymbol{x} + C_2\frac{\boldsymbol{U}^\infty}{r} + C_3\left(\frac{\boldsymbol{I}}{r^3} - \frac{3\boldsymbol{x}\boldsymbol{x}}{r^5}\right)\cdot\boldsymbol{U}^\infty, \tag{1.23}$$

where $\boldsymbol{x}$ is the position vector with its origin at the center of the sphere. The constants C_1, C_2 and C_3 can be determined by the use of the continuity equation and the first boundary condition Eq. (1.20). The disturbance pressure and velocity are given by

$$p = -\frac{3\eta a}{2}\frac{\boldsymbol{U}^\infty\cdot\boldsymbol{x}}{r^3}, \tag{1.24}$$

$$\boldsymbol{u} = -\frac{3a}{4}\left(\frac{\boldsymbol{I}}{r} + \frac{\boldsymbol{x}\boldsymbol{x}}{r^3}\right)\cdot\boldsymbol{U}^\infty - \frac{3a^3}{4}\left(\frac{\boldsymbol{I}}{3r^3} - \frac{\boldsymbol{x}\boldsymbol{x}}{r^5}\right)\cdot\boldsymbol{U}^\infty. \tag{1.25}$$

The above disturbance fields offer insights into modeling hydrodynamic interactions. First, by a change of reference frame, the case above is equivalent to a sphere sedimenting in a quiescent solvent with a velocity $\boldsymbol{U}^P = -\boldsymbol{U}^\infty$, one of the three important flow fields constituting a general linear flow. For the sake of brevity, the other two types of flow, rotational and straining flow, are not discussed here and readers are referred to [85, 62, 79, 148, 60] for detailed discussions. Second, the solutions demonstrate the slow decay of hydrodynamic interactions as $1/r$ in particular for the velocity, meaning that hydrodynamic disturbance cannot be neglected even when a neighboring sphere is far apart. As we shall see, this necessitates consideration of two- or many-body interactions.

Given the disturbance pressure and velocity fields that we obtained, Cauchy's traction vector $\boldsymbol{t} = \boldsymbol{\sigma}\cdot\boldsymbol{n}$ can be computed as $(3\eta/2a)\boldsymbol{U}^\infty$, where $\boldsymbol{n}$ is the outward unit normal from the sphere surface. The sum of hydrodynamic traction over the sphere surface gives the hydrodynamic force acting on the sphere by the fluid

$$\boldsymbol{F}^H = 6\pi\eta a\boldsymbol{U}^\infty, \tag{1.26}$$

which recovers the familiar Stokes drag $\boldsymbol{F}^H = -6\pi\eta a\boldsymbol{U}^P$ experienced by a sphere translating in a quiescent solvent with a velocity $\boldsymbol{U}^P = -\boldsymbol{U}^\infty$. The disturbance

velocity Eq. (1.25) can now be written in terms of the hydrodynamic force as

$$\boldsymbol{u} = -\left[\left(\frac{\boldsymbol{I}}{r} + \frac{\boldsymbol{xx}}{r^3}\right) + a^2\left(\frac{\boldsymbol{I}}{3r^3} - \frac{\boldsymbol{xx}}{r^5}\right)\right] \cdot \frac{\boldsymbol{F}^H}{8\pi\eta}. \tag{1.27}$$

In the limit $a \to 0$, the second term in Eq. (1.27) vanishes, leaving the solution

$$\boldsymbol{u}|_{a\to 0} = -\mathcal{J} \cdot \frac{\boldsymbol{F}^H}{8\pi\eta} = -\left(\frac{\boldsymbol{I}}{r} + \frac{\boldsymbol{xx}}{r^3}\right) \cdot \frac{\boldsymbol{F}^H}{8\pi\eta}, \tag{1.28}$$

which is called the Stokeslet, and is the solution to the Stokes equation with a point forcing represented by a Dirac delta function of magnitude F^H. Thus, the Oseen-Burgers tensor $\mathcal{J}$ is the Green's function for the Stokes equation, and is an important element in solution techniques utilizing distribution of forces, such as integral representation, multipole representation, slender-body theory, and boundary integral method, *etc.* [85, 62, 79, 148, 60].

Stokes' drag law describes the coupling between the hydrodynamic force (the zeroth force moment) and velocity. Similar couplings were deduced between the hydrodynamic torque $\boldsymbol{L}^H$ (the antisymmetric part of the first force moment) and rotation [81], and between the hydrodynamic stresslet $\boldsymbol{S}^H$ (the symmetric part of the first force moment) and straining motion [11]. The merit of these relations is that hydrodynamic drag, torque and stresslet can be computed without solving the corresponding boundary problem for the velocity moments and pressure, but they are limited to general linear flow fields where the gradient of the velocity field in the absence of any disturbance due to the sphere, $\nabla \boldsymbol{u}^\infty$, is a constant. This condition would be violated by specific flow fields such as Poiseuille flow or, in general and to our concern in this work, in the presence of another sphere in a suspension. In other words, if we consider a pair of spheres denoted as S_1 and S_2, the Stokes drag law and the other two coupling relations for the first force moments cannot be applied to S_1 itself nor to

S_2. It can be understood that, for the former, the motion of S_2 or simply its presence imposes another set of boundary conditions to the governing equations, creating disturbance flows that alter the motion of S_1. For the latter, as seen from the solution of the disturbance pressure and velocity, they decay slowly as $1/r$ and $1/r^3$, suggesting that long-ranged hydrodynamic interactions will alter the motion of S_2. Indeed, beginning from the two-body level, spheres' motion is coupled due to the curvature of the flow $\nabla^2 \boldsymbol{u}^\infty$ associated with the disturbance fields. Taking into account this effect, and utilizing Lorentz reciprocal theorem [94, 95], Faxen [46] and Batchelor and Green [17] generalized the Stokes drag law and the coupling relations for the torque and stresslet as

$$\boldsymbol{F}^H = 6\pi\eta a \left[\left(1 + \frac{a^2}{6}\nabla^2 \right) \boldsymbol{u}^\infty|_{r=0} - \boldsymbol{U}^P \right], \tag{1.29}$$

$$\boldsymbol{L}^H = 8\pi\eta a^3 \left(\boldsymbol{\omega}^\infty|_{r=0} - \boldsymbol{\omega}^P \right), \tag{1.30}$$

$$\boldsymbol{S}^H = \frac{20}{3}\pi\eta a^3 \left(1 + \frac{a^2}{10}\nabla^2 \right) \boldsymbol{E}^\infty|_{r=0}, \tag{1.31}$$

where $\boldsymbol{\omega}^\infty$ and $\boldsymbol{E}^\infty$ are the rotational velocity vector and straining rate tensor of the solvent in the absence of disturbance due to the sphere, and $\boldsymbol{\omega}^P$ is the rotation of the sphere. These generalized relations, known as Faxen's first, second and third laws, are key elements in modeling two-body interactions, as we shall see next.

To illustrate modeling of two-body interactions, we recapitulate our discussion above for sedimentation of a single sphere. Stokes drag law, $\boldsymbol{F}^H = -6\pi\eta a \boldsymbol{U}^P$, relates the hydrodynamic force to velocity of the sphere, and can be written as

$$\boldsymbol{U}_1 = -\boldsymbol{M}_{11}^{UF} \cdot \boldsymbol{F}_1^H, \tag{1.32}$$

where $\boldsymbol{F}_1^H$ and $\boldsymbol{U}_1 = \boldsymbol{U}^P$ are the hydrodynamic force and velocity of the sphere, and the mobility $\boldsymbol{M}_{11}^{UF} = \boldsymbol{I}/6\pi\eta a$ governs the strength of coupling between the

two, *i.e.* $\boldsymbol{M}_{ij}$ couples the hydrodynamic force acting on sphere j to the induced velocity on sphere i. For another identical sedimenting sphere that is very far away from the first sphere, one can similarly write $\boldsymbol{U}_2 = -\boldsymbol{M}_{22}^{UF} \cdot \boldsymbol{F}_2^H$. Nevertheless, as discussed above these couplings break down when the separation between the two spheres is not very large, owing to the slow decay of hydrodynamic disturbance. That is, the motion of sphere 1 affects that of sphere 2, and vice versa. This motives writing a coupled linearity relation

$$\begin{pmatrix} \boldsymbol{U}_1 \\ \boldsymbol{U}_2 \end{pmatrix} = -\begin{pmatrix} \boldsymbol{M}_{11}^{UF} & \boldsymbol{M}_{12}^{UF} \\ \boldsymbol{M}_{21}^{UF} & \boldsymbol{M}_{22}^{UF} \end{pmatrix} \cdot \begin{pmatrix} \boldsymbol{F}_1^H \\ \boldsymbol{F}_2^H \end{pmatrix}, \tag{1.33}$$

where $\boldsymbol{M}_{12}^{UF}$ and $\boldsymbol{M}_{21}^{UF}$ are the new mobility tensors introduced by hydrodynamic interactions between a pair of spheres.

To construct $\boldsymbol{M}_{12}^{UF}$ and $\boldsymbol{M}_{21}^{UF}$, we use the method of reflections. The technique has its name because it captures the reflective nature of hydrodynamic interactions: the disturbance caused by sphere 1 propagates through the solvent and alters the motion of sphere 2, which in turn generates disturbance and "reflected" back to sphere 1, and infinite reflections follow. To begin, we restate the Stokes drag law and the disturbance velocity caused by sphere 1 in the absence of pair-interaction,

$$\boldsymbol{U}_1^0 = -\frac{\boldsymbol{F}_1^H}{6\pi\eta a}, \tag{1.34}$$

$$\boldsymbol{u}_1^0 = -\left[\left(\frac{\boldsymbol{I}}{r} + \frac{\boldsymbol{xx}}{r^3}\right) + a^2\left(\frac{\boldsymbol{I}}{3r^3} - \frac{\boldsymbol{xx}}{r^5}\right)\right] \cdot \frac{\boldsymbol{F}^H}{8\pi\eta}, \tag{1.35}$$

where the superscript denotes the order of reflection. For sphere 2 located at $\boldsymbol{x} = \boldsymbol{r}$ and sedimenting, the velocity disturbance $\boldsymbol{u}_1^0$ causes it to translate with a first-reflection velocity given by the Faxen's first law [Eq. (1.29)]

$$\boldsymbol{U}_2^1 = \boldsymbol{u}_1^0(\boldsymbol{r}) + \frac{a^2}{6}\nabla^2\boldsymbol{u}_1^0(\boldsymbol{r}) = -\left(\frac{\boldsymbol{I}}{r} + \frac{\boldsymbol{rr}}{r^3}\right) \cdot \frac{\boldsymbol{F}^H}{8\pi\eta} + O(r^{-3}), \tag{1.36}$$

and the total velocity of sphere 2 can be obtained by superpositioning the zeroth- and first-reflection velocity, $\boldsymbol{U}_2^0$ and $\boldsymbol{U}_2^1$, giving

$$\boldsymbol{U}_2 = -\frac{\boldsymbol{I}}{6\pi\eta a} \cdot \boldsymbol{F}_2^H - \frac{1}{8\pi\eta}\left(\frac{\boldsymbol{I}}{r} + \frac{\boldsymbol{rr}}{r^3}\right) \cdot \boldsymbol{F}_1^H + O(r^{-3}), \tag{1.37}$$

where the second term on the right-hand side of Eq. (1.37) constitutes $\boldsymbol{M}_{21}^{UF}$. In principle, the reflection process continues infinitely, but as a demonstration we stop here at the first reflection. By the same token, the total velocity of sphere 1 and $\boldsymbol{M}_{12}^{UF}$ can be obtained. Finally, we can write down the pair mobility formulation coupling hydrodynamic force to induced velocity

$$\begin{pmatrix} \boldsymbol{U}_1 \\ \boldsymbol{U}_2 \end{pmatrix} = -\begin{pmatrix} \dfrac{\boldsymbol{I}}{6\pi\eta a} & \dfrac{1}{8\pi\eta}\left(\dfrac{\boldsymbol{I}}{r} + \dfrac{\boldsymbol{rr}}{r^3}\right) \\ \dfrac{1}{8\pi\eta}\left(\dfrac{\boldsymbol{I}}{r} + \dfrac{\boldsymbol{rr}}{r^3}\right) & \dfrac{\boldsymbol{I}}{6\pi\eta a} \end{pmatrix} \cdot \begin{pmatrix} \boldsymbol{F}_1^H \\ \boldsymbol{F}_2^H \end{pmatrix}. \tag{1.38}$$

We note that, in contrast to single particle hydrodynamics where only the particle size (and particle shape in general) matters, two-body interactions also depend on the relative separation between the particles. This brings up another issue that many reflections are required to capture the behavior of $\boldsymbol{M}_{12}^{UF}$ and $\boldsymbol{M}_{21}^{UF}$ when separation distance $r \to 0$. To circumvent this problem, a cutoff separation distance is set when modeling "near-field" hydrodynamic interactions, within which lubrication expressions were derived in replacement of the above "far-field" expressions. The development of lubrication expressions are relatively standard, and readers are referred to [75, 80, 79, 73, 74] for further discussions.

The example above presents one of the nine mobility couplings between prescribed hydrodynamic force moments and velocity moments to be determined. For the reverse problem where particle motion is prescribed and hydrodynamic force moments are unknown, resistance couplings and hydrodynamic resistance functions have been derived. The rest of these mobility and resistance couplings have been systematically documented in various texts, *e.g.* [79].

To this point, we present a framework for modeling pair interactions but in general higher-order interactions matter. However, both theories [12] and experiments [101] have shown that two-body interactions are responsible for many landmark results such as the aforementioned thinning and thickening of viscosity, force-induced diffusion, and normal stress differences. Thus, we pause here, and will continue our discussion on modeling many-body interactions when we examine the effect of particle concentration in Chapter 5.

In summary, it is important to take into account factors that could alter separation between particles in order to faithfully predict particle hydrodynamic interactions and thus the evolution of the microstructure and rheology. In the following sections, Sec. 1.3.2 and 1.3.3, we will present a model system for active microrheology and microscopic forces, then formulate a Smoluchowski equation governing the spatial evolution of the particle microstructure.

1.3.2 Model system and microscopic forces

We consider a suspension of volume $\mathcal{V}$ comprising N neutrally buoyant, colloidal hard spheres all of hydrodynamic radius a, immersed in an incompressible Newtonian fluid of density ρ and dynamic viscosity η. One of the particles, the probe, is driven by a fixed external force $\boldsymbol{F}^{\text{ext}}$ while the remaining $N-1$ bath particles are external force- and torque-free (Fig. 1.5). The probe is centered at $\boldsymbol{x}_1$, and a bath particle at a relative position $\boldsymbol{r} = \boldsymbol{x}_2 - \boldsymbol{x}_1$, where subscripts 1 and 2 denote quantities associated with the probe and bath particle, respectively. The strength of fluid inertia relative to viscous shear defines a Reynolds number, $Re = \rho U a/\eta$, where U is the characteristic velocity of the probe. Because the

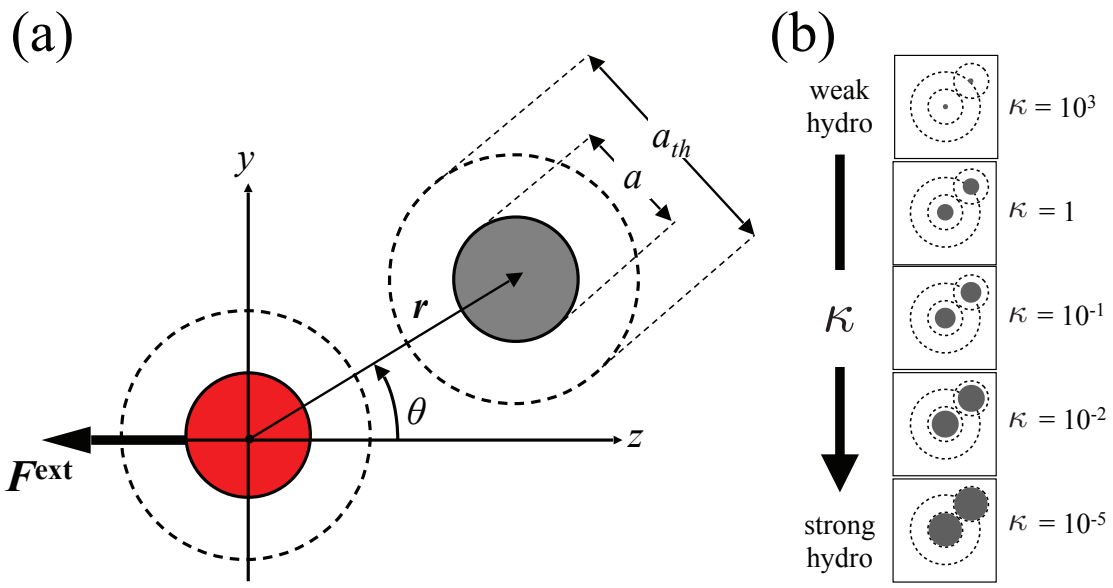

Figure 1.5: (a) The single-probe microrheology model system for equally-sized particles of hydrodynamic radius a and hard-sphere radius a_{th}, defining the no-slip and no-flux surfaces, respectively. (b) Minimum approach distance for a range of interparticle repulsion; grey circles of size a are probe and bath particles; dashed circle around each particle is thermodynamic radius a_{th}; large dashed circle is minimum approach distance r_{min}.

probe and bath particles are small, $Re \ll 1$, inertial forces can be neglected and thus the fluid mechanics are governed by Stokes' equations. The probe number density, $n_a = N_a/\mathcal{V}$, relative to the number density of bath particles, $n_b = N_b/\mathcal{V}$, is small. Probe motion distorts the equilibrium microstructure while the Brownian motion of the bath particles acts to recover their equilibrium configuration. This gives rise to an entropic restoring force, $2kT/a_{th}$, where k is Boltzmann's constant and T is the absolute temperature (the factor of two arises from the diffusive motion of both the probe and the bath particles). The degree of distortion of the microstructure, and hence its influence on probe motion, is set by the strength of probe forcing, F_0, relative to the entropic restoring force, defining a Péclet number: $Pe = F_0/(2kT/a_{th})$. Interactions between probe and the surrounding

microstructure change probe velocity, and these changes can be utilized to infer suspension properties [124, 102, 78, 144, 153, 154, 155, 131, 68, 69, 70, 34, 35].

We recognize that hydrodynamic interactions cannot be tuned independently of entropic repulsion since the range of the latter controls how close particles can approach each other, which in turn controls the strength of hydrodynamics. Hydrodynamic interactions between particles take place at the no-slip surfaces of the particles, a. In contrast, surface features of the particles, *e.g.* roughness, electrostatic repulsive layers, or polymer brushes, may also be present, and set the range of entropic repulsion, determining the minimum-approach distance r_{min} with which two particles can approach one another, in turn setting a thermodynamic size, a_{th}, where $r_{min} = 2a_{th}$ for equally-sized particles. In contrast to the no-slip particle surfaces defined by hydrodynamic forces, such non-hydrodynamic interparticle forces define a no-flux surface that may extend beyond the hydrodynamic radius, $r_{min} \geq 2a$. In this work, we employ the excluded-annulus model [118] to account for the short- and long-ranged nature of such interactions (Fig. 1.5).

An interparticle force derivable from a potential $V(r)$ between particles may include electrostatic or steric forces as from grafted polymers to stabilize a dispersion for example. Here we adopt a hard-sphere model, where particle overlaps are prevented by an infinite potential at contact between the no-flux surfaces, $r = 2a_{th}$; the particles exert no direct force on each other otherwise, *viz*,

$$V(r) = \begin{cases} \infty & \text{if} \quad r \leq r_{min} \\ 0 & \text{if} \quad r > r_{min}. \end{cases} \tag{1.39}$$

For a conservative potential, the interparticle force $\boldsymbol{F}_{\alpha}^{P}$ acting on a particle α can be obtained from the relation $\boldsymbol{F}_{\alpha}^{P} = -kT\nabla_{\alpha}V$, where the derivative is taken with

respect to the absolute position of the particle α.

The ratio of the thermodynamic to hydrodynamic radius defines the dimensionless repulsion range:

$$\kappa \equiv \frac{a_{th} - a}{a}. \tag{1.40}$$

When $\kappa \to \infty$, the long range of the interparticle repulsion keeps particles sufficiently separated so that even long-range hydrodynamic interactions are negligible. When $\kappa \sim O(1)$, hydrodynamic interactions strongly influence the configuration and relative motion of particles. In the limit of strong hydrodynamics, $\kappa \to 0$, particles can approach one another closely enough to experience lubrication forces.

1.3.3 Micromechanical model for microstructural evolution

The Smoluchowski equation governs the spatio-temporal evolution of the the N-particle probability distribution function $P_N(\boldsymbol{x}_N, t)$:

$$\frac{\partial P_N(\boldsymbol{x}_N, t)}{\partial t} + \sum_{i=1}^{N} \nabla_i \cdot \boldsymbol{j}_i = 0, \tag{1.41}$$

where $\boldsymbol{x}_N$ is the configuration vector. Advective, Brownian and interparticle forces drive particle flux $\boldsymbol{j}$, which for particle i is written

$$\boldsymbol{j}_i = \boldsymbol{U}_i P_N - \sum_{j=1}^{N} \boldsymbol{D}_{ij} P_N \cdot \nabla_j (\ln P_N + V_N / kT), \tag{1.42}$$

where $\boldsymbol{U}_i$ is the velocity due to the external probe forcing, kT is the thermal energy, and V_N is the N-particle interaction potential. The relative Brownian diffusivity between particles i and j is $\boldsymbol{D}_{ij} = kT\boldsymbol{M}_{ij}^{UF}$, where the hydrodynamic mobility tensor $\boldsymbol{M}_{ij}^{UF}$ governs the strength of the coupling between the force

exerted on particle j and the resultant velocity of particle i, and can be further expressed as

$$\boldsymbol{M}_{ij}^{UF} = \frac{1}{6\pi\eta a}\left[x_{ij}^{a}\hat{\boldsymbol{r}}\hat{\boldsymbol{r}} + y_{ij}^{a}\left(\boldsymbol{I} - \hat{\boldsymbol{r}}\hat{\boldsymbol{r}}\right)\right]. \tag{1.43}$$

In Eq. (1.43), $\hat{\boldsymbol{r}}$ is the unit vector along the line of centers of two particles, x_{ij}^{a} and y_{ij}^{a} govern the motion of particle α and β along and transverse to their line of centers, respectively. The three terms on the right-hand side of Eq. (1.42) give the flux of particles due to advection, Brownian diffusion, and interparticle forces, respectively. In the dilute limit, only pair interactions are important, and the probability $P_N(\boldsymbol{x}_N, t)$ in Eqs. (1.41) and (1.42) becomes the pair probability of finding the probe at position $\boldsymbol{x}_1$ and a bath particle at position $\boldsymbol{x}_2$, where subscripts 1 and 2 denote quantities associated with the probe and bath particle, respectively [124]. To analyze the relative flux between the probe and a bath particle, it is convenient to utilize a frame of reference moving with the probe, placing the probe at $\boldsymbol{z} = \boldsymbol{x}_1$, and a bath particle at $\boldsymbol{r} = \boldsymbol{x}_2 - \boldsymbol{x}_1$ (Fig. 1.5). The steady-state pair-Smoluchowski equation becomes [124, 78]:

$$\nabla_r \cdot (\boldsymbol{U}_r g) - \nabla_r \cdot \boldsymbol{D}_r \cdot (g\nabla_r V_N/kT + \nabla_r g) = 0, \tag{1.44}$$

where $g = g(\boldsymbol{r})$ is the pair distribution function defined as $n_b^2 g(\boldsymbol{r}) = [(N-2)]^{-1} \times \int P_N(\boldsymbol{r}_N) d\boldsymbol{r}_3 ... d\boldsymbol{r}_N$. The velocity and diffusivity of a bath particle relative to the probe are given by $\boldsymbol{U}_r = \boldsymbol{U}_2 - \boldsymbol{U}_1$ and $\boldsymbol{D}_r = \boldsymbol{D}_{11} + \boldsymbol{D}_{22} - \boldsymbol{D}_{12} - \boldsymbol{D}_{21}$ respectively, and derivatives are taken with respect to the relative separation $\boldsymbol{r}$. This expression governs the evolution of particle microstructure due to the advection and diffusion of a bath particle relative to the probe, where the hard-sphere force prescribes no relative velocity at contact, and there is no long-range order:

$$\hat{\boldsymbol{r}} \cdot \boldsymbol{D}_r \cdot \nabla_r g - \hat{\boldsymbol{r}} \cdot \boldsymbol{U}_r g = 0 \quad \text{at} \quad r = 2a_{th}, \tag{1.45}$$

$$g \sim 1 \quad \text{as} \quad r \to \infty. \tag{1.46}$$

The equations are made dimensionless by scaling the relative separation on the thermodynamic size of particles, and scaling the relative velocity and diffusivity on the Stokes velocity and the bare diffusivity of a colloidal particle of size a respectively, as

$$\boldsymbol{r} \sim a_{th}, \qquad \boldsymbol{U}_r \sim \frac{F_0}{6\pi\eta a}, \qquad \boldsymbol{D}_r \sim 2D_a = 2\frac{kT}{6\pi\eta a}. \tag{1.47}$$

The dimensionless governing equations are thus

$$Pe\ \nabla\cdot(\boldsymbol{U}g) - \nabla\cdot(\boldsymbol{D}\cdot\nabla g) = 0, \tag{1.48}$$

$$\hat{\boldsymbol{r}}\cdot\boldsymbol{D}\cdot\nabla g - Pe\ \hat{\boldsymbol{r}}\cdot\boldsymbol{U}g = 0 \quad \text{at} \quad r = 2, \tag{1.49}$$

$$g \sim 1 \quad \text{as} \quad r \to \infty, \tag{1.50}$$

where the superscript and subscripts on ∇_r, $\boldsymbol{U}_r$ and $\boldsymbol{D}_r$ are dropped for brevity.

Equation (1.48) gives a balance between Pe-strong advective forcing of the probe and the entropic restoring force exerted by the bath particles. The solution for the microstructure is solved in Chapter 2, and is employed in a statistical mechanics framework to compute the suspension stress averaged over the entire material. Before moving on to present the outline of this dissertation, we clarify the use of Batchelor's averaging technique [11] in the active microrheology framework.

In the classical framework of suspension mechanics developed by Batchelor [11], the procedure for computing bulk or average rheological quantities by averaging over an ensemble of microscopic configurations is shown to be equivalent to a volume averaging procedure, under certain conditions. This equality of an ensemble average and a volume average is based on the central assumption that the suspension is statistically homogeneous. In the active microrheology framework, we consider a set of probe particles with number density n_a in a

dilute suspension of bath particles with number density n_b. The probe phase is sufficiently dilute that one probe does not interact with another. In addition, the probes are dilute relative to the bath, $n_a \ll n_b$. We consider a unit volume of solvent and particles of a characteristic dimension l. In a dilute bath, interactions between the bath particles give rise to a suspension stress of $O(\phi_b^2)$, which is small compared to the $O(\phi_b)$ contribution arising from the probe-bath interactions [154]. Thus the probe-phase stress dominates the particle stress in any unit volume. Now, we consider the entire suspension, of characteristic dimension L, comprising many of these unit volumes. Since $l \ll L$, the variation of the local statistical properties on the microscale l (within each unit volume) is negligible on the macroscale L upon considering the suspension as a whole. In other words, on the suspension length scale L relevant to bulk rheology, such spatial variations in the suspension stress are negligibly small; thus the suspension can be treated as statistically homogeneous.

In justifying the statistical homogeneity of a suspension, another stipulation underlying the averaging process is that all particles are external-force free, implying that *in a closed system* there is no net migration of particles (no formation of particle-rich and particle-depleted regions, akin to formation of sediment and supernatant in sedimentation), that would yield a statistically inhomogeneous suspension. The model presented in the current work pertains to an unbound suspension which, in practice, corresponds to a large container. Indeed not all particles are external-force free in our system: the probes are driven by a fixed external force, producing net translation of probe particles. However, the probe phase is dilute relative to the bath ($n_a \ll n_b$), and thus the net migration of the probe phase is small compared to the container size. In a "large" container, the influence of the accumulation of particles in one region (and depletion in an-

other) on the statistical properties of the suspension is negligible, given that the vast majority of the large domain is statistically homogeneous. The influence of net particle migration can be further minimized in practice, by conducting active microrheology in a system in which one side is connected to a continuous supply of suspension while the other to drainage, *i.e.* an open system or, more simply, to utilize a container that is large compared to particle size and separation.

CHAPTER 2

ACTIVE MICRORHEOLOGY OF HYDRODYNAMICALLY INTERACTING COLLOIDS: NORMAL STRESSES AND ENTROPIC ENERGY DENSITY

2.1 Introduction

Equilibrium stress in colloidal dispersions arises when thermal fluctuations create temporary density gradients which are subsequently and rapidly dissipated by Brownian motion. The stress and osmotic pressure are fundamentally set by entropic forces and, in equilibrium hard-sphere dispersions, this is simply entropic exclusion to particle overlap. In the presence of strong hydrodynamic interactions, the osmotic pressure is given by $\Pi/nkT = 1 + 4\phi g(2a)$, valid for all volume fractions, where n is the number density of particles, kT is the thermal energy, $g(2a)$ is the pair-distribution function at contact, and the volume fraction $\phi \equiv 4\pi a^3 n/3$ is set by the hydrodynamic particle radius a, where the no-slip condition is obeyed. The effective size of particles are, however, set by a thermodynamic surface a_{th}, where the no-flux condition is obeyed (Fig. 2.1). The thermodynamic surface serves as a simplistic, yet useful, representation of various surface conditions, as arises in the presence of repulsive charges, surface asperities, or other features employed to sterically stabilize the dispersion; a_{th} may extend well beyond the hydrodynamic radius. The ratio of the two, $\kappa \equiv (a_{th} - a)/a$, determines how closely the no-slip surfaces of a pair of particles can approach one another, thus setting not only the strength of hydrodynamic coupling, but also the degree of entropic exclusion. When hydrodynamic interactions weaken (as κ becomes large), the osmotic pressure is given by $\Pi/nkT = 1 + 4\phi_{th} g(2a_{th})$, where

the volume fraction is defined by the no-flux surface, $\phi_{th} \equiv 4\pi a_{th}^3 n/3$. Because $\phi_{th}/\phi = (a_{th}/a)^3$, the osmotic pressure grows dramatically as hydrodynamic interactions weaken, *i.e.*, as entropic forces become strong. That is, entropic forces exert a direct influence on equilibrium stress: increasing thermodynamic particle size reduces the available free volume, thereby increasing osmotic pressure. This behavior is independent of particle configuration, depending only on particle density. However, flow or external fields drive a suspension from equilibrium, distorting the particle microstructure and can concurrently produce nonequilibrium stress. The connection of the microstructural distortion to nonequilibrium stress has been a focus of numerous investigations of suspension stress.

Early studies of nonequilibrium stress in colloidal suspensions showed that distortion in the microstructure does not guarantee additional (nonequilibrium) stress above and beyond the equilibrium stress; rather, structural asymmetry must be present to produce such non-Newtonian rheology. This began with Batchelor's pioneering study of the nonequilibrium stress in a hydrodynamically interacting suspension of hard spheres in which he developed a nonequilibrium statistical mechanics framework, *i.e.* the Smoluchowski equation, which governs structural evolution. He utilized its solutions to compute the average stress in dilute suspensions [16]. He found that for very strong flow, *i.e.* in the absence of Brownian motion, the structure is spherically symmetric in the pair-limit and bars the development of nonequilibrium stress, suggesting that structural asymmetry — not just distortion — is an essential element of non-Newtonian rheology. In that work, he predicted that the presence of even weak Brownian motion would destroy reversible Stokes-flow trajectories and lead to non-Newtonian rheology, a prediction confirmed by many subsequent studies.

He later sought to confirm this claim by incorporating the effects of Brownian motion into the Smoluchowski theory, studying its effects on stress in the limit of strong Brownian motion, $Pe \ll 1$. Here, the Péclet number, Pe, is a measure of the strength of advection, which distorts the suspension, relative to the strength of diffusion that acts to recover the equilibrium microstructure. However, in the linear-response regime, microstructural distortion was too weak to produce non-Newtonian stress, and he conjectured that appreciable structural asymmetry must be present to generate lasting nonequilibrium stress [14]. This suggests that thermodynamic fluctuations dissipate the stress as rapidly as it builds, *i.e.* as predicted by Green-Kubo theory. Later study by Brady and Vicic [27] interrogated Batchelor's hypothesis in an analytical study of the evolution of structure and stress in a dilute colloidal suspension undergoing simple shear flow, by extending the perturbation to weakly nonlinear flow, $O(Pe^2)$. They confirmed Batchelor's prediction that non-Newtonian stress appears in the weakly nonlinear regime where structural distortion is first appreciable, i.e at $O(Pe^2)$. These studies showed that both the shape and the extent of microstructural distortion plays a role in the development of stress in the limiting cases of strong hydrodynamic interactions under weak and strong flow; but how entropic forces alter the strength of hydrodynamics and, in turn, their influence on nonequilibrium stress, and their role with evolving flow strength was still unclear.

In an effort to elucidate the effect of hydrodynamic interactions on normal stress differences in strongly sheared suspensions, Brady and Morris [26] employed an excluded-annulus model [118] to study the two limits of very weak and very strong hydrodynamic interactions, finding that normal stress *differences* decrease moving from the former to the latter limit. However, subsequent Stokesian Dynamics simulations studies by Foss and Brady [50] of a suspension

sheared over a range of Pe showed that, in the limit of strong hydrodynamics, the first normal stress difference changes sign with increasing flow strength. The authors computed the hydrodynamic and entropic contributions to the stress arising from different regions of the anti-symmetric microstructure, and attributed the sign change to weakening Brownian stress as flow strength increases. Until $1/Pe$ is identically zero, the normal stress differences are nonzero, owing to the destruction of structural symmetry by Brownian motion. Such destruction of symmetry can also be achieved by particle roughness [142, 143, 141]; Bergenholtz *et al.* [19] investigated its effects on normal stress differences by studying the evolution of stress with Pe for several strengths of hydrodynamic interactions, by varying the range of interparticle repulsion (which can be small as in the case of surface roughness, or large as in the case of electrostatic repulsion, for example). They recovered the finding of Foss and Brady [50] that in the limit of strong hydrodynamic interactions, the first normal stress difference transitions from positive to negative as flow evolves from weak to strong. In the opposite limit of weak hydrodynamic interactions this behavior vanishes, giving a strictly positive first normal stress difference as Pe increases. We interpret these studies as a systematic study in which hydrodynamic interactions could be made strong compared to Brownian motion or strong compared to particle roughness, but a comprehensive picture of the influence of the interplay between hydrodynamic and entropic forces on the development of nonequilibrium suspension stress remains obscure, owing to a lack of connection to the microstructural mechanisms that generate stress.

As with an equilibrium suspension, growth of hydrodynamic interactions from weak to strong decreases the effective volume fraction, and increases the duration of pair encounters. The former configuration-independent effect

would suggest that stronger hydrodynamic interactions suppress nonequilibrium stress, but the latter, configuration-dependent effect suggests that they increase it. This leaves open the question of how changes in structure arising from hydrodynamic and entropic forces change stress, and points to the need for a fundamental analysis of normal stresses, rather than their differences, and how these evolve with flow and microscopic forces.

To wit, Bergenholtz *et al.* [19] showed that, in the limit of strong hydrodynamic interactions, the interparticle contribution to the normal stress differences is zero, consistent with the dogma that lubrication interactions prevent particle contact in this limit. While they did not report the normal stresses, these can be extracted by solving a set of linear equations constructed with their data for the osmotic pressure and the two normal stress differences. Doing so reveals that, in fact, their interparticle normal stresses are not zero, even in the limit of strong hydrodynamics. This could be viewed simply as an artifact of the authors' choice to move part of the trace of the interparticle stress to the Brownian stress for convenience of calculations — but to us this presents further confirmation of the idea that interparticle forces play an important role in suspension rheology even in the limit of perfectly smooth particles [68]. While they did devote attention to the evolving role of hydrodynamic, interparticle, and Brownian contributions to the stress, the sought-after connection between hydrodynamic interactions (and other microscopic forces) and the strength of the suspension stress is still smeared out by the aforementioned grouping of the thermodynamic stresses and by the lack of study of the normal stresses. It is thus clear that to gain a more fundamental understanding of the roles played by microscopic forces in the flow-induced evolution of suspension stress, a study of the fundamental quantity, the normal stresses, is necessary — as is

a re-examination of the interpretation of the thermodynamic stresses.

Progress in closing this gap in understanding of the origin of nonequilibrium stress in suspensions was made by Zia and Brady [154], who studied the normal stresses, normal stress differences, and osmotic pressure in a dilute colloidal dispersion of non-hydrodynamically interacting spheres via analytical theory and Brownian dynamics simulation, finding that the suspension stress can be expressed as a balance between fluctuations (particle diffusion) and dissipation (viscous stress), recovering the theory of Einstein and Batchelor in the limit of equilibrium but also enlarging the model to strong suspension flow. They showed that the thermal fluctuations dissipated by solvent drag (viscosity) at equilibrium have nonequilibrium analogs: flow-induced diffusion and microstructural drag produce structural asymmetry that persists over long times at steady state, giving rise to nonequilibrium stress. To form this connection they utilized the framework of microrheology — rather than traditional shear rheology. In the limit of no hydrodynamic interactions studied, the interparticle repulsion range is large and stress arises solely from direct collisions between particles (entropic exclusion). At equilibrium these give rise to a weakly asymmetric dipolar microstructural perturbation, and normal stresses that scale as Pe^2. To leading order, all three normal stresses are so close in value that the first normal stress difference is $O(Pe^4)$ (the second normal stress difference is identically zero owing to the axisymmetry of the perturbed structure), again confirming that appreciable asymmetry — *i.e.* at least weakly nonlinear flow – is required to produce lasting nonequilibrium stress. They found that, with increased flow strength, structural asymmetry becomes pronounced and the nonequilibrium stress becomes appreciable. The results were obtained via three approaches: a traditional statistical mechanics approach similar to those de-

scribed above; Brownian dynamics simulations; and a new phenomenological theory describing the nonequilibrium balance between fluctuation and dissipation that produces the stress, a nonequilibrium Stokes-Einstein relation. An interesting aspect of their model is its interpretation of the stress as energy stored via entropic rearrangement of the microstructure. In this initial work, hydrodynamic interactions between particles were neglected; an investigation of the variation of asymmetry in the structure with flow strength under the influence of hydrodynamic interactions is necessary to provide a more comprehensive view of the suspension stress and the role of entropic forces.

In the present work, we undertake the study of how the relative strengths of entropic and hydrodynamic forces give rise to the suspension stress via the framework of active microrheology, and systematically tune the range of interparticle repulsion utilizing an excluded-annulus model [118]. While much prior work focuses only on the normal stress *differences* and on the osmotic pressure, we place a primary focus on examining the normal stresses themselves. Doing so reveals that the nonequilibrium stress is set primarily by entropic forces and that entropic forces enhance suspension stress. While it could be equivalently stated that hydrodynamic interactions act to suppress the stress — both at and away from equilibrium — the entropic perspective provides a satisfying connection between stress and energy density in the suspension. To complement the traditional connection between average microstructure and macroscopic behavior, we utilize pair-trajectory analysis to explain the variation of microstructural asymmetry driven by microscopic forces. This trajectory perspective provides a unique window through which one can view the connection between entropic energy storage and suspension stress.

The remainder of this chapter is organized as follows: in Sec. 2.2, the microrheology system presented in Sec. 1.3.2 is recapitulated, followed by presentation of the theoretical framework that describes the evolution of the microstructure and suspension stress is presented. First, the two-body Smoluchowski equation governing the spatial evolution of the particle microstructure presented in Sec. 1.3.3 is recapitulated. Next, the contributions from the external, Brownian and interparticle forces to the total stress are derived in terms of the couplings between hydrodynamic traction moments and particle motion. From this, expressions for the average material stress are derived utilizing the statistical mechanics theory. Results are presented in Sec. 2.4, beginning with the evolution of the nonequilibrium microstructure under weak to strong probe forcing and hydrodynamic interactions, followed by an analysis of its impacts on nonequilibrium suspension stress. Focus is placed on the normal stresses parallel and perpendicular to the direction of the external force. Asymptotic behaviors in the limits of weak and strong probe forcing, and weak and strong hydrodynamic interactions are presented first. Next, the same quantities are computed for the full range of forcing and strength of hydrodynamic interactions, spanning six decades of Pe and eight decades of κ, revealing an important transition from the diffusion-dominated to advection-dominated regimes. To gain insight into the transport processes and microscopic forces underlying this behavior, the individual contributions due to external-force induced, Brownian and interparticle contributions are investigated. The entropic energy storage of suspensions is also examined via the pair-trajectory analysis. The study is concluded in Sec. 2.5 with a summary.

2.2 Model system

We recapitulate the microrheology framework presented in Sec. 1.3.2. We consider a suspension of neutrally buoyant, colloidal hard spheres all of hydrodynamic radius a, immersed in an incompressible Newtonian fluid of density ρ and dynamic viscosity η. One of the particles, the probe, is driven by a fixed external force $\boldsymbol{F}^{\text{ext}}$ through the suspension. The strength of fluid inertia relative to viscous shear defines a Reynolds number, $Re = \rho U a/\eta$, where U is the characteristic velocity of the probe. Because the probe and bath particles are small, $Re \ll 1$, inertial forces can be neglected and thus the fluid mechanics are governed by Stokes' equations. The probe number density, n_a, relative to the number density of bath particles, n_b, is small. Probe motion distorts the equilibrium microstructure while the Brownian motion of the bath particles acts to recover their equilibrium configuration. This gives rise to an entropic restoring force, $2kT/a_{th}$, where k is Boltzmann's constant and T is the absolute temperature (the factor of two arises from the diffusive motion of both the probe and the bath particles). The degree of distortion of the microstructure, and hence its influence on probe motion, is set by the strength of probe forcing, F_0, relative to the entropic restoring force, defining a Péclet number: $Pe = F_0/(2kT/a_{th})$.

We employ an excluded-annulus model [118] to tune the relative strength of hydrodynamic to entropic forces. Hydrodynamic interactions between particles take place at the no-slip surfaces of the particles, a, whereas entropic forces arising from various surface conditions interact at the no-flux surface, a_{th}, setting the minimum approach distance of two particles, $r_{min} = 2a_{th}$.

The ratio of the thermodynamic to hydrodynamic radius defines the dimen-

sionless repulsion range:

$$\kappa \equiv \frac{a_{th} - a}{a}. \tag{2.1}$$

When $\kappa \to \infty$, the long range of the interparticle repulsion keeps particles sufficiently separated so that even long-range hydrodynamic interactions are negligible. When $\kappa \sim O(1)$, hydrodynamic interactions strongly influence the configuration and relative motion of particles. In the limit of strong hydrodynamics, $\kappa \to 0$, particles can approach one another closely enough to experience lubrication forces.

2.3 Theoretical framework

Here, we present a model system that accounts for the effects of nonequilibrium flow and particle interactions. The dynamics of colloidal suspensions reside at the interface between statistical mechanics that describe the spatio-temporal particle distribution, and the continuum mechanics that govern fluid motion. To begin the analysis, we recapitulate the Smoluchowski equation governing the evolving spatial distribution of particles presented in Sec. 1.3.3. The average stress in the suspension is then expressed in terms of the external-force induced, Brownian and interparticle stresslets, which in turn are defined via the principles of low-Reynolds number hydrodynamics. Expressions for the average suspension stress are then derived via the statistical mechanics theory.

2.3.1 The nonequilibrium microstructure

In Sec. 1.3.3, we formulated the Smoluchowski equation governing the spatial-temporal evolution of the N-particle probability distribution function, and reduced it to a two-body Smoluchowski equation for pair distribution function that is suitable to describe dilute suspension dynamics. The dimensionless governing equations read,

$$Pe\ \nabla\cdot(\boldsymbol{U}g) - \nabla\cdot(\boldsymbol{D}\cdot\nabla g) = 0, \tag{2.2}$$

$$\hat{\boldsymbol{r}}\cdot\boldsymbol{D}\cdot\nabla g - Pe\ \hat{\boldsymbol{r}}\cdot\boldsymbol{U}g = 0 \quad \text{at} \quad r = 2, \tag{2.3}$$

$$g \sim 1 \quad \text{as} \quad r\to\infty, \tag{2.4}$$

where $g = g(\boldsymbol{r})$ is the pair distribution function, $\boldsymbol{U}$ and $\boldsymbol{D}$ are the velocity and diffusivity of a bath particle relative to the probe, $\hat{\boldsymbol{r}} = \boldsymbol{r}/r$ is the unit vector connecting centers of the probe and a bath particle.

Equation (2.2) gives a balance between Pe-strong advective forcing of the probe and the entropic restoring force exerted by the bath particles. Equations (2.2)–(2.4) have been solved elsewhere [124, 78, 153, 131] but are solved in detail in the present work as well. Following these prior approaches, the equations are solved in the present study in the limits of weak and strong forcing utilizing asymptotic analysis, and we employ a finite-difference scheme for arbitrary forcing. Because our focus is primarily on the nonequilibrium stress, we define the nonequilibrium distortion $f(\boldsymbol{r})$ of the microstructure, $g(\boldsymbol{r}) = g^{eq}(1 + f(\boldsymbol{r}))$, where g^{eq} is the equilibrium microstructure and is equal to unity in a dilute dispersion. The solutions are presented in Sec. 2.4.

2.3.2 The suspension stress

The particle-phase stress, $\langle \boldsymbol{\Sigma} \rangle$, can be divided into non-hydrodynamic and hydrodynamic contributions as [11, 14],

$$\langle \boldsymbol{\Sigma} \rangle = -n_a kT \boldsymbol{I} - n_a \langle \boldsymbol{r} \boldsymbol{F}^P \rangle + \langle \boldsymbol{\Sigma} \rangle^H, \tag{2.5}$$

where $\boldsymbol{I}$ is the isotropic tensor, and the angle brackets denote an ensemble average over all positions of the bath particles. The approach we shall take here is to consider a material through which there are a large number of probe particles moving in response to an external force. The probes are taken to be so dilute that they do not interact with one another, and are dilute relative to the bath particles, $n_a \ll n_b$. A detailed discussion of the averaging, following Batchelor's program [11], is given in Sec. 1.3.3. In Eq. (2.5), the first term, $-n_a kT \boldsymbol{I}$, is the ideal osmotic pressure associated with the equilibrium thermal energy of the Brownian particles. The second term, $-n_a \langle \boldsymbol{r} \boldsymbol{F}^P \rangle$, is the non-hydrodynamic interparticle stress and originates from interparticle elastic collisions to which we also refer as $\langle \boldsymbol{\Sigma} \rangle^{P,el} \equiv -n_a \langle \boldsymbol{r} \boldsymbol{F}^P \rangle$. The remaining term, $\langle \boldsymbol{\Sigma} \rangle^H$, is the hydrodynamic stress induced by external probe forcing, Brownian motion and interparticle force via hydrodynamic coupling. It is the stress exerted by the fluid on the particles, and can be written as

$$\langle \boldsymbol{\Sigma} \rangle^H = \langle \boldsymbol{\Sigma} \rangle^{H,ext} + \langle \boldsymbol{\Sigma} \rangle^B + \langle \boldsymbol{\Sigma} \rangle^{P,dis}. \tag{2.6}$$

The superscript P,dis refers to the dissipative part of the interparticle stress: when an interactive force between particles causes relative motion, if they are hydrodynamically coupled, the motion will produce a stresslet. The average stresses in Eq. (2.6) can be expressed in terms of the corresponding stresslets, *viz.* $\langle \boldsymbol{\Sigma} \rangle^H = n_a \langle \boldsymbol{S} \rangle^H$, $\langle \boldsymbol{\Sigma} \rangle^{H,ext} = n_a \langle \boldsymbol{S} \rangle^{H,ext}$, $\langle \boldsymbol{\Sigma} \rangle^B = n_a \langle \boldsymbol{S} \rangle^B$, and $\langle \boldsymbol{\Sigma} \rangle^{P,dis} = n_a \langle \boldsymbol{S} \rangle^{P,dis}$, such

that,

$$\boldsymbol{S}^{H} = \boldsymbol{S}^{H,ext} + \boldsymbol{S}^{B} + \boldsymbol{S}^{P,dis}. \tag{2.7}$$

The stresslets correspond to the symmetric part of the stress tensor, and arise due to disturbance flows created by particle motion. These are in turn given by the hydrodynamic couplings between particle motion and hydrodynamic tractions on the particle surfaces:

$$\begin{aligned} \boldsymbol{S}^{H,ext} &= -\boldsymbol{R}_{SU} \cdot (\boldsymbol{M}_{UF} \cdot \boldsymbol{F}^{\text{ext}}) - \boldsymbol{R}_{S\Omega} \cdot (\boldsymbol{M}_{\Omega F} \cdot \boldsymbol{F}^{\text{ext}}) \qquad (2.8) \\ &= -\boldsymbol{R}_{SU} \cdot \boldsymbol{U}^{ext} - \boldsymbol{R}_{S\Omega} \cdot \boldsymbol{\Omega}^{ext}, \\ \boldsymbol{S}^{B} &= -kT\nabla \cdot (\boldsymbol{R}_{SU} \cdot \boldsymbol{M}_{UF}) - kT\nabla \cdot (\boldsymbol{R}_{S\Omega} \cdot \boldsymbol{M}_{\Omega F}), \qquad (2.9) \\ \boldsymbol{S}^{P,dis} &= -\boldsymbol{R}_{SU} \cdot (\boldsymbol{M}_{UF} \cdot \boldsymbol{F}^{P}) - \boldsymbol{R}_{S\Omega} \cdot (\boldsymbol{M}_{\Omega F} \cdot \boldsymbol{F}^{P}) \qquad (2.10) \\ &= -\boldsymbol{R}_{SU} \cdot \boldsymbol{U}^{P} - \boldsymbol{R}_{S\Omega} \cdot \boldsymbol{\Omega}^{P}, \end{aligned}$$

where $\boldsymbol{U}^{ext}$ and $\boldsymbol{\Omega}^{ext}$ are the translational and rotational velocities of a particle due to the external force $\boldsymbol{F}^{ext}$applied to the probe, and $\boldsymbol{U}^{P}$ and $\boldsymbol{\Omega}^{P}$ are the translational and rotational velocities of a particle due to interparticle forces $\boldsymbol{F}^{P}$ between particles. The hydrodynamic resistance and mobility tensors $\boldsymbol{R}_{SU}$, $\boldsymbol{R}_{S\Omega}$, $\boldsymbol{M}_{UF}$ and $\boldsymbol{M}_{\Omega F}$ couple surface tractions on one particle to its own motion and the motion of other particles (a brief discussion of the hydrodynamic resistance and mobility functions is given in Appendix A). Physically, the advective flow arising from the externally applied force gives rise to a external-force induced stresslet $\boldsymbol{S}^{H,ext}$ on a particle surface because it cannot deform. The Brownian stresslet $\boldsymbol{S}^{B}$ on particle surfaces arises due to disturbance flows driven by the Brownian motion of bath particles as it acts to smooth microstructural gradients [14]. Finally, relative motion produced by interparticle forces gives rise to disturbance flows that in turn create a stresslet $\boldsymbol{S}^{P,dis}$ on particle surfaces. The sum

of the elastic and dissipative interparticle stresslets is the (total) interparticle stresslet,

$$\boldsymbol{S}^P = \boldsymbol{S}^{P,el} + \boldsymbol{S}^{P,dis} = -\boldsymbol{r}\boldsymbol{F}^P - \boldsymbol{R}_{SU} \cdot \boldsymbol{U}^P - \boldsymbol{R}_{S\Omega} \cdot \boldsymbol{\Omega}^P. \tag{2.11}$$

The external-force induced stresslet, $\boldsymbol{S}^{H,ext}$, the Brownian stresslet, $\boldsymbol{S}^B$, and the dissipative interparticle stresslet, $\boldsymbol{S}^{P,dis}$, all vanish in the absence of hydrodynamic interactions, as do their sum, the hydrodynamic stresslet $\boldsymbol{S}^H$. In contrast, the elastic interparticle stresslet, $\boldsymbol{S}^{P,el}$, is always present regardless of the strength of hydrodynamic interactions. A detailed derivation of the particle stresslet from mobility and resistance formulations is given in Appendix B.

Before moving on to evaluate the average stresses, we compare the definition of the stresslets given above with those found in previous literature [14, 20, 19]. The external-force induced stresslet, denoted as $\boldsymbol{S}^{H,ext}$ in this work, has often been called the hydrodynamic stresslet $\boldsymbol{S}^H$ following Batchelor's original notation, which he defined as part of his seminal work determining the bulk stress in a homogeneous suspension of *noncolloidal* particles subjected to a statistically uniform straining motion. In the absence of Brownian motion, he defined the particle stress due solely to external straining motion (analogous to our external-force induced stress) as the hydrodynamic stress. To generalize the framework to include Brownian motion, he considered a homogeneous suspension of colloids at equilibrium to obtain expressions for the thermodynamic (Brownian and interparticle) stresses. He then proposed that the total stress in a flowing colloidal suspension is a superposition of these two quantities. The carry-over of the nomenclature of the hydrodynamic stress from a noncolloidal system to a colloidal one has produced contradictory expressions — while the hydrodynamic stress equals the external-force induced stress in a noncolloidal system, the hydrodynamic stress (stresses that are induced via hydrodynamic coupling)

in general comprises the external-force induced stress, the Brownian stress and the dissipative interparticle stress in a colloidal suspension. In other words, for a colloidal suspension, the hydrodynamic stress should be defined as the sum of the external-force induced stress, the Brownian stress and the dissipative interparticle stress [cf. Eqs. (2.6) and (2.7)], instead of just the external-force induced stress.

Second, in prior approaches, *e.g.* Bergenholtz *et al.* [19], the trace of the dissipative interparticle stresslets are combined with the Brownian stresslet (see appendix A of that study). We choose not to combine these stresslets because, as will be shown in Sec. 2.4, the trace of the dissipative interparticle stress must reside in the interparticle stresslet if one wishes to recover the net negligible contribution from the hard-sphere interparticle force to the suspension stress in the limit of strong hydrodynamic interactions that is at the heart of the dogma that lubrication forces replace hard-sphere forces at contact. Doing so reveals the important role of interparticle forces, even in the pure-hydrodynamic limit.

We now derive the contributions to the total particle stress. In the dilute limit, the average external-force induced, Brownian, and interparticle stresses are obtained by integrating expressions (2.15)–(2.18) over all admissible pair configurations:

$$\begin{aligned}\frac{\langle \boldsymbol{\Sigma} \rangle^{H,ext}}{n_a k T \phi_b} = & -\frac{1}{\pi(1+\kappa)} Pe \int_{r\geq 2} \left\{ \left[X_{11}^G(\kappa r) x_{11}^A(\kappa r) + X_{12}^G(\kappa r) x_{12}^A(\kappa r) \right] \left(\hat{\boldsymbol{r}}\hat{\boldsymbol{r}}\hat{\boldsymbol{r}}\hat{\boldsymbol{r}} - \frac{1}{3}\boldsymbol{I}\hat{\boldsymbol{r}} \right) \right. \\ & + \left[Y_{11}^G(\kappa r) y_{11}^A(\kappa r) + Y_{12}^G(\kappa r) y_{12}^A(\kappa r) \right] (2\boldsymbol{I}\hat{\boldsymbol{r}} - 2\hat{\boldsymbol{r}}\hat{\boldsymbol{r}}\hat{\boldsymbol{r}}) \\ & \left. -3 \left[Y_{11}^H(\kappa r) y_{11}^B(\kappa r) - Y_{12}^H(\kappa r) y_{12}^B(\kappa r) \right] \left(2\boldsymbol{I}\hat{\boldsymbol{r}} - 2\hat{\boldsymbol{r}}\hat{\boldsymbol{r}}\hat{\boldsymbol{r}} \right) \right\} \cdot \hat{\boldsymbol{F}}^{\text{ext}} g(\boldsymbol{r}) d\boldsymbol{r} \\ & + \frac{1}{3\pi(1+\kappa)} Pe \int_{r\geq 2} \left[X_{11}^P(\kappa r) x_{11}^A(\kappa r) + X_{12}^P(\kappa r) x_{12}^A(\kappa r) \right] \boldsymbol{I}\hat{\boldsymbol{r}} \cdot \hat{\boldsymbol{F}}^{\text{ext}} g(\boldsymbol{r}) d\boldsymbol{r}, \end{aligned} \tag{2.12}$$

$$
\begin{aligned}
\frac{\langle \boldsymbol{\Sigma} \rangle^B}{n_a k T \phi_b} = \; & \frac{1}{2\pi(1+\kappa)} \int_{r \geq 2} \left\{ \frac{1}{r^2} \frac{d}{dr} \left[r^2 \left(X_{11}^G(\kappa r) - X_{12}^G(\kappa r) \right) G(\kappa r) \right] \right. \\
& - \frac{6}{r} \left(Y_{11}^G(\kappa r) - Y_{12}^G(\kappa r) \right) H(\kappa r) \\
& \left. - \frac{18}{r} \left(Y_{11}^H(\kappa r) - Y_{12}^H(\kappa r) \right) \left(y_{11}^B(\kappa r) - y_{12}^B(\kappa r) \right) \right\} \left(\hat{\boldsymbol{r}} \hat{\boldsymbol{r}} - \frac{1}{3} \boldsymbol{I} \right) g(\boldsymbol{r}) d\boldsymbol{r} \\
& + \frac{1}{6\pi(1+\kappa)} \int_{r \geq 2} \left\{ \frac{1}{r^2} \frac{d}{dr} \left[r^2 \left(X_{11}^P(\kappa r) - X_{12}^P(\kappa r) \right) G(\kappa r) \right] \right\} \boldsymbol{I} g(\boldsymbol{r}) d\boldsymbol{r},
\end{aligned}
\tag{2.13}
$$

$$
\begin{aligned}
\frac{\langle \boldsymbol{\Sigma} \rangle^P}{n_a k T \phi_b} = \; & - \frac{3}{\pi} \oint_{r=2} \hat{\boldsymbol{r}} \hat{\boldsymbol{r}} g(\boldsymbol{r}) d\Omega \\
& - \frac{2}{\pi(1+\kappa)} \left[X_{11}^G(2(1+\kappa)) - X_{12}^G(2(1+\kappa)) \right] G(2(1+\kappa)) \\
& \times \oint_{r=2} \left(\hat{\boldsymbol{r}} \hat{\boldsymbol{r}} - \frac{1}{3} \boldsymbol{I} \right) g(\boldsymbol{r}) d\Omega \\
& - \frac{2}{3\pi(1+\kappa)} \left[X_{11}^P(2(1+\kappa)) - X_{12}^P(2(1+\kappa)) \right] G(2(1+\kappa)) \oint_{r=2} \boldsymbol{I} g(\boldsymbol{r}) d\Omega.
\end{aligned}
\tag{2.14}
$$

Here, the volume fraction of bath particles $\phi_b = 4\pi n_b a^3/3$, and $\hat{\boldsymbol{F}}^{\text{ext}} = \boldsymbol{F}^{\text{ext}}/F_0$ is the unit vector pointing in the direction of the external probe force. In each of the three equations, the last term represents the trace of the stresslet, associated with an isotropic nonequilibrium pressure. All remaining terms are traceless, except the elastic stress term $-(3/\pi) \oint \hat{\boldsymbol{r}} \hat{\boldsymbol{r}} g(\boldsymbol{r}) d\Omega$ in Eq. (2.14). The isotropic and traceless contributions are identified here because historically, the stress tensor was computed as a traceless quantity with corresponding hydrodynamic functions [80, 73]. However, more recent work explored the trace of stress tensor in order to quantify the osmotic pressure and, in so doing, generated a distinct, corresponding set of hydrodynamic functions [74]. The components of the hydrodynamic resistance and mobility functions $X_{\alpha\beta}$, $Y_{\alpha\beta}$, $x_{\alpha\beta}$, $y_{\alpha\beta}$, G, and H are defined following the conventional notations [13, 75, 80, 79, 73, 74]. They depend only on the relative separation between a pair of particles, r, and the dimensionless repulsion range, κ. Further detail can be found in Appendix A.

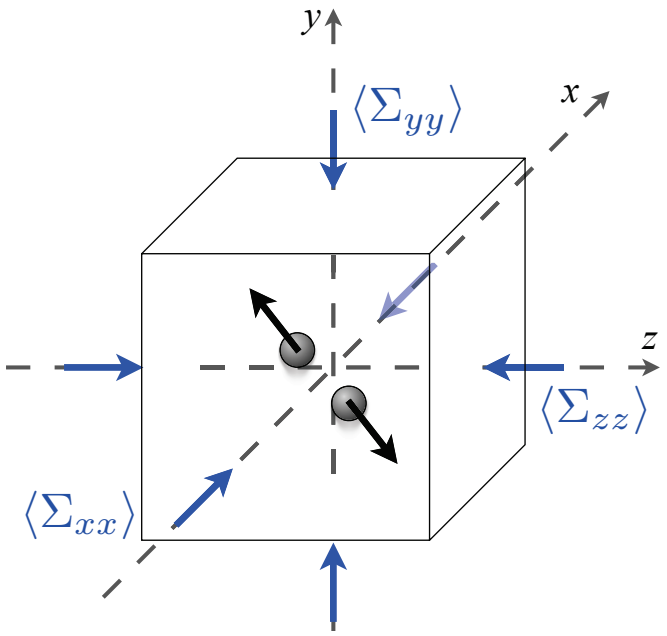

Figure 2.1: The osmotic pressure corresponds to the normal stress felt by a fictitious container enclosing the particles, whereas $\boldsymbol{\Sigma}$ corresponds to the stress felt by the particles as they encounter the container while they move outward or inward.

We note that the integrals above are absolutely convergent, as their integrands all scale as $r^{-(3+\gamma)}$, where $\gamma > 0$.

The particle-phase stress can be viewed analogously to the stress generated by a molecular gas on an enclosing volume [154]. We recall that diffusion in equilibrium suspensions is associated with an isotropic osmotic pressure. One can view these thermal particle fluctuations in analogy to gas particles which collide with "walls" of a fictitious container that encloses them, giving rise to pressure. Colloidal particles also exert a pressure on fictitious walls — the osmotic pressure. In an equilibrium suspension, the osmotic pressure reflects the tendency of the particles to push outward on the walls of the fictitious container, *i.e.*, the particle phase and the container tend to expand. Thus, the sign of the osmotic pressure, defined as the negative one-third of the trace of the stress tensor,

$\Pi = -tr(\mathbf{\Sigma})/3$, corresponds to expansion outward of the particle phase for $\Pi > 0$, and to contraction inward (condensation) of the particle phase when $\Pi < 0$. The minus sign is present because, while the particles attempt to push outward on a fictitious container, the container in turn tends to push inward on the particle phase, as indicated in Fig. 2.1. As such, the normal components of the stress tensor obey the following relationship:

$$\langle \Sigma_{xx} \rangle, \langle \Sigma_{yy} \rangle, \langle \Sigma_{zz} \rangle \begin{cases} < 0, & \text{compressive stress (expanding particle phase)} \\ > 0, & \text{tensile stress (contracting particle phase).} \end{cases} \tag{2.15}$$

That is, osmotic pressure corresponds to the normal stress felt by the "box", whereas $\mathbf{\Sigma}$ corresponds to the stress felt by the particles as they encounter the box while they move outward or inward. The normal stresses $\langle \Sigma_{xx} \rangle$, $\langle \Sigma_{yy} \rangle$ and $\langle \Sigma_{zz} \rangle$ are given by Eqs. (2.12)–(2.14). In single-particle active microrheology, $\langle \Sigma_{yy} \rangle = \langle \Sigma_{xx} \rangle$ owing to the axisymmetry of the structure around the probe. The normal stresses parallel and perpendicular to the direction of the probe forcing are thus denoted from here forward as:

$$\langle \Sigma_{\parallel} \rangle \equiv \langle \Sigma_{zz} \rangle, \tag{2.16}$$

$$\langle \Sigma_{\perp} \rangle \equiv \langle \Sigma_{yy} \rangle = \langle \Sigma_{xx} \rangle. \tag{2.17}$$

In the present study, we focus on the normal stresses; the non-Newtonian rheology revealed by the normal stress differences and nonequilibrium osmotic pressure are left for Chapter 3.

2.4 Results

The suspension stress evolves with the strength of flow, Pe, and with the dimensionless repulsion range, κ. Both factors exert a pronounced influence on

the evolving microstructure, which in turn impacts the stress. In the present section, we present solutions of the Smoluchowski equation to obtain the particle configuration in Sec. 2.4.1, and then utilize the solutions to compute and analyze the suspension stress in Sec. 2.4.2.

2.4.1 Evolving microstructure

The steady-state spatial evolution of the microstructure is governed by the pair-Smoluchowski equation given by Eqs. (2.2)–(2.4). Here, we divide its solution into two parts: first, the asymptotic limits of weak and strong forcing, and weak and strong hydrodynamic interactions; and second, for arbitrary strength of forcing and strength of hydrodynamic interactions, via numerical solution.

Asymptotically weak and strong forcing and hydrodynamic interactions

To gain insight into the role played by flow strength and microscopic forces in the evolving structure, we first examine their evolution in asymptotic limits. For weak forcing, $Pe \ll 1$, the microstructural disturbance created by the probe is easily smoothed by the Brownian motion of the bath particles. Because the disturbance is weak, a perturbation solution is appropriate. In the absence of hydrodynamic interactions, Squires and Brady [124] performed a regular perturbation expansion in Pe to obtain the leading order structural disturbance as $f(r,\theta) = Pe\hat{\boldsymbol{F}}^{\text{ext}} \cdot \hat{\boldsymbol{r}} f_1(r)$, where $f_1(r) = -4/r^2$. To obtain higher order disturbances, Khair and Brady [78] and Zia and Brady [153] recognized the singular nature of the problem in the cases of arbitrary strength of hydrodynamic interactions and no hydrodynamics, respectively: at some distance $\rho \sim rPe$ from the probe,

advection is as important as diffusion and cannot be neglected. The domain is thus divided into two regions, and matched asymptotic expansions are utilized to obtain a solution. Owing to its axisymmetric geometry surrounding the probe, the microstructure is independent of the azimuthal angle φ. Khair and Brady [78] performed a singular perturbation expansion to obtain the distortion $f(r,\theta)$ in the inner region,

$$f(r,\theta) = Pe\hat{\boldsymbol{F}}^{\text{ext}} \cdot \hat{\boldsymbol{r}} f_1(r) + Pe^2[\hat{\boldsymbol{F}}^{\text{ext}}\hat{\boldsymbol{F}}^{\text{ext}} : \hat{\boldsymbol{r}}\hat{\boldsymbol{r}} f_2(r) + h_2(r)] + O(Pe^3), \tag{2.18}$$

where $h_2(r)$, $f_1(r)$ and $f_2(r)$ are governed by a set of ordinary differential equations, and give the radial dependence of the structure corresponding to monopolar, dipolar and quadrupolar distortions, respectively. In the absence of hydrodynamic interactions, $\kappa \to \infty$, Zia and Brady [153] took a similar approach to derive the radial-dependent terms to $O(Pe^2)$. For hydrodynamically interacting particles, these differential equations were first solved numerically by Khair and Brady [78]. We recovered their results in the present study by carrying out the asymptotic expansion and developing a new numerical solution as discussed in the next section.

In the opposite limit of strong probe forcing, $Pe \gg 1$, advection dominates the evolution of the microstructure. However, diffusion cannot be neglected entirely, as it would result in the failure to satisfy the no-flux boundary condition. Inspection of Eq. (2.2) suggests that close to the probe, diffusion is as important as advection. The region upstream from the probe thus comprises two domains: an outer region in which only advection matters, and an $O(Pe^{-1})$-thin boundary layer at contact, where diffusion balances advection; a depletion wake trails the probe. A re-scaling of the radial coordinate as $y = Pe(r-2) \sim O(1)$ preserves diffusion in the boundary-layer. The solution of these boundary-layer equations reveals that the buildup of particles within the boundary layer depends on the

strength of hydrodynamic interactions: $g(r;\kappa) \sim Pe^{\delta}$, where $0.799 \leq \delta \leq 1$ as hydrodynamic interactions between particles range from strong ($\kappa \to 0$, $\delta = 0.799$) to negligible ($\kappa \to \infty$, $\delta = 1$). When hydrodynamic interactions are negligibly weak, the distorted microstructural evolution, to leading order, was derived by Squires and Brady [124] using a flux-balance argument,

$$f(r,\theta) = \begin{cases} -Pe\cos\theta\, e^{Pe(r-2)\cos\theta} + O(1) & , \quad \cos\theta \leq 0, \\ -1 & , \quad \cos\theta > 0. \end{cases} \tag{2.19}$$

Here, $\cos\theta \leq 0$ is the region upstream from the probe, and $\cos\theta > 0$ is the region trailing the probe. When hydrodynamic interactions are strong, the pair distribution function is found by a similarity solution inside the boundary layer. Matching to the spherically symmetric outer solution, Batchelor [15] showed that Brownian diffusion plays an important role in the shape of the microstructure even for very strong probe forcing; it is only at infinite Pe that diffusion can be neglected entirely. In this dual limit of strong forcing and strong hydrodynamic interactions, the distorted microstructure in the boundary layer was derived utilizing a matched asymptotic expansion, following Khair and Brady [78],

$$f(r,\theta) = f_0\Gamma\left(\frac{H_0}{G_1}\right)\left(\frac{Pe}{Y(\theta)}\right)^{W_0/G_1} \mathcal{M}\left(\frac{W_0}{G_1}, 1, -\frac{Pe(r-2)}{Y(\theta)}\right) - 1 \equiv \tilde{f}Pe^{\delta}, \tag{2.20}$$

modulo a negligible logarithmic correction. Here, f_0 is a constant determined by matching the inner and outer solutions, Γ is the gamma function, and $\mathcal{M}$ is the first confluent hypergeometric function (Kummer's function). The functions $G_1 = 2$, $H_0 = 0.402$, and $W_0 = 1.598$ are the leading order expansions of the hydrodynamic mobility functions $G(r)$, $H(r)$, and $W(r) = dG/dr + 2(G-H)/r$, respectively, at contact [13]. The variation of the polar-angle in the boundary-layer thickness is set by $Y(\theta) = (2G_1/H_0)(\sin\theta)^{-2G_1/H_0}\int_{\theta}^{\pi}(\sin\theta')^{2G_1/H_0-1}d\theta'$. For compact-

ness, we have defined

$$\tilde{f} \equiv f_0 \Gamma\left(\frac{H_0}{G_1}\right) Y(\theta)^{-W_0/G_1} \mathcal{M}\left(\frac{W_0}{G_1}, 1, -\frac{Pe(r-2)}{Y(\theta)}\right) - Pe^{-W_0/G_1}. \tag{2.21}$$

This analysis of the influence of asymptotically weak and strong flow, and asymptotically weak and strong hydrodynamic interactions illustrates that both play a qualitative role in particle structure. Regardless of the strength of hydrodynamic interactions, the low-*Pe* structure is a diffusive dipole, the high-*Pe* distorted structure is confined to a thin boundary layer, and the infinite-*Pe* structure is spherically symmetric. Such structure leads to a Newtonian plateau of the microviscosity in both low- and infinite-*Pe* limits [124, 78], whereas the evolution from dipole to boundary layer to spherical symmetry leads to force-thinning [124] and force-thickening [78]. Next we obtain the distorted microstructure as it evolves with flow, and elucidate how this evolution is influenced by modulation of the particle interaction distance.

Arbitrary forcing and hydrodynamic interactions

To obtain the distortion in the evolving microstructure under arbitrary probe forcing strength, and in the presence of arbitrary relative strengths of external, Brownian and interparticle forces, we solve the Smoluchowski equation (2.2) utilizing a finite-difference numerical method. A central-difference scheme projects the governing equations onto two-dimensional grids with a uniform angular distribution. As flow strength increases and a boundary layer forms at contact, a grid-point concentration function increases the radial density of grid points near contact to properly capture the physics throughout the entire domain. For N angular and N radial grid points, an $N \times N$ system of linear

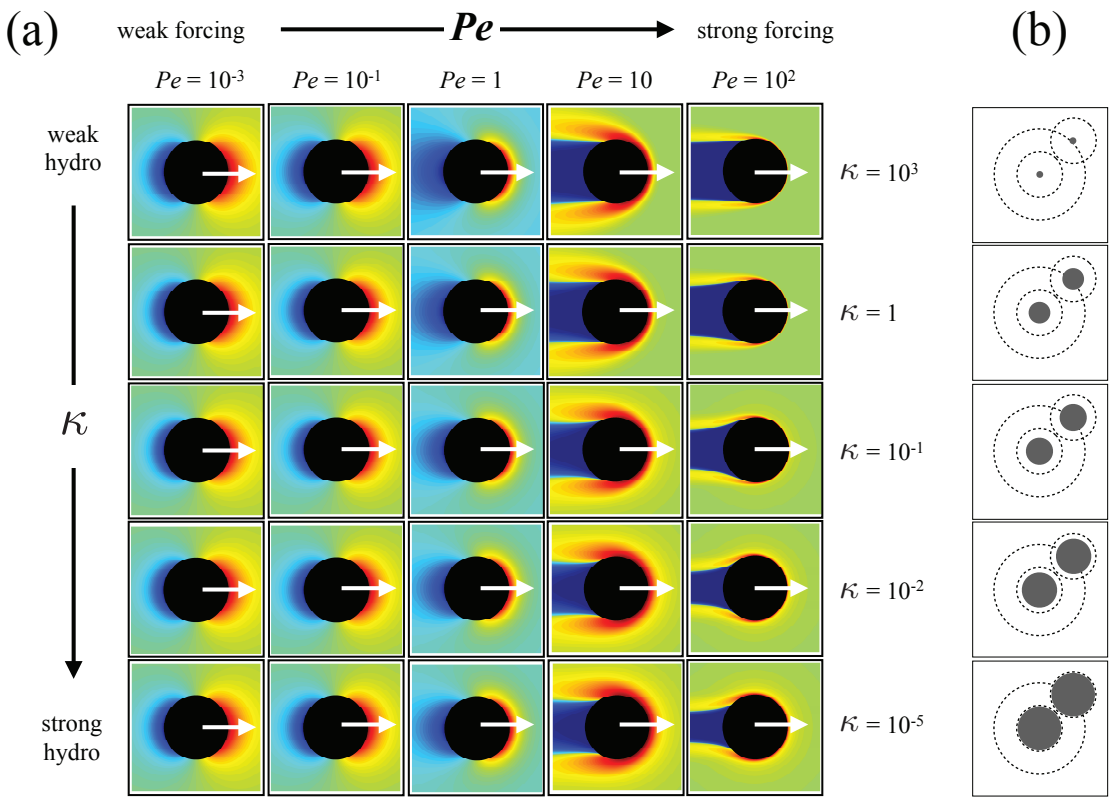

Figure 2.2: (a) The distortion to the microstructure $f(\boldsymbol{r}) \equiv g(\boldsymbol{r}) - 1$ in the symmetry plane of the probe particle as a function of the external forcing Pe and strength of hydrodynamic interactions κ. The black region is the excluded-volume surrounding the probe. Probe forcing increases from left to right, and the strength of hydrodynamic interactions increases from top to bottom, as labeled. Regions in red indicate particle accumulation; blue regions indicate particle depletion. (b) Sketch of excluded-annulus for the same range of κ.

equations is formed and solved utilizing MATLAB's sparse direct solver. For $N \geq 2000$, the relative error of solutions is less than 10^{-8}.

Contour plots of the distorted structure around the probe are shown in Fig. 2.2(a). Flow strength increases from left to right, and the strength of hydrodynamic interactions increases from top to bottom; exact values are labeled in the figure. In the leftmost column, when the microstructure is only slightly per-

turbed by a weakly-forced probe, the disturbance is a diffusive dipole, owing to the dominance of Brownian motion. In the low-*Pe* regime, hydrodynamic interactions exert little apparent influence on particle arrangement, going from top to bottom in the leftmost column. Moving from left to right across any row shows that increasing flow strength leads to more pronounced microstructural asymmetry. Regardless of the strength of hydrodynamic interactions, as *Pe* increases and advection begins to dominate, bath particles accumulate on the upstream face, accompanied by a depletion region behind the probe; a boundary-layer and wake structure emerge at $Pe \approx 10$. The qualitative effect of hydrodynamic interactions on the shape of the distorted microstructure is easy to see as *Pe* grows. For example, moving from top to bottom in the rightmost column, the boundary layer grows more diffuse as hydrodynamic interactions slow the approach of bath particles to the probe. At the same time, the boundary layer remains attached to the probe longer as the same lubrication forces prevent particles from separating downstream from the probe. As will be shown in Sec. 2.4.2, this microstructural effect exerts a pronounced influence on the nonequilibrium suspension rheology.

2.4.2 Suspension stress

The goal of the present section is to employ the solutions for the microstructure obtained in Sec. 2.4.1 to determine the macroscopic stress tensor and, in particular, to examine the relative contributions of external, Brownian, and interparticle forces on its evolution with flow. The primary focus is placed on nonequilibrium behavior; to this end, we define the nonequilibrium stress,

$\langle \boldsymbol{\Sigma}^{neq} \rangle$, as

$$\langle \boldsymbol{\Sigma} \rangle = \langle \boldsymbol{\Sigma}^{0} \rangle + \langle \boldsymbol{\Sigma}^{neq} \rangle, \tag{2.22}$$

where $\langle \boldsymbol{\Sigma}^{0} \rangle$ is the equilibrium suspension stress in the absence of external forcing. The stress is a tensor with six independent elements in general. In microrheology, however, only the normal stresses are nonzero, owing to the axisymmetric geometry of the structure around the probe. We begin with a detailed analysis of the stresses acting parallel and perpendicular to the direction of the external force, $\Sigma_{\parallel}$ and $\Sigma_{\perp}$, respectively.

The parallel and perpendicular normal stresses are obtained by projecting the stress tensor as

$$\langle \Sigma_{\parallel} \rangle = \langle \boldsymbol{\Sigma} \rangle : \boldsymbol{e}_z \boldsymbol{e}_z, \tag{2.23}$$

$$\langle \Sigma_{\perp} \rangle = \langle \boldsymbol{\Sigma} \rangle : \boldsymbol{e}_y \boldsymbol{e}_y, \tag{2.24}$$

where $\boldsymbol{e}_z$ and $\boldsymbol{e}_y$ are the unit vectors in the direction parallel and perpendicular to the external force respectively. The stress tensor $\langle \boldsymbol{\Sigma} \rangle$ comprises external-force induced, Brownian, and interparticle contributions as defined in Eq. (2.5). In turn, the integral expressions for each of these contributions are given by Eqs. (2.12)–(2.14). These forms are utilized throughout this section to compute the normal stresses.

Parallel normal stress

Weak probe force, $Pe \ll 1$

To compute the parallel normal stress under weak probe forcing, the asymptotic result for the distorted microstructure $f(\boldsymbol{r})$ obtained in Sec. 2.4.1 is inserted into expressions (2.12)–(2.14). The external-force induced, Brownian, and inter-

particle contributions to the nonequilibrium parallel normal stress can then be written to leading order as

$$\frac{\langle \Sigma_{\parallel}^{neq} \rangle^{H,ext}}{n_a kT\phi_b} = Pe^2 \int_2^{\infty} \left[\mathcal{A}^{H,ext}(r) + \mathcal{B}^{H,ext}(r) \right] f_1(r) r^2 dr + O(Pe^4), \tag{2.25}$$

$$\frac{\langle \Sigma_{\parallel}^{neq} \rangle^{B}}{n_a kT\phi_b} = Pe^2 \int_2^{\infty} \left\{ \mathcal{A}^{B}(r) f_2(r) + \mathcal{B}^{B}(r) \left[f_2(r) + 3h_2(r) \right] \right\} r^2 dr + O(Pe^4), \tag{2.26}$$

$$\frac{\langle \Sigma_{\parallel}^{neq} \rangle^{P}}{n_a kT\phi_b} = Pe^2 \left\{ \mathcal{A}^{P} f_2(2) + \mathcal{B}^{P}[f_2(2) + 3h_2(2)] + C^{P} \left[f_2(2) + \frac{5}{3} h_2(2) \right] \right\} + O(Pe^4), \tag{2.27}$$

where $\mathcal{A}$'s and $\mathcal{B}$'s are derived from the traceless and the isotropic part of the stress tensor respectively, following from the historical development of traceless and isotropic hydrodynamic functions (cf. Sec. 2.3.2). The term associated with the constant C^P corresponds to the elastic stress, $n_a \langle \boldsymbol{r}\boldsymbol{F}^P \rangle$. The detailed expressions for $\mathcal{A}$'s, $\mathcal{B}$'s, and C^P are given in Appendix C.

In the absence of hydrodynamic interactions, $\kappa \to \infty$, the hydrodynamic stress vanishes. Only the non-hydrodynamic elastic interparticle stress survives. The low-Pe asymptote can be written with its Pe^2 coefficients as:

$$\frac{\langle \Sigma_{\parallel}^{neq} \rangle^{P}}{n_a kT\phi_b} \sim -\frac{8}{3} Pe^2 \quad \text{for} \quad Pe \ll 1,\ \kappa \to \infty, \tag{2.28}$$

recovering the result of Zia and Brady [154].

In the opposite limit of strong hydrodynamic interactions, the external-force induced stress and the Brownian stress dominate, while the interparticle stress vanishes. The low-Pe asymptotes with their Pe^2 coefficients read:

$$\frac{\langle \Sigma_{\parallel}^{neq} \rangle^{H,ext}}{n_a kT\phi_b} \sim -0.34 Pe^2, \quad \frac{\langle \Sigma_{\parallel}^{neq} \rangle^{B}}{n_a kT\phi_b} \sim -0.79 Pe^2 \quad \text{for} \quad Pe \ll 1,\ \kappa \to 0, \tag{2.29}$$

which, when combined, grows as $1.1 Pe^2$.

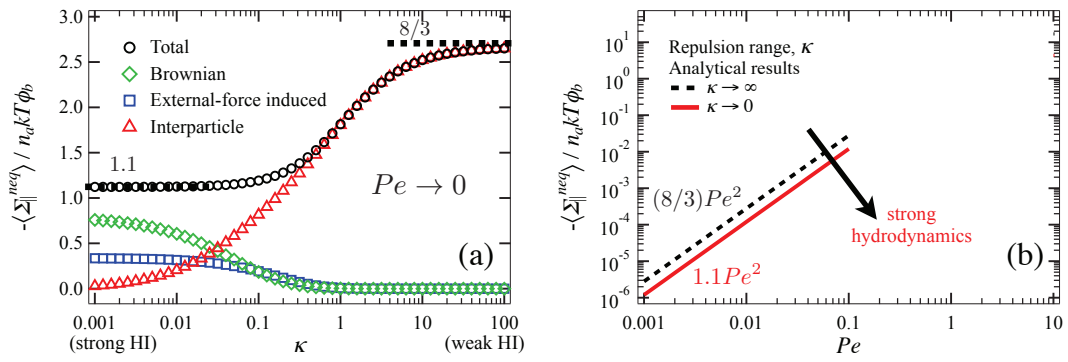

Figure 2.3: Effect of hydrodynamic interactions on the parallel nonequilibrium normal stresses in the low-*Pe* regime. (a) Individual contributions to total stress for $Pe \to 0$, as a function of strength of hydrodynamic interactions κ. External-force induced stress, Eq. (2.25) (□); Brownian stress, Eq. (2.26) (◊); interparticle stress, Eq. (2.27) (△); total stress, sum of Eqs. (2.25)–(2.27) (◯). The asymptotic results for weak and strong hydrodynamic interactions are 8/3 and 1.1, respectively. (b) Effect of weak versus strong hydrodynamic interactions in the low-*Pe* regime, on the *total* parallel normal stress. Black dashed line: low-*Pe* asymptote for weak hydrodynamic interactions, $\kappa \to \infty$. Red solid line: low-*Pe* asymptote for strong hydrodynamic interactions, $\kappa \to 0$.

Each of these contributions in Eqs. (2.25)–(2.27) is scaled by the ideal osmotic pressure $n_a kT$ and the volume fraction of bath particles ϕ_b, and is plotted in Fig. 2.3(a) as a function of the strength of hydrodynamic interactions κ. Toward the left end of the horizontal axis, $\kappa \to 0$, hydrodynamic interactions are strong. Here, the interparticle stress approaches zero because lubrication forces prevent direct particle contact. In this low-*Pe* limit, Brownian motion is much stronger than advection and, as a result, the disturbance flows that gives rise to the Brownian stress are stronger than the weak advective flow due to probe motion. The Brownian stress (diamond symbols) thus dominates, followed by the external-force induced contribution (square symbols), and the interparticle contribution

(triangle symbols). Each of them achieves its asymptotic value as described in Eq. (2.29), and the total stress $-\langle\Sigma_{\parallel}^{neq}\rangle/n_a kT\phi_b$ asymptotes to 1.1 as $Pe, \kappa \to 0$. In the opposite limit of weak hydrodynamic interactions, the right end of the horizontal axis, particles interact only when their surfaces contact. In this limit, the no-flux surface extends far beyond the no-slip surface, and thus particles are too far apart to interact hydrodynamically. The Brownian and external-force induced stresses, which arise only when particles interact through the solvent, thus become weak; they are identically zero when $\kappa^{-1} \equiv 0$. Interestingly, the total suspension stress is higher in this limit, reaching its asymptotic value 8/3, recovering Eq. (2.28). This can be understood by recalling the origin of the external-force induced and interparticle stresses. As discussed in Sec. 2.3.2, the external-force induced stress on the surface of hard particles arises under flow because the particles cannot deform, and it acts over the no-slip particle surface. The interparticle stress arises when particle overlaps are prevented; this entropic force acts over the entire no-flux surface. As κ increases from zero, the no-flux surface extends beyond the no-slip surface, leading to a growth in the effective particle size (cf. Fig. 2.2b). As hydrodynamic interactions become weaker, this growth in the effective size leads to a dramatic growth in entropic exclusion, which permits more frequent particle collisions. The decrease in the external-force induced stress is outweighed by the increase in the entropic stress, and so the total stress is higher in a suspension where hydrodynamic interactions are weak than when they are strong. This behavior can be seen in the plot in the intermediate-κ regime where the interparticle (entropic) contribution outpaces that due to external and Brownian forces.

The three contributions are combined to give the total nonequilibrium parallel normal stress, $\langle\Sigma_{\parallel}^{neq}\rangle$, plotted in Fig. 2.3(b), as a function of the external forc-

ing strength, Pe. Two asymptotes are shown corresponding to the limit of weak ($\kappa \to \infty$) and strong ($\kappa \to 0$) hydrodynamic interactions. In the linear-response regime, the parallel normal stress scales as Pe^2 regardless of the strength of hydrodynamic interactions, but becomes quantitatively weaker as hydrodynamic interactions grow stronger. The decrease in the stress is due to the shrinking effective particle size which increases the available free volume. Equivalently, it can be stated that hydrodynamics suppress the total parallel normal stress by preventing particle collisions.

Strong probe force, $Pe \gg 1$

The $O(Pe^{\delta})$ buildup of pair density inside the high-Pe boundary layer (Sec. 2.4.1) is accompanied by a relatively undisturbed upstream structure and a trailing wake depleted of particles. The effect of this highly asymmetric structure on the suspension stress is studied by inserting the asymptotic results for the microstructure, in the limits of strong and weak hydrodynamic interactions, into Eqs. (2.12)–(2.14). Careful separation of these expressions into integrals over the outer and inner regions is revealing. The outer region makes no appreciable contribution to the nonequilibrium stress regardless of the strength of hydrodynamic interactions. In particular, in the limit of strong hydrodynamic interactions, all terms are identically zero owing to the spherical symmetry of the outer microstructure, save one term that decays as $1/r^7$. In the pair limit, the suspension stress is thus determined entirely by the dynamics of the boundary layer. The high-Pe parallel normal stress can then be computed by inserting the boundary-layer solution for the distorted microstructure $f(\boldsymbol{r})$, Eqs. (2.19) and (2.20), for the limits of weak and strong hydrodynamic interactions respectively, into Eqs. (2.12)–(2.14), where the radial integration is now carried out over the

stretched radial coordinate y.

In the absence of hydrodynamic interactions, only the elastic interparticle stress matters,

$$\begin{aligned}\frac{\langle\Sigma_{\parallel}^{neq}\rangle^{P}}{n_a kT\phi_b} &= Pe\int_0^{\pi}(-6)\left(\cos^2\theta\sin\theta\right)\hat{f}(0,\theta)d\theta + O(1)\\ &\sim -\frac{3}{2}Pe \quad \text{for} \quad Pe\gg 1,\ \kappa\to\infty,\end{aligned} \tag{2.30}$$

where for compactness we have defined $\hat{f}\equiv\cos\theta\, e^{-Pe(r-2)\cos\theta}$. In this dual limit of strong forcing and weak hydrodynamic interactions, the suspension stress scales linearly in the external force Pe, recovering the result of Zia and Brady [154].

In the opposite limit of strong hydrodynamic interactions, external force, Brownian motion, and interparticle forces all play a role. In particular, we expect that the external-force induced stress dominates in this dual limit of $Pe\gg 1$ and $\kappa\to 0$. In this limit, the hydrodynamic functions in Eqs. (2.12)–(2.14) take on their lubrication-limit values, *viz.*

$$\begin{aligned}\frac{\langle\Sigma_{\parallel}^{neq}\rangle^{H,ext}}{n_a kT\phi_b} &= Pe^{\delta}\ln Pe\left[\int_{0+\epsilon}^{\pi}\int_0^{\infty}\left(\cos^3\theta\sin\theta-\cos\theta\sin\theta\right)\tilde{f}(y,\theta)dyd\theta\right]\mathcal{D}^{H,ext}\\ &\quad +Pe^{\delta}\left[\int_{0+\epsilon}^{\pi}\int_0^{\infty}\left(\cos^3\theta\sin\theta-\cos\theta\sin\theta\right)\tilde{f}(y,\theta)dyd\theta\right]\mathcal{E}^{H,ext}\\ &\quad +Pe^{\delta}\left[\int_{0+\epsilon}^{\pi}\int_0^{\infty}\left(\cos\theta\sin\theta\right)\tilde{f}(y,\theta)dyd\theta\right]\mathcal{F}^{H,ext}+O(Pe^{\delta-1}\ln Pe),\end{aligned} \tag{2.31}$$

$$\begin{aligned}\frac{\langle\Sigma_{\parallel}^{neq}\rangle^{B}}{n_a kT\phi_b} &= Pe^{\delta-1}\ln Pe\left\{\left[\int_{0+\epsilon}^{\pi}\int_0^{\infty}\left(\cos^2\theta\sin\theta-\frac{1}{3}\sin\theta\right)\tilde{f}(y,\theta)dyd\theta\right]\mathcal{D}^{B}\right.\\ &\quad \left.+\left[\int_0^{\pi}\int_{0+\epsilon}^{\infty}\left(\sin\theta\right)\tilde{f}(y,\theta)dyd\theta\right]\mathcal{F}^{B}\right\}+O(Pe^{\delta-1}),\end{aligned} \tag{2.32}$$

$$\begin{aligned}\frac{\langle \Sigma_{\parallel}^{neq} \rangle^P}{n_a kT\phi_b} = \; & Pe^{\delta}\left\{\left[\int_{0+\epsilon}^{\pi}\left(\cos^2\theta\sin\theta - \frac{1}{3}\sin\theta\right)\tilde{f}(0,\theta)d\theta\right]\mathcal{D}^P\right. \\ & + \left[\int_{0+\epsilon}^{\pi}(\sin\theta)\,\tilde{f}(0,\theta)d\theta\right]\mathcal{F}^P \\ & \left. + \left[\int_{0+\epsilon}^{\pi}\left(\cos^2\theta\sin\theta\right)\tilde{f}(0,\theta)d\theta\right]\mathcal{H}^P\right\} + O(Pe^{\delta-1}\ln Pe),\end{aligned} \tag{2.33}$$

where $\delta = 0.799$. For compactness, we have introduced the coefficients $\mathcal{D}$ and $\mathcal{E}$ associated with the traceless hydrodynamic functions, $\mathcal{F}$ with the isotropic ones, and $\mathcal{H}$ for the elastic stresslet $\langle \boldsymbol{rF}^P \rangle$. The detailed expressions for the $\mathcal{D}$'s, $\mathcal{E}$, $\mathcal{F}$'s and $\mathcal{H}$ are given in Appendix C. Again, as in the previous section for weak probe force, and Sec. 2.3.2, the separation into traceless and isotropic terms arises from a separate historical development of traceless and isotropic hydrodynamic functions [80, 79, 73, 74].

We pause to inspect Eqs. (2.31)–(2.33) for convergence behavior, noting that $O(1)$ angular diffusion (small compared to $O(Pe)$ radial diffusion, and radial and angular advection) was neglected in simplifying the boundary layer equation to obtain the analytical microstructural solution, $\tilde{f}$ [Eqs. (2.20)–(2.21)], as originally shown by Khair and Brady [78]. Angular advection and diffusion act to close the wake formed by the detaching boundary layer. The diffusive contribution is most important in a small region $\theta < \epsilon$, where $\epsilon/\pi \ll 1$, and thus its neglect near $\theta = 0$ produces divergent behavior. To avoid this behavior yet faithfully account for downstream physics, a value of ϵ is selected to meet two criteria: first, ϵ must be sufficiently large to avoid the divergent region at and very near $\theta = 0$. Second, ϵ must be sufficiently small to avoid enclosing a significant portion of the detaching boundary layer structure, where $f = O(Pe^{\delta})$, *i.e.* to primarily enclose the low-particle density wake [$f = O(1)$]. A value of $\epsilon = 0.1\pi$ was selected to meet both criteria. Further reduction of this value showed negligible improvement in accuracy of the computation.

Before discussing the scaling in Pe of the above (boundary layer) expressions, we emphasize that these expressions are valid only for finite (and large) Pe, where there is formation of a boundary layer around the probe due to the finite diffusion arising from residual Brownian motion. The behavior in the singular pure-hydrodynamic limit, $Pe^{-1} \equiv 0$ and $\kappa = 0$, where there is no contribution from Brownian (or interparticle) forces and thus no boundary-layer formation, requires special treatment. We recall from Sec. 2.4.1 that the microstructure around the probe is spherically symmetric when $Pe^{-1} \equiv 0$ and $\kappa = 0$. In this pure-hydrodynamic limit, inserting the microstructure into the only contribution from the external-force induced stress, Eq. (2.12), we can readily see that the integrals vanish, *i.e.* a net zero normal stress, recovering the Newtonian response in the limit $Pe^{-1} \equiv 0$ and $\kappa = 0$. Any stochastic force, *e.g.* interparticle repulsion or Brownian motion, breaks the spherically symmetric microstructure, resulting in a finite normal stress. For instance, when $\kappa \neq 0$, one will still obtain a finite normal stress even when $Pe^{-1} \equiv 0$. In the following, we utilize the asymptotic expressions, Eqs. (2.31)–(2.33), to predict the behavior when $Pe \gg 1$ and $\kappa \to 0$.

Let us inspect the scaling in Pe of each of these expressions, beginning with the Brownian stress, Eq. (2.32). All terms in this expression scale as $Pe^{-0.201} \ln Pe$. While all terms in the interparticle stress, Eq. (2.33), also have identical scalings, here they scale as $Pe^{0.799}$. The external-force induced stress, Eq. (2.31), exhibits different scalings in Pe for each of its terms: the first term (deriving from the traceless portion of the stress) scales as $Pe^{0.799} \ln Pe$, which arises from transverse relative motion between particles; whereas the second (also from traceless) and the third (isotropic) term both scale as $Pe^{0.799}$, which arise from longitudinal relative motion. From these two scalings, one may expect that the first term

dominates the scaling. However, a careful examination of Eq. (2.31) reveals that the associated hydrodynamic coupling, $\mathcal{D}^{H,ext}$, is negligibly weak in the present strong forcing limit, as shown in Eq. (B.9). Physically, the stress generated from the relative rotational motion and that from relative transverse translational motion of particles cancel each other precisely. As a result, the weak hydrodynamic coupling, $\mathcal{D}^{H,ext}$, yields a negligible contribution from the $O(Pe^{0.799} \ln Pe)$ term, and the external-force induced stress is dominated by the second and the third $O(Pe^{0.799})$ terms [whose hydrodynamic couplings, $\mathcal{D}^{H,ext}$ and $\mathcal{F}^{H,ext}$, are $O(1)$]. These scalings can be summarized as follows:

$$\langle \Sigma_{\parallel}^{neq} \rangle^{H,ext} \sim Pe^{0.799} \quad \text{for} \quad Pe \gg 1,\ \kappa \to 0, \tag{2.34}$$

$$\langle \Sigma_{\parallel}^{neq} \rangle^{B} \sim Pe^{-0.201} \ln Pe \quad \text{for} \quad Pe \gg 1,\ \kappa \to 0, \tag{2.35}$$

$$\langle \Sigma_{\parallel}^{neq} \rangle^{P} \sim Pe^{0.799} \quad \text{for} \quad Pe \gg 1,\ \kappa \to 0. \tag{2.36}$$

The three contributions are combined to give the total nonequilibrium parallel normal stress, $\langle \Sigma_{\parallel}^{neq} \rangle$, plotted in Fig. 2.4 as a function of the external force Pe. As seen by the two high-Pe asymptotes for $\kappa \to \infty$ and $\kappa \to 0$, the influence of the flow strength, Pe, on the stress changes qualitatively with the strength of hydrodynamic interactions. For weak hydrodynamic interactions, $\kappa \to \infty$, where only the elastic interparticle stress matters, the parallel normal stress scales linearly in Pe, recovering the result of Zia and Brady [154], and Eq. (2.30). In contrast, when hydrodynamic interactions are strong, $\kappa \to 0$, the behavior is set by lubrication interactions inside the boundary layer and, in consequence, the external-force induced stress [Eq. (2.31)] dominates the behavior. In particular, as discussed above, the $O(Pe^{0.799})$ terms dominate. The scaling reflects both the indirect and direct effect of hydrodynamics [14]. The indirect effect is the influence on structure, which reduces the scaling in Pe from unity to $Pe^{0.799}$; hydrodynamics also

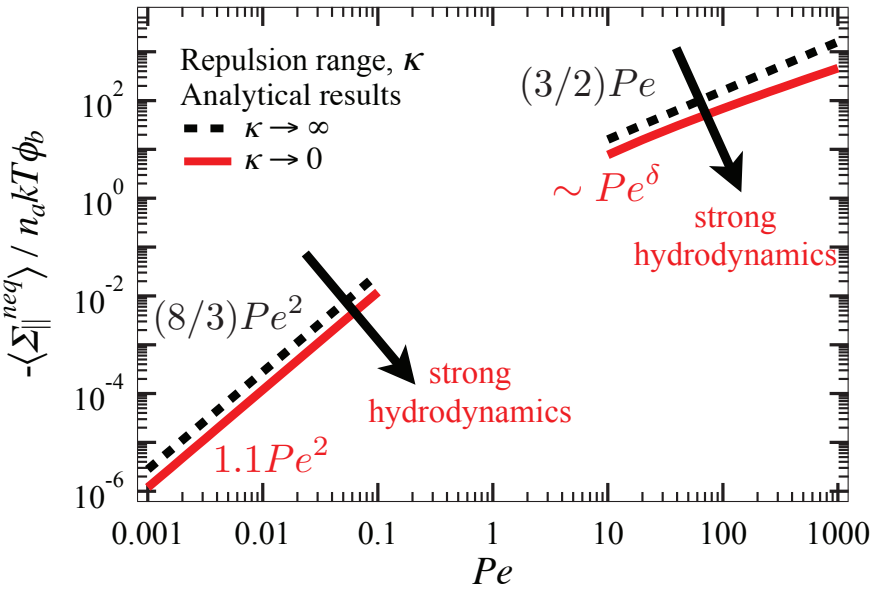

Figure 2.4: Asymptotic behavior of the parallel nonequilibrium normal stresses. Black dashed line: low- [Eq. (2.27)] and high-*Pe* [Eq. (2.30)] asymptote for weak hydrodynamic interactions, $\kappa \to \infty$. Red solid line: low- and high-*Pe* asymptote for strong hydrodynamic interactions, $\kappa \to 0$ [sum of Eqs. (2.25)–(2.27), and sum of Eqs. (2.31)–(2.33), respectively].

exert a direct influence via the hydrodynamic coupling (resistance and mobility functions), whose strength is $O(1)$. The overall effect is suppressive, giving rise to a parallel normal stress that is sublinear in *Pe*.

In summary, in the asymptotic limits of weak and strong external force ($Pe \ll 1$ and $Pe \gg 1$) and hydrodynamic interactions ($\kappa \to \infty$ and $\kappa \to 0$), the stress response mirrors an evolving interplay between external, Brownian and interparticle forces. Strengthening the entropic force signifies a growth in the effective particle size. This leads to a reduction in the accessible free volume, thereby increasing the parallel normal stress — quantitatively at small *Pe* and qualitatively at high *Pe*. Equivalently stated, the stress is suppressed by hydrodynamic interactions. The natural next step is to investigate the transition of

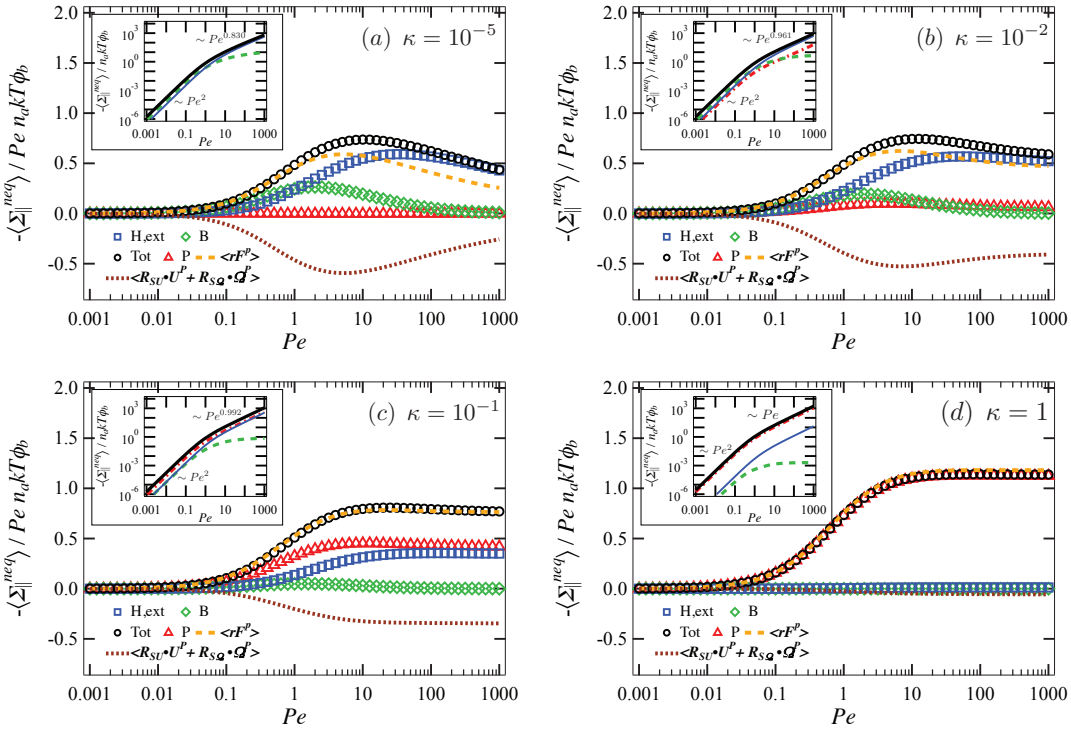

Figure 2.5: Parallel nonequilibrium normal stresses $\langle\Sigma_{\parallel}^{neq}\rangle$ scaled advectively by external probe forcing Pe, ideal osmotic pressure $n_a kT$ and volume fraction of bath particles ϕ_b, as a function of Pe for four different values of κ ranging from strong to weak hydrodynamic interactions: (a) $\kappa = 10^{-5}$, (b) $\kappa = 10^{-2}$, (c) $\kappa = 10^{-1}$, and (d) $\kappa = 1$. Each plot shows the external-force induced stress, Eq. (2.12) (□), Brownian stress, Eq. (2.13) (◇), interparticle stress, Eq. (2.14) (△), and the total stress (○). The interparticle contribution comprises two parts: dashed lines represent the elastic stresslet $\langle \boldsymbol{rF}^P\rangle$; dotted lines represent the dissipative stresslet $\langle \boldsymbol{R}_{SU}\cdot\boldsymbol{U}^P + \boldsymbol{R}_{S\Omega}\cdot\boldsymbol{\Omega}^P\rangle$. The insets illustrate the parallel nonequilibrium normal stress $\langle\Sigma_{\parallel}^{neq}\rangle$ scaled diffusively by $n_a kT\phi_b$. Dashed lines of corresponding colors are used for clarity.

this relationship by studying the evolution of stress under arbitrary strength of external force and hydrodynamic interactions.

Arbitrary strength of probe force and hydrodynamic interactions

We now turn our attention to the evolution of the total parallel nonequilibrium normal stress, $\langle \Sigma_{\parallel}^{neq} \rangle$, as probe force increases from weak to strong, with a focus on the underlying external-force induced, Brownian and interparticle contributions. Figure 2.5 shows these contributions as a function of the external probe forcing Pe for four different strengths of hydrodynamic interactions κ, going from strong (a) to weak (d). In the main plot of each panel (a)–(d), the stress is re-scaled advectively, $\langle \Sigma_{\parallel}^{neq} \rangle / Pe\, n_a kT \phi_b$, and plotted over six decades of Pe. The total stress (circles) comprises the external-force induced (squares), Brownian (diamonds), and interparticle (triangles) contributions. There are two components of the interparticle stress, deriving from the elastic $\langle \boldsymbol{rF}^P \rangle$ and dissipative parts $\langle \boldsymbol{R}_{SU} \cdot \boldsymbol{U}^P + \boldsymbol{R}_{S\Omega} \cdot \boldsymbol{\Omega}^P \rangle$, shown by dashed and dotted lines respectively.

The Brownian stress, the elastic interparticle stress, and the external-force induced stress are all negative where, as noted in Sec. 2.3.2, this corresponds to a stress on the particle phase that acts to drive a pair apart (along the z-direction). In contrast, the dissipative interparticle stress is positive, corresponding to a stress on the particle phase that acts to drive a pair together (along the z-direction). This macroscopic picture can be understood at the micro-mechanical level by considering a pair interacting along the trajectory of a bath particle moving past the probe, which we now illustrate.

We consider a reference frame of a stationary probe particle, whereby a bath particle is advected toward it, along an upstream trajectory at a distance ϵ_U from the stagnation streamline (line of the external force) as shown in Fig. 2.6. In the pure-hydrodynamic limit, where there is no Brownian motion or particle roughness, *i.e.*, $Pe^{-1} \equiv 0$ and $\kappa = 0$, the trajectories are symmetric upstream and downstream of the probe, owing to the reversibility of Stokes flow. At finite

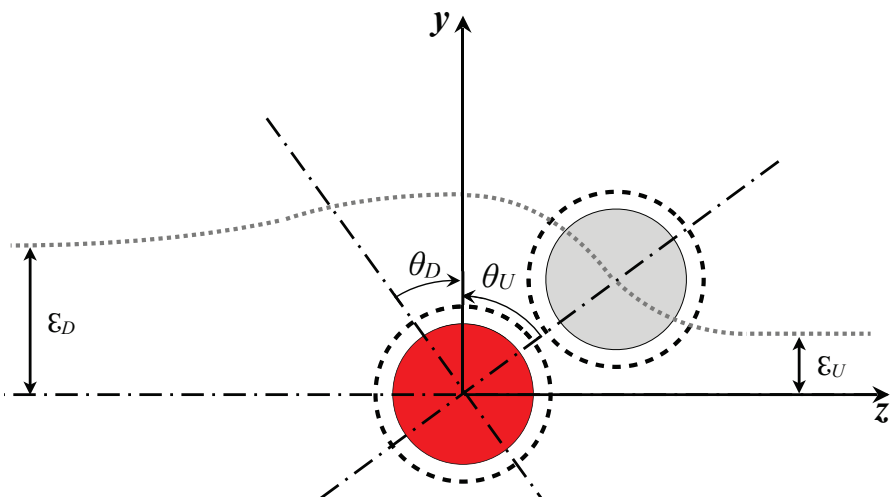

Figure 2.6: Illustration of the relative trajectory of a bath particle (grey) moving past a probe particle (red). Fore-aft symmetry is broken by *e.g.* particle roughness or Brownian forces.

Pe and/or finite κ, the interaction forces between the particles will displace the bath particle radially outward from its Stokes-flow trajectory (dashed lines). As the bath particle moves past the probe, its new trajectory is a distance $\epsilon_D > \epsilon_U$ from the stagnation streamline. The region of this encounter is confined to the boundary layer – both upstream and where it detaches into the trailing wake downstream. The duration of the encounter (at a given radial separation) spans an angle $\theta_U > \theta_D$ in the upstream and downstream regions, respectively. The duration of an encounter is set by the strength of the hydrodynamic coupling along the full trajectory and is a function of the radial separation between two particles. Let us examine how the hydrodynamic coupling – its strength and duration – sets the signs of the stress.

Stresslets are induced by relative motion between particles. The hydrodynamic functions couple particle motion along and transverse to the line of centers connecting the pair [cf. Eqs. (2.12)–(2.14)]. As discussed in the previous section for the high-*Pe* stress [cf. Eq. (2.31)], the longitudinal motion produces

a stresslet that scales as $O(1)\mathcal{E}^{H,ext}$ (computation of the average brings an additional $Pe^{0.799}$ with the microstructure). In contrast, the transverse motion produces a stresslet that scales as $O(\ln Pe)\mathcal{D}^{H,ext}$ (computation of the average brings an additional $Pe^{0.799}$). As noted above, $\mathcal{D}^{H,ext} \to 0$ for $Pe \gg 1$ and thus the longitudinal contribution dominates when Brownian motion is weak, for both $\Sigma_{\parallel}$ and $\Sigma_{\perp}$. Thus, relative trajectories are dominated by the longitudinal components of $\langle \Sigma_{\parallel} \rangle^{H,ext}$.

Let us now consider the evolution of the external-force induced stress, $\langle \Sigma_{\parallel}^{neq} \rangle^{H,ext}$ as a bath particle resolves an encounter with (passes) the probe. Its relative motion produces a disturbance flow that gives rise to a stresslet on the probe surface with an orientation downstream that is the mirror image of that produced during the upstream portion of the trajectory. The projection of the stresslet that acts parallel to the external force, $S_{\parallel}^{ext,H}$, is negative upstream, acting to drive particles apart, but is positive downstream, acting to pull particles together. But we recall from the trajectory analysis that the radial separation between particles is evolving: a bath particle departs with an angle θ_D smaller than the angle of incidence θ_U, when $\kappa \neq 0$. That is, while a bath particle can approach the probe along any upstream trajectory to generate a negative stress, the bath particle cannot travel to a downstream location with the same radial separation. Instead, its departing trajectory is deflected to one with a larger radial separation, generating a weaker (positive) stress. As a result, in resolving an encounter, the negative stress generated by a particle upstream is stronger than the positive stress generated downstream, yielding an averaged negative stress acting to drive particles apart.

Next, let us look at the Brownian stress, $\langle \Sigma_{\parallel}^{neq} \rangle^{B}$. Brownian motion conveys

particles to regions of higher mobility; that is, to regions of lower particle concentration. As illustrated in Fig. 2.6, the Brownian stress thus acts to separate two particles, whether a bath particle is in the upstream or the downstream region of the probe. As a result, the Brownian stress is always negative, signifying its tendency to drive particles apart.

Interestingly, the effect of interparticle force is twofold, contributing to both negative elastic stress and positive dissipative stress. The elastic interparticle stress arises from entropic exclusion of particle overlap (direct collisions). A hard probe will experience a repulsive force when colliding with a bath particle, driving them apart regardless of the angular position (both upstream and downstream) at which the collision occurs. This gives rise to a negative elastic stress. Upon collision, the interparticle force induces an interparticle velocity, $\boldsymbol{U}^P = \boldsymbol{M}_{UF} \cdot \boldsymbol{F}^P$, describing the separating motion of two particles. However, the separating particles are coupled hydrodynamically. The departing motion of one particle entrains the other, inducing a dissipative stress, hindering particle separation. That is, dissipative stress has the opposite effect of the elastic stress — its acts to pull particles together.

The stress shown in the main plots in Fig. 2.5 can be viewed in terms of its strength relative to the "advective stress", $(n_a F_0 a/2)\phi_b$,

$$\frac{\langle \Sigma_{\parallel}^{neq} \rangle}{Pe\, n_a kT \phi_b} = \frac{\langle \Sigma_{\parallel}^{neq} \rangle}{(n_a F_0 a/2)\phi_b}, \tag{2.37}$$

which, in the strong-forcing limit, is Pe-large. In the absence of hydrodynamic interactions, the normal stress $\langle \Sigma_{\parallel}^{neq} \rangle$ is $O(Pe)$ as well, and thus when scaled on Pe, reaches a plateau (Fig. 2.5d). But when hydrodynamic interactions are important (Fig. 2.5a), $\langle \Sigma_{\parallel}^{neq} \rangle / Pe\, n_a kT \phi_b$ decreases monotonically toward zero, as Pe increases. It vanishes entirely only in the noncolloidal limit $Pe^{-1} \equiv 0$ when

the structure is spherically symmetric. It is the external-force induced stress, $\langle \Sigma_{\parallel}^{neq} \rangle^{H,ext}$, that drives this behavior, again illustrating that hydrodynamic interactions *suppress the growth of the stress*. As a result, the external-force induced stress scaled advectively by Pe decays as $Pe^{-0.201}$ as Pe grows larger. This is more than a simple consequence of re-scaling. Rather, it reveals a deeper connection between particle motion and suspension stress, which can be viewed through the lens of the time scale of particle motion.

The Pécet number is a ratio of time scales, diffusive to advective: $Pe = \tau_{diff}/\tau_{adv}$, where $\tau_{diff} = a^2/D_a$ and $\tau_{adv} = a/U$. In the large-Pe limit, the time required for the probe to advect its size is much shorter than the time required for it to diffuse the same distance: $Pe = \tau_{diff}/\tau_{adv} \gg 1$. Insertion of this definition of Pe into $\langle \Sigma_{\parallel}^{neq} \rangle / Pe\, n_a kT\phi_b$ gives:

$$\frac{\langle \Sigma_{\parallel}^{neq} \rangle}{Pe\, n_a kT\phi_b} = \frac{\langle \Sigma_{\parallel}^{neq} \rangle}{n_a kT\phi_b} \left(\frac{\tau_{adv}}{\tau_{diff}} \right). \tag{2.38}$$

The quantity $\langle \Sigma_{\parallel}^{neq} \rangle / n_a kT$ (insets) represents a *diffusive* scaling of the stress; it is made dimensionless on the ideal osmotic pressure $n_a kT$, which arises from Brownian motion. The diffusive scaling of the stress thus reveals how distortions to the microstructure by probe motion give rise to stress as viewed on the Brownian time scale. As Pe grows, the distance that the probe can move in one such Brownian time also grows, and thus the number of encounters with other particles — interactions which produce stress — grows dramatically on the diffusive time scale. Hence the stress becomes very large compared with the ideal (Brownian) osmotic pressure, as shown by the continuous high-Pe growth labeled in each inset. Regardless of the strength of hydrodynamic interactions, the total stress grows without bound on the diffusive time scale (insets). However, when scaled advectively (main plots), the stress saturates to a plateau value

in the absence of hydrodynamic interactions and vanishes entirely in the pure-hydrodynamic (noncolloidal) limit. The latter result is somewhat surprising, and can be understood as follows.

Suspension stress is generated by encounters between particles and, as shown by Zia and Brady [154], is a balance between entropic storage and viscous dissipation of the energy of probe motion. In the high-Pe limit, the stress is dominated by encounters within the boundary layer at contact. The strength, frequency, and duration of such encounters determine the magnitude of the stress. The strength is $\sim kT$ as set simply by entropic exclusion: a pair of particles cannot pass through one another and thus must pass by each other. The frequency of encounters is set by how fast a particle can advect into contact and by particle size. It is during the encounter that probe energy is both stored and dissipated, because collisions distort microstructural configuration and thus give rise to entropic energy storage [155]. They also dissipate energy as a pair of particles must advect and diffuse through the boundary layer to pass, giving rise to both solvent and microstructural drag. In the absence of hydrodynamics, the fluid between particles is freely draining and thus the frequency of encounters scales as Pe. The duration of interactions is set by the bare diffusivity of the probe, $D_a = kT/6\pi\eta a_h$. A re-scaling of the stress on the advective time scales out the frequency of collisions, leading to the plateau behavior observed in Fig. 2.5(d).

Hydrodynamic coupling slows the advection of particles into the boundary layer, hinders their diffusion through it, and slows their separation. As hydrodynamic interactions begin to play a role, the frequency of interactions is hindered and, in the limit $\kappa \to 0$, reduced to $O(Pe^{0.799})$. *The key difference in the*

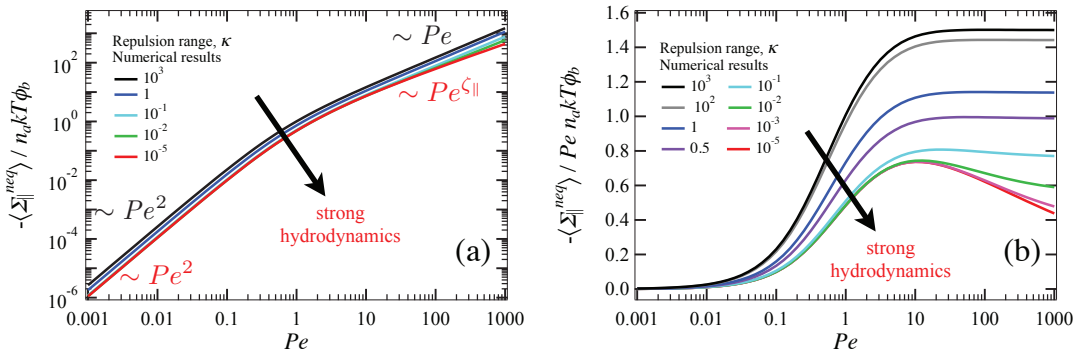

Figure 2.7: (a) Parallel nonequilibrium normal stresses $\langle \Sigma_{\parallel}^{neq} \rangle$ scaled diffusively by ideal osmotic pressure $n_a kT$ and volume fraction of bath particles ϕ_b, as a function of external probe forcing Pe for various strength of hydrodynamic interactions κ. (b) Parallel nonequilibrium normal stresses $\langle \Sigma_{\parallel}^{neq} \rangle$ scaled advectively by Pe, $n_a kT$ and ϕ_b, as a function of Pe for various κ.

stress when hydrodynamic interactions are present arises due to the duration of such encounters. Probe energy is expended throughout this viscous interaction. In the high-Pe limit, one diffusive time is much longer than one advective time. Thus, if one waits one diffusive time, particles have a long time to "resolve" collisions, and eventually pass by one another. One advective time however, is just a tiny fraction of a diffusive time and, over such short times, the particles cannot resolve a collision. Differently stated, they spend all the time trying to diffuse past one another in a very viscous interaction of long duration. If all the energy is dissipated, it cannot be stored [68]. As Pe increases, the duration and dissipation of such encounters increases. Thus, the nonequilibrium advectively-scaled parallel normal stress decays continuously as Pe increases, and vanishes entirely in the noncolloidal limit $Pe^{-1} \equiv 0$.

We now turn our focus to the interparticle contribution (triangles), which comprises the elastic stress, $n_a \langle \boldsymbol{r}\boldsymbol{F}^P \rangle$ (dashed lines), and the dissipative stress,

$n_a\langle \boldsymbol{R}_{SU} \cdot \boldsymbol{U}^P + \boldsymbol{R}_{S\Omega} \cdot \boldsymbol{\Omega}^P \rangle$ (dotted lines). As seen in Figs. 2.5(a)–(d) in the figure, these two interparticle contributions act against one another and, when combined, play a role that depends on the strength of hydrodynamic interactions. In the limit of strong hydrodynamic interactions (a), the interparticle stress makes no contribution for the entire range of Pe. This zero interparticle stress is typically explained by the dogma that asserts that lubrication forces prevent particle contact, and thus the (hard-sphere) interparticle force plays no dynamic role in the evolution of particle configuration, thereby generating no stress [20, 23]. But as seen in Fig. 2.5(a), this interpretation can be refined — the interparticle force does play a role in stress generation, as reflected by the nonzero contributions of the underlying elastic interparticle and dissipative interparticle stresses. Indeed, as explained earlier in our trajectory analysis, these two contributions correspond to stresses that drive particles apart and together, respectively. In the plot, these two contributions are equal in magnitude, but opposite in sign. The idea that the interparticle stress is zero in this limit is simply a consequence of their precise cancellation. In other words, the interparticle force does play a role in stress generation even in the limit of strong hydrodynamic interactions. Ultimately, one should expect a hard-sphere interparticle force to play a role in the evolution of *all* rheological quantities: Hoh and Zia [68] recently found that a hard-sphere interparticle force still influences the fluctuating field of particles and gives rise to longitudinal force-induced diffusion even in the pure-hydrodynamic limit with smooth particles.

The interparticle stress eventually becomes appreciable when the excluded annulus grows, *e.g.* for particles with surface asperities, as shown in Fig. 2.5(b) for $\kappa = 10^{-2}$. As discussed above, the interparticle velocity is reduced by the dissipative interparticle stresslet but, as κ grows, the reduction becomes weaker

and so does the dissipative interparticle stress. Surprisingly, this is accompanied by a weak increase in the external-force induced stress. This arises because a small increase in the excluded-annulus creates a region of higher relative mobility near contact or, equivalently, a weaker lubrication force near contact. While the strength of lubrication interactions is weaker, more particles are allowed into the boundary layer to exert stress on the probe, driving a (weak) increase in the external-force induced stress.

In Fig. 2.5(c), where $\kappa = 10^{-1}$, the interparticle stress overtakes that due to external force. The growth in the effective particle size drives up the stress due to entropic exclusion. The larger excluded annulus also weakens the strength of hydrodynamic interactions; the external-force induced stress becomes weaker than the interparticle stress over the full range of Pe. However, the total normal stress increases in magnitude, because the increased entropic exclusion outweighs the weakening external-force induced stress.

When the interparticle repulsion range reaches $\kappa = 1$ in Fig. 2.5(d), the interparticle force dominates the total stress. The Brownian stress is nearly zero for all Pe, and the external-force induced stress is several orders of magnitude weaker over all Pe. Notably, the dissipative part of the interparticle stress, which is hydrodynamic in origin, is negligibly small and, in the present case of weak hydrodynamic interactions, the interparticle stress derives primarily from elastic collisions, $n_a\langle \boldsymbol{r}\boldsymbol{F}^P\rangle$. In the high-$Pe$ limit, the total stress reaches a plateau, in contrast to the decay exhibited in Figs. 2.5(a)–(c). A practical implication is that non-Newtonian behaviors persist in a non-hydrodynamically interacting suspension for measurements taken on the advective time scale, that is, the moving frame of the probe; while they decay with increasing probe forcing when hy-

drodynamic interactions are present, and vanish in the noncolloidal limit where Brownian motion is absent.

The evolution of the total parallel normal stress is summarized in Fig. 2.7: in frame (a), at low Pe, the numerical results agree with the weak- and strong-hydrodynamic interactions asymptotes. In this limit, the influence of hydrodynamic interactions on the parallel normal stress is quantitative: the stress decreases with increasing strength of hydrodynamic interactions, but the Pe^2 scaling is unchanged. The stress increases monotonically when probe forcing increases; when probe forcing becomes strong, the effect of hydrodynamic interactions on the parallel normal stress is qualitative: the stress increases linearly in Pe when hydrodynamic interactions are weak, $\kappa \to \infty$. As hydrodynamic interactions get stronger, *i.e.* shortening the repulsion range κ via shrinking of effective particle size, the external-force induced stress dominates, and the growth is suppressed. Notably, in the limit of strong hydrodynamic interactions ($\kappa \to 0$), the stress at $Pe = 10^3$ scales as $Pe^{\zeta_\parallel}$, where $\zeta_\parallel \approx 0.830$, meaning that the actual high-Pe scaling, $Pe^{0.799}$, can be achieved only for $Pe > 10^3$. That is, the influence of Brownian motion on non-Newtonian rheology and structural asymmetry persists even when Brownian motion becomes very weak. Thus the approach to the infinite-Pe asymptote is quite slow. The same data, scaled advectively, are plotted in Fig. 2.7(b), where the effect of hydrodynamic interactions on the total stress at high Pe is evident.

In summary, the Pe-dependence of the parallel normal stress (and that of the external-force induced, Brownian, and interparticle contributions) is always quadratic when the external force is weak. When the forcing is strong, stress generation is governed by dynamics of the boundary layer, which give rise to

κ-dependent scalings: Pe and $Pe^{0.799}$ for the limits of weak and strong hydrodynamic interactions, respectively. The origins of stress generation by underlying microscopic forces are identified, where the force-induced, Brownian and the elastic interparticle stress are responsible to drive particles apart, whereas the dissipative interparticle stress pulls particles together. In the limit of strong hydrodynamic interactions, we showed that a hard-sphere interparticle force does play a role in stress generation. The observation that the interparticle stress is zero in this limit is a consequence of the exact cancellation between the elastic and dissipative interparticle stresses. Regardless of the strength of hydrodynamic interactions, the relative contribution of the Brownian stress shrinks as advection grows stronger. Enhancing the range of entropic repulsion, equivalently reducing the strength of hydrodynamic coupling, shortens the duration of particle encounter, but increases frequency of collisions while leading to a growth in the parallel normal stress for any strength of probe forcing. Re-scaling the normal stress advectively shows that it persists only in non-hydrodynamically interacting suspensions. The presence of hydrodynamic interactions leads to attenuation in the non-Newtonian response, and a suspension becomes Newtonian in the noncolloidal limit.

Perpendicular normal stress

Weak probe force, $Pe \ll 1$

We begin the investigation of the perpendicular normal stress by studying the limit of weak external forcing. The asymptotic result for the distorted microstructure $f(\boldsymbol{r})$ given by Eq. (2.18) is inserted into expressions (2.12)–(2.14). The external-force induced, Brownian, and interparticle contributions to the

nonequilibrium perpendicular normal stress thus become, to leading order,

$$\frac{\langle \Sigma_{\perp}^{neq} \rangle^{H,ext}}{n_a kT\phi_b} = Pe^2 \int_2^{\infty} \left[-\frac{1}{2}\mathcal{A}^{H,ext}(r) + \mathcal{B}^{H,ext}(r) \right] f_1(r) r^2 dr + O(Pe^4), \tag{2.39}$$

$$\frac{\langle \Sigma_{\perp}^{neq} \rangle^{B}}{n_a kT\phi_b} = Pe^2 \int_2^{\infty} \left\{ -\frac{1}{2}\mathcal{A}^{B}(r) f_2(r) + \mathcal{B}^{B}(r) \left[f_2(r) + 3h_2(r) \right] \right\} r^2 dr + O(Pe^4), \tag{2.40}$$

$$\frac{\langle \Sigma_{\perp}^{neq} \rangle^{P}}{n_a kT\phi_b} = Pe^2 \left\{ -\frac{1}{2}\mathcal{A}^{P} f_2(2) + \mathcal{B}^{P}[f_2(2) + 3h_2(2)] + \mathcal{G}^{P} \left[f_2(2) + 5h_2(2) \right] \right\} + O(Pe^4), \tag{2.41}$$

where $\mathcal{A}^{H,ext}$, $\mathcal{B}^{H,ext}$, $\mathcal{A}^{B}$, $\mathcal{B}^{B}$, $\mathcal{A}^{P}$, $\mathcal{B}^{P}$ and $\mathcal{G}^{P}$ are compact expressions for the hydrodynamic functions and are given in Appendix C. As was the case for the parallel normal stress, the $\mathcal{A}$'s and $\mathcal{B}$'s are derived from the traceless and the isotropic part of the stress tensor respectively, following from the historical development of traceless and isotropic hydrodynamic functions (Sec. 2.3.2). The constant $\mathcal{G}^{P}$ corresponds to the elastic stress.

In the absence of hydrodynamic interactions, $\kappa \to \infty$, the hydrodynamic stress vanishes and only the non-hydrodynamic elastic interparticle stress survives. The low-*Pe* asymptote can be written with its Pe^2 coefficients as:

$$\frac{\langle \Sigma_{\perp}^{neq} \rangle^{P}}{n_a kT\phi_b} \sim -\frac{8}{3}Pe^2 \quad \text{for} \quad Pe \ll 1,\ \kappa \to \infty, \tag{2.42}$$

where we note that its scaling in *Pe* is identical to that of the parallel normal stress, and it recovers the result of Zia and Brady [154].

In the opposite limit of strong hydrodynamic interactions, the interparticle stress vanishes because lubrication interactions prevent particle contact. The external-force induced stress and Brownian stress dominate. The low-*Pe* asymptotes with their Pe^2 coefficients read:

$$\frac{\langle \Sigma_{\perp}^{neq} \rangle^{H,ext}}{n_a kT\phi_b} \sim -0.062Pe^2, \quad \frac{\langle \Sigma_{\perp}^{neq} \rangle^{B}}{n_a kT\phi_b} \sim -0.94Pe^2 \quad \text{for} \quad Pe \ll 1,\ \kappa \to 0, \tag{2.43}$$

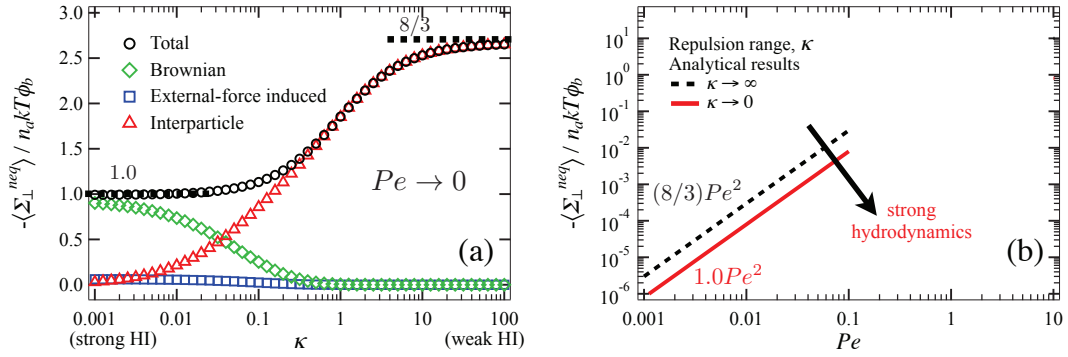

Figure 2.8: Effect of hydrodynamic interactions on the perpendicular nonequilibrium normal stresses in the low-*Pe* regime. (a) Individual contributions to total stress for $Pe \to 0$, as a function of strength of hydrodynamic interactions κ. External-force induced stress, Eq. (2.41) (□); Brownian stress, Eq. (2.42) (◇); interparticle stress, Eq. (2.43) (△); total stress, sum of Eqs. (2.39)–(2.41) (◯). The asymptotic results for weak and strong hydrodynamic interactions are 8/3 and 1.0, respectively. (b) Effect of weak versus strong hydrodynamic interactions in the low-*Pe* regime, on the *total* perpendicular normal stress. Black dashed line: low-*Pe* asymptote for weak hydrodynamic interactions, $\kappa \to \infty$. Red solid line: low-*Pe* asymptote for strong hydrodynamic interactions, $\kappa \to 0$.

which, when combined, grows as $1.0Pe^2$.

The contributions to the low-*Pe* stress given by Eqs. (2.39)–(2.41) are plotted in Fig. 2.8(a) as a function of the strength of hydrodynamic interactions κ. The evolution of these contributions with hydrodynamic interactions is qualitatively the same as that found for the parallel normal stress (cf. Fig. 2.3a): the interparticle stress is most prominent when hydrodynamic interactions are weak ($\kappa \to \infty$), recovering the asymptotic value 8/3 as described in Eq. (2.42), whereas it is negligible when hydrodynamic interactions are strong ($\kappa \to 0$). In this limit of strong Brownian motion and strong hydrodynamic interactions, the Brownian stress plays the dominant role. As seen for the parallel normal stress,

since advection is weak, the external-force induced stress is weaker than the Brownian stress. The total stress achieves its asymptotic value 1.0 [Eq. (2.43)].

All contributions are combined into the total nonequilibrium perpendicular normal stress, $\langle \Sigma_{\perp}^{neq} \rangle$, plotted in Fig. 2.8(b) as a function of small values of Pe. Comparison to Fig. 2.3(b) reveals two key similarities between the perpendicular and parallel normal stresses. First, both scale as Pe^2 regardless of the strength of hydrodynamic interactions. Second, reducing the entropic repulsion range, *i.e.* strengthening hydrodynamic interactions, leads to decrease in the normal stress. Hence, the suppressive role of hydrodynamic interactions in both normal stresses is quantitative when forcing is weak.

Strong probe force, $Pe \gg 1$

In the opposite limit of strong external probe forcing, the perpendicular normal stress is computed by inserting the boundary-layer solution for the distorted microstructure $f(\boldsymbol{r})$, Eqs. (2.19) and (2.21) for the limits of weak and strong hydrodynamic interactions respectively, into Eqs. (2.12)–(2.14). In the absence of hydrodynamic interactions, only interparticle forces matter. The high-Pe asymptote of the perpendicular normal stresses reads,

$$\frac{\langle \Sigma_{\perp}^{neq} \rangle^P}{n_a kT \phi_b} = Pe \int_0^{\pi} (-3) \left(\sin^3 \theta \right) \hat{f}(0, \theta) d\theta + O(1) \sim -\frac{3}{4} Pe \quad \text{for} \quad Pe \gg 1, \ \kappa \to \infty, \tag{2.44}$$

which scales linearly in Pe, the same scaling as the parallel normal stress in this limit, and recovers the result of Zia and Brady [154].

In the opposite limit of strong hydrodynamic interactions, the hydrodynamic functions in Eqs. (2.12)–(2.14) take on their lubrication forms. Carrying out integration over the stretched radial coordinate y, the high-Pe asymptotes of

the perpendicular normal stress read,

$$\begin{aligned}\frac{\langle\Sigma_{\perp}^{neq}\rangle^{H,ext}}{n_a kT\phi_b} = \; & Pe^{\delta}\ln Pe\left[-\int_0^{\pi}\int_0^{\infty}\left(\cos^3\theta\sin\theta-\cos\theta\sin\theta\right)\tilde{f}(y,\theta)dyd\theta\right]\frac{\mathcal{D}^{H,ext}}{2}\\ & +Pe^{\delta}\left[-\int_0^{\pi}\int_0^{\infty}\left(\cos^3\theta\sin\theta-\cos\theta\sin\theta\right)\tilde{f}(y,\theta)dyd\theta\right]\frac{\mathcal{E}^{H,ext}}{2}\\ & +Pe^{\delta}\left[\int_0^{\pi}\int_0^{\infty}(\cos\theta\sin\theta)\,\tilde{f}(y,\theta)dyd\theta\right]\mathcal{F}^{H,ext}+O(Pe^{\delta-1}\ln Pe),\end{aligned} \tag{2.45}$$

$$\begin{aligned}\frac{\langle\Sigma_{\perp}^{neq}\rangle^{B}}{n_a kT\phi_b} = \; & Pe^{\delta-1}\ln Pe\left\{\left[-\int_0^{\pi}\int_0^{\infty}\left(\cos^2\theta\sin\theta-\frac{1}{3}\sin\theta\right)\tilde{f}(y,\theta)dyd\theta\right]\frac{\mathcal{D}^{B}}{2}\right.\\ & \left.+\left[\int_0^{\pi}\int_0^{\infty}(\sin\theta)\,\tilde{f}(y,\theta)dyd\theta\right]\mathcal{F}^{B}\right\}+O(Pe^{\delta-1}),\end{aligned} \tag{2.46}$$

$$\begin{aligned}\frac{\langle\Sigma_{\perp}^{neq}\rangle^{P}}{n_a kT\phi_b} = \; & Pe^{\delta}\left\{\left[-\int_0^{\pi}\left(\cos^2\theta\sin\theta-\frac{1}{3}\sin\theta\right)\tilde{f}(0,\theta)d\theta\right]\frac{\mathcal{D}^{P}}{2}\right.\\ & +\left[\int_0^{\pi}(\sin\theta)\,\tilde{f}(0,\theta)d\theta\right]\mathcal{F}^{P}\\ & \left.+\left[\int_0^{\pi}\left(\sin^3\theta\right)\tilde{f}(0,\theta)d\theta\right]\mathcal{I}^{P}\right\}+O(Pe^{\delta-1}\ln Pe),\end{aligned} \tag{2.47}$$

where $\delta = 0.799$. Here, $\mathcal{D}^{H,ext}$, $\mathcal{E}^{H,ext}$, $\mathcal{F}^{H,ext}$, $\mathcal{D}^{B}$, $\mathcal{F}^{B}$, $\mathcal{D}^{P}$, $\mathcal{F}^{P}$ and $\mathcal{I}^{P}$ are compact expressions for the hydrodynamic functions and are given in Appendix C. Following the same nomenclature used for the parallel normal stress, the $\mathcal{D}$'s and $\mathcal{E}$ are associated with the traceless hydrodynamic functions, $\mathcal{F}$'s are with the isotropic ones, and $\mathcal{I}^{P}$ corresponds to the elastic stress. Again, the separation into traceless and isotropic terms arises from a separate historical development of traceless and isotropic hydrodynamic functions [80, 79, 73, 74].

As was the case for the parallel normal stress, the above asymptotes derived from boundary-layer analysis are valid only when Pe is finite. To examine the behavior in the singular pure-hydrodynamic limit, $Pe^{-1} \equiv 0$ and $\kappa = 0$, where contributions from Brownian and interparticle forces are absent and there is no formation of a boundary layer, one can take a different approach by inserting the

spherically symmetric microstructure into the only contribution, the external-force induced stress, Eq. (2.12). This results in a zero perpendicular stress, recovering the Newtonian response in this special limit. Any residual Brownian or interparticle forces, represented by finite Pe or κ respectively, break the spherical symmetry of the microstructure, giving rise to non-Newtonian behavior. In the following, we utilize the above asymptotes to study the behavior when $Pe \gg 1$ and $\kappa \to 0$.

Let us inspect the scaling in Pe of each of the asymptotes, beginning with the Brownian stress, Eq. (2.46). As was the case for the parallel normal stress, all terms in the Brownian stress scale as $Pe^{-0.201} \ln Pe$. All terms in the interparticle stress, Eq. (2.47), also have identical scalings in Pe, $\sim Pe^{0.799}$. The stress arising from the external-force induced motion, Eq. (2.45), exhibits different scalings in Pe for each of its terms: the first term (deriving from the traceless portion of the stress) scales as $Pe^{0.799} \ln Pe$, whereas the second (also from traceless) and the third (isotropic) term scales as $Pe^{0.799}$. As noted in the discussion for the parallel normal stress, the dominance of the hydrodynamic stress is not determined solely by the Pe scaling, but also by the coefficient governing the strength of hydrodynamic coupling. Since the hydrodynamic coupling coefficient, $\mathcal{D}^{H,ext}$, approaches zero in the present strong forcing limit, the $O(Pe^{0.799} \ln Pe)$ term is negligibly weak. The external-force induced stress is thus dominated by the $O(Pe^{0.799})$ terms. These scalings can be summarized as follows:

$$\langle \Sigma_{\perp}^{neq} \rangle^{H,ext} \sim Pe^{0.799} \quad \text{for} \quad Pe \gg 1,\ \kappa \to 0, \tag{2.48}$$

$$\langle \Sigma_{\perp}^{neq} \rangle^{B} \sim Pe^{-0.201} \ln Pe \quad \text{for} \quad Pe \gg 1,\ \kappa \to 0, \tag{2.49}$$

$$\langle \Sigma_{\perp}^{neq} \rangle^{P} \sim Pe^{0.799} \quad \text{for} \quad Pe \gg 1,\ \kappa \to 0, \tag{2.50}$$

which are identical to the parallel counterparts (cf. Eqs. (2.34)–(2.36)). As before

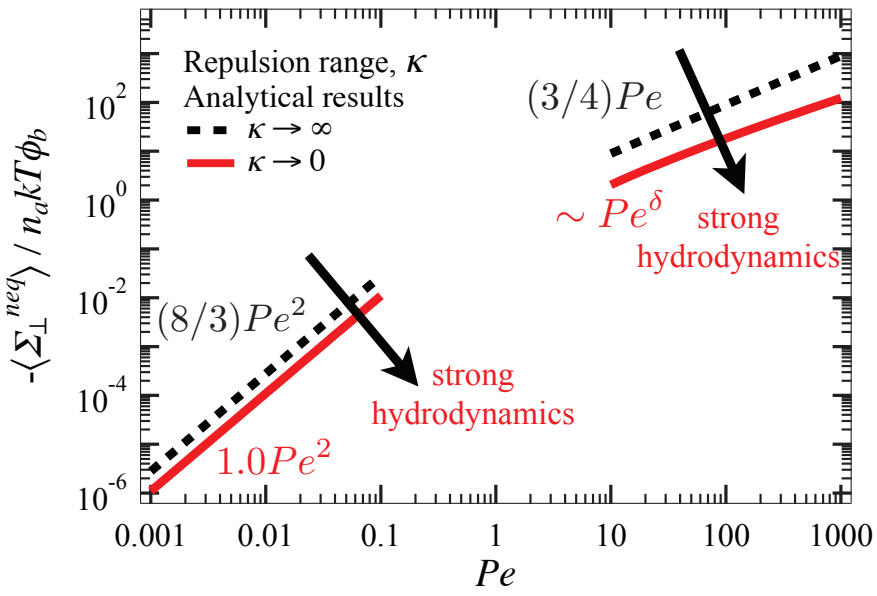

Figure 2.9: Asymptotic behavior of the perpendicular nonequilibrium normal stresses. Black dashed line: low- [Eq. (2.41)] and high-*Pe* [Eq. (2.44)] asymptote for weak hydrodynamic interactions, $\kappa \to \infty$. Red solid line: low- and high-*Pe* asymptote for strong hydrodynamic interactions, $\kappa \to 0$ [sum of Eqs. (2.39)–(2.41) and sum of Eqs. (2.45)–(2.47), respectively].

for the parallel stress, when hydrodynamic interactions are strong, $\kappa \to 0$, lubrication interactions inside the boundary layer sets the high-*Pe* stress, and thus, the external-force induced stress, Eq. (2.48), dominates the behavior.

The three contributions are combined to give the total nonequilibrium perpendicular normal stress, $\langle \Sigma_\perp^{neq} \rangle$, plotted in Fig. 2.9 as a function of the external forcing strength *Pe*. As was the case for the parallel normal stress, the two asymptotes for $\kappa \to \infty$ and $\kappa \to 0$ demonstrate that the influence of flow strength on the high-*Pe* stress changes qualitatively with the strength of hydrodynamic interactions. When hydrodynamic interactions are negligibly weak, $\kappa \to \infty$, the high-*Pe* perpendicular stress grows linearly in *Pe*, recovering the result of Zia and Brady [154], and the predicted scaling from Eq. (2.44). In the opposite

limit when hydrodynamic interactions are strong, $\kappa \to 0$, we again observe an indirect and a direct influence of hydrodynamic interactions, reflected by the reduced Pe-exponent and the introduction of an $O(1)$ hydrodynamic coupling, respectively. The combined influence is a weakening effect, yielding a suppressed perpendicular stress in the presence of hydrodynamic interactions.

In summary, the asymptotic results that we presented for the limits of weak and strong forcing ($Pe \ll 1$ and $Pe \gg 1$) and hydrodynamic interactions ($\kappa \to \infty$ and $\kappa \to 0$) demonstrate an evolving interplay between external, Brownian and interparticle forces. Increasing the entropic repulsion range leads to a larger effective particle size and thus weaker hydrodynamic interactions. As was the case for the parallel normal stress, as hydrodynamic interactions weaken the perpendicular normal stress grows, quantitatively at low Pe and qualitatively at high Pe. That is, when forcing is weak, the scaling of the perpendicular stress is Pe^2 in both asymptotic limits of weak and strong hydrodynamics, whereas when forcing is strong the scaling of the stress changes from $Pe^{0.799}$ to Pe from the limit of strong to weak hydrodynamics. To understand the transition of this relationship, in the next section we will examine the evolution of stress under arbitrary strength of external force and hydrodynamic interactions.

Arbitrary strength of probe force and hydrodynamic interactions

To examine the detailed evolution of the perpendicular normal stress for arbitrary external probe forcing Pe and arbitrary strength of hydrodynamic interactions κ, the total nonequilibrium perpendicular normal stress $\langle \Sigma_{\perp}^{neq} \rangle / n_a kT\phi_b$ is plotted in Fig. 2.10(a) as a function of Pe, for several values of κ. At low Pe, the numerical results show an excellent agreement with the asymptotic theory

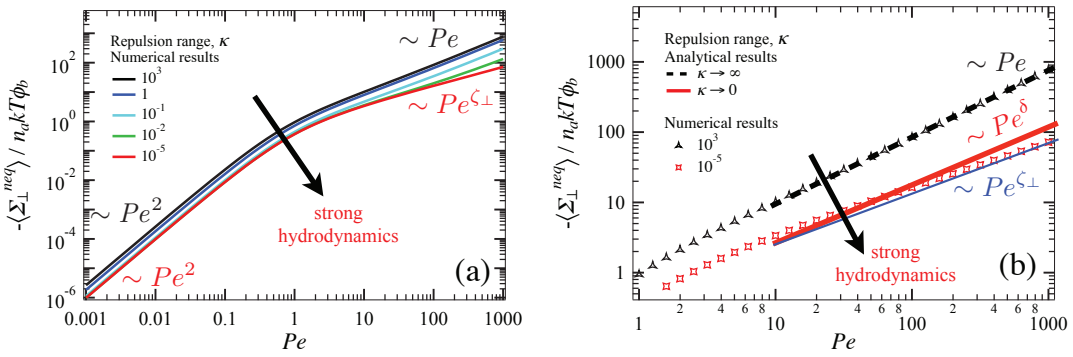

Figure 2.10: (a) Perpendicular nonequilibrium normal stresses $\langle\Sigma_\perp^{neq}\rangle$ scaled by ideal osmotic pressure $n_a kT$ and volume fraction of bath particles ϕ_b, as a function of external probe forcing Pe for various strength of hydrodynamic interactions κ. (b) Perpendicular nonequilibrium normal stresses $\langle\Sigma_\perp^{neq}\rangle/n_a kT\phi_b$ in the high-Pe regime. Black dashed line: high-Pe asymptote for weak hydrodynamic interactions, $\kappa \to \infty$ [Eq. (2.44)], which scales as Pe. Red solid line: high-Pe asymptote for strong hydrodynamic interactions, $\kappa \to 0$ [sum of Eqs. (2.45)–(2.47)], which scales as Pe^δ with $\delta = 0.799$. Symbols: numerical results, which grow as $Pe^{\zeta_\perp}$ with $\zeta_\perp = 0.648$ (blue solid line) for $Pe = 10^3$.

in the limits of strong and weak hydrodynamic interactions. The numerical results demonstrate that this Pe^2 scaling is preserved for all κ, that is, regardless of the strength of hydrodynamic interactions. As probe forcing strength increases, the perpendicular normal stress increases monotonically with Pe. When forcing is strong, the perpendicular stress grows linearly in Pe for weak hydrodynamic interactions, but sublinearly as hydrodynamic interactions grow stronger until, when $\kappa \to 0$, $\langle\Sigma_\perp^{neq}\rangle \sim Pe^{0.799}$. We note that the predicted scaling, $Pe^{0.799}$, is not achieved even at $Pe = 10^3$. Instead, it scales as $Pe^{\zeta_\perp}$, where $\zeta_\perp \approx 0.648$ (Fig. 2.10b). To understand this behavior, let us take a closer look at the high-Pe perpendicular stress.

Similar to the discussion in the previous section, the high-Pe perpendicular

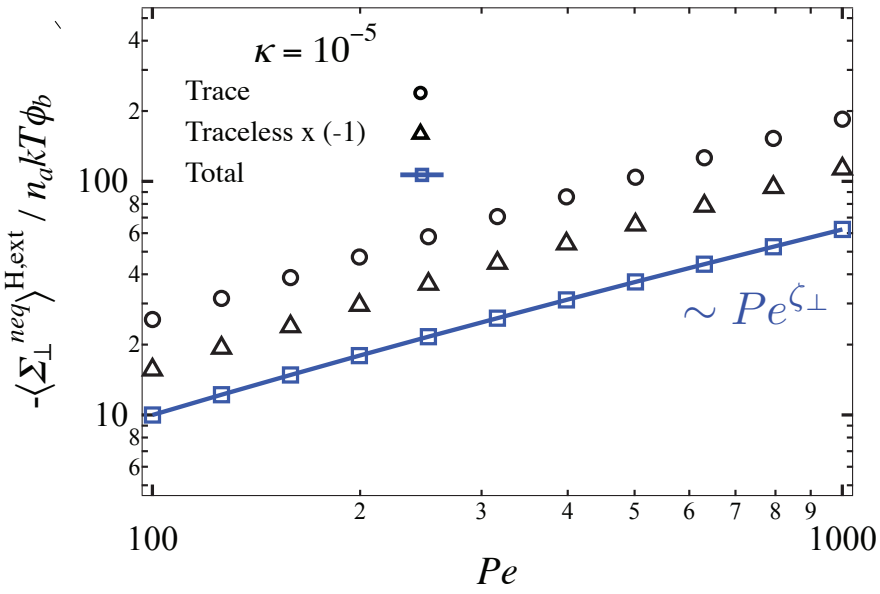

Figure 2.11: External-force induced perpendicular normal stress $\langle \Sigma_\perp^{neq} \rangle^{H,ext} / n_a kT\phi_b$ and its isotropic and traceless components in the limit of strong hydrodynamic interactions, $\kappa = 10^{-5}$. Symbols are numerical results: circles (◯), isotropic part of the external-force induced stress; triangles (△), traceless part of the external-force induced stress; squares (□), total external-force induced stress. The traceless term has been multiplied by −1 to make it visible on the log-log plot.

stress is dominated by its external-force induced contribution [Eq. (2.45)]. The external-force induced stress comprises an isotropic and a traceless component, both scaled as $Pe^{0.799}$ as $Pe \to \infty$ [as we discussed, the $O(Pe^{\delta} \ln Pe)$ term is negligible due to the weak hydrodynamic coupling $\mathcal{D}^{H,ext}$]. For finite but strong flow, $Pe = 10^3$, these two components compete: the negative isotropic term scaled as $Pe^{0.675}$, and the positive traceless term scaled as $Pe^{0.651}$. In Fig. 2.11, these two terms are plotted along with the total perpendicular stress, where the traceless term has been multiplied by −1 to make it visible on the log-log plot. From the plot, the oppositely-signed isotropic and the traceless terms are comparable in magnitude, although the former is larger. Thus the sum is a negative perpen-

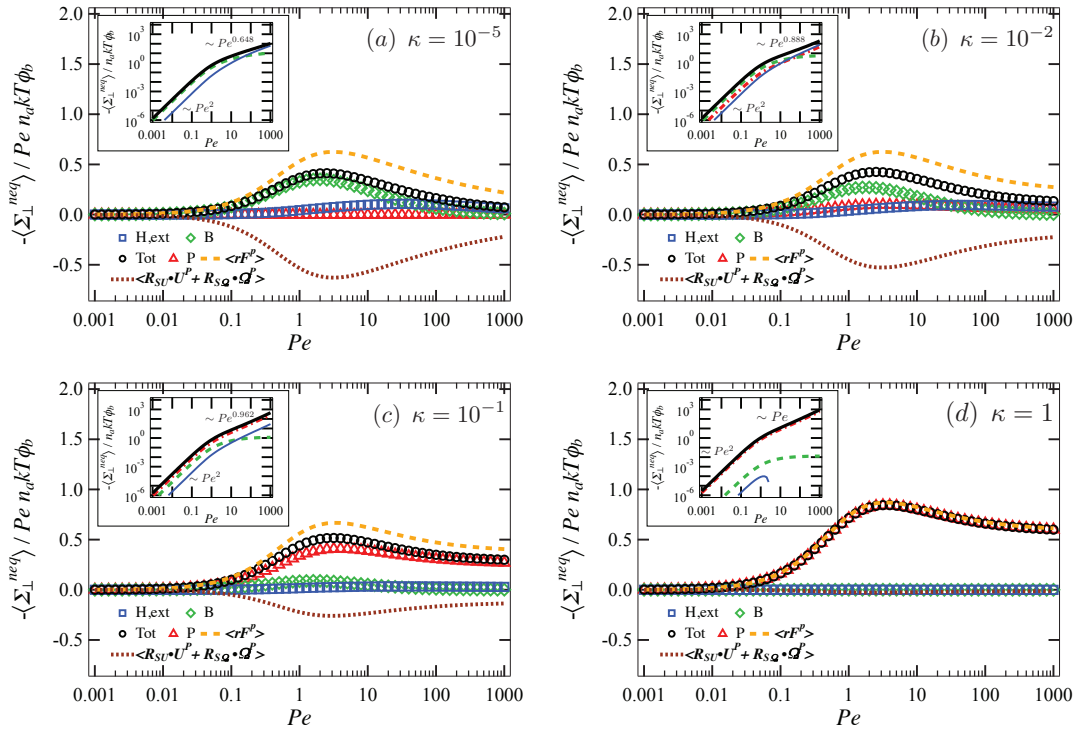

Figure 2.12: Perpendicular nonequilibrium normal stresses $\langle \Sigma_\perp^{neq} \rangle$ scaled advectively by external probe forcing Pe, ideal osmotic pressure $n_a kT$ and volume fraction of bath particles ϕ_b, as a function of Pe for four different values of κ ranging from strong to weak hydrodynamics: (a) $\kappa = 10^{-5}$, (b) $\kappa = 10^{-2}$, (c) $\kappa = 10^{-1}$, and (d) $\kappa = 1$. Each plot shows the external-force induced stress, Eq. (2.12) (□), Brownian stress, Eq. (2.13) (◇), interparticle stress, Eq. (2.14) (△), and the total stress (◯). The interparticle contribution comprises two parts: dashed lines represent the elastic stresslet $\langle \boldsymbol{rF}^P \rangle$; dotted lines represent the dissipative stresslet $\langle \boldsymbol{R}_{SU} \cdot \boldsymbol{U}^P + \boldsymbol{R}_{S\Omega} \cdot \boldsymbol{\Omega}^P \rangle$. The insets illustrate the perpendicular nonequilibrium normal stress $\langle \Sigma_\perp^{neq} \rangle$ scaled diffusively by $n_a kT\phi_b$. Dashed lines of corresponding colors are used for clarity.

dicular stress growing as $Pe^{0.648}$. We expect that, following the dominance of the isotropic term, the total perpendicular stress will stay negative on approaching the limit $Pe \gg 1$, recovering the predicted $Pe^{0.799}$ scaling in the high-Pe limit.

Let us now examine the individual contributions to the total stress. The

external-force induced, Brownian and interparticle contributions to the total nonequilibrium perpendicular normal stress $\langle \Sigma_{\perp}^{neq} \rangle / Pen_a kT\phi_b$ are shown in Fig. 2.12 as a function of Pe for four different strengths of hydrodynamic interactions κ, ranging from strong (a) to weak (d). As was the case for the parallel normal stress, the external-force induced stress, the Brownian stress, and the elastic interparticle stress are all negative for the entire range of Pe regardless of κ, corresponding to a stress on the particle-phase that tends to drive them apart (along the y-direction), whereas the positive dissipative interparticle stress represents a stress that tends to drive particles together (along the y-direction).

In the limit of strong hydrodynamic interactions (Fig. 2.12a), the elastic and dissipative components of the interparticle contribution combine to give negligible interparticle stress, signifying that particles cannot touch. Akin to its parallel counterpart (cf. Fig. 2.5a), one can see an overlap of data points in the low-Pe regime owing to the small contributions from all three external, Brownian and interparticle forces. As the probe forcing strength increases, the importance of the Brownian contribution diminishes, with the external-force induced stress overtaking its dominance. Once again, all the advectively-scaled stress components, including the dominant external-force induced contribution, decrease with increasing Pe in the high-Pe regime. Hydrodynamic interactions suppress the stress, and it no longer scales linearly in Pe. The stress now grows as $Pe^{0.799}$, which results in a decay in $\langle \Sigma_{\perp}^{neq} \rangle$ when scaled by Pe. Despite these similarities, there is a quantitative difference between the two normal stresses. The external-force induced perpendicular normal stress is in general smaller than the parallel counterpart for the entire range of Pe. This is a consequence of the fact that the traceless and isotropic parts of the external-force induced stress are of the opposite sign, which is true regardless of Pe and κ.

The interparticle stress starts to play a role as the dimensionless repulsion range, κ, increases to 10^{-2}, *i.e.* as hydrodynamic interactions become weaker. While the external-force induced stress is still enhanced slightly when κ increases from 10^{-5} to 10^{-2}, its significance in the perpendicular normal stress is curtailed compared to that in the parallel normal stress (cf. Fig. 2.5b), again due to the weakening of its oppositely-signed traceless and isotropic components. Even for Pe as high as 10^3, the external-force induced stress is still comparable to the interparticle stress.

In Fig. 2.12(c), when κ increases to 10^{-1}, the total normal stress increases since the enhanced entropic exclusion exceeds the weakening of the external-force induced and Brownian stresses. The interparticle contribution dominates both near and away from equilibrium. As hydrodynamic interactions get weaker, $\kappa = 1$ in Fig. 2.12(d), particles are sufficiently separated by the excluded-annulus that hydrodynamic interactions are not important: terms that are hydrodynamic in origin, including the external-force induced stress, Brownian stress, and the dissipative interparticle stress, are negligible. Owing to the ability of particles to make contact, the interparticle stress arising from elastic collisions dominates the total stress. As was the case for the parallel stress, the high-Pe plateau suggests that a constant stress response can be measured only in non-hydrodynamically interacting suspensions, in contrast to the decay shown in Figs. 2.12(a)–(c). It mirrors the negligible suppression from hydrodynamic coupling, and thus the perpendicular stress still scales linearly in Pe.

In summary, entropic repulsion (strength of hydrodynamic interactions) plays a central role in the evolution of structure and thus of rheology. A stronger entropic repulsion (longer repulsion range) results in weaker hydrodynamic

coupling, and thus a weaker perpendicular normal stress. Equivalently stated, the suppressive role of hydrodynamic interactions is confirmed by the reduction in the stress with increasing strength of hydrodynamic interactions, for the entire range of probe forcing Pe. Several key qualitative features of the perpendicular normal stress are found to be same as the parallel counterpart. In the asymptotic limit of weak probe forcing, the two normal stresses share the same quadratic dependence on Pe regardless of the strength of hydrodynamic interactions; while in the opposite limit of strong probe forcing, they have the same Pe and $Pe^{0.799}$ scalings in the limits of weak and strong hydrodynamic interactions respectively, where the $Pe^{0.799}$ scaling can be attained only for $Pe \gg 10^3$. Upon scaling the perpendicular stress advectively, the evolution of the underlying external-force induced, Brownian and interparticle contributions were shown to be qualitatively the same as those of the parallel stress. The only contribution tending to pull particles together is the dissipative interparticle stress, whereas the other contributions are all negative, signifying stresses that tend to drive particles apart. Akin to the parallel stress, a high-Pe plateau was demonstrated only in the case of weak hydrodynamic interactions, indicating that a constant stress response can be measured only in non-hydrodynamically interacting suspensions.

2.4.3 Suspension stress and energy storage

Stress can be viewed as the energy density of a suspension [154, 155]. In this section, we expand on this idea utilizing the stress response from Sec. 2.4.2, demonstrating the entropic nature of energy storage as well as the subtle connection between nonequilibrium stress, fluctuation and dissipation.

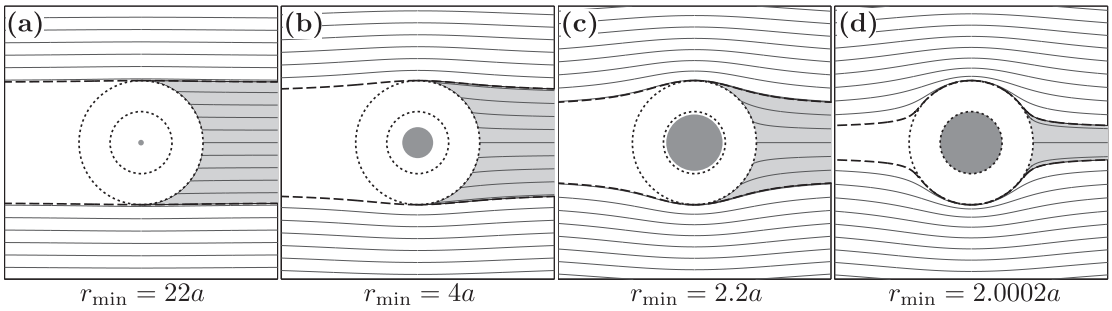

Figure 2.13: Effect of interparticle repulsion on Stokes-flow relative trajectories of probe and bath particle. The probe (grey shaded circle) is forced from left to right. Two dotted-line circles are shown, the smaller corresponds to the excluded-volume size of the probe, and the larger defines the minimum approach distance. The solid grey circle represents the hydrodynamic radius. The solid lines in each panel represent bath particle trajectories. (a) Long-range repulsion (weak hydrodynamic interactions); trajectories are not deflected by hydrodynamic interactions. As repulsion range κ decreases in figures (b), (c), and (d), some bath-particle trajectories are deflected around the probe by hydrodynamic interactions. From [68].

Let us consider the parallel stress as an example. Referring to Fig. 2.7(a), $\langle \Sigma_{\parallel}^{neq} \rangle / n_a kT\phi_b$ gives the energy density in the microstructure along the direction of the probe forcing relative to the thermal energy (density) $n_a kT$. The figure offers insights into energy storage in the parallel microstructure if we scale out the probe number density:

$$\frac{\langle \Sigma_{\parallel}^{neq} \rangle}{n_a kT} = \frac{\langle S_{\parallel}^{neq} \rangle}{kT}, \tag{2.51}$$

where $S_{\parallel}^{neq}$ is the component of the nonequilibrium stresslet parallel to the direction of the external force, and the right-hand side of Eq. (2.51) gives a ratio of the energy stored in a suspension due to probe motion relative to the thermal energy. Let us view Fig. 2.7(a) from the perspective of energy storage. First, let us consider a given flow strength, Pe, but varying repulsion range (strength of hydrodynamic interactions), κ.

The total stress, or energy density, decreases as κ decreases, regardless of flow strength, suggesting that the strength of hydrodynamic interactions influences the degree to which the energy of probe motion can be stored entropically in the deformed microstructure. This is consistent with the idea that nonequilibrium stress requires structural asymmetry; the hydrodynamic interactions that deflect pair collisions do so more effectively as hydrodynamic coupling grows stronger, *i.e.* as the interparticle repulsion range κ decreases. Following the example of Hoh and Zia [68], this idea is illustrated pictorially in Fig. 2.13 where, for simplicity, $Pe^{-1} \equiv 0$ and κ is varied from large to small. The structure around the probe becomes increasingly fore-aft symmetric as strengthening hydrodynamic interactions shield the probe from collisions. Conversely, enhancing entropic repulsion (growing effective particle size) breaks fore-aft structural symmetry, increasing structural distortion and in turn, entropic energy storage. Eventually when $\kappa \equiv 0$, the structure becomes spherically symmetric, recovering Batchelor's solution and Newtonian rheology [15]. When Pe is finite, Brownian motion plays the same role as particle roughness, destroying structural symmetry. As Pe grows large, the role played by Brownian motion is confined to the thin boundary layer, obtaining pronounced structural asymmetry and entropic energy storage, *i.e.* stress grows as Pe increases.

2.5 Conclusions

We have conducted a theoretical study of the suspension stress in a hydrodynamically interacting dispersion of hard colloidal spheres via the active microrheology framework, and elucidated the dependence of the nonequilibrium stress on flow strength and on the range of interparticle repulsion (strength of

hydrodynamics). The behavior was studied analytically in the asymptotic limits of weak and strong external force Pe and hydrodynamic interactions κ, and numerically for arbitrary Pe and κ. We found that entropic forces enhance suspension stress throughout the entire range of probe forcing: for weakly nonlinear departures from equilibrium, where Brownian diffusion dominates, entropic repulsion enhances stresses quantitatively and both normal stresses scale as Pe^2, regardless of the strength of hydrodynamic interactions. As the strength of the probe forcing increases, the degree of fore-aft structural asymmetry is amplified and, at the same time, the normal stress grows — consistent with the idea that structural asymmetry, not just distortion, is necessary to produce nonequilibrium stress. Indeed, when external forcing is strong and structural asymmetry most pronounced, the enhancement of stress by entropic repulsion is a qualitative effect where, at a given value of flow strength, the normal stress scales as Pe^{δ}, with $1 \geq \delta \geq 0.799$ as κ varies from large to small when $Pe \gg 1$; that is, as entropic forces become dominant and hydrodynamic interactions become weak, the growth in stress demonstrates a qualitatively different dependence on the flow strength, Pe. To connect this behavior to microscopic-scale forces, we systematically adjusted hydrodynamic interactions to be strong or weak compared to Brownian motion, and to be strong or weak compared to effects of particle roughness. Doing so revealed that the elastic contribution $n_b\langle \boldsymbol{rF} \rangle$ that dominates the stress when hydrodynamic interactions are weak is *not* replaced by the external-force induced hydrodynamic stress — in contrast to the view that lubrication interactions simply replace the hard-sphere force. Rather, hydrodynamic coupling between particles gives rise to a dissipative interparticle stress of hydrodynamic origin that is opposite in sign and grows in magnitude as κ shrinks, until it precisely cancels the elastic stress. The most interesting

discovery in this regard was that the inelastic part of the interparticle stress is the only contribution that, when considered over a complete trajectory, tends to resist particle separation. This may play a more important role in rheology than currently recognized, *e.g.* the phenomenon of shear-thickening. We next focused our efforts on understanding how, micromechanically, each of these effects alters the stress.

Utilizing a trajectory analysis, we showed exactly how hydrodynamic interaction or, equivalently, the range of interparticle repulsion, alters the stress. We found that a combination of particle-collision frequency and interaction duration, along with the degree to which a stresslet tends to bind a pair together or drive them apart, determines the extent of microstructural asymmetry. In the absence of hydrodynamic interactions, the suspension drains freely and the stress is set solely by $O(Pe)$-frequent hard-sphere collisions. In the opposite limit of no interparticle repulsion, particles are strongly coupled hydrodynamically and the frequency of interactions is reduced to $O(Pe^{0.799})$. Further, a pair remains coupled on the downstream side of the probe, producing a more symmetric microstructure. Eventually in the limit of smooth particles and no Brownian motion, the structure becomes spherically symmetric and the nonequilibrium stress vanishes entirely.

An important outcome of focusing on interparticle repulsion and entropic forces is that it allowed us to form a connection between nonequilibrium stress and entropic energy storage. Again, appealing to our pair-trajectory analysis, we pointed out that entropic forces permit collisions and promote the departure of a bath particle involved in a pair encounter, enhancing destruction of Stokes-flow symmetry and, in turn, entropic energy storage. Conversely, hy-

drodynamic interactions prevent energy storage by shielding particles from collisions and suppress energy storage by coupling particles for a longer duration, muting structural distortion and, in consequence the entropic energy storage. Phenomenologically, a suspension in which hydrodynamic interactions, which are dissipative, play a relatively stronger role, viscously dissipate energy which would otherwise be entropically stored.

Finally, while the focus of the present work was placed on the normal stresses themselves, the normal stress differences and osmotic pressure are two quantities of central importance in the study of the rheology of complex fluids. These are explored in the next chapter.

CHAPTER 3

THE NON-NEWTONIAN RHEOLOGY OF HYDRODYNAMICALLY INTERACTING COLLOIDS VIA ACTIVE, NONLINEAR MICRORHEOLOGY

3.1 Introduction

The non-Newtonian rheology of colloidal dispersions and other complex fluids is set by the asymmetry of the arrangement of the constituent particles in the embedding medium. In dilute suspensions of smooth noncolloids, structural symmetry under strong flow is preserved by the reversibility of relative Stokes-flow trajectories, giving Newtonian rheology. In the opposite limit of an equilibrium suspension of colloids, Brownian motion acts, on average, to preserve symmetry, thus preserving Newtonian rheology. Between these two limits, a rich non-Newtonian rheology emerges in tandem with the development of an asymmetric microstructure, as Brownian motion destroys the symmetry of Stokes-flow trajectories. The presence of other entropic forces such as those introduced by surface asperities gives rise to similar non-Newtonian phenomenology. Many previous studies have demonstrated that the strength of Brownian and hydrodynamic forces evolves with flow strength, producing well-known and familiar behaviors, such as flow thinning, flow thickening and normal stress differences. Detailed study of the connection between the evolving balance of microscopic forces and the formation of asymmetric microstructure has been carried out in focused flow regimes in prior work; a more comprehensive study aimed toward understanding the role played by entropic forces is the focus of the present work.

Experimental study of flow-induced non-Newtonian rheology of suspensions of noncolloidal spherical particles dates back to the work of Bagnold [7], in which he reported the appearance of normal stresses during shear flow. He hypothesized the presence of a particle microstructure, and that shear-flow induced changes in its shape were the origin of non-Newtonian rheology. Following this pioneering work, several studies convincingly inferred the presence of a shear-induced structure in concentrated noncolloidal suspensions [52, 53]. Direct visualization of the distorted structure soon followed in a systematic study of the pair distribution function of the suspended particles by Gadala-Maria and co-workers [72, 111] who, via video imaging, revealed an accumulation of particle pairs along the compressional axes and depletion in the extensional quadrants. In a landmark study of shear-induced migration under structural gradients, Leighton and Acrivos [90] attributed the origin of such structural asymmetry to three-body and higher-order interactions influenced by particle roughness. Numerous subsequent investigations were conducted for suspensions of a wider range of concentration [149, 122, 21], and also in suspensions comprising particles with controlled roughness [116], all confirming that structural asymmetry is necessary to produce non-Newtonian rheology. However, the influence of flow strength and entropic forces on the suspension stress had not been fully explored experimentally owing to two primary challenges: first, the dominance of Brownian noise under (weak) flow makes measurement of weak non-Brownian signals difficult in the low-Pe regime. Second, to interrogate entropic effects, the thermodynamic sizes of particles are required, but such measurement can be challenging. During the same timeframe, development of the nonequilibrium statistical mechanics theory for dilute colloidal dispersions provided guiding insight.

In a series of seminal papers [11, 16, 14], Batchelor confirmed that microstructural asymmetry, not just distortion, is necessary to generate non-Newtonian rheology and, in so doing, paved the path on which the pair-level origin of much non-Newtonian rheology was discovered. He developed the nonequilibrium Smoluchowski framework that governs the evolution of a flowing microstructure under the influence of thermodynamic and hydrodynamic forces, along with expressions for the average suspension stress in dilute colloidal dispersions undergoing flow, and examined them specifically in the pure-hydrodynamic limit under strong flow, $Pe^{-1} = 0$. Here, the Péclet number, Pe, is a measure of the strength of advection, which distorts the suspension, relative to the strength of diffusion that acts to recover the equilibrium microstructure. In the pair limit, the microstructure is fore-aft symmetric and, utilized as a weighting function to compute the average suspension stress, reveals that symmetric structure induces no non-Newtonian behavior. Batchelor predicted, however, that the presence of (even weak) Brownian motion or particle roughness would destroy reversible Stokes' flow trajectories and lead to non-Newtonian rheology. Brady and Vicic [27] validated Batchelor's hypothesis in a study of a weakly sheared suspension in the presence of strong Brownian motion, showing that an asymmetric structure arises from $O(Pe^2)$ flow disturbance, and indeed produces nonzero normal stress differences and a nonequilibrium osmotic pressure. These studies focused, however, only on the limit of strong hydrodynamics. The significance of and the interplay between entropic and hydrodynamic forces in the nonequilibrium stress, as well as the evolution of the stress with flow strength, remained unexplored.

The influence of hydrodynamic interactions on nonequilibrium rheology was later studied by Brady and Morris [26], who employed an excluded-

annulus model [118] to study a strongly-sheared suspension in the limits of asymptotically strong and weak hydrodynamics. Their results revealed that both normal stress differences decrease as hydrodynamic interactions become weak, for two limits: $Pe \ll 1$ and $Pe \gg 1$. In a subsequent work, Bergenholtz *et al.* [19] investigated the evolution of the suspension stress with arbitrary flow strength by solving the Smoluchowski equation numerically for a range of strengths of hydrodynamic interactions. They recovered the high-Pe behavior of the normal stress differences found by Brady and Morris, and further demonstrated that, in the presence of hydrodynamic interactions, the first normal stress difference changes sign from positive to negative, in contrast to the positive first normal stress difference shown for the entire range of flow strength in the absence of hydrodynamics, thus revealing their complex evolution with flow strength. To understand the influence of individual microscopic forces, they computed the hydrodynamic, Brownian and interparticle contributions to the total normal stress differences, and asserted that the interparticle force makes no contribution in the limit of strong hydrodynamics, consistent with the dogma that lubrication interactions prevent particle contact in this limit. However, Chu and Zia [34] extracted the normal stresses from the data of Bergenholtz *et al.*, and discovered that the interparticle normal stresses are not zero even in the limit of strong hydrodynamics. The idea that the interparticle force makes no contribution is unphysical, and was an artifact of the authors' choice to move part of the trace of the interparticle stress to the Brownian stress. This *ad hoc* grouping of stress contributions smears out the roles played by the Brownian and the interparticle forces, obscuring the sought-after connection of hydrodynamic interactions and other microscopic forces to strength of suspension stress.

In an effort to elucidate the dependence of the nonequilibrium stress on the range of interparticle repulsion and on flow strength, Chu and Zia undertook the study of the suspension stress in a dilute colloidal dispersion of hydrodynamically interacting spheres, utilizing the framework of active microrheology rather than traditional shear macrorheology, to leverage the connections between the Stokes-Einstein relation, single-particle motion, and fluctuation dissipation [154, 34]. Seeking a detailed understanding of the role played by interparticle forces in the evolution of the suspension stress, Chu and Zia examined the evolution of the normal stresses with the range of interparticle repulsion (equivalently, the strength of hydrodynamic interactions) and strength of external probe forcing (equivalently, flow strength), finding that the nonequilibrium stress grows with increasing flow strength at fixed interparticle repulsion range, whether a suspension is at or far from equilibrium. They connected this evolution of the rheological behavior to the trajectories of particle pairs. This was utilized to understand the mechanisms by which hydrodynamic and entropic forces generate stress, and to relate the nonequilibrium stress to entropic energy storage. The next step carried out here, is to examine the normal stress differences and osmotic pressure.

In a prior study, Zia and Brady [154] inspected the normal stress differences and the osmotic pressure for suspensions of nonhydrodynamically interacting colloids. They found that the second normal stress difference is identically zero due to the axisymmetry of the perturbed microstructure around the probe, and the evolution of the first normal stress difference and the osmotic pressure depends on the strength of the external force: $\Pi \sim Pe^2$ and $N_1 \sim Pe^4$ under weak forcing, and $N_1 \sim Pe$ and $\Pi \sim Pe$ under strong forcing. These results were obtained via three approaches: a traditional micromechanical framework

that requires the statistics of particle distribution as described above; Brownian dynamics simulations; and a new phenomenological theory describing the nonequilibrium fluctuation and dissipation that produces stress, a nonequilibrium Stokes-Einstein relation. But without an understanding of the role played by hydrodynamic interactions, which are important in many physical systems, a comprehensive understanding of how evolution of such forces with flow strength changes non-Newtonian rheology was still unknown. In a separate work, Yurkovetsky and Morris [147] utilized Stokesian Dynamics simulations to study the nonequilibrium particle pressure in a sheared concentrated Brownian suspension, showing the expected exchange of the dominance of the Brownian force for the hydrodynamic force when a suspension is driven from equilibrium. However, the Stokesian Dynamics framework that they employed only considered suspensions interacting with strong hydrodynamic interactions, leaving unexplored the effect of interparticle force on osmotic pressure. Overall, prior studies have left open the question of how radial interparticle forces and hydrodynamic interactions evolve in tandem to influence the normal stress differences and osmotic pressure. In Chapter 2, we conducted a theoretical study of the particle phase stress in a colloidal dispersion, and studied the dependence of the nonequilibrium normal stresses on flow strength and on arbitrary strengths of hydrodynamic interactions [34]. The richness of the discussion of the individual stress elements was sufficient to warrant separate treatment of the normal stress differences and osmotic pressure, which is presented here.

In the present work, we utilize the framework of active microrheology to study the influence of the relative strengths of entropic and hydrodynamic forces on normal stress differences and the osmotic pressure. This mathematical model is applicable to dilute, unbound colloidal suspensions in the Stokes' flow

regime, for arbitrary strength of flow and hydrodynamic interactions. Careful interpretation of the thermodynamic stresses and their evolving influence on the microstructure provides new insight into a sign change in the normal stress differences. While it was shown in our previous work that entropic forces enhance suspension stress for the entire range of flow strength, we examine if this behavior is preserved in the normal stress differences or the nonequilibrium pressure.

The remainder of this chapter is organized as follows: in Sec. 3.2, we begin with a brief review of the physical model for the evolution of the structure. In Sec. 3.3, we recapitulate the expressions for the total average material stress and its contributions from the external, Brownian and interparticle forces derived in Sec. 2.3, with which we use to compute normal stress difference and osmotic pressure in this chapter. Results are presented in Sec. 3.4, starting with analysis of the asymptotic behaviors of the normal stress differences and osmotic pressure in the limits of weak and strong probe forcing, and weak and strong hydrodynamic interactions. Next, the same quantities are computed numerically for the full range of strength of hydrodynamic interactions and forcing. To gain insight into the evolution of the total normal stress differences and osmotic pressure, their underlying external, Brownian and interparticle contributions are investigated. The study is concluded in Sec. 3.5 with a summary.

3.2 Model system

We recapitulate the microrheology framework presented in Sec. 1.3.2. We consider a suspension of neutrally buoyant, colloidal hard spheres of hydrody-

namic radius a, dispersed in an incompressible Newtonian solvent of dynamic viscosity η and density ρ. A fixed external force, $\boldsymbol{F}^{\text{ext}}$, drives one of the particles, the "probe", through the suspension. The strength of fluid inertia relative to viscous forces defines a Reynolds number, $Re = \rho U a/\eta$, where U is the characteristic velocity of the probe. For micron-sized particles, Re is much less than unity, allowing neglect of inertial forces; fluid motion is thus governed by Stokes' equations. The probe number density, n_a, is much smaller than the number density of bath particles, n_b. Probe motion deforms the microstructure while Brownian motion of the bath particles acts to recover their equilibrium configuration. The degree of microstructural deformation, and its influence of probe motion, is thus set by the strength of the probe forcing, F_0, relative to the Brownian restoring force, $2kT/a_{th}$, where k is Boltzmann's constant, T is the absolute temperature and a_{th} is the thermodynamic size of particles, defining a Péclet number: $Pe = F_0/(2kT/a_{th})$.

Particles can interact via various forces, *e.g.*, hydrodynamic, Brownian, and interparticle forces. Here we employ an excluded-annulus model [118] to account for short- and long-range nature of these interactions. The strength of hydrodynamic interactions is determined by how closely two particles can approach one another, characterized by a dimensionless interparticle repulsion range κ via the ratio between the thermodynamic and hydrodynamic radius, a_{th} and a,

$$\kappa \equiv \frac{a_{th} - a}{a}. \tag{3.1}$$

In the limit of strong hydrodynamics, $\kappa \ll 1$, particles can approach each other closely enough to experience lubrication interactions. As κ grows, $\kappa \sim O(1)$, hydrodynamic interactions are weakened, but their impacts on the evolution of the microstructure and rheology persist over long distances. In the limit of weak

hydrodynamics, $\kappa \gg 1$, the long-range interparticle repulsion keeps particles sufficiently separated such that even long-range hydrodynamic interactions are negligible.

3.3 Theoretical framework

The theoretical framework for a micromechanical analysis of the evolving structure and its connection to rheology requires three elements: the details of the microscopic forces between the particles; a description of the particle configuration set by microscopic forces and imposed fields or flow; and a means by which to relate the two to macroscopic rheological quantities. The first of these, microscopic forces, was described in Sec. 1.2 and 3.2. The latter two — formulation of a Smoluchowski equation governing microstructural evolution, and its use in calculating an average, probe-phase stress — were fully developed in Chapter 2 in which we studied the individual elements of the normal stresses. Here we shall briefly recapitulate the main aspects of the theory and present the final governing equations from which solutions are utilized to compute the normal stress differences and osmotic pressure.

3.3.1 Micromechanical description of the stress

In the present section, we recapitulate the key results of the suspension stress for a dilute bath driven from equilibrium by an externally forced probe, as presented in Sec. 2.3.2. In the dilute limit, we found previously the average

external-force induced, Brownian, and interparticle stresses:

$$\begin{aligned}
\frac{\langle \boldsymbol{\Sigma} \rangle^{H,ext}}{n_a kT\phi_b} = & -\frac{1}{\pi(1+\kappa)} Pe \int_{r\geq 2} \left\{ \left[X_{11}^G(\kappa r) x_{11}^A(\kappa r) + X_{12}^G(\kappa r) x_{12}^A(\kappa r) \right] \left(\hat{\boldsymbol{r}}\hat{\boldsymbol{r}}\hat{\boldsymbol{r}} - \frac{1}{3}\boldsymbol{I}\hat{\boldsymbol{r}} \right) \right. \\
& + \left[Y_{11}^G(\kappa r) y_{11}^A(\kappa r) + Y_{12}^G(\kappa r) y_{12}^A(\kappa r) \right] (2\boldsymbol{I}\hat{\boldsymbol{r}} - 2\hat{\boldsymbol{r}}\hat{\boldsymbol{r}}\hat{\boldsymbol{r}}) \\
& \left. -3 \left[Y_{11}^H(\kappa r) y_{11}^B(\kappa r) - Y_{12}^H(\kappa r) y_{12}^B(\kappa r) \right] \left(2\boldsymbol{I}\hat{\boldsymbol{r}} - 2\hat{\boldsymbol{r}}\hat{\boldsymbol{r}}\hat{\boldsymbol{r}} \right) \right\} \cdot \hat{\boldsymbol{F}}^{\text{ext}} g(\boldsymbol{r}) d\boldsymbol{r} \\
& + \frac{1}{3\pi(1+\kappa)} Pe \int_{r\geq 2} \left[X_{11}^P(\kappa r) x_{11}^A(\kappa r) + X_{12}^P(\kappa r) x_{12}^A(\kappa r) \right] \boldsymbol{I}\hat{\boldsymbol{r}} \cdot \hat{\boldsymbol{F}}^{\text{ext}} g(\boldsymbol{r}) d\boldsymbol{r},
\end{aligned} \tag{3.2}$$

$$\begin{aligned}
\frac{\langle \boldsymbol{\Sigma} \rangle^{B}}{n_a kT\phi_b} = & \frac{1}{2\pi(1+\kappa)} \int_{r\geq 2} \left\{ \frac{1}{r^2}\frac{d}{dr} \left[r^2 \left(X_{11}^G(\kappa r) - X_{12}^G(\kappa r) \right) G(\kappa r) \right] \right. \\
& - \frac{6}{r} \left(Y_{11}^G(\kappa r) - Y_{12}^G(\kappa r) \right) H(\kappa r) \\
& \left. - \frac{18}{r} \left(Y_{11}^H(\kappa r) - Y_{12}^H(\kappa r) \right) \left(y_{11}^B(\kappa r) - y_{12}^B(\kappa r) \right) \right\} \left(\hat{\boldsymbol{r}}\hat{\boldsymbol{r}} - \frac{1}{3}\boldsymbol{I} \right) g(\boldsymbol{r}) d\boldsymbol{r} \\
& + \frac{1}{6\pi(1+\kappa)} \int_{r\geq 2} \left\{ \frac{1}{r^2}\frac{d}{dr} \left[r^2 \left(X_{11}^P(\kappa r) - X_{12}^P(\kappa r) \right) G(\kappa r) \right] \right\} \boldsymbol{I} g(\boldsymbol{r}) d\boldsymbol{r},
\end{aligned} \tag{3.3}$$

$$\begin{aligned}
\frac{\langle \boldsymbol{\Sigma} \rangle^{P}}{n_a kT\phi_b} = & -\frac{3}{\pi} \oint_{r=2} \hat{\boldsymbol{r}}\hat{\boldsymbol{r}} g(\boldsymbol{r}) d\Omega \\
& + \frac{2}{\pi(1+\kappa)} \left[X_{11}^G(2(1+\kappa)) - X_{12}^G(2(1+\kappa)) \right] G(2(1+\kappa)) \\
& \times \oint_{r=2} \left(\hat{\boldsymbol{r}}\hat{\boldsymbol{r}} - \frac{1}{3}\boldsymbol{I} \right) g(\boldsymbol{r}) d\Omega \\
& + \frac{2}{3\pi(1+\kappa)} \left[X_{11}^P(2(1+\kappa)) - X_{12}^P(2(1+\kappa)) \right] G(2(1+\kappa)) \oint_{r=2} \boldsymbol{I} g(\boldsymbol{r}) d\Omega.
\end{aligned} \tag{3.4}$$

Normal stresses were examined in detail in Chapter 2. In this work, we focus on the non-Newtonian rheology revealed by the normal stress differences and nonequilibrium osmotic pressure, a hallmark of non-Newtonian behavior in complex fluids. The first and the second normal stress differences are ob-

tained from Eqs. (3.2)–(3.4) via the relations,

$$N_1 \equiv \Sigma_{zz} - \Sigma_{yy}, \tag{3.5}$$

$$N_2 \equiv \Sigma_{yy} - \Sigma_{xx}. \tag{3.6}$$

The distortion of microstructure can also bring forth a nonequilibrium osmotic pressure, giving rise to isotropic expansion or contraction of the particle phase. The osmotic pressure is defined as the negative one-third of the trace of the stress tensor, and is obtained from Eqs. (3.2)–(3.4) via the relations,

$$\Pi \equiv -\frac{1}{3}\boldsymbol{I} : \boldsymbol{\Sigma}. \tag{3.7}$$

Away from equilibrium, Zia and Brady [154] studied nonhydrodynamically interacting suspensions utilizing an active microrheology framework, and showed that a nonequilibrium osmotic pressure contributes to particle stress. In the present study, we will examine the nonequilibrium osmotic pressure in hydrodynamically interacting suspensions arising from the underlying external, Brownian and interparticle forces.

3.4 Results

The connection between microscopic forces and the evolution of particle configuration built in the previous section can be utilized to evaluate the particle stress in a dilute colloidal suspension. The individual *normal stresses* requires detailed interpretation and discussion, and were presented in Chapter 2. The seemingly simple calculation of the normal stress difference and osmotic pressure reveals sufficiently rich behavior to warrant separate examination, presented here. We divide the results into two parts: first, the asymptotic limits

of weak and strong forcing; and second, evolution of normal stress differences and osmotic pressure for arbitrary strength of forcing and strength of hydrodynamic interactions. The second normal stress difference is identically zero regardless of the strength of flow and hydrodynamics, owing to the axisymmetry of the perturbed structure around the probe (cf. Sec. 2.4.1). We begin the discussion with behavior of the first normal stress difference, followed by the study of the osmotic pressure.

3.4.1 Normal stress differences

To obtain the general expressions for the first normal stress difference, the expressions for the parallel and perpendicular normal stresses are first obtained by projecting the stress tensor, Eqs. (3.2)–(3.4), onto two orthogonal subspaces corresponding to planes normal and parallel to the external force, then subtracting the perpendicular from the parallel normal stress. Only the traceless portion of the normal stresses contributes. The external-force induced, Brownian, and interparticle contributions to the first normal stress difference are

$$\begin{aligned}\frac{\langle N_1^{neq}\rangle^{H,ext}}{n_a kT\phi_b} = & -\frac{3}{2\pi(1+\kappa)}Pe\int_{r\geq 2}\Big\{\Big[X_{11}^G(\kappa r)x_{11}^A(\kappa r)+X_{12}^G(\kappa r)x_{12}^A(\kappa r)\Big]\\ & \times\left(-\cos^3\theta+\frac{1}{3}\cos\theta\right)\\ & +\Big[Y_{11}^G(\kappa r)y_{11}^A(\kappa r)+Y_{12}^G(\kappa r)y_{12}^A(\kappa r)\Big]\left(-2\cos\theta+2\cos^3\theta\right)\\ & -3\Big[Y_{11}^H(\kappa r)y_{11}^B(\kappa r)-Y_{12}^H(\kappa r)y_{12}^B(\kappa r)\Big]\left(-2\cos\theta+2\cos^3\theta\right)\Big\}f(\boldsymbol{r})d\boldsymbol{r},\end{aligned} \tag{3.8}$$

$$\begin{aligned}\frac{\langle N_1^{neq}\rangle^B}{n_a kT\phi_b} = \quad & \frac{3}{4\pi(1+\kappa)}\int_{r\geq 2}\left\{\frac{1}{r^2}\frac{d}{dr}\left[r^2\left(X_{11}^G(\kappa r)-X_{12}^G(\kappa r)\right)G(\kappa r)\right]\right. \\ & -\frac{6}{r}\left(Y_{11}^G(\kappa r)-Y_{12}^G(\kappa r)\right)H(\kappa r) \\ & \left.-\frac{18}{r}\left(Y_{11}^H(\kappa r)-Y_{12}^H(\kappa r)\right)\left(y_{11}^B(\kappa r)-y_{12}^B(\kappa r)\right)\right\}\left(\cos^2\theta-\frac{1}{3}\right)f(\boldsymbol{r})d\boldsymbol{r},\end{aligned} \tag{3.9}$$

$$\begin{aligned}\frac{\langle N_1^{neq}\rangle^P}{n_a kT\phi_b} = \quad & -\frac{9}{2\pi}\oint_{r=2}\cos^2\theta f(\boldsymbol{r})d\Omega \\ & +\frac{3}{\pi(1+\kappa)}\left[X_{11}^G(2(1+\kappa))-X_{12}^G(2(1+\kappa))\right]G(2(1+\kappa)) \\ & \times\oint_{r=2}\left(\cos^2\theta-\frac{1}{3}\right)f(\boldsymbol{r})d\Omega,\end{aligned} \tag{3.10}$$

where the components of the hydrodynamic resistance and mobility functions $X_{\alpha\beta}$, $Y_{\alpha\beta}$, $x_{\alpha\beta}$, $y_{\alpha\beta}$, G, and H are given in Appendix A. We begin the investigation of the first normal stress difference by studying the limit of weak probe forcing.

Weak probe force, $Pe \ll 1$

To compute the first normal stress difference under weak flow, the asymptotic results for the weakly distorted microstructure, $f(\boldsymbol{r}; Pe \ll 1)$ [Eq. (2.18)], is inserted into expressions (3.8)–(3.10). To leading order, the external-force induced, Brownian, and interparticle contributions to the first normal stress difference are obtained as

$$\frac{\langle N_1^{neq}\rangle^{H,ext}}{n_a kT\phi_b} = Pe^2\int_2^\infty \frac{3}{2}\mathcal{A}^{H,ext}(r)f_1(r)r^2dr + O(Pe^4), \tag{3.11}$$

$$\frac{\langle N_1^{neq}\rangle^{B}}{n_a kT\phi_b} = Pe^2\int_2^\infty \frac{3}{2}\mathcal{A}^{B}(r)f_2(r)r^2dr + O(Pe^4), \tag{3.12}$$

$$\frac{\langle N_1^{neq}\rangle^{P}}{n_a kT\phi_b} = Pe^2\left\{\frac{3}{2}\mathcal{A}^P f_2(2) + C^P\left[f_2(2)+\frac{5}{3}h_2(2)\right] - \mathcal{G}^P\left[f_2(2)+5h_2(2)\right]\right\} + O(Pe^4), \tag{3.13}$$

where $\mathcal{A}^{H,ext}$, $\mathcal{A}^{B}$, $\mathcal{A}^{P}$, $\mathcal{C}^{P}$ and $\mathcal{G}^{P}$ are compact expressions for the hydrodynamic functions and are given in Appendix C. The coefficients $\mathcal{A}$ are associated with the traceless part of the stress tensor, and the term associated with the coefficients $\mathcal{C}^{P}$ and $\mathcal{G}^{P}$ correspond to the elastic stress.

In the absence of hydrodynamic interactions, $\kappa \gg 1$, the hydrodynamic stress vanishes. Only the nonhydrodynamic elastic interparticle stress survives. The low-Pe behavior is given, to $O(Pe^4)$, as

$$\frac{\langle N_1^{neq} \rangle}{n_a kT \phi_b} \cong -0.163 Pe^4 \qquad \text{for} \quad Pe \ll 1,\ \kappa \gg 1, \tag{3.14}$$

recovering the result of Zia and Brady [154]. In this limit, normal stresses are generated solely by direct elastic collisions between the probe and surrounding bath particles, which are equally likely in the parallel and perpendicular directions at equilibrium. Thus, even though the individual normal stresses grow as Pe^2, their scalar coefficients are identical [cf. Eqs. (2.28)–(2.42)] and cancel one another precisely, reflecting the weak anisotropy of the structure. This behavior is plotted in Fig. 3.1(a).

In the opposite limit of strong hydrodynamic interactions, the external-force induced stress and the Brownian stress dominate, while the interparticle stress vanishes. The low-Pe, strong hydrodynamics behavior is given, to $O(Pe^2)$, as

$$\begin{aligned} \frac{\langle N_1^{neq} \rangle^{H,ext}}{n_a kT \phi_b} &\cong -0.28 Pe^2 + O(Pe^4), \\ \frac{\langle N_1^{neq} \rangle^{B}}{n_a kT \phi_b} &\cong 0.15 Pe^2 + O(Pe^4) \qquad \text{for} \quad Pe \ll 1,\ \kappa \ll 1, \end{aligned} \tag{3.15}$$

which, when combined, grows as $\langle N_1^{neq} \rangle \sim 0.13 Pe^2$, shown by the solid asymptote in Fig. 3.1(a).

To examine how the strength of the first normal stress difference changes as entropic and hydrodynamic forces evolve from the $\kappa \to \infty$ limit to the $\kappa \to 0$

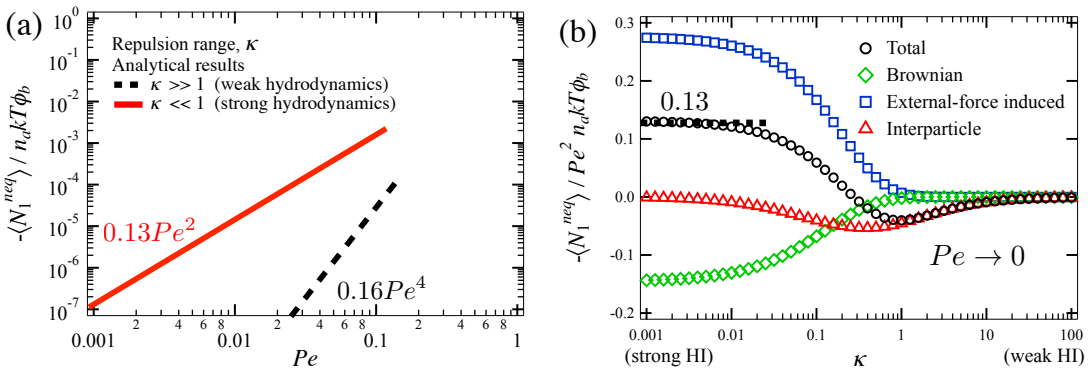

Figure 3.1: First normal stress difference in the linear-response regime. (a) Asymptotically weak versus strong hydrodynamic interactions [black dashed line, Eq. (3.14); and red solid line, Eq. (3.15), respectively]. (b) Individual contributions to total first normal stress difference for $Pe \to 0$, as a function of strength of hydrodynamic interactions κ. External-force induced contribution, Eq. (3.11) (□); Brownian contribution, Eq. (3.12) (◇); interparticle contribution, Eq. (3.13) (△); total first normal stress difference, sum of Eqs. (3.11)–(3.13) (○).

limit, each contribution [Eqs. (3.11)–(3.13)] is plotted over five decades of κ in Fig. 3.1(b). The external force-induced contribution $\langle N_1^{neq}\rangle^{H,ext}$ is negative for all ranges of repulsion κ, because $\langle \Sigma_{\parallel}^{neq}\rangle^{H,ext} < 0$ is larger in magnitude than $\langle \Sigma_{\perp}^{neq}\rangle^{H,ext} < 0$, for all κ. The uniformly negative value of $\langle N_1^{neq}\rangle^{H,ext}$ accompanies the tendency of the externally imposed flow to distort the structure. A stronger distortion along the flow produces the asymmetry required for non-Newtonian rheology, and owes its origin to the more rapid decay of relative radial motion [$G(r)$] compared to relative transverse motion [$H(r)$]. For any relative pair trajectory, each of the two orthogonal hydrodynamic couplings, $G(r)$ and $H(r)$, plays an evolving role throughout the pair encounter. The upstream and downstream portions of the trajectory are dominated by $G(r)$ and thus occupy the majority of the encounter. At the middle region of the encounter, $H(r)$, a weaker coupling, permits faster relative motion. The upstream and downstream interactions con-

tribute primarily to the parallel stress while the midpoint interactions contribute primarily to the perpendicular stress. In consequence, the resultant structural asymmetry produces a negative normal stress difference.

In contrast, the Brownian and interparticle contributions are both positive for the entire range of κ because, for each, the underlying normal stress components of $\langle \boldsymbol{\Sigma}^{neq} \rangle^B$ and $\langle \boldsymbol{\Sigma}^{neq} \rangle^P$ are all negative, with larger magnitudes in the perpendicular direction. The difference is weak in this near-equilibrium regime, but nonzero. Both $\langle \Sigma_{\parallel}^{neq} \rangle^B$ and $\langle \Sigma_{\perp}^{neq} \rangle^B$ are $O(1)$, differing only by 15% in magnitude owing to the strength of Brownian motion. The sign of these two entropic contributions is opposite that of the external force-induced hydrodynamic contribution since, at low Pe, entropic forces resist the relative particle motion induced by the flow, *i.e.*, tend to make uniform and symmetric the structure. This relation reflects the tendency of Brownian motion to act against the flow, restoring structural symmetry and thus making zero the total first normal stress difference. Physically, Brownian drift always acts to drive particles to regions of higher mobility. Along the azimuthal angle, this always separates a pair and reduces stress. In the fore and aft regions, the same force drives the pair apart upstream but drives them together downstream.

Similarly, entropic scattering from elastic collisions also tends to make zero the total normal stress difference by enhancing the perpendicular stress. Physically, when bath particles pass by the probe, elastic collisions in the direction perpendicular to the external force drive a pair apart to give an $O(1)$ contribution $\langle \Sigma_{\perp}^{neq} \rangle^P$. However, in the direction parallel to the external force, while weak advective motion of the probe enhances collisions on the upstream face of the probe, once a bath particle passes by and resolves the encounter, there is

low probability of a downstream elastic collision [69]. This results in a weaker $\langle \Sigma_{\parallel}^{neq} \rangle^P < 0$ compared to $\langle \Sigma_{\perp}^{neq} \rangle^P < 0$, and hence $\langle N_1^{neq} \rangle^P > 0$.

Overall, to have non-Newtonian rheology, structural asymmetry must be present. However, when flow is weak and Brownian motion is strong, such asymmetry cannot be maintained longer than the time scale of thermal fluctuations – it is relaxed quickly by Brownian motion. Thus, the only way to sustain a finite normal stress difference is to slow down this relaxation. In the limit of strong hydrodynamics, $\kappa \to 0$ [the left end of the axis of Fig. 3.1(b)], despite the presence of strong Brownian motion, hydrodynamic interactions slow down the approach and the separation of particles, resulting in a finite first normal stress, recovering the asymptotic coefficient, 0.13. The interparticle normal stress difference is identically zero in this limit because the pair collisions required to produce structural asymmetry are prevented entirely by hydrodynamic deflection. As the repulsion range κ grows, both the external force-induced and Brownian contributions to stress decay to zero approximately as $\kappa^{-1/5}$ and $\kappa^{-1/10}$ respectively, as the no-slip surfaces of particles are kept widely separated. The growth of the effective thermodynamic particle size also permits more frequent hard-sphere collisions, with a longitudinal bias owing to remaining weak hydrodynamic coupling. The elastic stress reaches a maximum near $\kappa = 0.5$, and then decays rapidly on approaching the limit of weak hydrodynamics, $\kappa \to \infty$, the right end of the axis.

Strong probe force, $Pe \gg 1$

When probe forcing is strong, the region upstream of the probe comprises two domains: an outer region where only advection matters, and an $O(Pe^{-1})$-

thin boundary layer at the probe surface where diffusion balances advection. That is, the presence of even very weak Brownian motion (or surface roughness) destroys Stokes-flow symmetry of pair trajectories and, as predicted by Batchelor [15], the Newtonian rheology associated with spherically symmetric structure is lost. The nonequilibrium stress is determined primarily by the dynamics of the boundary layer, and the contribution from the outer region is negligible [34]. The high-Pe first normal stress difference is computed by inserting the boundary-layer solutions for the distorted microstructure, Eqs. (2.19) and (2.20), for the limits of weak and strong hydrodynamic interactions respectively, into Eqs. (3.2)–(3.4).

The subtraction of the perpendicular normal stress from its parallel counterpart automatically eliminates the isotropic stress; only the traceless portion of the normal stresses contributes to the normal stress difference. In the absence of hydrodynamic interactions, only the interparticle stress matters, giving

$$\begin{aligned} \frac{\langle N_1^{neq} \rangle}{n_a kT\phi_b} &= Pe \int_0^{\pi} \left(-6\cos^2\theta \sin\theta + 3\sin^3\theta \right) \hat{f}(0,\theta) d\theta + O(1) \\ &= -\frac{3}{4} Pe + O(1) \qquad \text{for} \quad Pe \gg 1,\ \kappa \gg 1, \end{aligned} \tag{3.16}$$

where for compactness we have defined $\hat{f} \equiv \cos\theta\, e^{-Pe(r-2)\cos\theta}$. In this dual limit of strong forcing and weak hydrodynamic interactions, the first normal stress difference scales linearly in the external forcing strength Pe, recovering the result of Zia and Brady [154].

In the opposite limit of strong hydrodynamic interactions, the external force, Brownian motion, and interparticle forces all play a role. In this dual limit of $Pe \gg 1$ and $\kappa \ll 1$, the external-force induced stress dominates because Brownian motion is weak when flow is strong, and strong hydrodynamic interactions shield pairs from elastic collisions. The hydrodynamic functions in Eqs. (3.2)–

(3.4) take on their lubrication forms, and the high-Pe asymptotic forms of the interparticle, Brownian, and external-force induced contributions are

$$\begin{aligned}\frac{\langle N_1^{neq}\rangle^P}{n_a kT\phi_b} = \; & Pe^{\delta}\left\{\left[\int_{\epsilon}^{\pi}\left(\cos^2\theta\sin\theta-\frac{1}{3}\sin\theta\right)\tilde{f}(0,\theta)d\theta\right]\frac{3\mathcal{D}^P}{2}\right. \\ & +\left[\int_{\epsilon}^{\pi}\left(\cos^2\theta\sin\theta\right)\tilde{f}(0,\theta)d\theta\right]\mathcal{H}^P \\ & \left.-\left[\int_{\epsilon}^{\pi}\left(\sin^3\theta\right)\tilde{f}(0,\theta)d\theta\right]\mathcal{I}^P\right\}+O(Pe^{\delta-1}\ln Pe),\end{aligned} \tag{3.17}$$

$$\begin{aligned}\frac{\langle N_1^{neq}\rangle^B}{n_a kT\phi_b} = \; & Pe^{\delta-1}\ln Pe\left\{\left[\int_{\epsilon}^{\pi}\int_0^{\infty}\left(\cos^2\theta\sin\theta-\frac{1}{3}\sin\theta\right)\tilde{f}(y,\theta)dyd\theta\right]\frac{3\mathcal{D}^B}{2}\right. \\ & \left.+O(Pe^{\delta-1}),\right.\end{aligned} \tag{3.18}$$

$$\begin{aligned}\frac{\langle N_1^{neq}\rangle^{H,ext}}{n_a kT\phi_b} = \; & Pe^{\delta}\ln Pe\left[\int_{\epsilon}^{\pi}\int_0^{\infty}\left(\cos^3\theta\sin\theta-\cos\theta\sin\theta\right)\tilde{f}(y,\theta)dyd\theta\right]\frac{3\mathcal{D}^{H,ext}}{2} \\ & +Pe^{\delta}\left[\int_{\epsilon}^{\pi}\int_0^{\infty}\left(\cos^3\theta\sin\theta-\cos\theta\sin\theta\right)\tilde{f}(y,\theta)dyd\theta\right]\frac{3\mathcal{E}^{H,ext}}{2} \\ & +O(Pe^{\delta-1}\ln Pe),\end{aligned} \tag{3.19}$$

where the radial integration is carried out over the stretched radial coordinate $y = Pe(r-2)$, and $\delta = 0.799$. For compactness, we have introduced the coefficients $\mathcal{D}$ and $\mathcal{E}$ associated with the traceless hydrodynamic functions, and $\mathcal{H}$ and $\mathcal{I}$ for the elastic stresslet $\langle \boldsymbol{rF}^P\rangle$. The detailed expressions for the $\mathcal{D}$, $\mathcal{E}$, $\mathcal{H}$ and $\mathcal{I}$ coefficients are given in Appendix C. Before discussing the scaling of Eqs. (3.17)–(3.19), we note again the apparently divergent behavior noted in Sec. 2.4.2 for the normal stresses under strong probe force, where again the region of angular integration carefully avoids an ϵ-small region to maintain convergent behavior and accurate modeling of the physics.

Let us inspect the scaling in Pe of each of these expressions, beginning with the interparticle contribution. The interparticle contribution to the high-Pe first

normal stress difference, Eq. (3.17), scales as $Pe^{0.799}$. However, the terms corresponding to the dissipative and the elastic stress cancel precisely, giving an overall zero contribution as lubrication forces prevent particle collisions. The Brownian contribution, Eq. (3.18), is much weaker, $\langle N_1^{neq}\rangle^B \sim Pe^{-0.201}\ln Pe$. Lastly, the external-force induced contribution, Eq. (3.19), comprises an $O(Pe^{0.799}\ln Pe)$ and an $O(Pe^{0.799})$ term. Of these two terms, the $O(Pe^{0.799}\ln Pe)$ makes the least contribution because the coefficient $\mathcal{D}^{H,ext} \to 0$; physically, the stress generated by the relative rotational motion exactly balances (cancels) that generated by relative transverse translational motion [34]. Thus, the $O(Pe^{0.799})$ term dominates the high-Pe behavior. We summarize these scalings as follows:

$$\langle N_1^{neq}\rangle^{H,ext} \sim Pe^{0.799} \quad \text{for} \quad Pe \gg 1,\ \kappa \ll 1, \tag{3.20}$$

$$\langle N_1^{neq}\rangle^{B} \sim Pe^{-0.201}\ln Pe \quad \text{for} \quad Pe \gg 1,\ \kappa \ll 1, \tag{3.21}$$

$$\langle N_1^{neq}\rangle^{P} \sim Pe^{0.799} \quad \text{for} \quad Pe \gg 1,\ \kappa \ll 1. \tag{3.22}$$

The three contributions are combined to give the total first normal stress difference, $\langle N_1^{neq}\rangle$, plotted in Fig. 3.2 as a function of the external force, Pe. As shown by the asymptotes for $\kappa \gg 1$ and $\kappa \ll 1$, hydrodynamic interactions qualitatively change the influence of flow strength on the first normal stress difference. As either hydrodynamic interactions or flow strength grow stronger, entropic contributions weaken, because at small κ interparticle repulsion is weak, and at high Pe Brownian motion is weak. As discussed in the previous section for weak probe force, hydrodynamic interactions act to *enhance* the *small Pe* first normal stress difference by amplifying the disparity in the duration of longitudinal versus transverse particle encounters, and the disparity in Brownian drift in the two orthogonal directions. In contrast, hydrodynamic interactions act to *suppress* the first normal stress difference when Pe is large, owing to a deflection

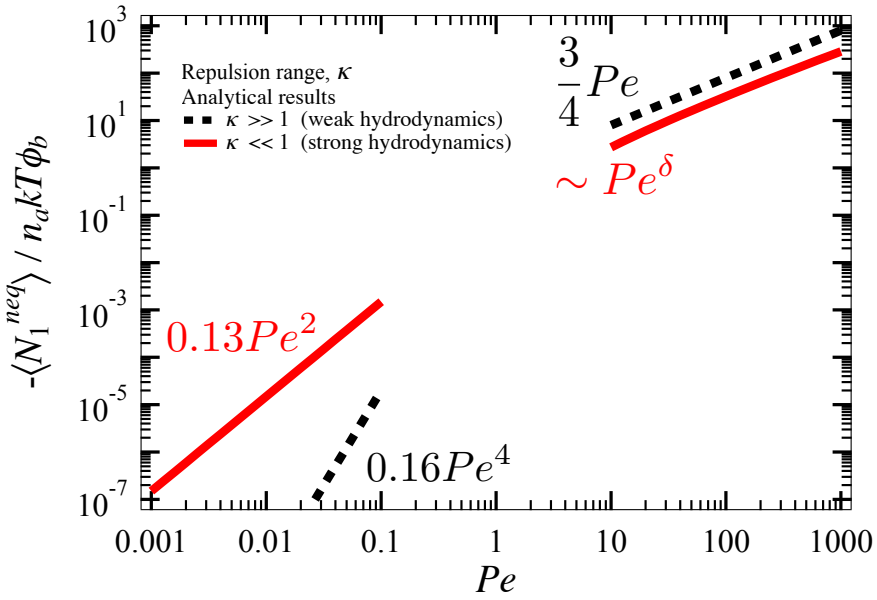

Figure 3.2: Asymptotic behavior of the first normal stress difference. Black dashed line: low- [Eq. (3.13)] high-Pe [Eq. (3.16)] asymptote for weak hydrodynamic interactions, $\kappa \gg 1$. Red solid line: low- and high-Pe asymptote for strong hydrodynamic interactions, $\kappa \ll 1$ [sum of Eqs. (3.11)–(3.13), and sum of Eqs. (3.17)–(3.19), respectively].

of collisions that preserves microstructural symmetry.

Arbitrary strength of probe force and hydrodynamics

To explore the regime where the external probe forcing Pe and strength of hydrodynamic interactions κ take on arbitrary values, the first normal stress difference is computed numerically via a finite difference discretization of the Smoluchowski equation (2.2)–(2.4) and inserting the microstructural solution into Eqs. (3.8)–(3.10). Fig. 3.3 shows the total first normal stress difference $\langle N_1^{neq} \rangle$, along with the external force-induced, Brownian and interparticle contributions, as a function of Pe for four different strengths of hydrodynamic in-

teractions, κ, going from weak (a) to strong (d). The stress is made dimensionless by the ideal (Brownian) osmotic pressure $n_a kT$ and volume fraction of bath particles ϕ_b, and is scaled by Pe to give an advective scaling of the stress [34],

$$Pe\, n_a kT\phi_b \equiv \frac{n_a F_0 a}{2}\phi_b. \tag{3.23}$$

In the presence of weak hydrodynamic interactions [$\kappa = 1$, panel (a)], the first normal stress difference is primarily set by elastic interparticle collisions, and linear in Pe in the strong-flow limit, because elastic collisions destroy Stokes-flow symmetry and thus produce non-Newtonian rheology, even in the limit $Pe^{-1} \equiv 0$, for $\kappa \neq 0$.

The same elastic interparticle collisions are responsible for a (weak) change in sign of the first normal stress difference, where hydrodynamic interactions are just weak enough to permit collisions, but still strong enough to create the disparity in parallel versus perpendicular hydrodynamic forces that produces a normal stress difference. This behavior is highlighted in the inset of panel (a), where the first normal stress difference (solid line) is shown alongside the parallel (dashed line) and perpendicular normal (dash-dotted line) components. In previous studies, the sign change was attributed to a transition from dominant Brownian forces to dominant hydrodynamic forces [50, 19]. However, the results in the present study suggested a new mechanism causing such a sign change: the interparticle force also produce a sign change. When $Pe < 1$, elastic collisions are more numerous in the direction perpendicular to the line of the external force (dash-dotted line) compared to the parallel direction (dashed line), resulting in a stronger perpendicular normal stress and thus a positive normal stress difference (solid line). As flow strength increases, $Pe > 1$, the microstructure becomes increasingly asymmetric with accumulation of bath particles in front of the probe, giving rise to more frequent collisions in the direction along

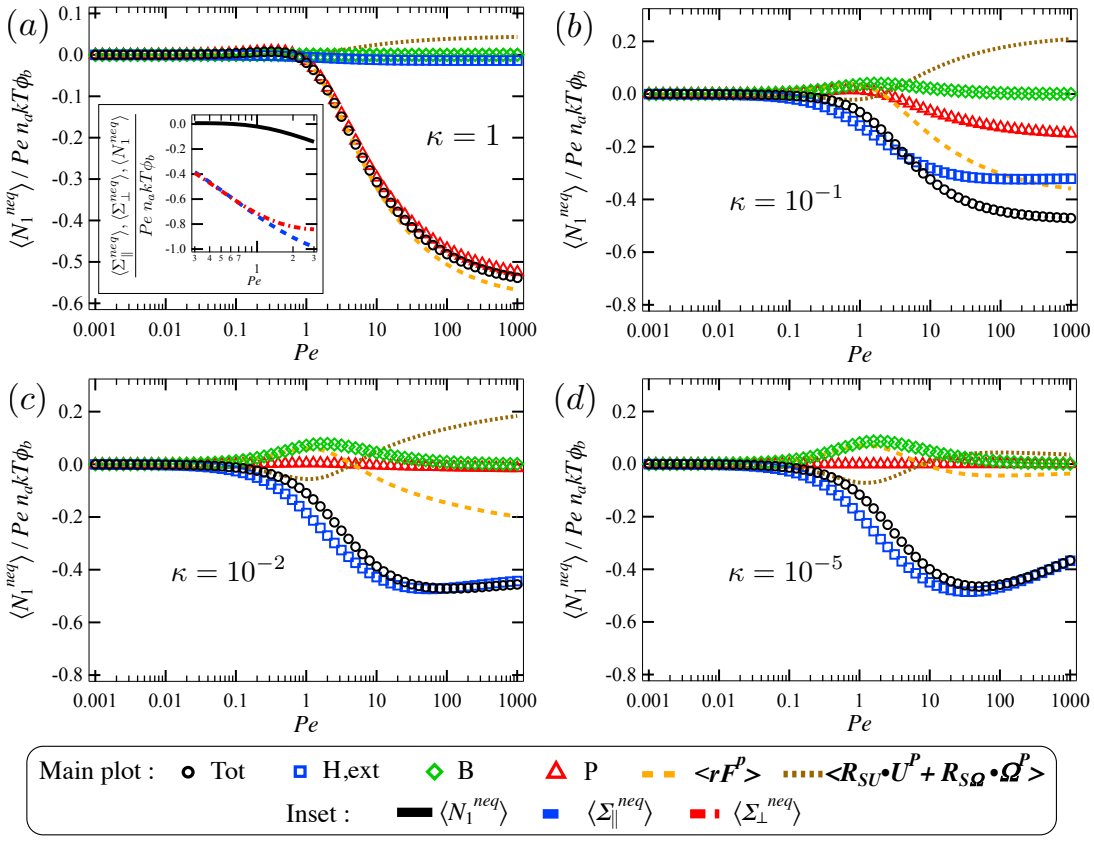

Figure 3.3: The first normal stress difference $\langle N_1^{neq} \rangle$ scaled advectively by external probe forcing Pe, ideal osmotic pressure $n_a kT$ and volume fraction of bath particles ϕ_b, as a function of Pe for four different values of κ ranging from weak to strong hydrodynamic interactions: (a) $\kappa = 1$, (b) $\kappa = 10^{-1}$, (c) $\kappa = 10^{-2}$, and (d) $\kappa = 10^{-5}$.

the line of the external force. The parallel normal stress overtakes the perpendicular, changing the sign of the normal stress difference from positive to negative. In fact, for $\kappa \in [0.5, 500]$, the interparticle contribution is at least an order of magnitude larger than the Brownian and the external force-induced components, for the entire range of Pe. Thus, the *interparticle force alone* can lead to a sign change in the first normal stress difference.

Physically, a sign change in the normal stress differences affects the

anisotropic expansion or contraction of the particle phase (cf. Fig. 2.1). We recall from the normal stresses that both parallel and perpendicular components are negative for the entire range of Pe, representing the tendency of the particle phase to expand in the corresponding direction [34]. A negative first normal stress difference indicates that the parallel stress is more negative (larger in magnitude) than the perpendicular stress, signifying an expansion of the particle phase along the line of the external force, accompanied by a contraction in the perpendicular direction. In contrast, a positive first normal stress difference corresponds to a contraction in the parallel direction and an expansion in the perpendicular direction. While these results may be challenging to measure in hard-sphere suspensions in the low-Pe regime, a suspension of deformable particles may show a more pronounced prolate-to-oblate shape transition.

In panel (b), the interparticle repulsion range shrinks, $\kappa = 10^{-1}$, and the growing importance of hydrodynamic coupling permits the emergence of the dissipative part of the interparticle stress, $\langle \boldsymbol{R}_{SU} \cdot \boldsymbol{U}^P + \boldsymbol{R}_{S\Omega} \cdot \boldsymbol{\Omega}^P \rangle$. For all Pe, its sign is opposite that of the elastic interparticle stress, $\langle \boldsymbol{r}\boldsymbol{F}^P \rangle$, which itself decreases in magnitude as κ shrinks, overall leading to a smaller interparticle stress. The reduction of the total interparticle stress is accompanied by a growth of the external and Brownian stresses. The Brownian contribution is positive over the entire range of Pe. In contrast, the external force-induced contribution is negative. In this competition between the external and Brownian forces, the former acts to expand the particle phase along the line of the probe forcing and contract it in the perpendicular directions, whereas the latter counteracts the motion, acting to restore the equilibrium configuration. Despite the opposite signs of these components, the Brownian contribution is never strong enough to dominate the external force-induced contribution, even in the low-Pe regime, which can be

understood as follows. As discussed in the section for weak probe force, when Pe is small, the majority of the Brownian contribution to the normal stresses lies in the trace, and computation of the first normal stress difference automatically eliminates it. That is, for $\kappa < 0.5$, the evolution of the total first normal stress difference follows that of its external-force induced component, and there is no change of sign in the quantity with Pe.

The interparticle contribution continues to diminish when the repulsion range, κ, decreases [panel (c)], as hydrodynamic and Brownian contributions grow. When hydrodynamic interactions are strong [panel (d)], only the external and Brownian forces matter. At high Pe, the suppressive effect of hydrodynamic interactions becomes clear, as the growth of the normal stress difference decays toward an eventual Newtonian plateau that can be reached when $Pe^{-1} = 0$ and $\kappa = 0$. In this pure-hydrodynamic limit, the microstructure is spherically symmetric and the first normal stress difference vanishes, and the suspension behaves as a Newtonian fluid as predicted by Batchelor [15]. This is consistent with the idea that structural asymmetry is required for non-Newtonian response in suspensions of smooth hard-spheres.

Surprisingly, the interparticle force still plays a prominent role when hydrodynamic interactions are strong: In panel (d), when $\kappa \to 0$, the interparticle contribution to the first normal stress difference is indeed negligible, but only because the elastic and dissipative parts are of identical strength and opposite sign. Each is nonzero, meaning that the interparticle force still plays a role in preventing particle *overlaps*, whereas the external-force induced stress is responsible for preventing particle *touching* via lubrication interactions. In fact, a pair-trajectory analysis shows that the elastic and the dissipative interparti-

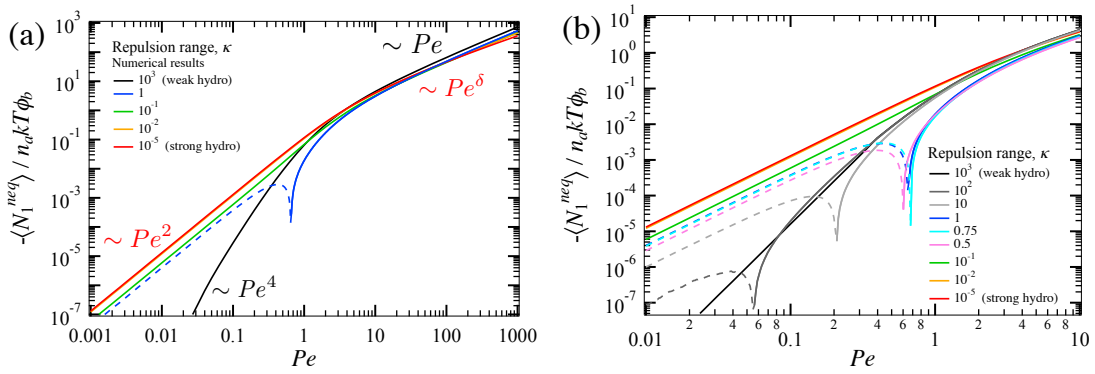

Figure 3.4: The first normal stress difference $\langle N_1^{neq} \rangle / n_a kT\phi_b$ scaled by ideal osmotic pressure $n_a kT$ and volume fraction ϕ_b, as a function of external probe forcing Pe for various strength of hydrodynamic interactions κ. For $\kappa \in [0.5, 100]$, the segment displayed with dashed line has been multiplied by -1 to make it visible on the log-log plot.

cle stresses act against each other — the former drives particles apart and the latter pulls particles together [34]. Prior studies of normal stress differences in sheared suspensions did not identify the role of interparticle force in the strong hydrodynamics regime, owing to a choice to combine the trace of the dissipative interparticle stresslet with the Brownian stresslet. The interparticle force then appeared to contribute nothing to the first normal stress difference as, by definition, the first normal stress difference comes only from the traceless part of the stresslet. However, with such a grouping, the interparticle portion of the two normal stresses would then no longer be zero, contradicting the dogma that the interparticle force is zero and "replaced" by lubrication forces. Indeed, both must play a role, even in the pure-hydrodynamic limit [68].

The evolution of the total first normal stress difference is summarized in Fig. 3.4, where the sign change arising with changes in structural symmetry is shown for several values of κ. When flow is weak, the numerical results recover the weak- and strong-hydrodynamics asymptotic solutions. The first normal

stress difference is positive when entropic forces dominate, $\kappa \in [0.5, 500]$, and becomes strongly negative when entropic forces are suppressed, $\kappa < 0.5$. When flow is strong, hydrodynamic interactions suppress the growth of the first normal stress difference, from linear in Pe to sublinear. The approach to the asymptotic strong-flow limit, $\langle N_1^{neq} \rangle \sim Pe^{0.799}$, grows as $Pe^{0.867}$, becoming perceptible only when $Pe > 10^3$, owing to the influence of the residual Brownian force. When flow goes from weak to strong, $\langle N_1^{neq} \rangle$ changes sign, but only if hydrodynamic interactions are weak enough to permit interparticle collisions and, in this case, the dominance of perpendicular normal stress over parallel normal stress reverses, owing to an increase in force-aft asymmetry from $O(1)$ at small Pe to $O(Pe^{\delta})$ at large Pe.

3.4.2 Osmotic pressure

The particle-phase osmotic pressure, given by one-third of the negative of the trace of the stress tensor, describes the tendency of particle motion to isotropically expand or contract. In this section, we examine the role of flow and microscopic forces in producing nonequilibrium osmotic pressure. The three contributions to the osmotic pressure found by taking the trace of Eqs. (3.2)–(3.4):

$$\frac{\langle \Pi^{neq} \rangle^{H,ext}}{n_a kT\phi_b} = -\frac{1}{3\pi(1+\kappa)} Pe \int_{r\geq 2} \left[X_{11}^P(\kappa r) x_{11}^A(\kappa r) + X_{12}^P(\kappa r) x_{12}^A(\kappa r) \right] f(\boldsymbol{r}) d\boldsymbol{r}, \tag{3.24}$$

$$\frac{\langle \Pi^{neq} \rangle^{B}}{n_a kT\phi_b} = -\frac{1}{6\pi(1+\kappa)} \int_{r\geq 2} \left\{ \frac{1}{r^2} \frac{d}{dr} \left[r^2 \left(X_{11}^P(\kappa r) - X_{12}^P(\kappa r) \right) G(\kappa r) \right] \right\} f(\boldsymbol{r}) d\boldsymbol{r}, \tag{3.25}$$

$$\begin{aligned} \frac{\langle \Pi^{neq} \rangle^{P}}{n_a kT\phi_b} = \; & \frac{1}{\pi} \oint_{r=2} f(\boldsymbol{r}) d\Omega \\ & -\frac{2}{3\pi(1+\kappa)} \left[X_{11}^P(2(1+\kappa)) - X_{12}^P(2(1+\kappa)) \right] G(2(1+\kappa)) \oint_{r=2} f(\boldsymbol{r}) d\Omega. \end{aligned} \tag{3.26}$$

where the components of the hydrodynamic resistance and mobility functions $X_{\alpha\beta}$, $x_{\alpha\beta}$, and G are given in Appendix A. We begin the investigation of the nonequilibrium osmotic pressure by studying the limit of weak probe forcing.

Weak probe force, $Pe \ll 1$

In the limit of a weak external force, the nonequilibrium osmotic pressure is set by the weakly deformed microstructure, $f(\boldsymbol{r}; Pe \ll 1)$ [Eq. (2.18)]. Insertion into expressions (3.24)–(3.26) gives the external-force induced, Brownian and interparticle contributions to the osmotic pressure:

$$\frac{\langle \Pi^{neq} \rangle^{H,ext}}{n_a kT\phi_b} = Pe^2 \int_2^\infty \mathcal{B}^{H,ext}(r) f_1(r) r^2 dr + O(Pe^4), \tag{3.27}$$

$$\frac{\langle \Pi^{neq} \rangle^{B}}{n_a kT\phi_b} = Pe^2 \int_2^\infty \mathcal{B}^{B}(r) \left[f_2(r) + 3h_2(r) \right] r^2 dr + O(Pe^4), \tag{3.28}$$

$$\frac{\langle \Pi^{neq} \rangle^{P}}{n_a kT\phi_b} = Pe^2 \left[f_2(2) + 3h_2(2) \right] \left(\mathcal{J}^P - \mathcal{B}^P \right) + O(Pe^4), \tag{3.29}$$

where $\mathcal{B}^{H,ext}$, $\mathcal{B}^B$, $\mathcal{B}^P$ and $\mathcal{J}^P$ are compact expressions for the hydrodynamic functions, and are given in Appendix C. The coefficients $\mathcal{B}$ are associated with the isotropic part of the stress tensor, and the term associated with the constant $\mathcal{J}^P$ corresponds to the elastic stress. The first-order nonequilibrium osmotic pressure is weakly nonlinear, as indicated by the Pe^2 scaling in Eqs. (3.27)–(3.29).

In the absence of hydrodynamic interactions, $\kappa \gg 1$, the external-force induced and Brownian stresses vanish, and only the elastic interparticle stress survives:

$$\frac{\langle \Pi^{neq} \rangle}{n_a kT\phi_b} = \frac{8}{3} Pe^2 + O(Pe^4) \qquad \text{for} \quad Pe \ll 1,\ \kappa \gg 1, \tag{3.30}$$

recovering the result of Zia and Brady [154].

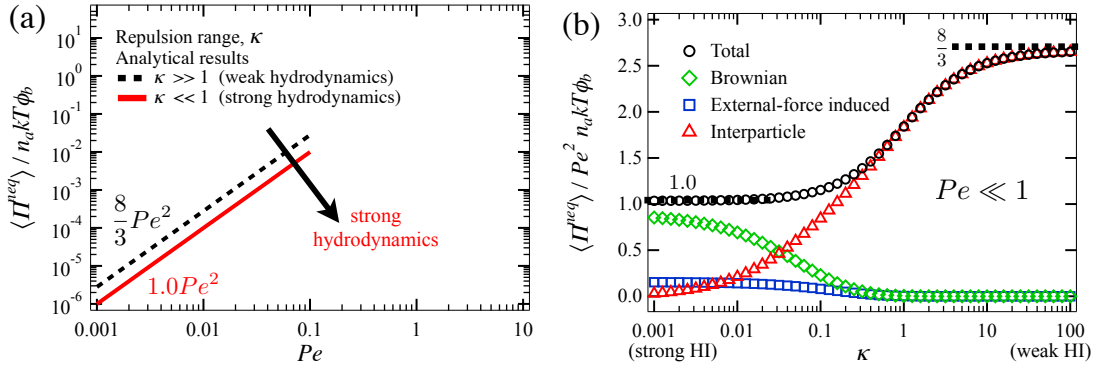

Figure 3.5: Nonequilibrium osmotic pressure, $Pe \ll 1$, plotted as a function of (a) hydrodynamic interactions κ [external-force induced, Eq. (3.27) □; Brownian, Eq. (3.28) ◇; interparticle, Eq. (3.29) △; total ○]; (b) forcing strength, Pe. Black dashed line: low-Pe asymptote for weak hydrodynamic interactions, $\kappa \gg 1$, Eq. (3.30). Red solid line: low-Pe asymptote for strong hydrodynamic interactions, $\kappa \ll 1$, Eq. (3.31).

In the opposite limit of strong hydrodynamic interactions, the external-force induced stress and the Brownian stress dominate, and the interparticle stress vanishes. The low-Pe asymptotes reveal that the first effect of flow is weakly nonlinear:

$$\begin{aligned} \frac{\langle \Pi^{neq} \rangle^{H,ext}}{n_a kT\phi_b} &\cong 0.15Pe^2 + O(Pe^4), \\ \frac{\langle \Pi^{neq} \rangle^{B}}{n_a kT\phi_b} &\cong 0.89Pe^2 + O(Pe^4) \qquad \text{for} \quad Pe \ll 1,\ \kappa \ll 1, \end{aligned} \tag{3.31}$$

to give a total nonequilibrium osmotic pressure $\langle \Pi^{neq} \rangle \cong 1.0Pe^2$. The total osmotic pressure is plotted in Fig. 3.5(a), as a function of the strength of the external probe forcing, Pe. Two asymptotes are shown, corresponding to the limit of weak ($\kappa \gg 1$) and strong ($\kappa \ll 1$) hydrodynamic interactions, giving $\langle \Pi^{neq} \rangle \sim Pe^2$ in both limits of κ. Overall, hydrodynamic interactions suppress the osmotic pressure. From an entropic prospective, shrinking the effective particle size increases the available free volume, resulting in a decrease in the osmotic pressure.

To examine how osmotic pressure evolves with thermodynamic size and the strength of hydrodynamic coupling, Eqs. (3.27)–(3.29) are plotted for several values of κ in Fig. 3.5(b). On the left end of the horizontal axis, the repulsion range is short and hydrodynamic interactions are strong ($\kappa \ll 1$). Hydrodynamic shielding prevents most interparticle collisions, leading to negligible interparticle osmotic pressure. Disturbance flows from Brownian motion and the external force drive the osmotic pressure, with the former dominant in this regime of weak advection. The total pressure asymptotes to $1.0Pe^2$. Toward the right end of the horizontal axis, $\kappa \gg 1$, hydrodynamic interactions are weak and the interparticle repulsion range is long. The growth in effective particle size keeps particles so far apart that the disturbance flows decay over distances much smaller than the thermodynamic size. Thus, as the effective size of particles increases, the importance of both external-force induced and Brownian osmotic pressure decreases, accompanied by a dramatic enhancement in entropic exclusion that permits frequent and numerous particle collisions. Because the increase in entropic stress is more pronounced than the reduction in the external-force induced and Brownian stress, the overall nonequilibrium osmotic pressure is higher in suspensions with weak hydrodynamic interactions, reaching the value of $8/3$, recovering the asymptotic result of Eq. (3.30). Overall, hydrodynamic interactions suppress small-Pe osmotic pressure.

Strong probe force, $Pe \gg 1$

Here we examine the nonequilibrium osmotic pressure for asymptotically strong probe forcing. In the limit of weak hydrodynamic interactions, both external and Brownian forces are negligible, and only the interparticle force

matters. Inserting the boundary-layer solution for the distorted microstructure $f(\boldsymbol{r}; Pe \gg 1; \kappa \gg 1)$, Eq. (2.19), into Eq. (3.26), the high-Pe asymptote of the osmotic pressure obtained here reads

$$\begin{aligned} \frac{\langle \Pi^{neq} \rangle}{n_a kT \phi_b} &= Pe \int_0^{\pi} (2) (\sin\theta)\, \hat{f}(0,\theta) d\theta + O(1) \\ &= 1 \times Pe + O(1) \qquad \text{for} \quad Pe \gg 1,\ \kappa \gg 1, \end{aligned} \tag{3.32}$$

which demonstrates that the osmotic pressure scales linearly in Pe with a prefactor of unity, recovering the result of Zia and Brady [154].

Osmotic pressure in the opposite limit of strong hydrodynamic interactions can be obtained by inserting the solution for the distorted microstructure $f(\boldsymbol{r}; Pe \gg 1; \kappa \ll 1)$, Eq. (2.20), into Eqs. (3.24)–(3.26), and utilizing the lubrication forms of the hydrodynamic functions to obtain

$$\frac{\langle \Pi^{neq} \rangle^{H,ext}}{n_a kT \phi_b} = Pe^{\delta} \left[\int_{\epsilon}^{\pi} \int_0^{\infty} (\cos\theta \sin\theta)\, \tilde{f}(y,\theta) dy d\theta \right] \mathcal{F}^{H,ext} + O(\ln(Pe) Pe^{\delta-1}), \tag{3.33}$$

$$\frac{\langle \Pi^{neq} \rangle^{B}}{n_a kT \phi_b} = Pe^{\delta-1} \ln Pe \left[\int_{\epsilon}^{\pi} \int_0^{\infty} (\sin\theta)\, \tilde{f}(y,\theta) dy d\theta \right] \mathcal{F}^{B} + O(Pe^{\delta-1}), \tag{3.34}$$

$$\frac{\langle \Pi^{neq} \rangle^{P}}{n_a kT \phi_b} = Pe^{\delta} \left[\int_{\epsilon}^{\pi} (\sin\theta)\, \tilde{f}(0,\theta) d\theta \right] \left(\mathcal{F}^{P} + \mathcal{K}^{P} \right) + O(\ln(Pe) Pe^{\delta-1}), \tag{3.35}$$

where $\delta = 0.799$. Here, $\mathcal{F}^{H,ext}$, $\mathcal{F}^{B}$, $\mathcal{F}^{P}$ and $\mathcal{K}^{P}$ are compact expressions for the hydrodynamic functions, and are given in Appendix C. The coefficients $\mathcal{F}$ are associated with the isotropic stress, and $\mathcal{K}$ corresponds to the elastic stress. The excluded region of angular integration, ϵ, is identical to that discussed in the computation of high-Pe first normal stress difference (cf. Sec. 3.4.1).

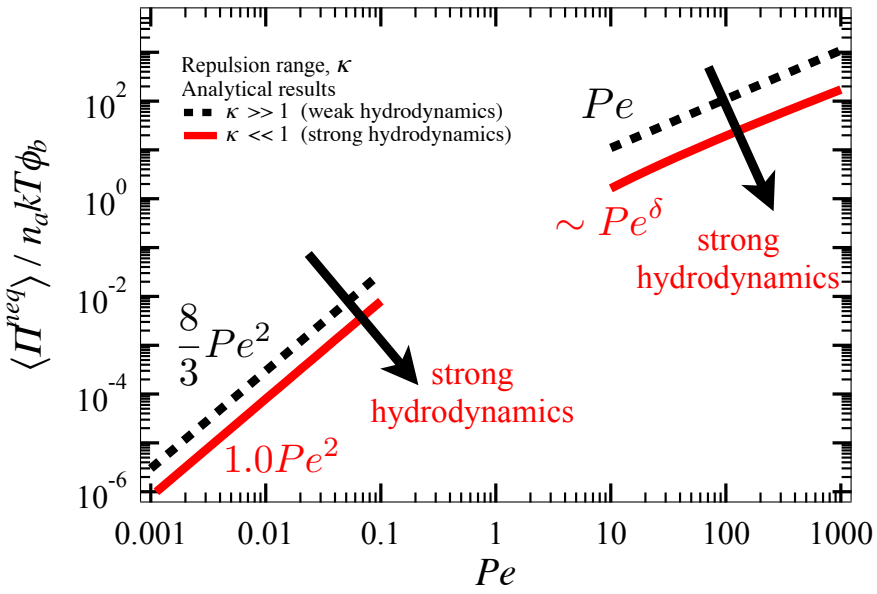

Figure 3.6: Nonequilibrium osmotic pressure, $Pe \gg 1$. Black dashed line: low- [Eq. (3.29)] and high-Pe [Eq. (3.30)] asymptote for weak hydrodynamic interactions, $\kappa \gg 1$. Red solid line: low- and high-Pe asymptote for strong hydrodynamic interactions, $\kappa \ll 1$ [sum of Eqs. (3.27)–(3.29), and sum of Eqs. (3.33)–(3.35), respectively].

The scaling of each contribution can be written compactly as

$$\langle \Pi^{neq} \rangle^{H,ext} \sim Pe^{0.799} \quad \text{for} \quad Pe \gg 1,\ \kappa \ll 1, \tag{3.36}$$

$$\langle \Pi^{neq} \rangle^{B} \sim Pe^{-0.201} \ln Pe \quad \text{for} \quad Pe \gg 1,\ \kappa \ll 1, \tag{3.37}$$

$$\langle \Pi^{neq} \rangle^{P} \sim Pe^{0.799} \quad \text{for} \quad Pe \gg 1,\ \kappa \ll 1. \tag{3.38}$$

The total nonequilibrium osmotic pressure for both $Pe \gg 1$ and $Pe \ll 1$ is plotted in Fig. 3.6 as a function of the external forcing strength, Pe, which reveals that hydrodynamic interactions suppress nonequilibrium osmotic pressure in the high-Pe limit as well. When $Pe \gg 1$, the pressure decays from a linear growth in Pe when hydrodynamic interactions are weak, $\kappa \gg 1$, to $\langle \Pi^{neq} \rangle \sim Pe^{0.799}$ when hydrodynamic interactions are strong, $\kappa \ll 1$. The latter

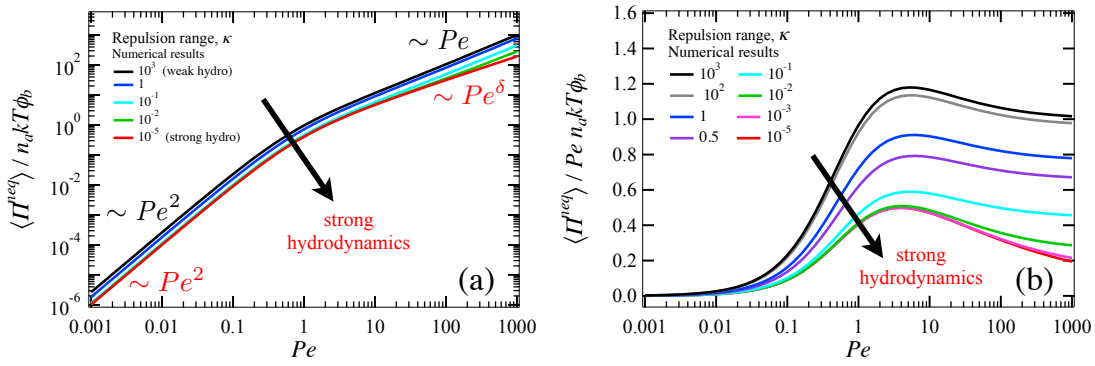

Figure 3.7: (a) Nonequilibrium osmotic pressure $\langle \Pi^{neq} \rangle$ scaled diffusively by ideal osmotic pressure $n_a kT$ and volume fraction of bath particles ϕ_b, as a function of external probe forcing Pe for various strength of hydrodynamic interactions κ. (b) Nonequilibrium osmotic pressure $\langle \Pi^{neq} \rangle$ scaled advectively by Pe, $n_a kT$ and ϕ_b, as a function of Pe for various κ.

limit reflects both a direct and an indirect effect of hydrodynamic interactions. The direct effect is an $O(1)$ hydrodynamic coupling represented by the hydrodynamic function $\mathcal{E}^{H,ext}$ in Eq. (3.33). Hydrodynamic interactions also reduce bath particle accumulation in the boundary layer from $g(r;\kappa) \sim Pe$ for $\kappa \to \infty$ to $g(r;\kappa) \sim Pe^{0.799}$ for $\kappa \to 0$, indirectly decreasing the osmotic pressure. Each suppresses the osmotic pressure.

In summary, entropic forces enhance the osmotic pressure in the two asymptotic limits of Pe or, equivalently, hydrodynamic interactions shield particles from collisions, preserving microstructural symmetry, and suppressing the asymmetry required for non-Newtonian rheology. To discover whether this trend persists for all Pe, we next numerically compute the osmotic pressure for arbitrary κ and Pe.

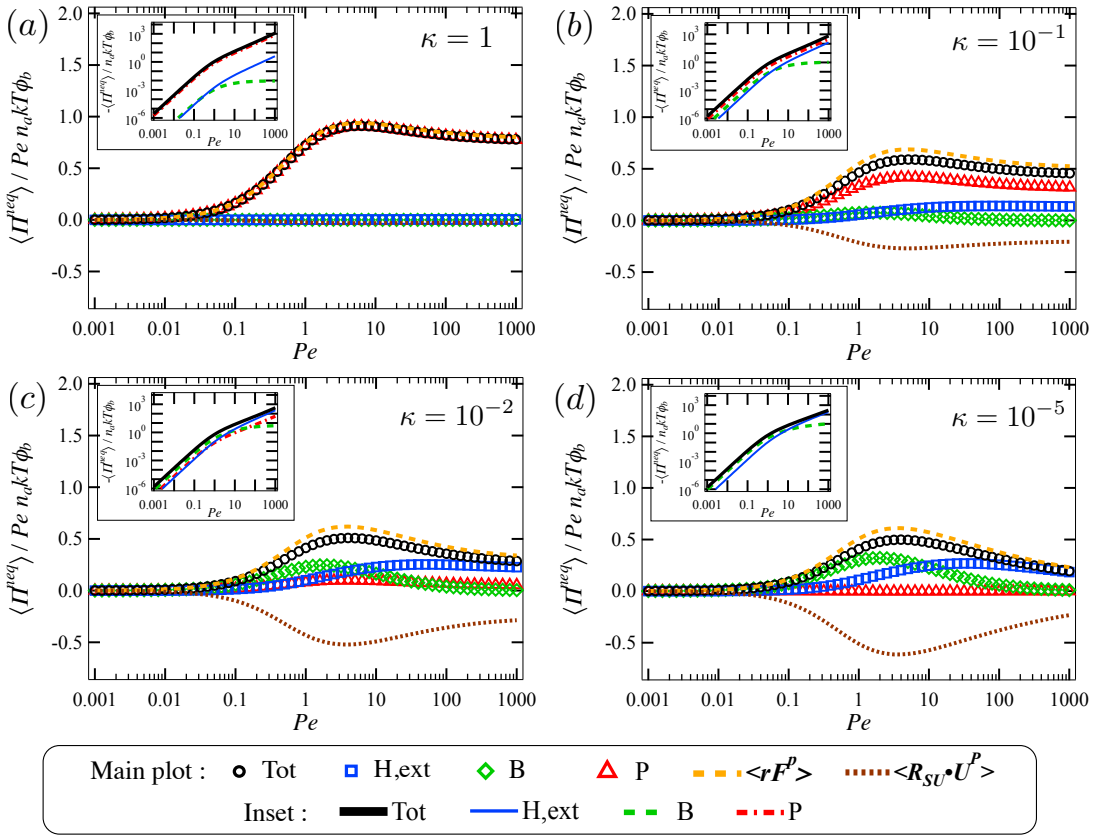

Figure 3.8: Nonequilibrium osmotic pressure $\langle \Pi^{neq} \rangle$ scaled advectively by external probe forcing Pe, ideal osmotic pressure $n_a kT$ and volume fraction of bath particles ϕ_b, as a function of Pe for four different values of κ ranging from weak to strong hydrodynamic interactions: (a) $\kappa = 1$, (b) $\kappa = 10^{-1}$, (c) $\kappa = 10^{-2}$, and (d) $\kappa = 10^{-5}$.

Arbitrary strength of probe force and hydrodynamics

To analyze the evolution of the nonequilibrium osmotic pressure for arbitrary strength of external force Pe and hydrodynamic interactions κ, the total nonequilibrium osmotic pressure $\langle \Pi^{neq} \rangle$ is computed numerically via the finite difference scheme utilized in Sec. 3.4.1. The results are plotted in Fig. 3.7(a) as a function of Pe, for several values of κ. When probe forcing is weak or strong, the numerical results recover the asymptotic theory in the limits of weak and

strong hydrodynamic interactions. Between these two limits, the total osmotic pressure rises monotonically with increasing Pe, as advective distortion of the structure outpaces Brownian smoothing. In the previous two sections, we saw that hydrodynamic interactions suppress the osmotic pressure for asymptotically weak and strong forcing. Fig. 3.7(a) shows that hydrodynamic interactions suppress the osmotic pressure for all values of Pe. The data from fig. 3.7(a) are scaled by Pe, and this advectively scaled osmotic pressure is plotted in panel (b), where the suppressive effect of hydrodynamic interactions on the nonequilibrium osmotic pressure shows an approach to Newtonian rheology in the pure-hydrodynamic limit. To understand the underlying mechanisms for the evolution of the osmotic pressure, we study the individual contributions arising from the various microscopic forces.

In Fig. 3.8, the external-force induced, Brownian and interparticle contributions of the total nonequilibrium osmotic pressure, $\langle \Pi^{neq} \rangle$, are plotted as a function of Pe for four different values of κ, ranging from (a) weak to (d) strong hydrodynamic interactions. In the case of weak hydrodynamic interactions, plot (a), only the elastic interparticle stress $n_a \langle \boldsymbol{r}\boldsymbol{F}^P \rangle$ contributes to the osmotic pressure. When scaled diffusively as shown in the inset, the quadratic and linear growth in Pe in the low- and high-Pe limits are recovered. The advective scaling of the data in the main plot of (a) effectively scales out the $O(Pe)$ frequency of particle collisions, giving a high-Pe plateau in the pressure. From the rheological perspective, the nonzero constant high-Pe pressure indicates that non-Newtonian rheology persists in a nonhydrodynamically interacting suspension, even at $Pe^{-1} = 0$, owing to the destruction of Stokes flow symmetry by particle collisions.

When hydrodynamic interactions begin to play a role, $\kappa = 10^{-1}$ in plot (b), hydrodynamic shielding results in fewer particle collisions, as indicated by a weaker elastic contribution $\langle \boldsymbol{rF}^P \rangle$; but now the dissipative part of the interparticle stress, $\langle \boldsymbol{R}_{SU} \cdot \boldsymbol{U}^P \rangle$, grows. The overall interparticle contribution weakens but still dominates the external-force induced and Brownian contributions over the entire range of Pe.

As repulsion range continues to shrink, $\kappa = 10^{-2}$ in plot (c), the elastic and dissipative parts of the interparticle stress become nearly equal but opposite in sign, leading to a negligibly small interparticle stress. But this entropically induced stress is replaced by the Brownian stress, which dominates the total stress for $Pe \leq 1$, until the external force contribution dominates. In the high-Pe regime, the Pe-dependence of the osmotic pressure weakens to a sublinear scaling, owing to the reduction in particle encounters by hydrodynamic shielding. Upon further shrinking of the repulsion range, the limit of strong hydrodynamic interactions is reached [plot (d)]. The interparticle osmotic pressure becomes negligible for the entire range of Pe which, as was the case for the normal stresses [34] and the first normal stress difference, is due to the precise counter-balance between the elastic and dissipative interparticle stresses. In the pure-hydrodynamic limit, $\kappa = 0$ and $Pe^{-1} = 0$, the high-Pe asymmetric boundary layer and wake structure becomes fore-aft symmetric. The nonequilibrium osmotic pressure vanishes, recovering Newtonian rheology.

In summary, we find that the low- and high-Pe growth of the nonequilibrium osmotic pressure scale as $\langle \Pi^{neq} \rangle \sim Pe^2$ and $\langle \Pi^{neq} \rangle \sim Pe^{\delta}$ respectively, where δ ranges from 0.799 to 1 from strong to weak hydrodynamics. Hydrodynamic interactions suppress the total osmotic pressure for all values of Pe, signaling

a weaker tendency of the particle phase to expand [equivalently, weaker collisions with a fictitious boundary [154]]. In the advective frame of reference, hydrodynamic interactions were shown to weaken the non-Newtonian response far from equilibrium. The weakening effect becomes more prominent as Pe increases, resulting in a vanishing nonequilibrium osmotic pressure in the pure-hydrodynamic limit. Only in a nonhydrodynamically interacting suspension can one measure a nonzero nonequilibrium osmotic pressure at $Pe^{-1} = 0$.

3.5 Conclusions

We have developed a theoretical model of the non-Newtonian rheology of semi-dilute dispersions of hydrodynamically interacting colloidal spheres, forming a connection between microscopic forces and microstructural evolution to normal stress difference and osmotic pressure, utilizing active microrheology. The influence of the strength of entropic and hydrodynamic forces on non-Newtonian rheology was studied over six decades of flow strength, Pe, and eight decades of hydrodynamic strength (interparticle repulsion range), κ, alongside limiting behaviors for asymptotically weak and strong hydrodynamic interactions and flow. The first normal stress difference, $\langle N_1 \rangle$, and nonequilibrium osmotic pressure, $\langle \Pi^{neq} \rangle$, both evolve in magnitude with changes in strength of flow or hydrodynamic coupling. In addition, $\langle N_1 \rangle$ exhibits a sign change with growing flow strength Pe, if hydrodynamic interactions are only moderately strong and permit interparticle collisions.

When flow is strong, $Pe \gg 1$, a short repulsion range permits particles to experience strong hydrodynamic interactions that shield them from collisions,

preserving structural symmetry and suppressing the growth of the first normal stress difference. When flow is weak, $Pe \ll 1$, decreasing the repulsion range, in contrast, enhances the first normal stress difference by amplifying both the disparity in the duration of longitudinal versus transverse particle encounters, and the disparity in Brownian drift in the two orthogonal directions. Between the weak- and strong-flow limits, the first normal stress difference exhibits a sign change, but only if hydrodynamic interactions are weakened by surface roughness or other repulsive forces. In this regime, the first normal stress difference is dominated by elastic interparticle interactions; when flow is weak, the stress normal to the flow is stronger than that along it, $|\Sigma_{\perp}^{P,el}| > |\Sigma_{\parallel}^{P,el}|$, but this reverses as flow strength grows and interparticle collisions along the line of forcing grow in frequency.

While in prior work the sign change in the first normal stress difference was ascribed solely to the growing dominance of hydrodynamic over Brownian forces [50, 19], here we identified a novel mechanism that interparticle repulsion alone can lead to such sign change. Interrogation of this behavior revealed that, even when hydrodynamic interactions are very strong, the hard-sphere interparticle force still plays a role in the first normal stress difference. The vanishing of the interparticle stress in this limit results from the precise balance between its elastic and dissipative contributions; this physical description cannot be recovered from prior approaches that extract and move the trace of the dissipative interparticle stress to the Brownian stress.

The present work also revealed that entropic repulsion enhances the nonequilibrium osmotic pressure; that is, hydrodynamic interactions act to suppress osmotic pressure, regardless of the strength of flow. The effect is quanti-

tative when flow is weak but, as flow strength increases, $O(1)$ structural asymmetry becomes $O(Pe^{\delta})$, leading to a corresponding amplification of the pressure. The suppressive influence of hydrodynamics is qualitative when forcing is strong: the growth of the pressure changes from $\langle \Pi^{neq} \rangle \sim Pe$ in the limit of weak hydrodynamics to $\langle \Pi^{neq} \rangle \sim Pe^{0.799}$ when hydrodynamic interactions are strong.

This theoretical framework can provide guidance for the interpretation of experimental measurements of non-Newtonian rheology of colloidal dispersions. For example, it can provide a means by which to detect the relative strength of hydrodynamic interactions, a quantity that can be difficult to measure. One would expect a high-Pe plateau of the advectively scaled osmotic pressure and first normal stress difference, if hydrodynamic interactions are weak. For dispersion in which hydrodynamic interactions are strong, this non-Newtonian plateau will give way to a slow, $O(Pe^{\delta-1})$ decay, where the slope of the decay can be utilized to infer the interparticle repulsion range.

CHAPTER 4

TOWARD A NONEQUILIBRIUM STOKES-EINSTEIN RELATION IN COLLOIDAL DISPERSIONS

4.1 Introduction

The fluctuation-dissipation theorem governs various physical processes at thermodynamic equilibrium, *e.g.* Brownian motion, Johnson-Nyquist noise, thermal radiation: common among them is a balance between the dissipation of spontaneous system fluctuations. An early attempt to relate fluctuation and dissipation dates back to the work of Einstein [44], who considered sedimentation of a dilute suspension of non-interacting hard-sphere particles. Appealing to a hypothetical equilibrium state, he asserted that the advective flux arising from sedimentation is balanced exactly by an upward Fickian diffusive flux caused by the weak spatial concentration gradient from bottom to top. The result is the famous Stokes-Einstein relation, $\boldsymbol{D}_a = kT\boldsymbol{M}_a$: fluctuation of solvent molecules imparts an average kinetic energy $3kT/2$ to a colloid, giving rise to its "spontaneous" fluctuating motion described by $\boldsymbol{D}_a = D_a\boldsymbol{I}$, where D_a is the bare diffusivity of a colloid of hydrodynamic size a and $\boldsymbol{I}$ is the identity tensor. As the colloid fluctuates, energy exchange occurs at the no-slip surface of the colloid and the solvent: the motion of the colloid is dissipated by the (hydrodynamic) Stokes' drag $\boldsymbol{R}_a = \boldsymbol{M}_a^{-1} = 6\pi\eta a\boldsymbol{I}$ (η is the dynamic viscosity of the solvent), and the energy returned to the solvent is precisely the original amount causing fluctuation. Since diffusivity of a particle relates to its mean-square displacement, and Boltzmann's constant relates to Avogadro's number, the Stokes-Einstein relation offers strong support for the existence of atoms by linking quantitatively a mi-

croscopic quantity to experimentally accessible macroscopic quantities. Practically, it allows determination of macroscopic properties of a *Newtonian* material by simply tracking the movement of a single, embedded tracer particle — a microrheology technique. Today, much is known about fluctuation-dissipation behavior in general [108, 30, 83] and in complex fluids specifically, but most of this work is confined to the linear-response regime. When a suspension undergoes flow, the resulting suspension stress can no longer be obtained via thermodynamic equilibrium arguments. However, single-particle interrogation of complex fluids, so-called active microrheology, is an important technique for studying complex fluids [61, 124, 78, 102, 126, 153, 154, 155, 131, 68, 69, 70, 34, 35]; connections between the motion of an actively forced tracer have recently been shown to reveal the suspension stress, viscosity, and flow-induced diffusion via a nonequilibrium Stokes-Einstein relation [154]. However, this prior model neglected the influence of hydrodynamic interactions between particles, a severe restriction. The goal of this study is to generalize the nonequilibrium Stokes-Einstein relation for flowing suspensions to account for the influence of hydrodynamic interactions between particles.

The primary influence of particle and hydrodynamic interactions on the Stokes-Einstein relation is a change in the timescale over which fluctuations are dissipated. This can be appreciated by recovering the Stokes-Einstein relation via the Langevin equation [87, 66], central to which is the assumption that the random forcing obeys Gaussian statistics on the timescale of solvent-molecule motion. The autocorrelation of the Brownian force is instantaneous, with an amplitude set by the relaxation processes in the material. For a lone colloid, this correlation is intransient because the Stokes' drag on a single particle never changes. However, in a suspension, hydrodynamic interactions couple parti-

cles together and, in consequence, the noise-averaged random force lasts much longer than the individual particle momentum relaxation timescale. Brownian forces are thus correlated longer in time, because the drag responsible for viscous dissipation is now configuration-dependent. This time dependence gives rise to linear viscoelastic behavior at or near equilibrium, which has been modeled with some success by a generalization of the Stokes-Einstein relation by Mason and Weitz [100] for continuum complex fluids, *e.g.* polymer melts. They modeled its viscoelastic response by replacing the instantaneous memory kernal (delta function) with a time-dependent memory function, yielding a relation between the diffusivity of an embedded probe to its frequency-dependent complex mobility, and the complex mobility to the complex viscosity of the material. These extensions of the "Stokes" and "Einstein" component together gave a generalized Stokes-Einstein relation which links the mean-square displacement of the probe to frequency-dependent linear viscoelasticity of a continuous complex fluid. However, this general theory cannot recover the bulk shear moduli of colloidal suspensions and other non-continuum fluids; a one-to-one correspondence between probe diffusion and linear-response model can only be obtained via linear-response active microrheology [69]. It has recently been pointed out that diffusion arises from motion that generates a Stokeslet and so it should not give the same result as a sheared (stresslet-producing) flow [152]. While linear-response active microrheology can appropriately capture the fluctuation-dissipation relation in suspensions only weakly perturbed from equilibrium, it leaves open the question of whether single particle fluctuations in flowing suspensions are precisely dissipated with a similar relation.

Zia and Brady [154] recognized that Einstein's idea could be generalized to nonequilibrium systems if one modeled the system via an equation of mo-

tion rather than an equation of state. Their approach revealed that gradients in stress drive not only diffusive flux but advective flux as well and, from this, they inferred that nonequilibrium stress and osmotic pressure in suspensions are measures of the duration required for fluctuations to dissipate in a flowing suspensions. In the freely draining limit modeled via their "nonequilibrium equation of state", the configuration-independence of particle mobility gave a simple flow-rate dependence of this balance. Here we seek to understand how this nonequilibrium fluctuation and dissipation change when suspension configuration evolves with the strength of hydrodynamic interactions and strength of flow.

The focus of this work is to derive a generalized nonequilibrium Stokes-Einstein relation addressing arbitrary strengths of hydrodynamic and interparticle interactions, external forcing and thermal motion. While this relation maintains the robustness of the original nonequilibrium Stokes-Einstein relation [154] that a colloidal suspension can be fully characterized by measuring the movement of a single probe, it accounts for the intricate, non-monotonic evolution of dissipation (viscosity) and fluctuation (diffusivity) for hydrodynamically interacting colloids, allowing accurate determination of non-Newtonian rheology, including normal stresses, normal stress differences and osmotic pressure, in the asymptotically limits of weak and strong hydrodynamic interactions and flow strength, and any intervening regimes. To complement the connection between pair-interaction in our theory and many-body interactions in non-dilute suspensions, we compare our predictions with the results from Accelerated Stokesian Dynamics simulations, shedding light on the development of a scaling theory for the concentrated suspension stress.

The remainder of this paper is organized as follows: in Sec. 4.2, the microrheology model system is presented. Next, in Sec. 4.3, we present the derivation of a generalized nonequilibrium Stokes-Einstein relation connecting the suspension stress to nonequilibrium fluctuation and dissipation, for arbitrary strengths of hydrodynamic, external, Brownian and interparticle forces, utilizing an active microrheology framework. An anisotropic effective resistance tensor is constructed from microviscosity and flow-induced diffusivity to model the effect of hindered and fluctuating particle motion in the presence of hydrodynamics which, upon coupled with particle flux, constitutes the advective and diffusive components of a Cauchy momentum balance. Results are presented in Sec. 4.4, starting with comparing four rheological quantities, namely the parallel and perpendicular normal stress, the first normal stress difference and osmotic pressure, predicted from the generalized nonequilibrium Stokes-Einstein relation and values obtained from statistical mechanics theory [34, 35], for the full range of hydrodynamic interactions and flow strength from weak to strong. In Sec. 4.5, the predictions from theory are compared with results obtained by particle dynamics simulations in the limit of strong hydrodynamics. From this, we draw insights into the connection between dilute theory and data for non-dilute suspensions, and discuss the development of a scale-up theory enabling application of the former to effectually predict the latter. Experimental measurements required in the generalized nonequilibrium Stokes-Einstein relation are discussed in Sec. 4.6. This study is concluded in Sec. 4.7 with a summary.

4.2 Model system

We recapitulate the microrheology framework presented in Sec. 1.3.2. We consider a suspension of N_b hard-sphere colloidal bath particles of hydrodynamic radius a, dispersed homogeneously in a volume $\mathcal{V}$ of incompressible Newtonian solvent of dynamic viscosity η and density ρ. A constant external force, $\boldsymbol{F}^{\text{ext}}$, drives a "probe" particle also a hard-sphere colloid of radius a, through the suspension. The strength of fluid inertia relative to viscous forces defines a Reynolds number, $Re = \rho U a/\eta$, where U is the characteristic velocity of the probe. Dominance of viscous forces in our system requires $Re \ll 1$ such that the fluid motion is governed by Stokes' equations. The probe number density, n_a, is much smaller than the number density of bath particles, n_b. The external force drives the probe to deform the microstructure while Brownian motion of particles acts to recover the equilibrium configuration. The degree of microstructural distortion, and its influence of probe motion, is thus set by the strength of the probe forcing, F_0, relative to the Brownian restoring force, $2kT/a_{th}$, where k is Boltzmann's constant, T is the absolute temperature and a_{th} is the thermodynamic size of particles, defining a Péclet number: $Pe = F_0/(2kT/a_{th})$.

Particles can interact through various forces, *e.g.*, external, hydrodynamic, and thermodynamic forces. Here we employ the excluded-annulus model [118] to account for short- and long-range nature of these interactions. The hydrodynamic size of the particles, a, is set by the surface at which the no-slip condition is obeyed. The effective size of particles can be, however, larger than their hydrodynamic size owing to various surface conditions, such as repulsive charges and grafted polymer hairs utilized to sterically stabilize a dispersion. This sets

a thermodynamic radius a_{th}, where the no-flux condition is obeyed and determines the minimum-approach distance r_{min} with which two particles can approach one another. For equally-sized particles, $r_{min} = 2a_{th}$ and, in general, the no-flux surface can extend beyond the no-slip surface, $r_{min} > 2a$.

A conservative interparticle potential $V(r)$ serves as a simplified model for electrostatic or steric repulsion as arises in the presence of surface roughness or surface modifications to promote dispersion stability. This interparticle potential induces an interparticle force where, in the present hard-sphere model, particles exert no force on one another until their no-flux surfaces touch, $r = 2a_{th}$, at which an infinite potential prevents them from overlapping:

$$V(r) = \begin{cases} \infty & \text{if} \quad r \leq r_{min} \\ 0 & \text{if} \quad r > r_{min}. \end{cases} \tag{4.1}$$

The strength of hydrodynamic interactions is determined by how close two particles can approach one another, characterized by a dimensionless interparticle repulsion range:

$$\kappa \equiv \frac{a_{th} - a}{a}. \tag{4.2}$$

The interparticle repulsion varies between $\kappa \in [0, \infty]$, ranging from the limit of strong hydrodynamic interactions ($\kappa = 0$) where particles can approach each other closely enough to interact through lubrication interactions to the limit of weak hydrodynamic interactions ($\kappa \gg 1$) where the long-range repulsion keeps particles sufficiently separated such that even long-range hydrodynamic interactions are negligible.

4.3 Generalized non-equilibrium Stokes-Einstein relation

In the original work, Zia and Brady [154] demonstrated that an naive application of the equilibrium Stokes-Einstein relation to a nonequilibrium colloidal suspension yields quantitative differences from results obtained from statistical mechanics and Brownian dynamics simulations in the limit of weak hydrodynamic interactions. They identified that such differences arise from the very origin of the governing equations: while an equation of state is sufficient to account for particle migrations solely due to diffusion at equilibrium, a nonequilibrium system should be described by an equation of motion to account for both diffusive and advective fluxes, giving rise to a nonequilibrium Stokes-Einstein relation [154]. In this section, we generalize the original theory for a hydrodynamically interacting system.

The momentum balance in the Stokes flow regime reads [154],

$$\mathbf{0} = \nabla \cdot \langle \boldsymbol{\Sigma} \rangle + n_a \langle \boldsymbol{F}^{\text{ext}} \rangle + n_a \langle \boldsymbol{F}^{\text{int}} \rangle, \tag{4.3}$$

where the angle brackets denote an ensemble average over all permissible positions of the bath particles relative to the probe, $\boldsymbol{\Sigma}$ is the stress tensor associated with the probes, and the equivalence between the probe phase stress and the suspension stress was discussed in previous work [154, 34]. In Eq. (4.3), $\boldsymbol{F}^{\text{int}}$ is an interactive force between the probes and the surrounding material (solvent and bath particles), written constitutively as [154],

$$n_a \langle \boldsymbol{F}^{\text{int}} \rangle = -n_a \langle \boldsymbol{R} \cdot \boldsymbol{U} \rangle + \langle \boldsymbol{f}_P \rangle = -\langle \boldsymbol{R} \cdot \boldsymbol{j} \rangle + \langle \boldsymbol{f}_P \rangle, \tag{4.4}$$

where $\boldsymbol{R}$ is an anisotropic tensor describing the resistance of the medium to the probes' motion, $\boldsymbol{j} = n_a \boldsymbol{U}$ is the probe flux, and $\boldsymbol{f}_P$ is an isotropic pressure

flux arising from the entropic restriction due to the presence of bath particles. Substituting Eq. (4.4) into Eq. (4.3) gives,

$$\mathbf{0} = \nabla \cdot \langle \boldsymbol{\Sigma} \rangle + n_a \langle \boldsymbol{F}^{\text{ext}} \rangle - \langle \boldsymbol{R} \cdot \boldsymbol{j} \rangle + \langle \boldsymbol{f}_P \rangle. \tag{4.5}$$

Equation (4.5) can be written as a linear combination of the equilibrium and nonequilibrium parts, denoted by the superscript *eq* and *neq*, respectively,

$$\mathbf{0} = \nabla \cdot \langle \boldsymbol{\Sigma}^{eq} \rangle + \nabla \cdot \langle \boldsymbol{\Sigma}^{neq} \rangle - \langle (\boldsymbol{R} \cdot \boldsymbol{j})^{eq}) \rangle - \langle (\boldsymbol{R} \cdot \boldsymbol{j})^{neq}) \rangle + \langle \boldsymbol{f}_P^{eq} \rangle + \langle \boldsymbol{f}_P^{neq} \rangle + n_a \langle \boldsymbol{F}^{\text{ext}} \rangle. \tag{4.6}$$

Simplification of Eq. (4.6) can be made by considering the momentum balance at and away from equilibrium. In the former case, when external force is absent and particles are driven solely by particle-density-gradient-diffusion, $\boldsymbol{F}^{\text{ext}} = 0$ and $\nabla \cdot \langle \boldsymbol{\Sigma}^{eq} \rangle \neq 0$, giving

$$0 = \nabla \cdot \langle \boldsymbol{\Sigma}^{eqm} \rangle - \langle (\boldsymbol{R} \cdot \boldsymbol{j})^{eqm}) \rangle + \langle \boldsymbol{f}_P^{eqm} \rangle; \tag{4.7}$$

whereas in the latter case, the flow-induced nonequilibrium flux $\langle (\boldsymbol{R} \cdot \boldsymbol{j}^{neq}) \rangle$ should contain both advective and diffusive contributions

$$\langle (\boldsymbol{R} \cdot \boldsymbol{j}^{neq}) \rangle = \langle \boldsymbol{R}^{neq} \cdot \boldsymbol{j}^{neq} \rangle + \langle \boldsymbol{R}^{neq'} \cdot \boldsymbol{j}^{neq'} \rangle = \langle \boldsymbol{R}^{neq} \rangle \cdot \langle \boldsymbol{j}^{neq} \rangle + \langle \boldsymbol{R}^{neq'} \cdot \boldsymbol{j}^{neq'} \rangle, \tag{4.8}$$

where the definition that the average of a product is the sum of the product of the averages and the average of the fluctuations is applied. In Eq. (4.8), the first term on the right-hand side corresponds to the mean advective motion of the probe, $\boldsymbol{R}^{neq} \equiv \boldsymbol{R}^{adv}$ and $\boldsymbol{j}^{neq} \equiv \boldsymbol{j}^{adv}$, and thus allows the dot-product to be taken outside the ensemble average. The second term is the diffusive flux, $\boldsymbol{R}^{diff} \equiv \boldsymbol{R}^{diff}$ and $\boldsymbol{j}^{neq'} \equiv \boldsymbol{j}^{diff}$. Combining Eqs. (4.6)-(4.8), the momentum balance becomes,

$$-\nabla \cdot \langle \boldsymbol{\Sigma}^{neq} \rangle = -\langle \boldsymbol{R}^{diff} \cdot \boldsymbol{j}^{diff} \rangle + n_a \langle \boldsymbol{F}^{\text{ext}} \rangle - \langle \boldsymbol{R}^{adv} \rangle \cdot \langle \boldsymbol{j}^{adv} \rangle + \langle \boldsymbol{f}_P^{neq} \rangle. \tag{4.9}$$

So far, we have derived a macroscopic momentum balance of the particle stress, Eq. (4.9), which is identical to the one for a non-hydrodynamically interacting system [154]. However, to generalize the original theory to one applicable

to a hydrodynamically interacting suspension, one must obtain a quantitative description of the effect of hydrodynamic interactions. In the following, we will constitutively model the flux on the right-hand side of Eq. (4.9).

We begin by modeling the nonequilibrium diffusive flux, $\langle \boldsymbol{R}^{diff} \cdot \boldsymbol{j}^{diff} \rangle$. The presence of the microstructure in a suspension hinders the probe's mean motion, and probe/bath particle encounters deflect the probe from its mean path. These nonequilibrium fluctuations are characterized by the flow-induced diffusivity $\boldsymbol{D}^{flow}$, which is the $O(\phi_b)$ forced-induced diffusion of the probes, also known as the microdiffusivity [153, 68, 69] (cf. Appendix E)). The volume fraction of bath particles is defined as $\phi_b = 4\pi n_b a^3/3$. Here, we assume a Fickian form for the diffusive flux,

$$\boldsymbol{j}^{diff} = -\boldsymbol{D}^{micro} \cdot \nabla n_a. \tag{4.10}$$

We recognize that the evolution of the microstructure and the fluctuation field, and in turn the diffusive flux, alters as the strengths of flow and hydrodynamic interactions vary. Thus, we account for the configuration-dependent fluctuations by $\boldsymbol{D}^{flow}$, and since configuration-dependence has been represented, the diffusive resistance tensor is captured by the resistance experienced by an isolated particle, $\boldsymbol{R}^{diff} = \boldsymbol{R}_a \equiv 6\pi\eta a \boldsymbol{I}$. Overall, the diffusive flux is written as

$$\langle \boldsymbol{R}^{diff} \cdot \boldsymbol{j}^{diff} \rangle = \boldsymbol{R}_a \cdot \boldsymbol{D}^{micro} \cdot \nabla n_a. \tag{4.11}$$

Next, we model the flux induced by the external force, $n_a \langle \boldsymbol{F}^{\text{ext}} \rangle$ [cf. Eq. (4.9)]. The presence of the microstructure hinders the probe's mean motion, giving rise to an effective suspension viscosity higher than the solvent viscosity. The effective viscosity changes with the degree of microstructural distortion which, in turn, depends on the flow strength and the range of entropic repulsion associated with the strength of hydrodynamic interactions (cf. Appendix D)). The

advective motion of the probes can be related to the configuration-dependent effective viscosity η^{eff} of a suspension via the Stokes' drag law [124, 78, 131]

$$\langle \boldsymbol{F}^{\text{ext}} \rangle \equiv \langle \boldsymbol{F}_F^{\text{ext}} \rangle = \boldsymbol{F}^{\text{ext}} = \frac{\eta_F^{eff}}{\eta} \boldsymbol{R}_a \cdot \langle \boldsymbol{U} \rangle = \boldsymbol{R}_F \cdot \langle \boldsymbol{U} \rangle, \tag{4.12}$$

and

$$\langle \boldsymbol{F}_U^{\text{ext}} \rangle = \frac{\eta_U^{eff}}{\eta} \boldsymbol{R}_a \cdot \boldsymbol{U} = \boldsymbol{R}_U \cdot \boldsymbol{U}, \tag{4.13}$$

where the subscripts F and U correspond to active microrheology operated under the fixed-force and fixed-velocity mode, respectively. In the fixed-force mode, a probe is driven by a fixed external force and experiences fluctuating motion. In contrast, in the fixed-velocity mode, the probe velocity is fixed and the external force is the fluctuating quantity. In dilute suspensions where pair-interactions dominate, the microviscosity η^{micro} is defined as the $O(\phi_b)$ coefficient of the effective viscosity

$$\frac{\eta^{eff}}{\eta} = 1 + \eta^{micro} \phi_b + O(\phi_b^2). \tag{4.14}$$

The flux $n_a \langle \boldsymbol{F}^{\text{ext}} \rangle$ can then be expressed in terms of the microviscosity as,

$$n_a \langle \boldsymbol{F}^{\text{ext}} \rangle = n_a \left(1 + \eta_F^{micro} \phi_b \right) \boldsymbol{R}_a \cdot \langle \boldsymbol{U} \rangle. \tag{4.15}$$

In addition to the flux above, the external force induces another advective flux $\langle \boldsymbol{R}^{adv} \rangle \cdot \langle \boldsymbol{j}^{adv} \rangle$ associated with the mean motion of the probe [cf. Eq. (4.9)]. In modeling the advective resistance tensor $\langle \boldsymbol{R}^{adv} \rangle$, one must account for the difference between the fixed-force and fixed-velocity motion [154]: the drag experienced by a probe in the fixed-force mode is lower by virtue of the freedom of fluctuations in its motion. Since we are considering fixed-force active microrheology, we follow Zia and Brady [154] to model the advective resistance tensor constitutively as

$$\langle \boldsymbol{R}^{adv} \rangle = (\boldsymbol{R}_U - \tilde{\boldsymbol{R}}), \tag{4.16}$$

where $\boldsymbol{R}_U = \boldsymbol{R}_a(\eta_U^{eff}/\eta)$ [cf. Eq. (4.13)], and $\tilde{\boldsymbol{R}} = \boldsymbol{R}(\tilde{\eta}/\eta)$ is the additional resistance experienced by a fixed-velocity probe, and its magnitude is proportional the the number of particle encounters, *i.e.* $\tilde{\eta}/\eta = \phi_b$. However, the magnitude of particle flux depends not only on the frequency of particle encounters but also on their strength and duration [34]. The latter two factors are accounted for by relating the fixed-velocity and fixed-force microviscosity via the anisotropic tensor $\boldsymbol{\alpha}$

$$\boldsymbol{R}_U = \boldsymbol{R}_a \cdot \left[\boldsymbol{I} + (\boldsymbol{I} + \boldsymbol{\alpha})\eta_F^{micro}\phi_b\right], \tag{4.17}$$

with

$$\boldsymbol{\alpha} = \begin{pmatrix} \alpha_\perp & 0 & 0 \\ 0 & \alpha_\perp & 0 \\ 0 & 0 & \alpha_\parallel \end{pmatrix} = \begin{pmatrix} f(\kappa)D_\parallel^{flow}/D_\perp^{flow} & 0 & 0 \\ 0 & f(\kappa)D_\parallel^{flow}/D_\perp^{flow} & 0 \\ 0 & 0 & x_{11}^a[(x_{11}^a + y_{11}^a)/2] \end{pmatrix}. \tag{4.18}$$

where $x_{ij}^a = x_{ij}^a(2a_{th}, \kappa)$ and $y_{ij}^a = y_{ij}^a(2a_{th}, \kappa)$ are the components of the hydrodynamic mobility function that couples the force on particle j to the induced translational velocity of particle i, and they govern the motion of particle i and j along and transverse to their line of centers, respectively [75]. Here, the contact values of x_{11}^a and y_{11}^a are taken, and thus they are functions of κ. Physically, the additional drag in the direction parallel to the external force $\alpha_\parallel\eta_F^{micro}$ is chiefly governed by the longitudinal mobility x_{11}^a, as the drag in a squeezing flow is higher than that in a shearing flow. However, the external force does not always align with the axis longitudinal to the centers of two particles throughout a particle encounter. This geometric effect, in addition to the effect of transverse relative motion, is accounted for by a correction estimated as $[(x_{11}^a + y_{11}^a)/2]$. In contrast, in the direction perpendicular to the external force, the additional drag $\alpha_\perp\eta_F^{micro}$ changes with the anisotropy in diffusivity. It can be understood that a probe driven by a fixed velocity permits no fluctuations, and the additional drag in the perpendicular direction on a fixed-force probe relates to the strength of

its fluctuations, measured by the ease of a probe to fluctuate in the direction parallel to the external force $D_{\parallel}^{flow}$ relative to that in the perpendicular direction $D_{\perp}^{flow}$. The flow-induced diffusivity parallel and perpendicular to the line of the external force, $D_{\parallel}^{flow}$ and $D_{\perp}^{flow}$, are obtained by projecting the tensor in the corresponding directions, $D_{\parallel}^{flow} = \boldsymbol{D}^{flow} : \boldsymbol{e}_z\boldsymbol{e}_z$ and $D_{\perp}^{flow} = \boldsymbol{D}^{flow} : \boldsymbol{e}_y\boldsymbol{e}_y$, where $\boldsymbol{e}_z$ and $\boldsymbol{e}_y$ are the unit vectors in the direction parallel and perpendicular to the external force, respectively. The anisotropy of the diffusivity $D_{\parallel}^{flow}/D_{\perp}^{flow}$ is complemented by the equilibrium diffusivity $f(\kappa) \sim D^{eq}$, which must be present due to the structure regardless of the strength of flow. Plots of $\alpha_{\parallel}$ and $\alpha_{\perp}$ are presented in Appendix E). Overall, the advective flux $\langle \boldsymbol{R}^{adv} \rangle \cdot \langle \boldsymbol{j}^{adv} \rangle$ is written constitutively as

$$\langle \boldsymbol{R}^{adv} \rangle \cdot \langle \boldsymbol{j}^{adv} \rangle = n_a \left[\boldsymbol{I} + (\boldsymbol{I} + \boldsymbol{\alpha}) \eta_F^{micro} \phi_b - \phi_b \right] \cdot \boldsymbol{R}_a \cdot \langle \boldsymbol{U} \rangle. \tag{4.19}$$

The remaining term to be modeled in Eq. (4.9) is the nonequilibrium particle pressure $\langle \boldsymbol{f}^{neq} \rangle$, which arises from bombardments of the embedded colloidal particles onto a fictitious boundary of a suspension [154, 34, 35]. A traveling probe imparts energy into a suspension, simultaneously increasing fluctuations of the embedded particles and thus osmotic pressure in the system. Analogous to the kinetic theory of molecular gas, these fluctuations can be modeled as an effective temperature of the system [154]. Since temperature is proportional to the average of the square of the probes' velocity fluctuations, which is also proportional to the flow-induced diffusivity, the nonequilibrium pressure can be written as,

$$\langle \boldsymbol{f}^{neq} \rangle = \frac{1}{3} tr(\boldsymbol{D}^{flow}) \boldsymbol{R}_a \cdot \nabla n_a, \tag{4.20}$$

where this "force-induced temperature" is assumed to be isotropic.

Inserting Eqs. (4.11), (4.15), (4.19) and (4.20) into Eq. (4.9), the momentum

balance becomes,

$$-\nabla\cdot\langle\boldsymbol{\Sigma}^{neq}\rangle = \boldsymbol{R}_a\cdot\boldsymbol{D}^{flow}\cdot\nabla n_a - n_a\phi_b\left(\boldsymbol{\alpha}\eta_F^{micro}-\boldsymbol{I}\right)\cdot\boldsymbol{R}^a\cdot\langle\boldsymbol{U}\rangle + \frac{1}{3}tr(\boldsymbol{D}^{flow})\boldsymbol{R}_a\cdot\nabla n_a. \quad (4.21)$$

Equation (4.21) can be simplified by approximating the gradient of the probes' number density by a Fickian scaling,

$$\nabla n_a \sim \frac{j}{D^{flow}} \sim \frac{n_a U}{D^{flow}} \sim \frac{n_a Pe D_a}{D^{flow} a}, \quad (4.22)$$

where $D^{flow} = \boldsymbol{D}^{flow}/\phi_b$ is the magnitude of the flow-induced diffusivity, and the relation for a dilute suspension [154],

$$\nabla\cdot\langle\boldsymbol{\Sigma}^{neq}\rangle = \frac{\partial\langle\boldsymbol{\Sigma}^{neq}\rangle}{\partial n_a}\cdot\nabla n_a = \frac{\langle\boldsymbol{\Sigma}^{neq}\rangle}{n_a}\cdot\nabla n_a, \quad (4.23)$$

the momentum balance reads,

$$-\frac{\langle\boldsymbol{\Sigma}^{neq}\rangle}{n_a kT} = \left(2\boldsymbol{I}-\eta_F^{micro}\boldsymbol{\alpha}\right)\cdot\frac{\boldsymbol{D}^{flow}}{D_a} + \frac{1}{3}tr\left(\frac{\boldsymbol{D}^{flow}}{D_a}\right)\boldsymbol{I}. \quad (4.24)$$

Rearrangements leads to the Stokes-Einstein form,

$$\boldsymbol{D}^{flow} = -\left(\frac{\boldsymbol{\Sigma}^{neq}}{n_a}+\boldsymbol{P}\right)\cdot\boldsymbol{M}^{neq}, \quad (4.25)$$

where $\boldsymbol{P}\equiv\boldsymbol{R}_a\cdot tr(\boldsymbol{D}^{flow})\boldsymbol{I}/3$, and the nonequilibrium mobility tensor is given by,

$$\boldsymbol{M}^{neq} = \left(2\boldsymbol{I}-\eta_F^{micro}\boldsymbol{\alpha}\right)^{-1}\cdot\boldsymbol{M}_a, \quad (4.26)$$

where $\boldsymbol{M}_a = \boldsymbol{I}/6\pi\eta a$. Taking into account the effect of hydrodynamic interactions, Eq. (4.25) is a generalized nonequilibrium Stokes-Einstein relation — a nonequilibrium fluctuation-dissipation relation, where the imparted energy to a suspension, represented by $\boldsymbol{\Sigma}^{neq}$ and $\boldsymbol{P}$, drives fluctuations $\boldsymbol{D}^{flow}$, and is dissipated back to the solvent precisely by viscous drag $(\boldsymbol{M}^{neq})^{-1}$. In Sec. 4.4, we test this relation by comparing its prediction to results obtained from statistical mechanics theory.

4.4 Results

The generalized nonequilibrium Stokes-Einstein relation, Eq. (4.24), expresses suspension stress as an balance between nonequilibrium fluctuation and dissipation. To test this relation, in this section we compare its prediction [the right-hand side of Eq. (4.24)] with the statistical mechanics theory [the left-hand side of Eq. (4.24)] via four quantities, namely the suspension stress parallel and perpendicular to the line of the external force, the first normal stress difference, and the particle osmotic pressure, for the full range of flow strength and strength of hydrodynamic interactions, spanning four decades of Pe and eight decades of κ. Details of the suspension stress and its statistical mechanics theory are given in Chapters 2 and 3. We begin with analyzing the normal stresses.

4.4.1 Normal stresses

The suspension stress is a second-order tensor with six independent elements for an isotropic material. In microrheology, only the normal stresses, Σ_{xx}, Σ_{yy} and Σ_{zz}, are nonzero owing to the axisymmetric microstructure around the probe. The axisymmetric geometry also produces identical normal stresses along the orthogonal axes, $\Sigma_{yy} = \Sigma_{xx}$. This leaves only two relevant quantities: the normal stresses acting parallel and perpendicular to the direction of the external force, $\Sigma_{\parallel} \equiv \Sigma_{zz}$ and $\Sigma_{\perp} \equiv \Sigma_{yy} = \Sigma_{xx}$, which are obtained by projecting the stress tensor in the corresponding directions. The generalized nonequilibrium Stokes-Einstein relations for the normal stresses read

$$-\frac{\langle \Sigma_{\parallel}^{neq} \rangle}{n_a kT\phi_b} = \left(2 - \alpha_{\parallel}\eta_F^{micro}\right)\frac{D_{\parallel}^{flow}}{D_a\phi_b} + \frac{1}{3}\left(\frac{D_{\parallel}^{flow} + 2D_{\perp}^{flow}}{D_a\phi_b}\right), \tag{4.27}$$

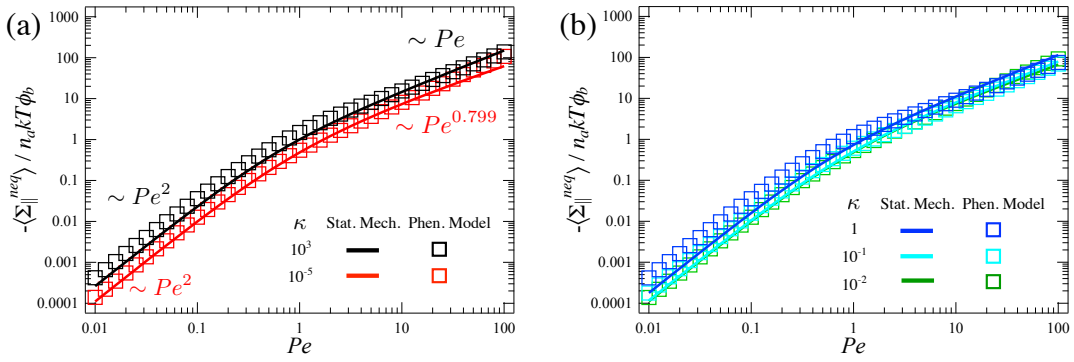

Figure 4.1: Nonequilibrium parallel normal stress, $\langle\Sigma_{\parallel}^{neq}\rangle$, scaled by ideal osmotic pressure $n_a kT$ and volume fraction of bath particles ϕ_b, as a function of flow strength Pe for (a) asymptotically weak ($\kappa \gg 1$) and strong hydrodynamic interactions ($\kappa \ll 1$), and (b) various intermediate strengths of hydrodynamic interactions. Solid lines: statistical mechanics model [154, 34], left-hand side of Eq. (4.27). Squares: phenomenological model, right-hand side of Eq. (4.27).

$$-\frac{\langle\Sigma_{\perp}^{neq}\rangle}{n_a kT\phi_b} = \left(2 - \alpha_{\perp}\eta_F^{micro}\right)\frac{D_{\perp}^{flow}}{D_a\phi_b} + \frac{1}{3}\left(\frac{D_{\parallel}^{flow} + 2D_{\perp}^{flow}}{D_a\phi_b}\right). \tag{4.28}$$

We test the generalized nonequilibrium Stokes-Einstein relation first by examining the parallel normal stress in the asymptotic limit of weak and strong hydrodynamic interactions, $\kappa \gg 1$ and $\kappa \ll 1$ respectively. Prediction from the new theory, right-hand side of Eq. (4.27), is plotted in Fig. 4.1(a) as a function of the flow strength, Pe, along with the results obtained from statistical mechanics model [154, 34], left-hand side of Eq. (4.27). In the asymptotic limit of weak hydrodynamics (black line and squares), the phenomenological model gives excellent prediction of the stress for the entire range of flow strength and, in particular, recovering the low- and high-Pe scalings in the asymptotic limits of weak and strong flow. In the opposite limit of strong hydrodynamics (red line and squares), the phenomenological model captures the effects of hydrodynamic interactions accurately: hydrodynamics suppress normal stresses, where

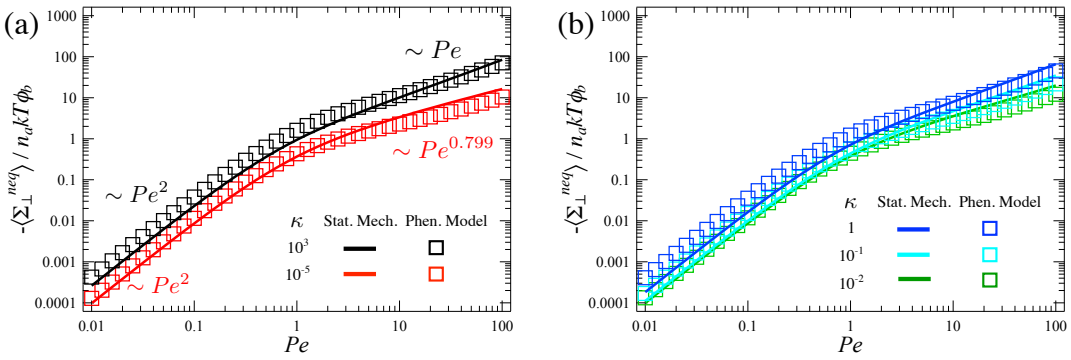

Figure 4.2: Nonequilibrium perpendicular normal stress, $\langle\Sigma_\perp^{neq}\rangle$, scaled by ideal osmotic pressure $n_a kT$ and volume fraction of bath particles ϕ_b, as a function of flow strength Pe for (a) asymptotically weak ($\kappa \gg 1$) and strong hydrodynamic interactions ($\kappa \ll 1$), and (b) various intermediate strengths of hydrodynamic interactions. Solid lines: statistical mechanics model [154, 34], left-hand side of Eq. (4.28). Squares: phenomenological model, right-hand side of Eq. (4.28).

the reduction is quantitative and qualitative in the low- and high-Pe regimes, respectively [34]. Parallel normal stresses of various intermediate strengths of hydrodynamic interactions are plotted in Fig. 4.1(b). The prediction by the new theory and statistical mechanics theory matches very well for all values of Pe and κ.

The comparison for the perpendicular normal stress is plotted in Fig. 4.2. The phenomenological model offers accurate predictions for the full range of flow strength and hydrodynamics, and it captures the monotonically decreasing trend of the stress with increasing strength of hydrodynamic interactions — a significant manifestation of the suppressive nature of hydrodynamics [34].

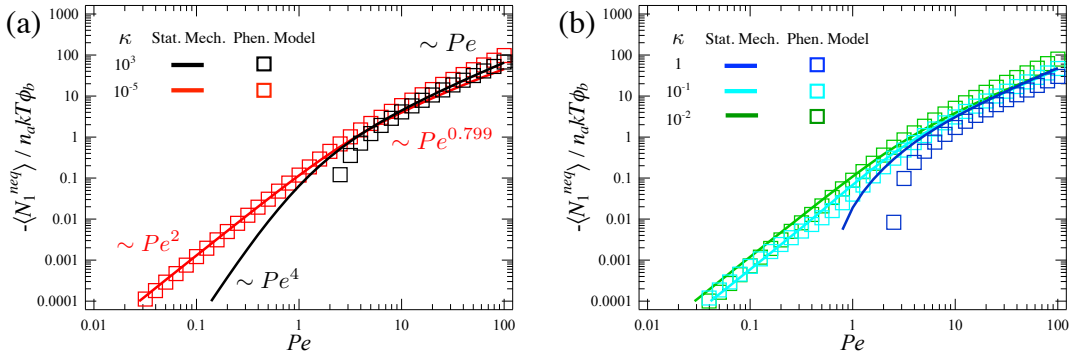

Figure 4.3: Nonequilibrium first normal stress difference, $\langle N_1^{neq}\rangle$, scaled by ideal osmotic pressure $n_a kT$ and volume fraction of bath particles ϕ_b, as a function of flow strength Pe for (a) asymptotically weak ($\kappa \gg 1$) and strong hydrodynamic interactions ($\kappa \ll 1$), and (b) various intermediate strengths of hydrodynamic interactions. Solid lines: statistical mechanics model [154, 35], left-hand side of Eq. (4.29). Squares: phenomenological model, right-hand side of Eq. (4.29).

4.4.2 Normal stress differences

Owing to the axisymmetry of the microstructure, the second normal stress difference is identically zero regardless of the strength of flow and hydrodynamic interactions (cf. Sec. sec:Sec3). In this section, we focus on testing the generalized nonequilibrium Stokes-Einstein relation via the first normal stress difference, defined as $N_1 \equiv \Sigma_{zz} - \Sigma_{yy}$. The corresponding expression from the generalized nonequilibrium Stokes-Einstein relation read

$$-\frac{\langle N_1^{neq}\rangle}{n_a kT\phi_b} = \left(2 - \alpha_{\parallel}\eta_F^{micro}\right)\frac{D_{\parallel}^{flow}}{D_a\phi_b} - \left(2 - \alpha_{\perp}\eta_F^{micro}\right)\frac{D_{\perp}^{flow}}{D_a\phi_b}. \tag{4.29}$$

Fig. 4.3(a) shows the first normal stress difference evaluated from the generalized nonequilibrium Stokes-Einstein relation, right-hand side of Eq. (4.29), and that from statistical mechanics theory [154, 35], left-hand side of Eq. (4.29), in the limits of asymptotically weak ($\kappa \gg 1$) and strong hydrodynamic inter-

actions ($\kappa \ll 1$). In the limit of weak hydrodynamics (black line and squares), the phenomenological model predicts the strong-flow response accurately, but a discrepancy is shown when flow is weak. The latter can be explained that in the dual limit of weak flow and hydrodynamics, normal stresses are induced solely by elastic interparticle collisions between the probe and surrounding bath particles, and grow as Pe^2 [cf. Figs. 4.1(a) and 4.2(a)]. At equilibrium, the collisions are equally likely in the parallel and perpendicular directions as reflected from the identical scalar coefficients of the Pe^2 contribution of the normal stresses which, cancel precisely, leading to a much smaller Pe^4 first normal stress difference [35]. Thus, given the smallness and the sensitivity to Pe of the first normal stress difference at this limit, any minor discrepancies in predicting the normal stresses would cause inaccuracy in capturing such a weak response. However, we emphasize that such discrepancy is relatively insignificant since normal stress differences at $Pe < 1$ is practically formidable to measure [149, 122, 56, 54] and, to practical concern, the more important strong-flow response is captured accurately.

In the opposite limit of strong hydrodynamics (red line and squares), the prediction by the new theory agrees well with the statistical mechanics results. Good agreement between two sets of data is also demonstrated for other values of κ [panel (b)]. In particular, the phenomenological model captures the change of sign of the first normal stress difference with Pe for suspensions with moderately strong hydrodynamics that still permit interparticle collisions ($\kappa = 1$). In prior work, a novel mechanism was identified that interparticle repulsion alone can lead to such sign change [35], instead of owing to the growing dominance of hydrodynamic over Brownian forces [50, 19].

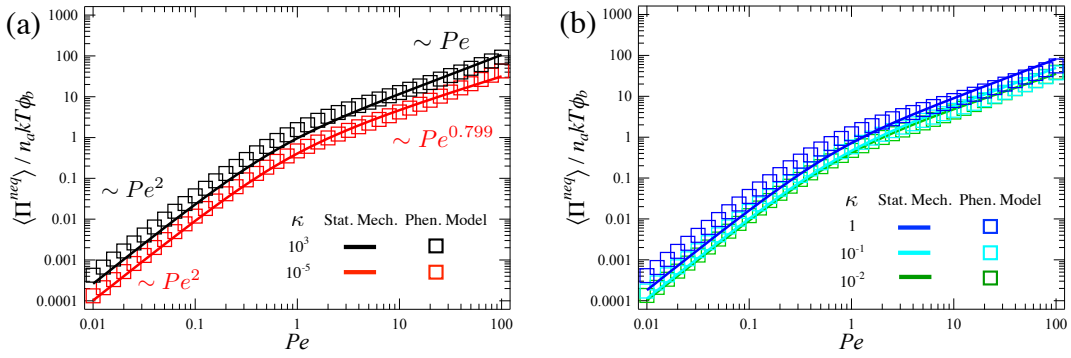

Figure 4.4: Nonequilibrium osmotic pressure, $\langle \Pi^{neq} \rangle$, scaled by ideal osmotic pressure $n_a kT$ and volume fraction of bath particles ϕ_b, as a function of flow strength Pe for (a) asymptotically weak ($\kappa \gg 1$) and strong hydrodynamic interactions ($\kappa \ll 1$), and (b) various intermediate strengths of hydrodynamic interactions. Solid lines: statistical mechanics model [154, 35], left-hand side of Eq. (4.30). Squares: phenomenological model, right-hand side of Eq. (4.30).

4.4.3 Osmotic pressure

In addition to an anisotropic deformation of a suspension described by the normal stress differences, the presence of particles brings forth a osmotic pressure governing an isotropic expansion or contraction. In this section, we test the generalized nonequilibrium Stokes-Einstein relation by comparing its prediction of the particle pressure with that by the statistical theory. The generalized nonequilibrium Stokes-Einstein relation for the osmotic pressure reads

$$\frac{\langle \Pi^{neq} \rangle}{n_a kT\phi_b} = \frac{1}{3}\left(\frac{D_{\parallel}^{flow} + 2D_{\perp}^{flow}}{D_a \phi_b}\right)\left[3 - \eta_F^{micro}\left(\frac{\alpha_{\parallel} D_{\parallel}^{flow} + 2\alpha_{\perp} D_{\perp}^{flow}}{D_{\parallel}^{flow} + 2D_{\perp}^{flow}}\right)\right]. \tag{4.30}$$

The particle osmotic pressure predicted by the new theory [right-hand side of Eq. (4.30)] and the micromechanical model (left-hand side) is plotted in Fig. 4.4(a) in the limits of asymptotically weak and strong hydrodynamic interactions. In both limits, the prediction by the phenomenological model matches

very well with the statistical mechanics theory. When flow is weak, the osmotic pressure grows quadratically with Pe regardless of the strength of hydrodynamic interactions. The pressure increases with flow strength and, when flow is strong, it scales as $Pe^{0.799}$ in the limit of strong hydrodynamics, and as Pe when hydrodynamic interactions are weak. The predictions for other strengths of hydrodynamics are plotted in panel (b), and excellent agreements are also seen for the full range of Pe.

Overall, we showed an very good agreement between results obtained from the generalized nonequilibrium Stokes-Einstein relation and the statistical mechanics theory. The accurate predictions shown by the new model have two major impacts: first, in prior work only the microviscosity and flow-induced diffusivity could be measured. The present model broadens the scope of active microrheology such that the suspension stress can be inferred from the mean (microviscosity) and mean-square motion (flow-induced diffusivity) of a probe particle via a nonequilibrium balance of stress, dissipation and fluctuations. Second, evaluating the suspensions stress from statistical theory demands information of the microstructure, which is labor-intensive and can be tedious in practice. The present model circumvents this problem and permits determination of the suspension stress form the motion of a single probe particle. In Sec. 4.5, we shall further compare these results with Accelerated Stokesian Dynamics simulations, and discuss the development of a scaling theory for the stress in suspensions with different particle concentrations.

4.5 Accelerated Stokesian Dynamics simulations

We begin with a brief review of the Stokesian Dynamics simulation framework. The basis of Stokesian Dynamics simulations is to obtain the evolution of particle positions in a suspension [22, 121, 8]. For a system of N hard-sphere colloidal particles of hydrodynamic radius a dispersed homogeneously in an incompressible, Newtonian solvent of dynamic viscosity η and density ρ, the particle motion is described by the coupled N-body Langevin equation

$$\boldsymbol{m} \cdot \frac{d\boldsymbol{U}}{dt} = \boldsymbol{F}^{ext} + \boldsymbol{F}^{H} + \boldsymbol{F}^{B} + \boldsymbol{F}^{P}, \tag{4.31}$$

where $\boldsymbol{m}$ is a generalized mass/moment of inertia tensor of dimension $6N \times 6N$ and $\boldsymbol{U}$ is a vector of dimension $6N$ for the translational/rotational particle velocities relative to the solvent. The force/torque vectors $\boldsymbol{F}$ on the right-hand side are of dimension $6N$, comprising contributions from external, hydrodynamic, Brownian and interparticle forces. In colloidal suspensions, particle size is small, and fluid and particle inertia are negligible.

In fixed-force active microrheology, there is no externally applied forces or torques on all particles, $\boldsymbol{F}^{ext} = \boldsymbol{0}$, except on the probe. As a particle moves relative to the solvent, the solvent exerts hydrodynamic forces and torques on the particle. In Stokes flow, moments of the hydrodynamic surface traction acted on the particles are linearly coupled to the particle motion,

$$\boldsymbol{F}^{H} = -\boldsymbol{R}_{FU} \cdot \boldsymbol{U}, \tag{4.32}$$

where the configuration-dependent hydrodynamic resistance tensor $\boldsymbol{R}_{FU}$ is the kernal for the coupling.

The random Brownian force and torque $\boldsymbol{F}^{B}$ arise due to the collisions between the particle and solvent molecules during time intervals much longer

than the inertial relaxation time scale of the particle $\tau_I = m/6\pi\eta a$. The Brownian force and torque satisfy Gaussian statistics: they are zero on average, but has a nonzero temporal correlations on τ_I,

$$\overline{\boldsymbol{F}^B} = 0, \qquad \overline{\boldsymbol{F}^B(0)\boldsymbol{F}^B(t)} = 2kT\boldsymbol{R}_{FU}\delta(t), \tag{4.33}$$

where the overbar denotes a noise averaging over times much longer than individual solvent collisions and long compared to τ_I, and $\delta(t)$ is the Dirac delta function.

The interparticle force, $\boldsymbol{F}^P$, is general to represent any non-hydrodynamic, deterministic force, *e.g.* electrostatic forces or frictional force as arises in the presence of particle roughness. In the present simulation framework, we employ a hard-sphere force, $\boldsymbol{F}^P = kT\hat{\boldsymbol{r}}\delta(r-2a)$ (r is the separation distance between particle pairs and $\hat{\boldsymbol{r}}$ is the unit vector connecting centers of two particles) such that particle overlaps are prevented by an infinite potential at contact, and the particles exert no direct force on each other otherwise. However, since particles interact with full hydrodynamic interactions in our model, $\kappa = 0$, where lubrication forces prohibit particles from touching, the hard-sphere interparticle force has no effect on the evolution of particle evolution and rheology.

Evolution equations of particle position can be obtained by integrating Eq. (4.31) over a time step Δt which is large compared to the inertial relaxation time of the particle, τ_I, but small compared to the diffusive time of the particle $\tau_D = a^2/D$ over which the configuration changes. We nondimensionalize the length scale by the particle hydrodynamic radius a; and to accurately capture the particle dynamics in different flow regimes, the diffusive time a^2/D and advective time scales a/U are used when flow is weak and strong, respectively.

The evolution equation of particle position in the weak flow regime reads

$$\Delta x = \hat{Pe}\left(\boldsymbol{R}_{FU}^{-1} \cdot \hat{\boldsymbol{F}}^{\text{ext}}\right)\Delta t + \Delta \boldsymbol{x}^{P} + \nabla \cdot \boldsymbol{R}_{FU}^{-1}\Delta t + \boldsymbol{X}(\Delta t) + O(\Delta t), \tag{4.34a}$$

$$\overline{\boldsymbol{X}} = 0, \qquad \overline{\boldsymbol{X}(\Delta t)\boldsymbol{X}(\Delta t)} = 2\boldsymbol{R}_{FU}^{-1}\Delta t; \tag{4.34b}$$

whereas in the strong forcing regime it is given by

$$\Delta x = \left(\boldsymbol{R}_{FU}^{-1} \cdot \hat{\boldsymbol{F}}^{\text{ext}}\right)\Delta t + \Delta \boldsymbol{x}^{P} + \frac{1}{\hat{Pe}}\nabla \cdot \boldsymbol{R}_{FU}^{-1}\Delta t + \frac{1}{\hat{Pe}^{1/2}}\boldsymbol{X}(\Delta t) + O(\Delta t), \tag{4.35}$$

where $\hat{Pe} = F_0/(kT/a)$, and $\hat{\boldsymbol{F}}^{\text{ext}} = \boldsymbol{F}^{\text{ext}}/F_0$ is the unit vector pointing in the direction of the external probe force. In Eqs. (4.34a) and (4.35), the first term is the particle displacement induced by the external force; the second term by the interparticle force; the third term by the mean drift of Brownian motion due to particle concentration gradients; and the fourth term is a random Brownian displacement which has a zero mean and covariance given by the inverse of the resistance tensor [cf. Eq. (4.34b)].

While the evolution of particle position is obtainable with the resistance tensor $\boldsymbol{R}_{FU}$, computing the suspension stress requires couplings between stresslet and particle motion. To this end, we invoke the grand resistance matrix,

$$\mathcal{R} = \begin{pmatrix} \boldsymbol{R}_{FU} & \boldsymbol{R}_{FE} \\ \boldsymbol{R}_{SU} & \boldsymbol{R}_{SE} \end{pmatrix}, \tag{4.36}$$

where $\boldsymbol{R}_{SU}$ governs the coupling between stresslet and particle motion, and $\boldsymbol{R}_{FE}$ and $\boldsymbol{R}_{SE}$ describe the coupling between force/torque and flow rate of strain, and the coupling between stresslet and flow rate of strain, respectively. As an improvement to the original Stokesian Dynamics framework [22, 121], the resistance tensors $\boldsymbol{R}_{SU}$ and $\boldsymbol{R}_{SE}$ in our model are not traceless such that their trace couple particle motion to the pressure moment on the surface of particles, giving rise to an induced particle osmotic pressure [74, 128].

The grand resistance matrix captures hydrodynamic interactions among particles in the entire simulation domain, comprising both near-field two-body interactions, and far-field many-body interactions. Since the construction of the grand resistance matrix is standard and our focus here is to compare our new theory with simulation results, we refer readers to the literature for further details [22, 121, 8, 128]. Equation (4.31) can now be written in a general form as

$$\begin{pmatrix} \mathbf{0} \\ \boldsymbol{S} \end{pmatrix} = -\boldsymbol{\mathcal{R}} \cdot \begin{pmatrix} \boldsymbol{U} \\ \mathbf{0} \end{pmatrix} + \begin{pmatrix} \boldsymbol{F}^B + \boldsymbol{F}^P + \boldsymbol{F}^{ext} \\ -\boldsymbol{r}\boldsymbol{F}^P \end{pmatrix}, \tag{4.37}$$

where straining flow is identically zero as prescribed by the rigidity of particles and no imposed straining flow. Once the grand resistance matrix is constructed with particle configurations at every time step, particle motion $\boldsymbol{U}$ and stresslet $\boldsymbol{S}$ are obtained upon solving Eq. (4.37). In this study, we conduct simulations of 187 particles, with values of $Pe \in [0.1, 100]$. An average suspension stress $\langle \boldsymbol{\Sigma} \rangle$ is obtained by averaging over a set of 200 simulations of 2.5×10^4 time steps each for each Pe.

Figure 4.5 shows the simulation data (filled symbols) of the normal stresses, first normal stress difference, and the osmotic pressure, along with the results from the generalized nonequilibrium Stokes-Einstein relation (squares) and statistical mechanics theory (solid lines), all in the limit of strong hydrodynamics, $\kappa \ll 1$. We use the simulation results with the lowest bath particle volume fraction, $\phi_b = 0.05$ (filled circles), to compare with the phenomenological model and the statistical mechanics theory. Very good agreements between three sets of data are exhibited by all four quantities, especially in the strong-flow regime where the adverse effect of Brownian noise from simulations is attenuated. Again, the good matching of the results highlights the merit of the generalized nonequilibrium Stokes-Einstein relation that suspension stress can be inferred

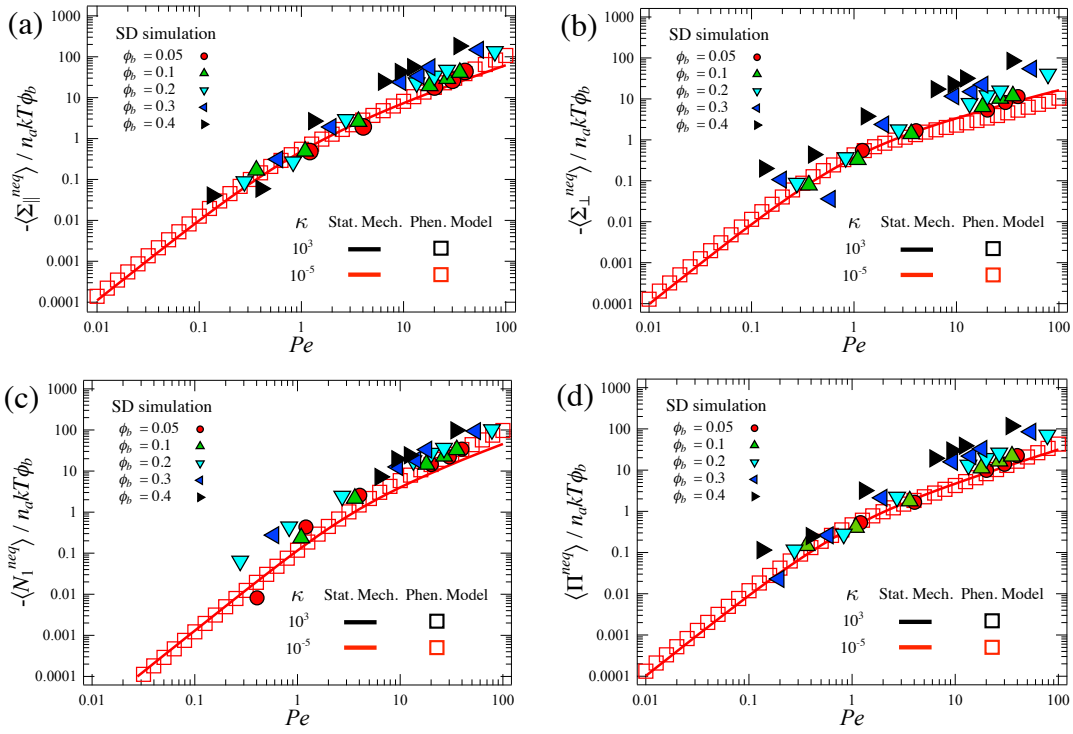

Figure 4.5: Nonequilibrium (a) parallel and (b) perpendicular normal stress, $\langle\Sigma_{\parallel}^{neq}\rangle$ and $\langle\Sigma_{\perp}^{neq}\rangle$, (c) first normal stress difference $\langle N_1^{neq}\rangle$, and (d) osmotic pressure $\langle\Pi^{neq}\rangle$, scaled by ideal osmotic pressure $n_a kT$ and volume fraction of bath particles ϕ_b, as a function of flow strength Pe in the asymptotic limit of strong hydrodynamics $\kappa \ll 1$. Solid lines: statistical mechanics theory [34, 35], left-hand side of Eq. (4.24). Squares: phenomenological model, right-hand side of Eq. (4.24). Filled symbols: Accelerated Stokesian Dynamics simulations, $\phi_b = 0.05$ (●), 0.1 (▲), 0.2 (▼), 0.3 (◀) and 0.4 (▶).

from the mean (microviscosity) and mean-square motion (flow-induced diffusivity) of a single probe particle, without intensive computational simulations or measurements of the microstructure.

The normal stresses, first normal stress difference and particle osmotic from suspensions with higher particle volume fraction are also presented in Fig. 4.5 (filled triangles). All four quantities were shown to increase with increasing particle volume fraction. Physically, it can be understood that suspension stress can

be interpreted as the density of entropic energy in a suspension [154, 155, 34]. As particle concentration increases, probe motion causes more configuration distortion, meaning that more energy is stored entropically in a suspension and, therefore, the stress increases. Interesting, the increase with particle volume fraction is not quantitative, but the Pe-scaling of the strong-flow response strengths with increasing ϕ_b. To connect the response of suspensions with different concentrations, we propose a scaling theory as follows. We recall from statistical mechanics theory that the high-Pe asymptotes of all four quantities scale as $g^{eqm}(2a_{th})Pe^{\delta}$ [34, 35], where $g^{eqm}(2a_{th})$ is the equilibrium structure at contact and $\delta = (G_1 - H_0)/G_1$ is the mobility ratio with H_0 and G_1 associated with the transverse and longitudinal relative mobility, respectively [75, 78]. As a suspension is no longer dilute, we expect that both $g^{eqm}(2a_{th})$ and δ become volume-fraction-dependent. We propose that the concentration-dependent equilibrium structure $g^{eqm}(2a_{th}, \phi_b)$ can be estimated from the Carnahan-Starling equation of state [31], whereas the concentration-dependent mobility ratio $\delta(\phi_b)$ can be constructed with recently-derived concentrated mobility functions [157]. A detailed discussion of the development of this scaling theory will be presented in Chapter 5, and results show that the scaling theory unifies dilute and concentrated suspensions response by collapsing the stress from different suspensions onto a single curve. In Sec. 4.6, we discuss the experimental measurements required to apply the nonequilibrium Stokes-Einstein relation.

4.6 Experimental measurement

The significance of the generalized nonequilibrium Stokes-Einstein theory is pronounced: in contrast to traditional rheometry where suspension stress is

measured either directly via stress transducers [149, 122, 56, 54] or by measuring particle microstructure via fast or dynamic confocal microscopy [55, 91, 146], the present theory opens a new avenue that suspension stress of a hydrodynamically interacting suspension can be obtained simply by tracking the mean (microviscosity) and mean-square motion (flow-induced diffusivity) of a single probe. In the following, we discuss the measurements of these two quantities in the experimental context.

To obtain the microviscosity, the only measurement required is the total displacement of the probe motion over time, from which one can compute the average speed as $\langle U \rangle = d\langle x \rangle / dt$. The average speed is then utilized to evaluate the microviscosity via the Stokes' drag law [61, 124, 78]

$$\frac{\eta_F^{micro}}{\eta} = \frac{6\pi\eta a}{F_0}\langle U \rangle, \tag{4.38}$$

where angle brackets signify an average over many realizations, and F_0 is the strength of a constant probe forcing. In Eq. (4.38), the subscript F indicates fixed-force active microrheology where the external force imposed on the probe is fixed and the probe velocity is free to fluctuate. In fixed-velocity active microrheology [102, 126, 131], measurements are taken analogously, with the external velocity being held fixed and the external force being the fluctuating quantity.

To obtain the flow-induced diffusivity, the mean displacement of the probe is required in addition to the total displacement

$$\boldsymbol{D}^{flow} = \frac{1}{2}\frac{d}{dt}\langle \boldsymbol{x}'(t)\boldsymbol{x}'(t) \rangle, \tag{4.39}$$

where $\boldsymbol{x}'(t) \equiv \boldsymbol{x}(t) - \langle \boldsymbol{x}(t) \rangle$ is the displacement from the mean as a function of time. Clearly from Eqs. (4.38)–(4.39), one only needs the movement of a single probe

particle to give a full rheological description of a hydrodynamically interacting suspension — microviscosity, flow-induced diffusivity, and suspension stress. Detailed knowledge of the embedding material, such as microstructure of the entire suspension, is not required.

4.7 Conclusions

We derived a generalized nonequilibrium Stokes-Einstein relation for predicting stress in a hydrodynamically interacting suspension via an active microrheology framework. This novel phenomenological model was derived based on a volume-averaged, pointwise Cauchy equation of motion which takes into account both advective and diffusive flux arising from the relative motion between the probe and surrounding materials. We related the advective flux to the reduction in the mean speed of the probe, the microviscosity, and the diffusive flux to the magnitude of the fluctuating motion, the flow-induced diffusivity. A new anisotropic effective resistance tensor was constructed utilizing developed pair mobility functions to constitutively model the difference in the hydrodynamically coupled particle motion between fixed-force and fixed-velocity active microrheology. The resulting balance of the nonequilibrium stress, fluctuations and dissipation is the generalized Stokes-Einstein relation which enables determination of the suspension stress from the motion of a single probe particle.

We compared the normal stresses, first normal stress difference and particle osmotic pressure predicted by the generalized nonequilibrium Stokes-Einstein relation to statistical mechanics theory and Accelerated Stokesian Dynamics

simulations, and very good agreements were shown between the three sets of data. In particular, the suppressive nature of hydrodynamics to the normal stresses and osmotic pressure for the full range of flow strength was recovered by the phenomenological model, and the new theory also accurately captured the change of sign with flow strength in the first normal stress difference in a suspension when the strength of hydrodynamics is moderate. The generalized nonequilibrium Stokes-Einstein relation not only expands the scope of active microrheology such that a full characterization of a suspension, including the material stress tensor, can be obtained, but also such characterization requires only motion of a single probe, negating the needs for otherwise labor-intensive microstructure measurements or expensive computational simulations.

The influence of particle concentration on suspension stress response was also studied, where the normal stresses, first normal stress difference and osmotic pressure are all strengthened with increasing particle volume fraction. We proposed a scaling theory collapsing stress response of concentrated suspensions onto a single curve, and we referred readers to Chapter 5 for its details. In closing of this work, we discussed the laboratory measurements required to apply the generalized nonequilibrium Stokes-Einstein relation.

CHAPTER 5

MICROVISCOSITY, NORMAL STRESS AND OSMOTIC PRESSURE OF BROWNIAN SUSPENSIONS BY ACCELERATED STOKESIAN DYNAMICS SIMULATION

5.1 Introduction

Complex fluids comprise a broad class of materials, including everyday examples such as ketchup, paint, and personal-care products as well as more exotic complex fluids such as the interior of living cells, pharmaceutical preparations, and liquid crystals. What sets them apart from simple Newtonian fluids is the dependence of their rheological behavior on flow. This difference arises from the presence of a secondary, non-continuum phase that gives the fluid a microscopic structure. Asymmetric distortion and relaxation of this microstructure produces well-known non-Newtonian rheology, such as shear-thinning and thickening [10, 135], viscoelasticity [107], normal stress differences [50], and flow-induced diffusion [49], among others. Many of these effects are explained at the pair level, while three-body interactions can further impose qualitative, concentration-dependent changes in non-Newtonian rheology. Theoretical models of suspension behavior have successfully predicted non-Newtonian flow behavior in suspensions undergoing shear, extensional flow, and falling-ball rheometry, *i.e.*, macroscale flows. Microrheology is an important complement to these macroscopic techniques, especially for interrogation of microscopically small systems, and has successfully recovered many rheological behaviors traditionally measured via macroscale techniques, including viscosity, diffusivity and normal stress differences. Detailed theoretical connec-

tions of microstructure to rheology are well-established in both macroscopic and microscopic approaches.

Non-Newtonian rheology in hard-sphere suspensions arises when microstructural symmetry is broken and this asymmetry is sustained over time or length scales long compared to the particle relaxation time scale. In a dilute dispersion, where only pair interactions matter, non-Newtonian rheology corresponds to a loss of Stokes-flow reversibility in relative pair trajectories, where Brownian motion or particle roughness, for example, drive particles off Stokes-flow trajectories. For instance, while a suspension of smooth spheres undergoing simple shear or polydisperse sedimentation in the absence of Brownian motion has spherically symmetric structure and Newtonian rheology, even very weak Brownian motion destroys this symmetry, leading to flow-dependent viscosity. In the same flows of non-colloids, particle roughness also destroys Stokes-flow reversibility. Indeed, surface asperities as small as one ten-thousandth of a particle size produce similar effects [40]. The excluded-annulus model [118], which served as a simplistic, yet useful, representation simulating various surface conditions, has been employed to incorporate the effect of particle roughness into the dilute theory and recover non-Newtonian behaviors. However, missing in all these dilute models is the detailed effect of three-body interactions.

Many-body interactions give rise to qualitative changes in suspension rheology that cannot be captured by the dilute theory where only pair-level particle interactions are considered. The leading-order effect is the loss of Stokes-flow fore-aft symmetry, time reversibility, and thus Newtonian rheology. The presence of three-body or higher-order interactions breaks fore-aft symmetry, but

in principle, particle trajectories are still time reversible. As a result, if the initial configuration is random, the structure of the suspension is still symmetric on average, even though for one realization a third particle breaks the fore-aft symmetry. To trigger non-Newtonian rheology, time reversibility must be destroyed, which is nearly unavoidable in experiments or simulations, owing to the chaotic sensitivity of three-body trajectories to infinitesimally small perturbations, such as residual Brownian motion or particle roughness. That is, in the presence of many-body hydrodynamic interactions, small perturbations quickly amplify and propagate to give time-irreversible suspension mechanics. This idea was first discussed by Leighton and Acrivos [90] in their seminal study of shear-induced migration of non-colloids, an effect the authors attributed to irreversible diffusion arising from a combination of many-body hydrodynamic interactions and particle roughness. More recent work has captured this behavior, beginning most notably with the study of Jnosi *et al.* [76], who numerically modeled the sedimentation of three particles in Stokes flow, showing that particle motions are extremely sensitive to their initial configurations. They found that the particle trajectories separate exponentially in time with a positive Lyapunov exponent, thus quantifying the chaotic nature of hydrodynamic interactions. Marchioro and Acrivos [99] and Drazer *et al.* [42] connected this phenomenon to many-body interactions between sheared non-colloids and resultant non-Brownian diffusion. They further showed that, in simple shear flow of non-colloids, even if all external and microscopic forces are deterministic, particle trajectories are stochastic and chaotic. When particle roughness is significant, pair encounters break fore-aft symmetry, and thus produce an $O(\phi)$ transverse diffusivity, where ϕ is the particle volume fraction of the suspension. For nearly smooth particles, three-body hydrodynamic interactions are responsible

for the loss of fore-aft symmetry, giving rise to irreversible diffusion that scales as $O(\phi^2)$. Pine *et al.* [115] found a threshold shear rate that separates reversible particle trajectories from chaotic behaviors, by measuring the diffusivity of non-colloidal particles in an oscillatory shear flow with both experiments and simulations. Overall, these studies show that small perturbations and three-body interactions are essential to introducing time irreversibility, but how three-body hydrodynamic interactions quantitatively give rise to non-Newtonian rheology is still not clear.

One way to view the shear-rate and concentration dependence of loss of Stokes-flow symmetry, and its connection to the influence of many-body hydrodynamic interactions on non-Newtonian rheology, is to recognize that from a trajectory perspective, the loss of memory occurs as a pair encounter progresses. In the present work, we utilize Accelerated Stokesian Dynamics (ASD) simulations to study the effect of many-body hydrodynamic interactions on particle trajectories, microstructure, and non-Newtonian rheology. To focus on the connection between particle trajectories and non-Newtonian rheology, we study flow-dependent rheology via active microrheology, in both dilute and concentrated suspensions with varying volume fraction and strength of probe forcing. The active microrheology framework has been described in a review article by Zia [152].

The ASD algorithm rigorously accounts for many-body far-field hydrodynamic interactions and near-field lubrication interactions, thus allowing the study of suspensions ranging from dilute to maximum packing. Here, we study the evolution of structure and rheology as it evolves with strength of probe forcing. The microviscosity, normal stresses, normal stress differences and osmotic

pressure are measured over a range of volume fractions, $0.05 \leq \phi \leq 0.4$. We find that, as concentration increases, the osmotic pressure and normal stresses increase, indicating greater storage of flow energy relative to that dissipated by viscous drag. Structural distortion is more pronounced as volume fraction increases, supporting this view. An increase of osmotic pressure with increasing volume fraction is unsurprising at equilibrium, given the connection of osmotic pressure to the chemical potential. The viscosity also increases as concentration grows. An increase in dissipation (viscosity) with increasing volume fraction also makes sense physically, if one draws on a similar dependence at equilibrium where no-slip surfaces increase stress and viscosity. However, under flow, at the pair level, hydrodynamic coupling lengthens the duration of pair encounters, suppressing the formation of structural asymmetry and thus non-Newtonian rheology. One might then expect an increase in concentration to exaggerate this response. While we do find that increasing volume fraction drives up the non-equilibrium viscosity, we find just the opposite for the normal stress difference and osmotic pressure: increasing volume fraction leads to increased structural asymmetry and enhanced energy storage. This behavior must owe its origins to three-body and higher-order hydrodynamic interactions. We hypothesize that the loss of time- and fore-aft symmetry of relative trajectories caused by three-body hydrodynamic interactions leads to this behavior. To interrogate this idea, we developed scaling theories to bridge the dilute theory for the rheological quantities in suspensions to arbitrary concentration, where the concentrated mobility functions derived recently by Zia *et al.* [157] are introduced to collapse the concentrated results onto dilute theory. Agreement between our scaling theory and simulation results in suspension stress suggests that three-body hydrodynamic interactions are most pronounced when probe forcing is

strong. Further study shows that the transverse mobility of the particle pair in the presence of the third particle is responsible for the non-Newtonian rheology, since physically it gives rise to loss of fore-aft symmetry. In weak probe forcing, the irreversibility from three-body encounters is not important because advection is weak.

The remainder of this paper is organized as follows: in Sec. 5.2, the microrheology model system is presented, where the excluded annulus model is utilized to tune the strength of hydrodynamic interactions. The method to evaluate microviscosity and suspension stress from the particle motion is addressed in Sec. 5.3, followed by presentation of the simulation techniques in Sec. 5.4 for the evolution of particle configurations from N-body Langevin equations. Results are presented in Sec. 5.5, beginning with the evolution of the non-equilibrium microstructure under weak to strong probe forcing and dilute to dense particle concentration. Focus is placed on the microviscosity, normal stresses parallel and perpendicular to the direction of the external force, the normal stress difference and the osmotic pressure. The quantities are measured for the full range of forcing, spanning five decades of probe forcing and for volume fraction $0.05 \leq \phi \leq 0.4$, revealing an important transition from the dilute, two-body interaction-dominated regimes to concentrated regimes, where three-body hydrodynamic interactions also matter. To gain insight into the role of many-body hydrodynamic interactions in Non-Newtonian behaviors, we developed a scaling theory to bridge the concentrated rheology to the dilute theory. The study is concluded in Sec. 5.6 with a summary.

5.2 Microrheology model system

We recapitulate the microrheology framework presented in Sec. 1.3.2. We consider a suspension of neutrally buoyant, colloidal hard spheres all of hydrodynamic radius a, immersed in an incompressible Newtonian fluid of density ρ and dynamic viscosity η. In active microrheology, a probe particle is dragged by an external force, $\boldsymbol{F}^{\text{ext}}$, through a bath of particles. The characteristic velocity $\boldsymbol{U}$ of probe motion sets the Reynolds number, $Re \equiv \rho U a/\eta$. Because the probe and bath particles are small, $Re \ll 1$, inertial forces can be neglected and thus the fluid mechanics are governed by the Stokes equations. The probe number density, n_a, relative to the number density of bath particles, n_b, is small. Probe motion distorts the equilibrium microstructure while the Brownian motion of the bath particles acts to recover their equilibrium configuration. This gives rise to an entropic restoring force, kT/a, where k is Boltzmann's constant and T is the absolute temperature. The degree of distortion of the microstructure, and hence its influence on probe motion, is set by the strength of probe forcing, F^{ext}, relative to the entropic restoring force, defining a Péclet number: $Pe = F^{ext}/(kT/a)$. The volume fraction of bath particles is defined as $\phi_b \equiv (4\pi a^3/3)N_b/V$, where N_b is the number of bath particles, and V is the system volume.

As discussed in Sec. 1.3.2, the strength of hydrodynamic interactions are determined by how close particles can approach each other, characterized by the dimensionless interparticle repulsion range, $\kappa \equiv (a_{th} - a)/a$. The (effective) thermodynamic size of particles a_{th} arises from various surface conditions such as surface roughness or grafted polymers, and may be larger than the hydrodynamic size a. In the Stokesian Dynamics simulation framework utilized in this work, we focus on examining the structure and rheological response in the limit

of strong hydrodynamics, where $\kappa = 0$.

5.3 Measurement of rheological quantities

Dynamic simulations provide the same particle displacements and interactions as would be measured in experiments. Here we relate probe behavior and bath particle configurations to the rheological quantities we seek. We begin with the microviscosity, which is related to average probe speed via Stokes' drag law. This is followed by the suspension stress, and its connection to particle configuration.

5.3.1 Microviscosity

In microrheology, since the probe is dragged through a suspension, the neighboring particles are entrained by the motion of the probe. The perturbed bath particles changes the equilibrium configuration, formed a microstructure. This microstructure in turn hinders the probe, slowing its motion. Squires and Brady [124] and Khair and Brady [78] interpreted the mean-speed reduction as a viscous drag of the bath and defined an effective viscosity η^{eff} via the application of Stokes' drag law:

$$\frac{\eta^{eff}}{\eta} \equiv \frac{F^{ext}}{6\pi\eta a\langle U\rangle}, \tag{5.1}$$

where $\langle U\rangle = -\langle \boldsymbol{U}\rangle \cdot \boldsymbol{F}^{\text{ext}}/F^{ext}$, and $\langle \boldsymbol{U}\rangle$ is the velocity of the probe, averaged over many encounters with background particles.

The effective viscosity can be written as that due to the solvent drag on the

probe, plus the drag due to microscopic forces between the probe and the bath particles:

$$\frac{\eta^{eff}}{\eta} = 1 + \frac{\eta^{micro}}{\eta}. \tag{5.2}$$

The microviscosity, η^{micro}, measures the viscosity arising from both the equilibrium hindrance due to the presence of the particles, and that due to the non-equilibrium distortion of the particle structure. Combing Eqs. (5.1) and (5.2) gives the expression of microviscosity,

$$\frac{\eta^{micro}}{\eta} = \frac{F^{ext}}{6\pi\eta a\langle U\rangle} - 1, \tag{5.3}$$

In experiments and simulation, the microviscosity is measured in a straightforward way as the mean probe velocity over a range of time, whereas in theory it is calculated as an integration over the whole space via probe-bath mobility couplings [124, 78].

5.3.2 Suspension stress

In rheology, the bulk stress $\langle\boldsymbol{\Sigma}\rangle$ can be divided into fluid-phase stress and particle-phase stress [11, 14]:

$$\langle\boldsymbol{\Sigma}\rangle = \langle p\rangle\boldsymbol{I} + 2\eta\langle\boldsymbol{E}\rangle + \langle\boldsymbol{\Sigma}^{p}\rangle, \tag{5.4}$$

where $\langle p\rangle$ is the pressure of the incompressible fluid, $\boldsymbol{I}$ is the identity tensor, $2\eta\langle\boldsymbol{E}\rangle$ is the deviatoric stress contribution from the fluid, and $\langle\boldsymbol{\Sigma}^{p}\rangle$ is the particle-phase stress. The stresses are ensemble averaged over the whole volume V containing N bath particles, denoted as $\langle\cdot\rangle$. In active microrheology, the particle-phase stress, $\langle\boldsymbol{\Sigma}^{p}\rangle$, is studied by Chu and Zia [34] for dilute suspensions, where

they divided the particle-phase stress into non-hydrodynamic and hydrodynamic contributions, respectively,

$$\langle \boldsymbol{\Sigma}^{p} \rangle = -n_a kT\boldsymbol{I} - n_a \langle \boldsymbol{r}\boldsymbol{F}^{P} \rangle + n_a \left(\langle \boldsymbol{S} \rangle^{H,ext} + \langle \boldsymbol{S} \rangle^{B} + \langle \boldsymbol{S} \rangle^{P,dis} \right). \tag{5.5}$$

The first term, $-n_a kT\boldsymbol{I}$, is the equilibrium particle stress from thermal fluctuations of Brownian particles. The second term, $-n_a \langle \boldsymbol{r}\boldsymbol{F}^{P} \rangle$, is the non-hydrodynamic interparticle stress and originates from interparticle elastic collisions. The remaining term represents the particle-phase stress arising from hydrodynamic interactions. The stresslets, $\boldsymbol{S}$, correspond to the symmetric part of the first moment of the stress tensor. Physically, microscopic forces induce relative motion between particles. The relative motion further gives rise to stresslet on the particle surfaces since particles are hydrodynamically coupled. Specifically, the stresslets induced by external probe forcing, Brownian motion, and interparticle forces are represented by stresslets $\boldsymbol{S}^{H,ext}$, $\boldsymbol{S}^{B}$, and $\boldsymbol{S}^{P,dis}$, as shown in Equation 5.5. These stresslets are formulated as:

$$\langle \boldsymbol{S}^{H,ext} \rangle = -\langle \boldsymbol{R}_{SU} \cdot (\boldsymbol{R}_{FU}^{-1} \cdot \boldsymbol{F}^{\text{ext}}) \rangle, \tag{5.6}$$

$$\langle \boldsymbol{S}^{B} \rangle = -kT \langle \nabla \cdot \left(\boldsymbol{R}_{SU} \cdot \boldsymbol{R}_{FU}^{-1} \right) \rangle, \tag{5.7}$$

$$\langle \boldsymbol{S}^{P,dis} \rangle = -\langle \boldsymbol{R}_{SU} \cdot (\boldsymbol{R}_{FU}^{-1} \cdot \boldsymbol{F}^{P}) \rangle. \tag{5.8}$$

In these equations, $\boldsymbol{F}^{P}$ denotes the interparticle force, $\boldsymbol{R}$ represents the hydrodynamic resistance tensors which couple surface traction of particles to their motion. Specifically, $\boldsymbol{R}_{FU}$ denotes the resistance tensors coupling force and torque to translation and rotation; $\boldsymbol{R}_{SU}$ denotes the coupling between stresslet on the surface of particles and particle translation or rotation. Physically, the advective flow arising from the externally applied force gives rise to an external-force induced stresslet $\boldsymbol{S}^{H,ext}$ on a particle surface because it cannot deform. The Brownian stresslet $\boldsymbol{S}^{B}$ on particle surfaces arises due to disturbance flows driven by

the Brownian motion of bath particles as it acts to smooth microstructural gradients [13]. Finally, relative motion produced by interparticle forces gives rise to disturbance flows that in turn create a stresslet $\boldsymbol{S}^{P,dis}$ on particle surfaces.

The stress tenor, $\boldsymbol{\Sigma}^{p}$, has six independent elements in general. In microrheology, however, only the normal stresses are non-zero, owing to the axisymmetric geometry of the structure around the probe. We denote the three normal stresses as Σ_{xx}, Σ_{yy} and Σ_{zz}, where x is the direction parallel to the external force. The axisymmetric structure also implies that the stresses perpendicular to the direction of the external force are equal, *i.e.*, $\Sigma_{yy} = \Sigma_{zz}$. Thus in active microrheology, the suspension stresses are expressed by only two components: the parallel normal stress, $\Sigma_{\parallel}$, and the perpendicular normal stress, $\Sigma_{\perp}$, where $\Sigma_{\parallel} \equiv \Sigma_{xx}$, $\Sigma_{\perp} \equiv \Sigma_{yy}$.

The normal stress differences characterize the anisotropic deformation of a suspension arising from the distortion of the microstructure, and are formulated as:

$$\begin{aligned} N_1 &= \Sigma_{xx} - \Sigma_{yy}, \\ N_2 &= \Sigma_{yy} - \Sigma_{zz}, \end{aligned} \tag{5.9}$$

where N_1 represents the first normal stress difference, N_2 represents the second normal stress difference. Because the two perpendicular components are identical due to the axisymmetric microstructure, N_2 is always zero. Thus only the first normal stress difference is measured.

The tendency for isotropic expansion or contraction of the particle phase is described by the osmotic pressure, which is defined as negative one third of the trace of the stress tensor,

$$\langle \Pi \rangle = -\frac{1}{3}\boldsymbol{I} : \langle \boldsymbol{\Sigma}^{p} \rangle. \tag{5.10}$$

To evaluate the microviscosity, and suspension stress in simulations via Eqs. (5.3), (5.6), (5.7), (5.8), (5.10), hydrodynamic couplings and forces must be provided. The external force is prescribed. The interparticle force $\boldsymbol{F}^P$ is evaluated as the gradient of the interparticle potential between particles, $\boldsymbol{F}^P = -\nabla\mathcal{V}$, given an arbitrary particle potential, $\mathcal{V}$. The resistance tensors, $\boldsymbol{R}$, are functions of only particle configurations and can be evaluated given the positions of all the particles in the suspension. Thus in simulations, to measure the microviscosity and suspension stress, we must solve for the particle motion and evolve the suspension configurations in each time step. The method of our approach is given next.

5.4 Simulation method

The basis of Stokesian Dynamics simulations is to obtain the evolution of particle positions in a suspension [22, 121, 8]. For a system of N hard-sphere colloidal particles of hydrodynamic radius a dispersed homogeneously in an incompressible, Newtonian solvent of dynamic viscosity η and density ρ, the particle motion is described by the coupled N-body Langevin equation

$$\boldsymbol{m} \cdot \frac{d\boldsymbol{U}}{dt} = \boldsymbol{F}^{ext} + \boldsymbol{F}^H + \boldsymbol{F}^B + \boldsymbol{F}^P, \tag{5.11}$$

where $\boldsymbol{m}$ is a generalized mass/moment of inertia tensor of dimension $6N \times 6N$ and $\boldsymbol{U}$ is a vector of dimension $6N$ for the translational/rotational particle velocities relative to the solvent. The force/torque vectors $\boldsymbol{F}$ on the right-hand side are of dimension $6N$, comprising contributions from external, hydrodynamic, Brownian and interparticle forces. In colloidal suspensions, particle size is small, and fluid and particle inertia are negligible.

In the present fixed-force active microrheology model, there is no externally applied forces or torques on all particles, $\boldsymbol{F}^{ext} = \boldsymbol{0}$, except on the probe. As a particle moves relative to the solvent, the solvent exerts hydrodynamic forces and torques on the particle. In Stokes flow, moments of the hydrodynamic surface traction acted on the particles are linearly coupled to the particle motion,

$$\boldsymbol{F}^H = -\boldsymbol{R}_{FU} \cdot \boldsymbol{U}, \tag{5.12}$$

where the configuration-dependent hydrodynamic resistance tensor $\boldsymbol{R}_{FU}$ is the kernal for the coupling.

The random Brownian force and torque $\boldsymbol{F}^B$ arise due to the collisions between the particle and solvent molecules during time intervals much longer than the inertial relaxation time scale of the particle $\tau_I = m/6\pi\eta a$. The Brownian force and torque satisfy Gaussian statistics: they are zero on average, but has a nonzero temporal correlations on τ_I,

$$\overline{\boldsymbol{F}^B} = 0, \qquad \overline{\boldsymbol{F}^B(0)\boldsymbol{F}^B(t)} = 2kT\boldsymbol{R}_{FU}\delta(t), \tag{5.13}$$

where the overbar denotes a noise averaging over times much longer than individual solvent collisions and long compared to τ_I, and $\delta(t)$ is the Dirac delta function.

The interparticle force, $\boldsymbol{F}^P$, is general to represent any non-hydrodynamic, deterministic force, *e.g.* electrostatic forces or frictional force as arises in the presence of particle roughness. In the present simulation framework, we employ a hard-sphere force, $\boldsymbol{F}^P = kT\hat{\boldsymbol{r}}\delta(r - 2a)$ (r is the separation distance between particle pairs and $\hat{\boldsymbol{r}}$ is the unit vector connecting centers of two particles) such that particle overlaps are prevented by an infinite potential at contact, and the particles exert no direct force on each other otherwise. However, since particles

interact with full hydrodynamic interactions in our model, $\kappa = 0$, where lubrication forces prohibit particles from touching, the hard-sphere interparticle force has no effect on the evolution of particle evolution and rheology.

Evolution equations of particle position can be obtained by integrating Eq. (5.11) over a time step Δt which is large compared to the inertial relaxation time of the particle, τ_I, but small compared to the diffusive time of the particle $\tau_D = a^2/D$ over which the configuration changes. We nondimensionalize the length scale by the particle hydrodynamic radius a; and to accurately capture the particle dynamics in different flow regimes, the diffusive time a^2/D and advective time scales a/U are used when flow is weak and strong, respectively. The evolution equation of particle position in the weak flow regime reads

$$\Delta x = Pe\left(\boldsymbol{R}_{FU}^{-1} \cdot \hat{\boldsymbol{F}}^{\text{ext}}\right)\Delta t + \Delta \boldsymbol{x}^P + \nabla \cdot \boldsymbol{R}_{FU}^{-1}\Delta t + \boldsymbol{X}(\Delta t) + O(\Delta t), \tag{5.14a}$$

$$\overline{\boldsymbol{X}} = 0, \qquad \overline{\boldsymbol{X}(\Delta t)\boldsymbol{X}(\Delta t)} = 2\boldsymbol{R}_{FU}^{-1}\Delta t; \tag{5.14b}$$

whereas in the strong forcing regime it is given by

$$\Delta x = \left(\boldsymbol{R}_{FU}^{-1} \cdot \hat{\boldsymbol{F}}^{\text{ext}}\right)\Delta t + \Delta \boldsymbol{x}^P + \frac{1}{Pe}\nabla \cdot \boldsymbol{R}_{FU}^{-1}\Delta t + \frac{1}{Pe^{1/2}}\boldsymbol{X}(\Delta t) + O(\Delta t), \tag{5.15}$$

where $Pe = F_0/(kT/a)$, and $\hat{\boldsymbol{F}}^{\text{ext}} = \boldsymbol{F}^{\text{ext}}/F_0$ is the unit vector pointing in the direction of the external probe force. In Eqs. (5.14a) and (5.15), the first term is the particle displacement induced by the external force; the second term by the interparticle force; the third term by the mean drift of Brownian motion due to particle concentration gradients; and the fourth term is a random Brownian displacement which has a zero mean and covariance given by the inverse of the resistance tensor [cf. Eq. (5.14b)].

While the evolution of particle position is obtainable with the resistance tensor $\boldsymbol{R}_{FU}$, computing the suspension stress requires couplings between stresslet

and particle motion. To this end, we invoke the grand resistance matrix,

$$\boldsymbol{\mathcal{R}} = \begin{pmatrix} \boldsymbol{R}_{FU} & \boldsymbol{R}_{FE} \\ \boldsymbol{R}_{SU} & \boldsymbol{R}_{SE} \end{pmatrix}, \tag{5.16}$$

where $\boldsymbol{R}_{SU}$ governs the coupling between stresslet and particle motion, and $\boldsymbol{R}_{FE}$ and $\boldsymbol{R}_{SE}$ describe the coupling between force/torque and flow rate of strain, and the coupling between stresslet and flow rate of strain, respectively. As an improvement to the original Stokesian Dynamics framework [22, 121], the resistance tensors $\boldsymbol{R}_{SU}$ and $\boldsymbol{R}_{SE}$ in our model are not traceless such that their trace couple particle motion to the pressure moment on the surface of particles, giving rise to an induced particle osmotic pressure [74, 128].

An extension of Eq. (5.11) is obtained according to the grand resistance tensor, $\boldsymbol{\mathcal{R}}$, viz.,

$$\begin{pmatrix} \boldsymbol{0} \\ \boldsymbol{S} \end{pmatrix} = -\boldsymbol{\mathcal{R}} \cdot \begin{pmatrix} \boldsymbol{U} \\ \boldsymbol{0} \end{pmatrix} + \begin{pmatrix} \boldsymbol{F}^B + \boldsymbol{F}^P + \boldsymbol{F} \quad ext \\ -\boldsymbol{r}\boldsymbol{F}^P \end{pmatrix}. \tag{5.17}$$

The resistance tensor, $\boldsymbol{\mathcal{R}}$, captures the many-body hydrodynamic interactions between all the particles in a suspension. For a pair of particles closely spaced, two-body interactions are pronounced and are well-established analytically in the literature [75, 73]. For particles far from each other, many-body interactions must be considered because the effect of intervening particles between the pair is significant. Thus $\boldsymbol{\mathcal{R}}$ is evaluated as a sum of the near-field two-body hydrodynamic interactions, and the far-field many-body hydrodynamic interactions,

$$\boldsymbol{\mathcal{R}} = \boldsymbol{\mathcal{R}}_{nf} + (\boldsymbol{\mathcal{M}}^{\infty})^{-1}. \tag{5.18}$$

The two-body near-field resistance matrix, $\boldsymbol{\mathcal{R}}_{nf}$, is directly computed by linear superposition of the analytical, pairwise resistance functions from [75, 73, 74].

The far-field grand mobility matrix, $\mathcal{M}^{\infty}$, is constructed from a Taylor expansion of the Green's function of Stokes equation, and truncating the expansion to the first traction moment [25], which estimates the first reflection of long-range hydrodynamic interactions. Furthermore, the inverse of the far-field mobility, $(\mathcal{M}^{\infty})^{-1}$, captures the many-body interactions [43]. To accelerate the computation, Particle-Mesh-Ewald (PME) method is utilized to avoid constructing $\mathcal{M}^{\infty}$ explicitly and an iterative method is utilized to evaluate matrix inverse [121].

To compute the osmotic pressure in simulations, the trace of the resistance $\boldsymbol{R}_{SU}$, defined as $\boldsymbol{P} = \boldsymbol{I} : \boldsymbol{R}_{SU}$, must be evaluated, where $\boldsymbol{P}$ represents the coupling between the pressure moment on the surface of particles and particle motion. Similarly like the construction of resistance matrix $\mathcal{R}$, $\boldsymbol{P}$ is computed from the analytical expression of two-body hydrodynamic interactions [74], and the far-field many-body estimation [63].

In our study, each simulation has 25 advective time with time step 0.001 advective time unit. The number of particles is ranging from 187 to 382. We implemented simulations for volume fraction ϕ_b ranging from 0.05 to 0.4, with flow strength ranging from 0.1 to 30000, each case with $100 - 200$ simulations. The measured quantities in the simulations are averaged over all the time steps and all simulations.

5.5 Results

Here we examine the influence of volume fraction on the evolution of microstructure with flow strength and on the non-Newtonian rheology of the suspension.

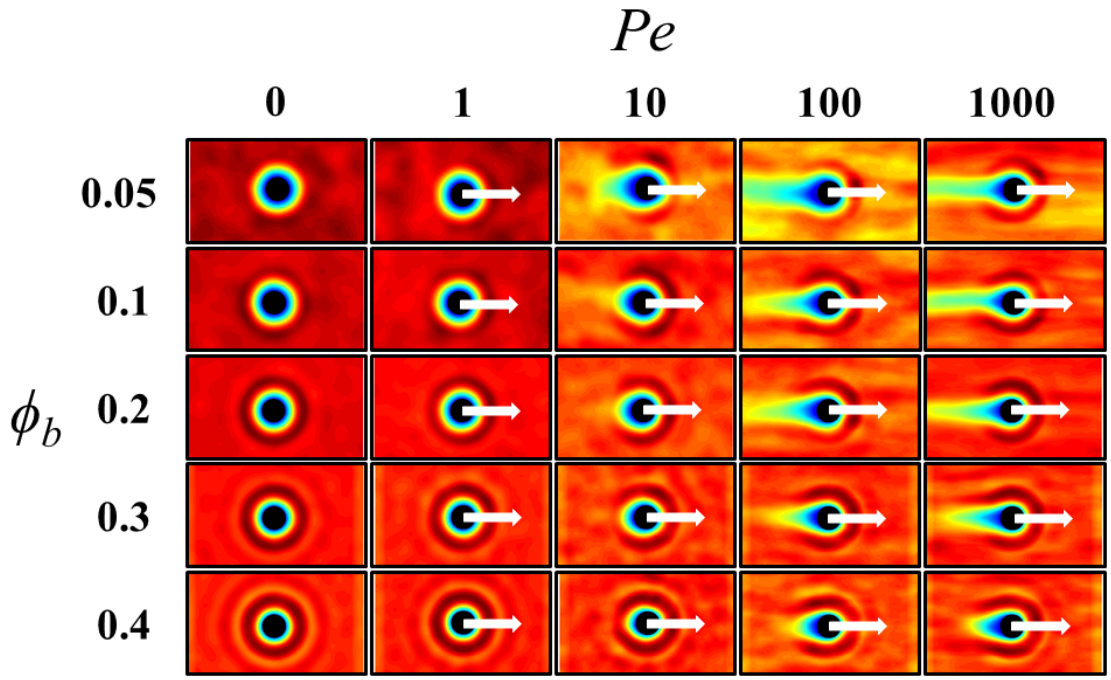

Figure 5.1: Evolution of the microstructure from a side-view of the simulation cell transverse to probe forcing. The black region represents the probe and it is surrounded by a region excluded to particle centers. Probe forcing *Pe* increases from left to right, and volume fraction ϕ increases from top to bottom, as labeled. Regions in dark red indicate particle-center accumulation; blue regions indicate particle-center depletion.

5.5.1 Microstructure

As the probe moves through the bath, its interaction with the bath particles distorts their arrangement. Over long times, the probe encounters many different particle configurations. At steady state, an average of these structures over time approaches an ensemble average over all permissible arrangements, giving the average steady-state microstructure. The positions of all particles were monitored throughout simulation, giving the distribution of bath particles relative to the probe in a frame of reference moving with the probe. The steady-state

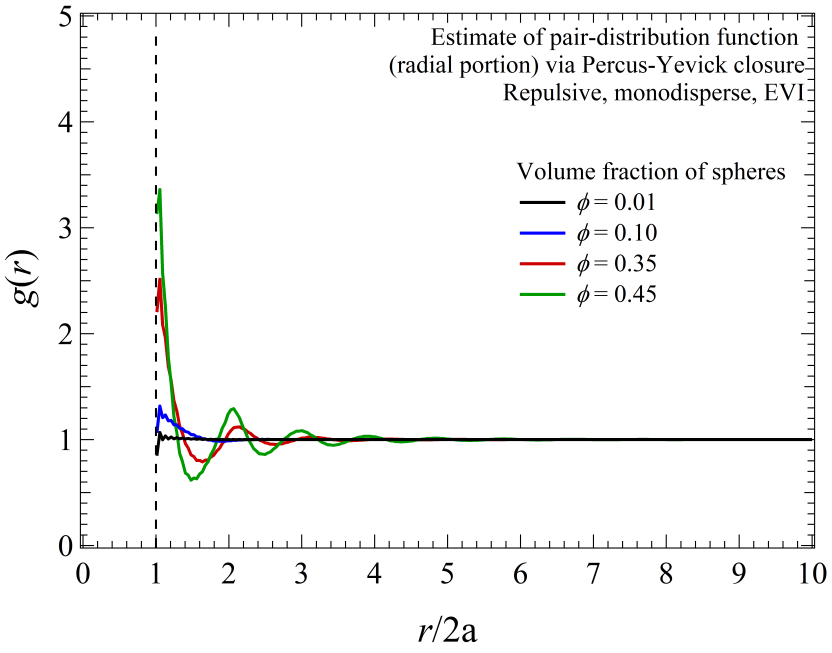

Figure 5.2: Equilibrium pair distribution function $g(r)$ computed from Percus-Yevick equation [112] for different volume fractions.

temporal average was computed and is plotted in Fig. 5.1 for several values of forcing strength, Pe, and volume fraction, ϕ. Each column in the figure corresponds to one value of Pe, increasing from left to right. Across each row, volume fraction is held fixed, increasing from top to bottom. The black circle at the center represents the probe and, at equilibrium (far left column) it is surrounded by a blue ring showing the exclusion of bath-particle centers closer than $r = 2a$. A bath-particle accumulation ring (dark red) shows the nearest-neighbor ring that emerges distinctly as volume fraction becomes high enough to produce liquid-like structure.

In the second column, $Pe = 1$ and, in this regime, advection is as important as Brownian motion. Thus, probe motion is able to distort the structure, and Brownian motion cannot fully erase the disturbance, at least for $\phi_b \leq 0.3$. However, at $\phi_b = 0.4$ the isotropic structure is still intact. This persistence of

structural distortion arises from the volume-fraction dependence of the gradient of particle density that in turn produces local Brownian drift, a deterministic force driving the probe toward more mobile regions, $\langle \nabla \cdot \boldsymbol{M} \rangle_{nn}$, where $\boldsymbol{M} = \boldsymbol{R}^{-1}$ is the configuration-dependent hydrodynamic mobility and $\langle \cdot \rangle_{nn}$ indicates an average over many probe-bath particle relative configurations around the nearest-neighbor ring of particles surrounding the probe. In the concentrated regime, a liquid-like structure forms and produces fluctuations in particle density that become more pronounced as volume fraction grows. This is illustrated in Fig. 5.2, which is a plot of the pair distribution function $g(r)$ for several volume fractions estimated by the Percus-Yevick equation [112]. These density peaks and troughs produce corresponding mobility troughs and peaks, respectively, and influence relative particle motion. As volume fraction grows, the particle density in the nearest-neighbor region increases as free volume decreases. Consequently, at high concentration, the relative motion between the probe and bath particles at the nearest-neighbor ring is slowed by the increase in nearby no-slip surfaces (lower relative mobility). Since relative particle velocity decreases but more bath particles flow into the nearest-neighbor region as volume fraction grows, the relative advective flux is relatively unchanged as volume fraction grows at $Pe = 1$. At $Pe = 1$, the advective flux is balanced by the relative diffusive flux, which is driven by radial gradients in the structure, $\partial g/\partial r$, projected through the suspension at a strength given by the radial relative mobility [78, 68]. Close to the probe the relative mobility decreases as volume fraction grows and the nearest neighbor region becomes crowded; the density gradient must thence increase to enforce no relative flux at contact. Consequently, in the $Pe \sim 1$ regime, where Brownian drift is as strong as advection, increases in concentration effectively reduce the Peclet number: concentration-gradient dependent Brownian

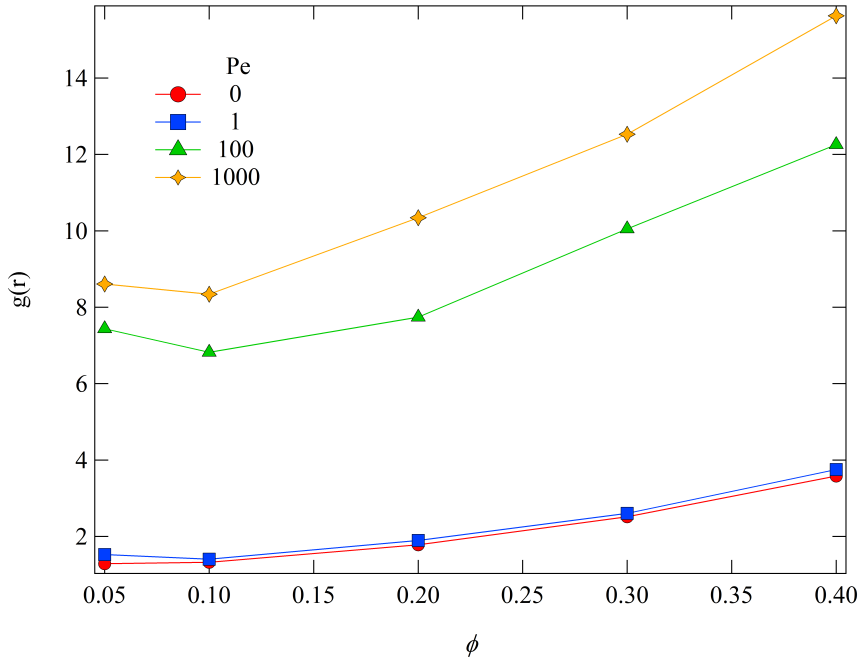

Figure 5.3: Estimated upstream pair distribution function $g(r)$ as a function of volume fraction and Pe.

drift outpaces advection and restores structural isotropy. Overall, when advection is not strong, increased particle concentration preserves the symmetry of microstructure.

As probe forcing grows, however, hindrance from Brownian motion is overcome by advection and the nearest-neighbor ring is broken open in the downstream region, as seen in the columns for $Pe \geq 10$, all ϕ_b rows. Here, the familiar boundary-layer and trailing wake structure emerge - and the qualitative effect exerted by particle concentration becomes more pronounced. At a fixed value of $Pe \geq 10$, particle density in the upstream boundary layer increases as volume fraction increases. However, the non-equilibrium particle density varies nonlinearly with volume fraction. To exhibit this behavior, we estimate the boundary layer particle density by calculating the pair distribution function at the upstream of probe. We ensemble average all bath particles upstream and ignore

the angular deviation to get a radial dependent pair distribution, which gives qualitative behavior of bath particle density variation as volume fraction increases. The result is shown in Fig. 5.3. For all Pe, increasing volume fraction gives rise to a growth of particle density at the first peak. However, for $Pe \sim 1$, the trend is almost small as equilibrium suspension. As Pe increases, the slope of the curves increases as volume fraction increases. There are more bath particles accumulated upstream of the probe, comparing with $Pe \sim 1$ regime. Since we consider fully hydrodynamically interacting suspension, this change of particle density must arise from three-body interactions. A detailed discussion of the density variation owning to the three-body interactions will be given in the next section. Furthermore, as volume fraction increases, the boundary layer remains attached to the probe farther downstream, wrapping more closely around the trailing side of the probe. Meanwhile, the trailing wake shortens at fixed Pe as volume fraction increases. Since higher concentration also gives rise to higher particle density outside the boundary layer, and the particle density inside the trailing wake is very low for all volume fractions, a sharper density gradient across the wake is produced for higher volume fraction. This leads to a more pronounced Brownian drift force that closes the wake more rapidly. One can anticipate rheological consequences of the thicker boundary layer and shorter trailing wake arising from the high volume fraction. In the next section it will be shown that non-Newtonian rheological behaviors arise from three-body interactions that emerge at higher concentrations.

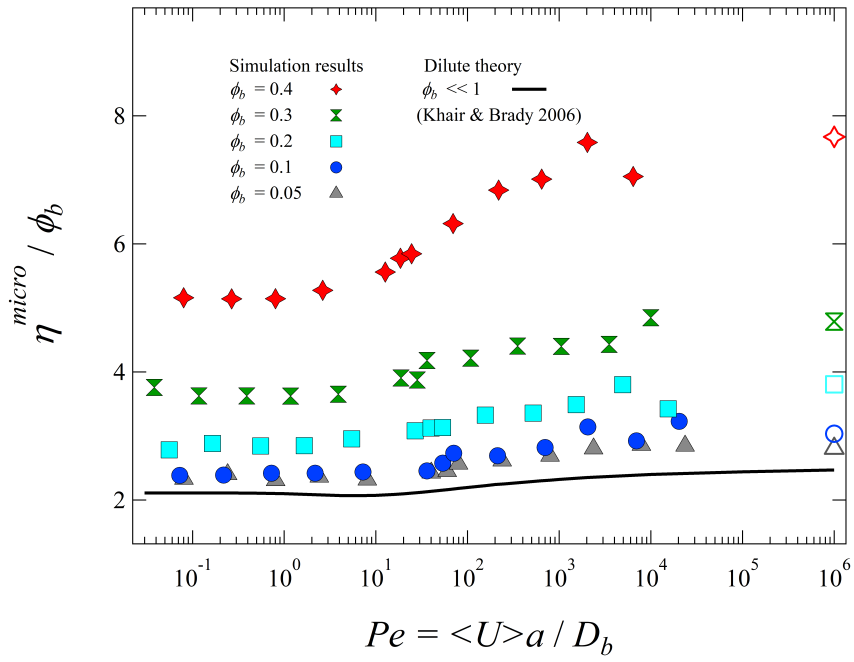

Figure 5.4: Microviscosity as a function of Pe and ϕ_b. Symbols are simulation results from present study; open symbols at far right correspond to $Pe^{-1} = 0$.

5.5.2 Rheology

In the previous section, contour plots of the deformed microstructure around the forced probe showed that increasing particle concentration exerts a qualitative effect on the evolving structure that is expected to alter probe motion and hence the rheology inferred by tracking its motion. In the present section, we examine how microviscosity and stress mirror these structural effects with concentration-dependent non-Newtonian rheology.

Microviscosity

The intrinsic ($Pe \to 0$) viscosity of colloidal suspensions increases as $O(\phi_b^2)$ when concentration is low, but at $\phi_b \geq 0.35$, many-body hydrodynamic interactions produce $O(\phi_b^3)$ contributions that set the speed of divergence as ϕ_b approaches maximum packing. Here we investigate how concentration affects non-Newtonian rheology of a flowing suspension. In microrheology, the microviscosity is inferred from reductions in average probe speed through the suspension, via application of Stokes' drag law [124, 78]. Fig. 5.4 shows the microviscosity η^{micro} as a function of forcing strength Pe, for several volume fractions, ϕ_b. The solid line represents the theoretical results in dilute suspensions [78] for very strong hydrodynamic interactions and the symbols are our simulation results for arbitrary concentration. The microviscosity is scaled by the volume fraction, ϕ_b. When forcing is weak, observable flow thinning occurs in dilute suspensions [78] as advection grows in strength and Brownian motion is too slow to restore structural equilibrium. As flow strength increases, the viscosity force-thickens at $Pe \sim O(10)$ since particles get closer to experience strong lubrication, and thus longer-duration coupling between particle pairs. As Pe tends to infinity, the viscosity asymptotes to the limiting value, 2.51, which corresponds to the falling-ball limit [18, 3]. In this limit, the boundary layer is vanishingly thin. There is negligible contributions from Brownian and interparticle forces, and thus only hydrodynamic viscosity matters.

Filled symbols in Fig. 5.4 show the simulation results from weak to strong forcing with volume fraction ranging from 0.05 to 0.4. When $Pe^{-1} = 0$, there is no Brownian motion. The empty symbols represent the microviscosity at infinite Pe, measured by turning off the Brownian motion in simulations. Pair

encounter contributes $O(\phi_b)$ energy dissipation and it is evaluated by the $O(\phi_b)$ scaling in Fig. 5.4, for both dilute theory and simulation results. The difference between the simulation results and dilute theory represents the effect of many-body interactions. The increased difference with the growth of concentration shows that higher concentration leads to more significant many-body interactions. A higher concentration signifies a more closely-spaced structure. As shown in the microstructure (Fig. 5.1), for all Pe, higher concentration gives rise to higher particle density around the probe. Since the strength of hydrodynamic interactions is inversely proportional to the separation between particles, interactions in concentrated suspensions are stronger, leading to stronger dissipation and thus a higher viscosity. Though concentration varies, the viscosity still shows two plateaus in weak and strong probe forcing. However, the slope of force thickening region grows as volume fraction increases, indicating a qualitative change of microviscosity in the presence of three-body interactions. From the microstructure (Fig. 5.1), one can observe the change of microviscosity from the nonlinear evolution of structure in high Pe as volume fraction increases. First, bath particles in front of the probe (inside the boundary layer) hinders probe motion via lubrication interactions, and the particle density increases as the volume fraction increases. Second, the lubrication interactions between probe and bath particles downstream also hinder probe motion and increase viscosity. The shorter trailing wake indicates larger hindrance downstream as volume fraction increases. In Sec. 5.5.3, we will show that three-body interactions enhance the particle density nonlinearly inside the boundary layer and thus give rise to stronger hindrance. As a result, the high-Pe plateau increases faster as volume fraction increases due to the stronger three-body interactions in high concentration. The enhancement of low-Pe plateau is relatively

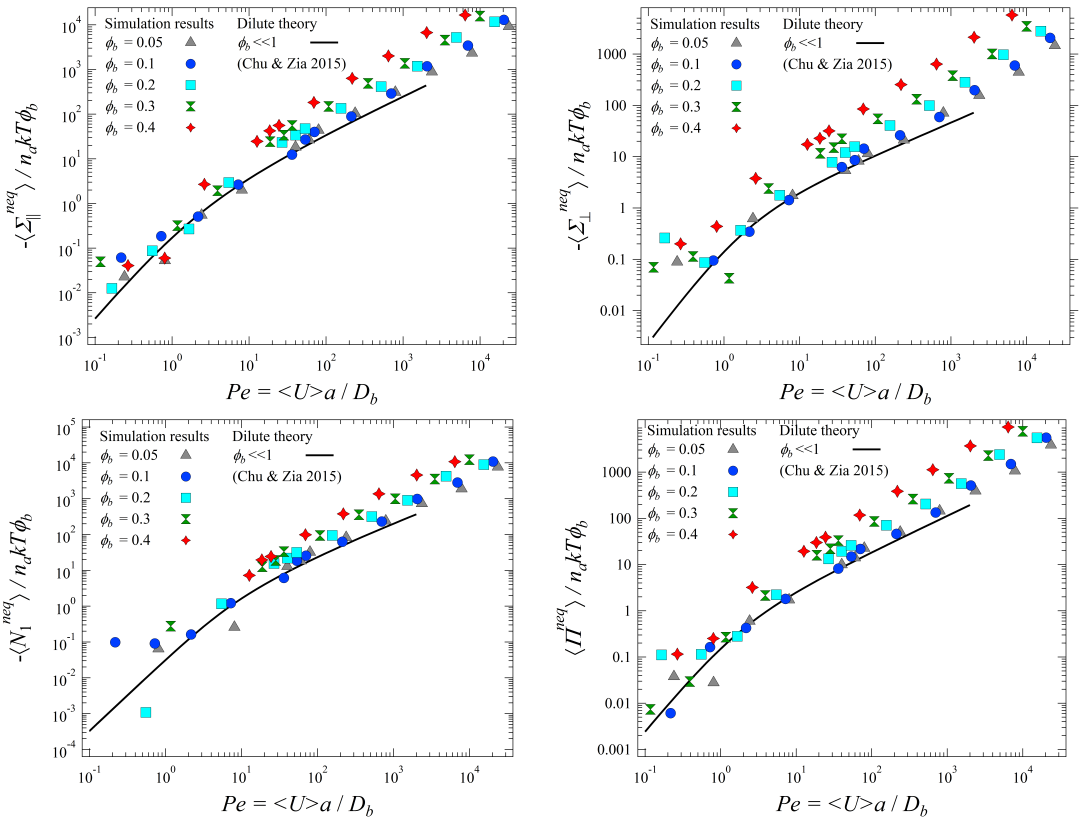

Figure 5.5: Suspension stress as functions of ϕ_b and Pe: (a) parallel normal stress; (b) perpendicular normal stress; (c) first normal stress difference; (d) osmotic pressure. Filled symbols are simulation results, solid lines are dilute theory from [34, 35].

small since three-body interactions are negligible and Brownian motion dominates the rheology. This difference in growth of viscosity in low- and high- Pe regime for different volume fractions determines the qualitative change of the slopes in the forcing thickening region.

Suspension stress

In dilute suspensions, Chu and Zia [34, 35] analytically derived the parallel normal stress, $\Sigma_{\parallel}$, perpendicular normal stress, $\Sigma_{\perp}$, first normal stress difference,

N_1, and osmotic pressure, Π. Their results for strong hydrodynamics limit are shown by the solid lines in Fig. 5.5. The stresses are made dimensionless by $n_a kT\phi_b$, where $n_a kT$ is the ideal osmotic pressure associated with the equilibrium thermal energy of the Brownian particles. Pair-level hydrodynamic interactions are assumed to dominate the higher-order interactions, thus the stresses are scaled by volume fraction, ϕ_b. In low-Pe, Brownian motion dominates advection. Consequently the disturbance flows that give rise to the Brownian stress are stronger than the weak advective flow due to probe motion. The stresses in this linear-response regime all scales as Pe^2, which represents a dipolar microstructure disturbance [34]. As Pe grows, the distance that a probe can move in one Brownian time scale grows, and thus give rise to more pair encounters with bath particles and lead to the increase of the suspension stress. For strong probe forcing, Chu and Zia [34] shows that hydrodynamic encounters of probe and bath particles along the line of centers are most pronounced. The scaling is set by their lubrication interactions inside the boundary layer, as $Pe^{0.799}$. These non-Newtonian rheology behaviors (non-zero suspensions stress) arise from the asymmetry of the microstructure. In high-Pe regime for dilute suspensions, this asymmetry arises from small particle roughness and residual Brownian motion.

The filled symbols in Fig. 5.5 denotes our simulation results for dilute and concentrated suspensions with volume fraction $0.05 \leq \phi_b \leq 0.4$. In the most dilute suspension, ϕ_b=0.05, the simulation data and dilute theory of all four stress quantities agree well. However, as concentration increases, the stresses at a given Pe deviate from the dilute theory, and increase monotonically. The suspension stress can be viewed as the energy density of a suspension [154]. This distortion of the microstructure gives rise to entropic energy storage. In dilute theory when only pair interactions matter, two-body hydrodynamic inter-

actions preserve fore-aft symmetry and thus suppress structure distortion and give rise to less energy storage and thus a decrease of suspension stress. However, as concentration increases, three-body interactions become important. In the presence of a third particle, the pair trajectory loses fore-aft symmetry and thus the microstructure is more distorted. As concentration increases where stronger three-body interactions are involved, the probe motion causes more configuration distortion, *i.e.*, more entropic energy storage on the probe, leading to the enhancement of the suspension stress. This is totally opposite to the effect of pair hydrodynamic interactions in dilute theory, where in dilute limit hydrodynamic interactions are considered to give rise to a decrease of suspension stress and preserve Newtonian rheology. The scaling of stress in high-Pe regime shows a nonlinear evolution, which again corresponds to the nonlinear distortion of the microstructure. A detailed discussion of this nonlinear behavior will be given in Sec. 5.5.3.

5.5.3 Scaling theory

In dilute theory, only pair interactions are considered. However, higher concentration leads to non-negligible many-body hydrodynamic interactions. As shown by the microviscosity and suspension stress in both dilute and concentrated suspensions, even scaled out the pair level effect ϕ_b, difference between dilute theory and simulations is significant, which tells that three-body factor ϕ_b^2 and even higher order factors matter when concentration increases. Thus, a new predictive theory is necessary to describe concentrated suspensions with the consideration of the many-body hydrodynamic interactions. We obtain this by bridging the pair-level dilute theory to our concentrated simulation results

utilizing our new simple scaling theory. Different scaling regimes are applied for microviscosity and suspension stress respectively. For the suspension stress, we implement different scalings for low and high Pe regime. To facilitate introducing the idea, we start with the scalings of the suspension stress.

Scaling for suspension stress

Chu and Zia [34, 35] derived the high-Pe asymptote of the suspension stress for a dilute suspension,

$$\frac{\langle \Sigma^{neq} \rangle}{n_a kT \phi_b} \sim Pe^{\delta} g^{eq}(2) \int_0^{\pi} A(\theta) f(2;\theta) d\theta. \tag{5.19}$$

Here Σ^{neq} denotes the parallel and perpendicular normal stress, the first normal stress difference and the osmotic pressure because the four quantities have the same high-Pe asymptote formulation. The asymptote comprises a Pe scaling, Pe^{δ}, the equilibrium microstructure $g^{eq}(2)$, and an integral involving the non-equilibrium microstructure f. The strength of the hydrodynamic interactions inside the boundary layer is evaluated by $A(\theta)$, a function of probe surface angle, θ. Physically, Pe^{δ} represents the scaling of particle density inside boundary layer. In dilute theory, it is derived by Batchelor [13] as:

$$\delta = \frac{W_0}{G_1} = 0.799, \tag{5.20}$$

where W_0 and G_1 are the leading orders of hydrodynamic mobility functions transverse to and along the line of centers, respectively [75]. The pair-distribution function outside the boundary layer, g, is estimated as

$$g(2;\theta) = g^{eq}(2)[1 + f(2;\theta)], \tag{5.21}$$

where $g^{eq}(2)$ represents the equilibrium contribution of the pair-distribution function outside the boundary layer, and is identically equal to 1 for dilute

suspensions. Inside the bracket, $f(2;\theta)$ represents the non-equilibrium distortion of the microstructure normalized by the equilibrium microstructure, and is only angular dependent. As particle approach each other, the boundary layer thickness is $O(Pe^{-1})$ and the strength of the stress for an individual probe-bath encounter is proportional to the probe forcing, $O(Pe)$. Thus, the average stress on the surface of the probe is proportional to the thickness of the boundary layer $[O(Pe^{-1})]$, the number density of bath particles inside the boundary layer $[O(Pe^{\delta})]$, the pair-distribution function around the surface $[g(2;\theta)]$, and the strength per probe-bath hydrodynamic encounter $[O(Pe)]$. The combination of all these factors sets the high-Pe asymptote in Eq. (5.19), and gives rise to the high-Pe scaling $Pe^{0.799}$ in dilute suspension.

In concentrated suspensions, many-body interactions become significant. To bridge the dilute theory with the concentrated suspensions, we consider the hydrodynamic interactions in dense suspensions still in the pair level. In dilute suspensions, one particle can only "see" another and they interact hydrodynamically through the solvent. Thus theoretical solutions of two-body hydrodynamic functions derived by Jeffrey and Onishi [75] are utilized to model particle interactions. In contrast, a pair of particles in concentrated suspensions do not only interact through the solvent, but also are influenced by the intervening particles between them. Here we consider the effect of both intervening particles and solvent together, *i.e.*, we view them as an intermediate medium. Thus the particle pairs directly interact through this effective "solvent". From this perspective, all the formulations in dilute theory still hold. The only difference which characterizes the medium properties are the hydrodynamic mobility functions. In dilute theory, the hydrodynamic couplings only depend on the separation distance between the pair. However, when intervening particles

matter, if considering particle pairs in a mean-field, the couplings also depend on the volume fraction ϕ_b of the intervening particles. Thus, in concentrated suspensions, new hydrodynamic mobility tensors, which are functions of both volume fraction of the suspension and separation distance between the pair, must substitute the two-body hydrodynamic functions from previous analytical study [75]. Zia *et al.* [157] derived these concentrated mobility functions for a range of volume fractions by stochastically averaging the hydrodynamic couplings of all possible particle pairs in certain configurations via ASD simulations. We will utilize these new mobilities functions to develop the scaling theory for suspension stress in the concentrated regime.

As discussed above, the high-*Pe* asymptote of suspension stress in dilute theory [Eq. (5.19)] still holds from a view of intermediate medium, but volume fraction matters appropriately in this formulation. In dilute theory, $g^{eq}(2)$ represents the equilibrium pair-distribution function outside the boundary layer. As concentration increases, there is larger probability to find a bath particle outside the boundary layer, thus the equilibrium pair-distribution is also a function of volume fraction, *i.e.*, $g^{eq}(2;\phi_b)$. It can be estimated from the Carnahan-Starling equation of state [31]:

$$g^{eq}(2;\phi_b) = \frac{1-0.5\phi_b}{(1-\phi_b)^3}. \tag{5.22}$$

The change of microstructure distortion $f(2;\theta)$ is neglected as concentration increases because the crucial contribution to average stress on the particle surface is the number of bath particles around the surface, which is captured by $g^{eq}(2;\phi_b)$. The non-equilibrium distribution of bath particles surrounded the surface varies the stress evaluation sufficiently small.

Furthermore, the increasing concentration give rise to a higher particle den-

sity inside the boundary layer, which implies that the scaling of the suspension stress, Pe^{δ}, also evolves with volume fraction, *i.e.*, $\delta = \delta(\phi_b)$. As shown in Eq. 5.20, δ is a ratio of leading orders of mobility functions transverse to and along the line of centers. Thus for an arbitrary concentration, this ratio can be estimated by evaluating the concentrated mobility functions derived by Zia *et al.* [157], in the limit of particles near contact:

$$\delta(\phi_b) = \frac{W_0(\phi_b)}{G_1(\phi_b)}. \tag{5.23}$$

A more careful examination of these two mobility functions for arbitrary concentrations indicate that the leading order term along the line of centers, G_1, almost keep same, but the one transverse to the line of centers, W_0, grows with the increase of concentration. Thus quantitatively, the transverse mobility changes the high-Pe stress scaling. Physically, inside the boundary layer, lubrication interactions dominate. For parallel hydrodynamic couplings, two-body interactions dominate because a third particle is not able to fit in the thin fluid gap between the pair, which makes G_1 keep consistent as concentration increases. However, a third particle placed transverse to the line of centers contributes to the coupling and leads to a three-body hydrodynamic interaction transverse to the line of centers. More importantly, the transverse interaction gives rise to a transverse particle motion, and thus breaks the fore-aft symmetry of pair trajectory, and owes to non-Newtonian rheology. That is, the non-Newtonian rheology arising from hydrodynamic interactions is set by the three-body transverse mobility couplings. Involving all the concentration effects, the high-Pe scaling of the suspension stress is written as:

$$\frac{\langle \Sigma^{neq} \rangle^{conc}}{n_a kT \phi_b} \sim Pe^{\delta(\phi_b)} g^{eq}(2; \phi_b). \tag{5.24}$$

Remind that the scaling of the dilute theory reads

$$\frac{\langle \Sigma^{neq} \rangle^{dilu}}{n_a kT\phi_b} \sim Pe^{\delta_D} g^{eq}(2;\phi_b \ll 1), \tag{5.25}$$

where the subscript D denotes dilute limit and $\delta_D \equiv 0.799$. A comparison of Eqs. (5.24) (5.25) gives a scaling theory to bridge dilute theory and concentrated suspensions:

$$\frac{\langle \Sigma^{neq} \rangle^{conc}}{g^{eq}(2;\phi_b)Pe^{\delta(\phi_b)-\delta_D}} \sim \langle \Sigma^{neq} \rangle^{dilu}. \tag{5.26}$$

In Fig. 5.6, we apply this scaling to the parallel and perpendicular normal stress, the first normal stress difference and the osmotic pressure. At high Pe, concentrated stresses with different volume fractions all collapse onto the dilute theory. Thus this validates our idea that the concentrated suspensions can be considered as particle pairs interacting through a medium of intervening particles and solvent, where the formulations are consistent with the dilute theory but concentrated mobilities are utilized to model the medium property.

After providing the scaling theory for high-Pe regime, next we will apply the scaling theory into low-Pe regime. The low-Pe asymptote of the suspension stress is given as

$$\frac{\langle \Sigma^{neq} \rangle}{n_a kT\phi_b} \sim Pe^2 g^{eq}(2;\phi_b \ll 1). \tag{5.27}$$

The low-Pe scaling Pe^2 arises from the entropic recovery of the structure distortion, thus does not change with volume fraction. Similarly to the discussion for the high Pe, a simpler scaling regime can be suggested only based on g^{eq}, the equilibrium pair-distribution function just outside the boundary layer:

$$\frac{\langle \Sigma^{neq} \rangle^{conc}}{g^{eq}(2;\phi_b)} \sim \langle \Sigma^{neq} \rangle^{dilu}. \tag{5.28}$$

We select osmotic pressure as an example to show the validation of the low-Pe scaling theory for the suspension stress. Fig. 5.7(a-b) represents the osmotic

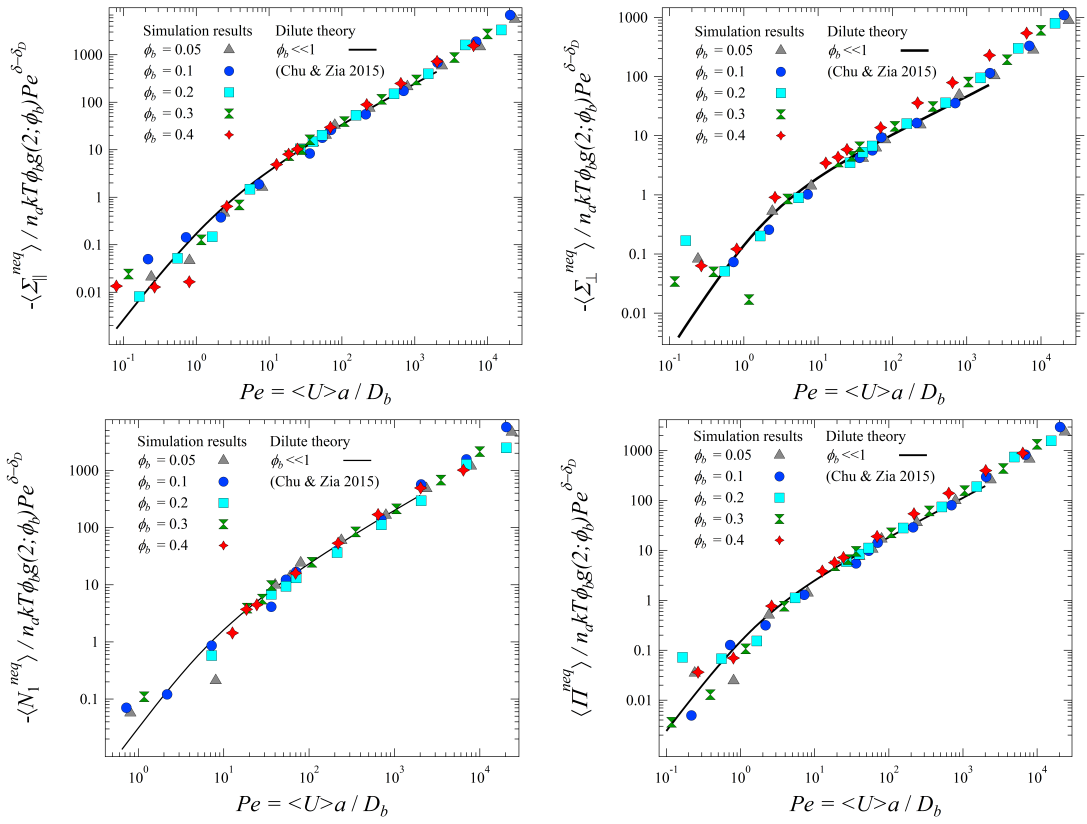

Figure 5.6: High-*Pe* scaling theory [Eq. 5.26] of suspension stress, as a function of ϕ_b and *Pe*: (a) parallel normal stress; (b) perpendicular normal stress; (c) first normal stress difference; (d) osmotic pressure. The filled symbols are simulation results. The solid lines are dilute theory from [34, 35].

pressure in the concentrated suspensions after applying the scaling theory in Eq. (5.28), compared with the dilute theory. However, disparity can be observed at low *Pe*. This is because the Brownian contribution to the suspension stress is significant at low *Pe*, and the variance of Brownian stress is high, as shown by the error bars in Fig. 5.7. To validate the scaling theory, we can justify it by just looking at the hydrodynamic contribution, which is the same order of magnitude as the Brownian part at $Pe \sim O(1)$. In Figure 5.7(c-d), we compare the hydrodynamic osmotic pressure before and after applying the low-*Pe* scaling. Clearly, with the scaling, hydrodynamic osmotic pressure of all volume frac-

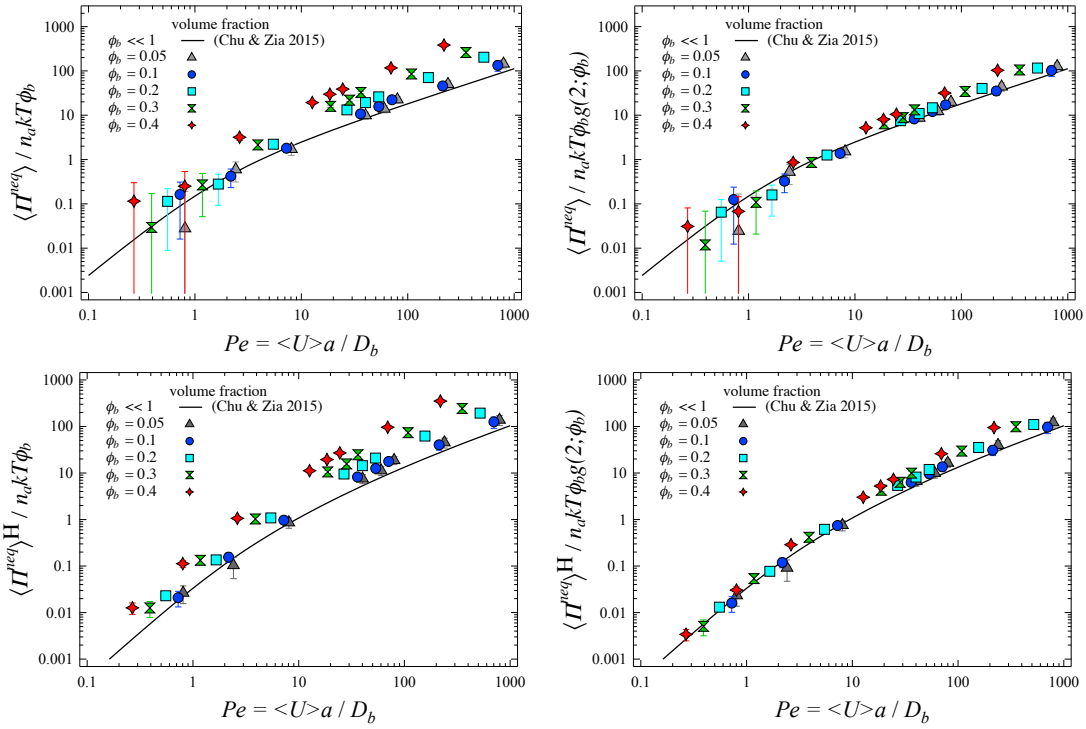

Figure 5.7: Low-*Pe* scaling [Eq. 5.26] of the osmotic pressure as a function of ϕ_b and *Pe*: (a) total osmotic pressure before scaling; (b) total osmotic pressure after scaling; (c) hydrodynamic osmotic pressure before scaling; (d) hydrodynamic osmotic pressure after scaling. The solid lines are dilute theory from [35].

tions collapse onto the dilute theory.

To summary, in a suspension with arbitrary concentration, the interactions between probe and bath particles can be modeled as pair interactions through an intermediate medium. The medium models the effect of solvent, as well as the intervening particles between the pair. The properties of the medium is captured by the concentrated hydrodynamic couplings derived by Zia *et al.* [157], as a function of both suspension concentration and pair separation. In an arbitrary concentration, two effects may influence the suspension stress. The probability for the probe to interact with a bath particle depends on the concentration, and is captured by the equilibrium pair-distribution function, which gives rise

to a change of magnitude of the suspension stress. More importantly, for strong probe forcing, the hydrodynamic couplings transverse to the line of centers give rise to break of fore-aft symmetry when three-body encounters. This distortion of microstructure contributes to the non-Newtonian rheology, and leads to the change of high-Pe scaling of the suspension stress. For weak probe forcing, Brownian motion dominates. Because the relative motion of particles is small and quickly recovered by the Brownian motion, the effect of breaking fore-aft symmetry owing to the three-body encounters is weak. As a result, only pair-distribution function contributes to the change of suspension stress. The non-Newtonian behaviors mainly arise from the Brownian motion, which destroys the time reversibility. The effect of many-body hydrodynamic interactions may be negligible.

Scaling for microviscosity

Khair and Brady [78] derived the high Pe asymptote of the microviscosity in the dilute suspension, $\eta^{micro} \sim \alpha + \beta Pe^{\delta-1}$. Here, α and β are functions of pair mobilities, which are derived by Jeffrey and Onishi [75]. The constant denotes viscosity arising from interactions outside the boundary layer, whereas the Pe dependent term represents that inside the boundary layer. In concentrated suspensions, following the idea above, the asymptote formulation still holds. But now α and β are functions of concentrated mobilities. However, these two coefficients are difficult to directly compute due to their complicated relations to the mobilities. As $Pe \to \infty$, asymmetric structure and thus the boundary layer vanishes, and the microstructure recovers its spherical symmetry. The microviscosity totally arises from the hydrodynamic interactions in the outer region,

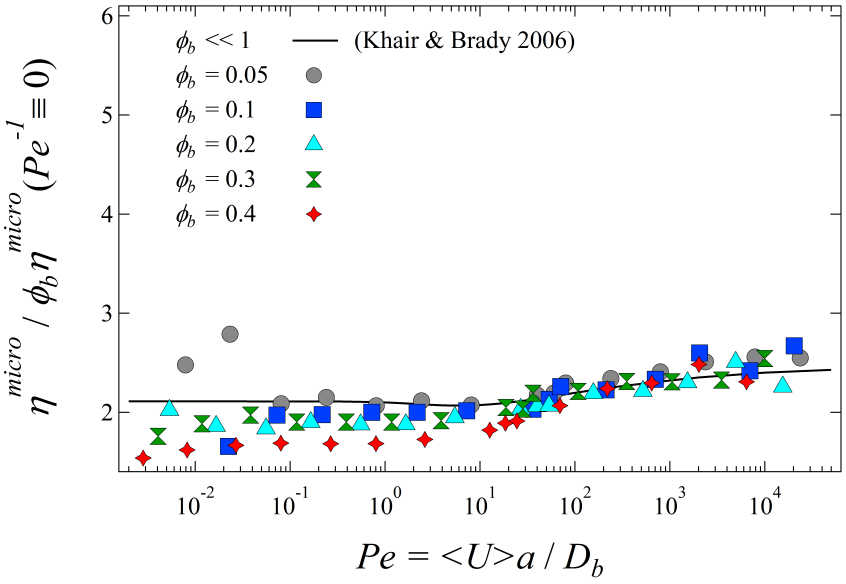

Figure 5.8: Microviscosity as a function of Pe and ϕ_b. The solid line is dilute theory [78]. The filled symbols are the scaled simulation results with finite Pe.

i.e., α. In simulations, this constant can be measured with setting $Pe^{-1} \equiv 0$ by turning off the Brownian motion. This suggests that in high Pe we can scale the microviscosity with the microviscosity in the infinite-Pe limit since it captures the many-body hydrodynamic effects at high Pe.

$$\frac{\eta^{micro}_{conc}(\phi_b)}{\eta^{micro}_{conc}(Pe^{-1} \equiv 0)/\eta^{micro}_{dilu}(Pe^{-1} \equiv 0)} \sim \eta^{micro}_{dilu}(\phi_b \ll 1). \tag{5.29}$$

Fig. 5.8 shows the microviscosity comparing with the dilute theory after the scaling above and in high Pe the agreement is excellent.

5.6 Conclusions

We have studied the microstructure, microviscosity and suspension stress in a fully hydrodynamically interacting dispersion of hard colloidal spheres in the

active microrheology for arbitrary concentrations via ASD simulation, and elucidated the effect of three-body interactions on rheological quantities. The behavior was studied for probe forcing from weak to strong, for suspensions from dilute to concentrated. For microstructure, we found that increased particle concentration preserves the symmetry of microstructure for $Pe \sim 1$, and three-body interactions enhance particle density inside the boundary layer more significantly in high Pe than low Pe regime. For microviscosity, three-body interactions produce a qualitative change for force-thickening. Since more particles accumulate inside the boundary layer in high Pe via three-body interactions, the asymptote value of high-Pe plateau grows faster for strong probe forcing, compared with the low-Pe plateau where the effect of three-body interactions is relatively small. For suspension stress, instead of suppressing energy storage as two-body hydrodynamic interaction does in dilute theory [34, 35], three-body interactions enhance suspension stress. Two-body hydrodynamic interactions preserve fore-aft symmetry of a pair trajectory and introduce Newtonian rheology. In contrast, three-body hydrodynamic interactions give rise to loss of fore-aft symmetry in the presence of a third particle in a pair trajectory and thus lead to non-Newtonian rheology. This behavior is shown in the change of Pe scaling in high-Pe suspension stress. An analytical examination of the scaling exhibits that the non-Newtonian behaviors are introduced by the change of transverse mobility, as the third particle produces a deviation transversely for the pair trajectory. Since the Pe scaling is determined by the near-contact interactions, the third particle cannot influence much in longitudinal direction.

As the microviscosity is directly related to particle motion, and the force-velocity coupling is a long-range interaction, the effect of long-range hydrodynamic interactions may influence the microviscosity in high concentration.

Such behaviors may be viewed by directly applying the concentrated mobility functions into Smoluchowski equation and deriving analytical solutions in the future work.

CHAPTER 6

CONCLUSIONS

In this dissertation, we utilized a combination of micromechanics theories, phenomenological model, and particle dynamics simulations to study single-probe active microrheology in an unbound, hard-sphere suspension comprising hydrodynamically interacting colloids. In the low Reynolds number regime, we took advantage of the linearity of Stokes flow to develop a novel micromechanics theory for the particle stress in a hydrodynamically interacting suspension, and examined the evolution of four rheological quantities with flow strength and hydrodynamic interactions (interparticle repulsion range), namely the parallel and perpendicular normal stresses, first normal stress difference, and particle osmotic pressure. We further analyzed the balance of nonequilibrium fluctuation and dissipation in the presence of hydrodynamic forces, and derived a generalized nonequilibrium Stokes-Einstein relation which relates suspension stress to microviscosity and diffusivity, empowering the active microrheology technique that one can fully describe a steady state suspension by measuring the motion of a single, embedded probe particle. To broaden the scope to examine the effect of particle concentration, we employed Accelerated Stokesian Dynamics framework to simulate the microstructure, microviscosity and particles stress of various dilute to concentrated suspensions. We constructed a new scaling theory to collapse the results of suspensions of different concentrations, offering a robust predictive model for concentrated suspension rheology.

The model system in the present research is single-probe active microrheology in an unbound, hard-sphere suspension comprising hydrodynamically interacting colloids. In Chapter 2 to 4, we studied the dynamics of dilute sus-

pensions where pair-interactions dominate. We started by formulating a two-body Smoluchowski equation governing the spatial evolution of the particle microstructure and, by the virtue of Stokes flow linearity, we derived analytical expressions for the particle stresslets arising from three major microscopic forces: external, Brownian and interparticle forces. The microstructure was then utilized to compute the average suspension stress, analytically in the asymptotic limits of weak and strong flow strength and hydrodynamic interactions, and numerically for the full range of flow and hydrodynamic strength via a finite difference scheme. In deriving our micromechanical theory, we clarified the definition of the hydrodynamic and thermodynamic stress, and emended the confusion stemmed from prior work [14, 20, 19]. We focused on examining the normal stresses in Chapter 2. We found that hydrodynamic interactions, whose strength is inversely proportional to the range of entropic repulsion, weaken the parallel and perpendicular normal stresses regardless of the strength of flow. When flow is weak, the timescale at which Brownian motion restores the equilibrium particle configuration is shorter than that for distortion by advection, and the particle normal stresses scale uniformly as Pe^2 despite hydrodynamic dissipation. As flow strengthens, particle-rich boundary layer forms in front of the probe and particle-depleted trailing wake forms behind it simultaneously, and such structural asymmetry leads to an increase in the normal stresses. When advection dominates diffusion, boundary layer dynamics govern the evolution of the normal stresses, where their growth scale as the particle density inside the boundary layer as Pe^{δ}, with $0.799 \leq \delta \leq 1$ as hydrodynamic interactions vary from strong to weak. We further conducted a pair-trajectory analysis to examine the origin of the particle stress arising from the three microscopic forces, and demonstrated that hydrodynamic coupling

brings forth a dissipative interparticle stress always acting against the elastic interparticle stress which, in the limit of strong hydrodynamics, precisely cancel, suggesting that interparticle force still plays a role even in such limit. The trajectory analysis also exhibited clearly how a combination of particle attraction and repulsion, and interaction duration and frequency determines the extent of microstructural asymmetry and thus the magnitude of the particle stress. In relating the particle stress and energy density in a suspension, hydrodynamic interactions shield particle collisions and suppress energy storage by prolonging particles coupling and reducing interaction frequency, thus reducing structural asymmetry and entropic energy density. In the limit of no Brownian motion and perfectly smooth spheres, the pair-trajectories become fore-aft symmetric, statistically forming a spherically symmetric particle structure, and therefore the nonequilibrium stress and energy vanish completely.

Non-Newtonian rheology of a suspension is characterized by the aggregate effect of the normal stresses — an anisotropic deformation by the normal stress differences, and an isotropic expansion or contraction by particle osmotic pressure. We investigated the non-Newtonian rheology of a dilute, hydrodynamically interacting suspension in Chapter 3, in which the normal stress differences and particle osmotic pressure were studied across the asymptotic limits of weak and strong flow strength and hydrodynamic interactions. We found that the second normal stress difference is identically zero regardless of the strength of flow and hydrodynamics owing to the axisymmetry of the particle microstructure around the probe. The evolution of the first normal stress difference is more intricate: when flow is weak, a hydrodynamically interacting suspension has a stronger first normal stress difference than its non-hydrodynamically interacting counterpart, owing to the enhanced disparity in the duration of longitudinal

versus transverse particle encounters. On the contrary, when flow is strong, hydrodynamic interactions shield particle collisions and suppress the growth of the first normal stress difference. Interesting, the first normal stress difference demonstrated a change of sign from positive to negative transitioning from the weak- to strong-flow regimes. We showed that this sign change is present only when hydrodynamic interactions are moderately strong and, distinct from the finding in prior work that such behavior is solely due to a switch of dominance between the Brownian and hydrodynamic forces [50, 19], we identified a novel mechanism that interparticle repulsion alone can lead to a change of sign in the first normal stress difference. For the particle osmotic pressure, we showed that its evolution follows that of the normal stresses, that is the osmotic pressure grows as Pe^2 and Pe^δ in the asymptotic limits of weak and strong flow, respectively; and hydrodynamic interactions suppress the osmotic pressure regardless of the strength of flow. In this chapter, we also presented our data scaled by the advective stress, equivalently the response that one would measure in experiments following an advecting probe.

The novel micromechanical theory in Chapter 2 and 3 provides a means through which one could predict the response of a dilute, hydrodynamically interacting suspension if the particle microstructure is known. Nevertheless, measuring the particle structure is labor-intensive. To circumvent this problem, we developed a generalized nonequilibrium Stokes-Einstein relation in Chapter 4 linking the suspension stress to the microviscosity and flow-induced diffusivity so that the stress can be inferred from the mean and mean-square motion of a single probe particle. Our derivation started with an equation of motion, taking into account the effect of both advection and diffusion arising from the mean flow and its variation of a suspension. We related the advection flux

to the reduction of the mean flow via the microviscosity, the diffusive flux to the fluctuation of the mean motion via the diffusivity, and the additional hydrodynamic dissipation via hydrodynamic mobility functions associated with the longitudinal and transverse relative motion of a pair. These together constitute a novel anisotropic effective resistance tensor governing the balance of nonequilibrium momentum fluxes. The resultant phenomenological relation between suspension stress, viscosity and diffusivity is a generalized nonequilibrium Stokes-Einstein relation that permits a full rheological characterization of a hydrodynamically interacting suspension by tracking the motion of a single probe particle. Predictions by the new theory agrees well with the micromechanical theories from Chapter 2 and 3 as well as with dynamic simulations, for the full range of flow strength and hydrodynamic interactions.

In Chapter 5, we turned our attention to study the effect of particle concentration. Utilizing Accelerated Stokesian Dynamics framework, we simulated single-probe active microrheology of hydrodynamically interacting suspensions with different particle concentrations, ranging from dilute $\phi = 0.05$ to concentrated $\phi = 0.40$, over six decades of flow strength and eight decades of hydrodynamic strength. Particle concentration was shown to play a role in altering the particle structure and the rheology qualitatively. For the microstructure, when flow is weak and Brownian motion dominates, a higher particle concentration and the associated local liquid structure give rise to a large particle concentration gradient and strong Brownian drift, allowing the ring-like structure to retain to a larger extent compared to a dilute suspension. When flow is strong, boundary layer and wake structures form regardless of particle concentration but it changes the fore-aft asymmetry qualitatively: the accumulation of particles inside the boundary layer of a concentrated suspension is higher due

to the larger entropic hindrance of particles, whereas the wake of a concentrated suspension is shorter since a larger Brownian drift acts to close the wake. Particle concentration was shown to enhance the microviscosity and the suspensions stress. For the former, more closely-packed structure results in stronger hydrodynamic interactions, leading to increased dissipation and thus viscosity. For the latter, a concentrated suspension has a higher particle density, suggesting a higher energy density, equivalently a higher suspension stress. Despite accurate prediction, computational simulations are expensive. In the last part of this chapter, we developed scaling theories, utilizing recently derived concentrated hydrodynamic mobility functions, to collapse the microviscosity and suspension stress of suspensions of different particle concentrations, offering a robust predictive model for concentrated suspension rheology.

In conclusion, the present work has developed a novel micromechanical theory for computing the suspension stress in a dilute, hydrodynamically interacting, hard-sphere suspension; a generalized nonequilibrium Stokes-Einstein relation for predicting the stress requiring just the motion of a single probe particle; and a scaling theory for predicting concentrated suspension response. Many interesting questions remain. While the statistical mechanics model in Chapters 2 to 4 and the numerical model in Chapter 5 are fully generalizable for arbitrary probe- to bath-particle size ratio, the details of this behavior were not explored here. In practice, active microrheological studies often utilize probes with a range of sizes relative to the bath particles [133, 51], and recent studies have shown that the size ratio of the probe and bath particles exerts a pronounced influence on rheological measurements [102, 126, 144, 70]. In an active microrheology system with small or large probe, size ratio exerts only a quantitative effect on viscosity [124], force-induced diffusion [153] and suspension

stress [154]. However, it was recently shown that when hydrodynamic interactions matter, changes in probe size relative to bath particles reveals a pronounced, qualitative change in force-induced diffusion [70]. Future studies of suspension stress should interrogate this dependence.

In addition, the interparticle force need not be purely repulsive, which could lead to interesting changes in rheology, particularly in the limit of weak Brownian motion. Attractive interparticle forces break symmetry by driving bath particles off trajectory and closer to the probe, and would delay downstream decoupling, giving a trailing trajectory that is closer to the line of forcing than what would occur for a purely repulsive or hydrodynamic interaction. The models developed in this research can be easily extended to attractive interparticle forces to interrogate these ideas and examine their effects on suspension stress. Future work could address many different types of interparticle forces, connecting with, for example, osmotic pressure in colloidal gels [156, 86].

The results in Chapter 3 motivate a connection of the sign change in the first normal stress difference observed in sheared suspensions. In the plane transverse to forcing in active microrheology, the axisymmetric external force results in particle accumulation and depletion that lie along the line of the forcing. In the corresponding flow/flow-gradient plane of a shear flow, particles accumulate and deplete along the compressional and extensional axis respectively, giving an anti-symmetric structure. Despite the difference in the structures, Zia and Brady [154] showed that the first normal stress difference (as well as the normal stresses and osmotic pressure) between two flows demonstrate qualitatively similar evolution in the absence of hydrodynamic interactions. As pointed out in that work, a rotation of quadrants makes structures between two

flows nearly identical. It is possible that a "normal stress difference" defined by coordinates aligned to the compressional and extensional axes in a shear flow might reveal more clearly behavior common to both flows. Reconciling the difference in structures between two flows will provide insight into devising a unified means to control the evolution of normal stress differences and other rheological behaviors.

In Chapter 4, the formulation of the phenomenological model is based on a Cauchy momentum balance, and is general for complex materials in which there is a separation of length scale between the dispersed and the suspending phase. In this work, its application is specified to hard-sphere colloidal suspensions by constitutively modeling the advective and diffusive particle flux using the microviscosity and flow-induced diffusivity taken from studies of hard-sphere suspensions. We conjecture that the present model can be readily generalized to examine suspensions comprising attractive colloids, colloids of arbitrary shape, and even emulsions, with the hard-sphere viscosity and diffusivity replaced by corresponding quantities in other model systems.

Similarly, the present model can be extended to study the temporal-dependence of the nonequilibrium fluctuation and dissipation. Recent work on active microrheology of start-up suspension flows [155, 105] recovers qualitatively the evolution of the viscosity observed in traditional macrorheology of suspensions [48] and colloidal gels [134, 106, 77], including an overshoot before it reaches the steady-state response. As the disparity between the advective and diffusive timescales explain the temporal evolution of the viscosity [105], the same notion can be employed to understand the transient development of the corresponding particle fluxes, their lasting effect on the microstructure, and in

turn the generation of suspension stress.

APPENDIX A

HYDRODYNAMIC RESISTANCE AND MOBILITY FUNCTIONS

In this section, the hydrodynamic functions required to obtain the stresslets and the average stresses in Chapter 2 and 3 are presented. These functions depend only on the relative separation between a pair of particles, r, and the dimensionless repulsion range, κ. The hydrodynamic resistance function that couples the translational velocity of particle β to the induced stresslet on particle α, $\boldsymbol{R}^{SU}_{\alpha\beta}$; and the hydrodynamic resistance function that couples the rotational velocity of particles β to the induced stresslet on particle α, $\boldsymbol{R}^{S\Omega}_{\alpha\beta}$, are defined respectively as [73, 74],

$$\boldsymbol{R}^{SU}_{\alpha\beta} = 4\pi\eta a^2 \left[X^{G}_{\alpha\beta}\left(\hat{r}_i\hat{r}_j\hat{r}_k - \frac{1}{3}\delta_{ij}\hat{r}_k\right) + \frac{1}{3}X^{P}_{\alpha\beta}\delta_{ij}\hat{r}_k + Y^{G}_{\alpha\beta}\left(\hat{r}_i\delta_{jk} + \hat{r}_j\delta_{ik} - 2\hat{r}_i\hat{r}_j\hat{r}_k\right)\right], \quad \text{(A.1)}$$

$$\boldsymbol{R}^{S\Omega}_{\alpha\beta} = 8\pi\eta a^3 Y^{H}_{\alpha\beta}\left(\hat{r}_i\epsilon_{jkm}\hat{r}_m + \hat{r}_j\epsilon_{ikm}\hat{r}_m\right), \quad \text{(A.2)}$$

where r_i is the unit vector along the line of centers of particles α and β, δ_{ij} is the identity tensor, ϵ_{ijk} is the Levi-Civita tensor, $X_{\alpha\beta}$ and $Y_{\alpha\beta}$ govern the motion of particle α and β along and transverse to their line of centers respectively. Two remarks are made regarding the above resistance functions. First, $\boldsymbol{R}^{SU}_{\alpha\beta}$ gives the complete relation between particle kinematics and the induced stresslet since the stresslet is not restricted to be traceless. The hydrodynamic function $X^{P}_{\alpha\beta}$, which is associated with the trace of the stresslet or osmotic pressure, has been grouped into $\boldsymbol{R}^{SU}_{\alpha\beta}$. Second, $\boldsymbol{R}^{S\Omega}_{\alpha\beta}$ is traceless, signifying that rotations of spheres do not contribute to the trace or osmotic pressure [74].

The hydrodynamic mobility function that couples the force on particle β to the induced translational velocity of particle α, $\boldsymbol{M}^{UF}_{\alpha\beta}$; and the hydrodynamic mobility function that couples the force on particle β to the induced rotational

velocity on particle α, $\boldsymbol{M}^{\Omega F}_{\alpha\beta}$, are defined respectively as, [75]

$$\boldsymbol{M}^{UF}_{\alpha\beta} = \frac{1}{6\pi\eta a}\left[x^{a}_{\alpha\beta}\hat{r}_i\hat{r}_j + y^{a}_{\alpha\beta}\left(\delta_{ij} - \hat{r}_i\hat{r}_j\right)\right], \tag{A.3}$$

$$\boldsymbol{M}^{\Omega F}_{\alpha\beta} = \frac{1}{4\pi\eta a^2}y^{b}_{\alpha\beta}\left(\epsilon_{ijk}\hat{r}_k\right), \tag{A.4}$$

where $x_{\alpha\beta}$ and $y_{\alpha\beta}$ govern the motion of particle α and β along and transverse to their line of centers, respectively.

APPENDIX B

DERIVATION OF THE PARTICLE STRESSLET FROM MOBILITY AND RESISTANCE FORMULATIONS

In Sec. 2.3.2, we derived the particle stresslet and the average suspension stress arising from the external, Brownian and interparticle forces. In this section, we elucidate the derivation in the context of the classical mobility and resistance formulations [79], and comment on the matrix representation in prior studies, *e.g.* [20, 8].

Let us start with the mobility formulation, where hydrodynamic traction moments on particles surface are prescribed and velocity derivatives are to be determined. In the end of this derivation, we will show that the mobility and resistance formulations are in fact interchangeable to compute the hydrodynamic stresslet provided that proper steps are taken. To begin, the mobility formulation truncated at the first moment of hydrodynamic traction and straining motion reads [80, 79]

$$\begin{pmatrix} \boldsymbol{U}_1 - \boldsymbol{U}^\infty(\boldsymbol{x}_1) \\ \boldsymbol{U}_2 - \boldsymbol{U}^\infty(\boldsymbol{x}_2) \\ \boldsymbol{\Omega}_1 - \boldsymbol{\Omega}^\infty(\boldsymbol{x}_1) \\ \boldsymbol{\Omega}_2 - \boldsymbol{\Omega}^\infty(\boldsymbol{x}_2) \\ -\boldsymbol{S}_1^H \\ -\boldsymbol{S}_2^H \end{pmatrix} = - \begin{pmatrix} \boldsymbol{M}_{11}^{UF} & \boldsymbol{M}_{12}^{UF} & \boldsymbol{M}_{11}^{UL} & \boldsymbol{M}_{12}^{UL} & \boldsymbol{M}_{11}^{UE} & \boldsymbol{M}_{12}^{UE} \\ \boldsymbol{M}_{21}^{UF} & \boldsymbol{M}_{22}^{UF} & \boldsymbol{M}_{21}^{UL} & \boldsymbol{M}_{22}^{UL} & \boldsymbol{M}_{21}^{UE} & \boldsymbol{M}_{22}^{UE} \\ \boldsymbol{M}_{11}^{\Omega F} & \boldsymbol{M}_{12}^{\Omega F} & \boldsymbol{M}_{11}^{\Omega L} & \boldsymbol{M}_{12}^{\Omega L} & \boldsymbol{M}_{11}^{\Omega E} & \boldsymbol{M}_{12}^{\Omega E} \\ \boldsymbol{M}_{21}^{\Omega F} & \boldsymbol{M}_{22}^{\Omega F} & \boldsymbol{M}_{21}^{\Omega L} & \boldsymbol{M}_{22}^{\Omega L} & \boldsymbol{M}_{21}^{\Omega E} & \boldsymbol{M}_{22}^{\Omega E} \\ \boldsymbol{M}_{11}^{SF} & \boldsymbol{M}_{12}^{SF} & \boldsymbol{M}_{11}^{SL} & \boldsymbol{M}_{12}^{SL} & \boldsymbol{M}_{11}^{SE} & \boldsymbol{M}_{12}^{SE} \\ \boldsymbol{M}_{21}^{SF} & \boldsymbol{M}_{22}^{SF} & \boldsymbol{M}_{21}^{SL} & \boldsymbol{M}_{22}^{SL} & \boldsymbol{M}_{21}^{SE} & \boldsymbol{M}_{22}^{SE} \end{pmatrix} \cdot \begin{pmatrix} \boldsymbol{F}_1^H \\ \boldsymbol{F}_2^H \\ \boldsymbol{L}_1^H \\ \boldsymbol{L}_2^H \\ \boldsymbol{E}^\infty \\ \boldsymbol{E}^\infty \end{pmatrix}, \tag{B.1}$$

where $\boldsymbol{F}_\alpha^H$, $\boldsymbol{L}_\alpha^H$ and $\boldsymbol{S}_\alpha^H$ are the hydrodynamic force, torque and stresslet acted on particle α by the fluid, respectively; $\boldsymbol{U}^\infty(\boldsymbol{x}_\alpha)$, $\boldsymbol{\Omega}^\infty(\boldsymbol{x}_\alpha)$ and $\boldsymbol{E}^\infty$ are the imposed far-field fluid translational velocity, rotational velocity, and straining motion respectively in the absence of particles evaluated at the position of particle α; $\boldsymbol{U}_\alpha$

and $\boldsymbol{\Omega}_\alpha$ are the total translational and rotational velocity of particle α, respectively; and the subscript 1 and 2 denote the probe and the bath particle, respectively. The mobility function $\boldsymbol{M}^{XY}_{\alpha\beta}$ couples Y — the hydrodynamic force, torque and imposed straining motion acting on particle β as shown in the vector on the right-hand side of Eq. (B.1) to X — the translational and rotational velocities, and stresslets acting on particle α as shown in the vector on the left-hand side of Eq. (B.1) [79]. The stresslet exerted on the probe is obtained from Eq. (B.1) as

$$\boldsymbol{S}^H_1 = \boldsymbol{M}^{SF}_{11} \cdot \boldsymbol{F}^H_1 + \boldsymbol{M}^{SF}_{12} \cdot \boldsymbol{F}^H_2 + \boldsymbol{M}^{SL}_{11} \cdot \boldsymbol{L}^H_1 + \boldsymbol{M}^{SL}_{12} \cdot \boldsymbol{F}^H_2 + \boldsymbol{M}^{SE}_{11} \cdot \boldsymbol{E}^\infty + \boldsymbol{M}^{SE}_{12} \cdot \boldsymbol{E}^\infty. \quad \text{(B.2)}$$

Equation (B.2) can be simplified by recalling that in the present active microrheology model all particles are net torque- and external torque-free. We also note that the rotation caused by Brownian and interparticle forces does not alter the configuration of a sphere with uniform surface property, *i.e.*, it is indistinguishable if a sphere is rotated or not because of the uniformity of its surface, $\boldsymbol{L}^B_\alpha = \boldsymbol{L}^P_\alpha = 0$. Thus, a torque balance gives zero hydrodynamic torque

$$\boldsymbol{L}^H_\alpha = 0. \quad \text{(B.3)}$$

Further, there is no imposed far-field fluid translational and rotational velocity, and straining flow:

$$\boldsymbol{U}^\infty(\boldsymbol{x}_\alpha) = \boldsymbol{\Omega}^\infty(\boldsymbol{x}_\alpha) = \boldsymbol{E}^\infty = 0. \quad \text{(B.4)}$$

Substituting Eqs. (B.3) and (B.4) into Eq. (B.2) gives

$$\boldsymbol{S}^H_1 = \boldsymbol{M}^{SF}_{11} \cdot \boldsymbol{F}^H_1 + \boldsymbol{M}^{SF}_{12} \cdot \boldsymbol{F}^H_2. \quad \text{(B.5)}$$

However, one still cannot determine the stresslet exerted on the probe $\boldsymbol{S}^H_1$ from Eq. (B.5) for two reasons. First, analytic formulae for implementing $\boldsymbol{M}^{SF}_{\alpha\beta}$ are not complete in the literature and, second, hydrodynamic force $\boldsymbol{F}^H_\alpha$ is unprescribable. For the former issue, we note that lubrication expressions and far-field

recursive relations for $\boldsymbol{M}_{\alpha\beta}^{SF}$ (and in fact also for $\boldsymbol{M}_{\alpha\beta}^{SL}$ and $\boldsymbol{M}_{\alpha\beta}^{SE}$) had not been derived until the work by Kim and Karrila [79], and thus it could not be implemented efficiently as, *e.g.* $\boldsymbol{M}_{\alpha\beta}^{UF}$ and other hydrodynamic functions as in [75]. Due to this historical development of hydrodynamic functions, authors in prior work circumvented this issue by expressing the "unknown" $\boldsymbol{M}_{\alpha\beta}^{SF}$ in terms of some well-studied, "known" resistance and mobility functions. We adopt this approach in this work and employ the following relations [79]:

$$\boldsymbol{M}_{11}^{SF} = \boldsymbol{R}_{11}^{SU} \cdot \boldsymbol{M}_{11}^{UF} + \boldsymbol{R}_{12}^{SU} \cdot \boldsymbol{M}_{21}^{UF} + \boldsymbol{R}_{11}^{S\Omega} \cdot \boldsymbol{M}_{11}^{\Omega F} + \boldsymbol{R}_{12}^{S\Omega} \cdot \boldsymbol{M}_{21}^{\Omega F}, \tag{B.6}$$

$$\boldsymbol{M}_{12}^{SF} = \boldsymbol{R}_{11}^{SU} \cdot \boldsymbol{M}_{12}^{UF} + \boldsymbol{R}_{12}^{SU} \cdot \boldsymbol{M}_{22}^{UF} + \boldsymbol{R}_{11}^{S\Omega} \cdot \boldsymbol{M}_{12}^{\Omega F} + \boldsymbol{R}_{12}^{S\Omega} \cdot \boldsymbol{M}_{22}^{\Omega F}. \tag{B.7}$$

Substituting Eqs. (B.6) and (B.7) into Eq. (B.5) gives

$$\begin{aligned} \boldsymbol{S}_1^H = \; & \boldsymbol{R}_{11}^{SU} \cdot (\boldsymbol{M}_{11}^{UF} \cdot \boldsymbol{F}_1^H + \boldsymbol{M}_{12}^{UF} \cdot \boldsymbol{F}_2^H) + \boldsymbol{R}_{12}^{SU} \cdot (\boldsymbol{M}_{21}^{UF} \cdot \boldsymbol{F}_1^H + \boldsymbol{M}_{22}^{UF} \cdot \boldsymbol{F}_2^H) \\ & + \boldsymbol{R}_{11}^{S\Omega} \cdot (\boldsymbol{M}_{11}^{\Omega F} \cdot \boldsymbol{F}_1^H + \boldsymbol{M}_{12}^{\Omega F} \cdot \boldsymbol{F}_2^H) + \boldsymbol{R}_{12}^{S\Omega} \cdot (\boldsymbol{M}_{21}^{\Omega F} \cdot \boldsymbol{F}_1^H + \boldsymbol{M}_{22}^{\Omega F} \cdot \boldsymbol{F}_2^H). \end{aligned} \tag{B.8}$$

Next, to resolve the issue of unprescribable hydrodynamic force $\boldsymbol{F}_\alpha^H$, we express it in terms of the microscopic forces, namely external, Brownian and interparticle forces (cf. Sec. 4.5), in the present net force-free system via a force balance,

$$\begin{aligned} & \boldsymbol{F}_\alpha^{Tot} = \boldsymbol{F}_\alpha^H + \boldsymbol{F}_\alpha^{ext} + \overline{\boldsymbol{F}_\alpha^B} + \boldsymbol{F}_\alpha^P \\ \implies \quad & \boldsymbol{F}_\alpha^H = -\boldsymbol{F}_\alpha^{ext} - \overline{\boldsymbol{F}_\alpha^B} - \boldsymbol{F}_\alpha^P. \end{aligned} \tag{B.9}$$

As noted in Sec. 4.5, Eq. (B.9) is a noise-averaged Langevin equation, and that inertia can be neglected in the overdamped limit ($Re \ll 0$). This is a configuration-dependent equation that can describe one trajectory of a particle each time it is solved. The hydrodynamic, external and interparticle forces are deterministic whereas the Brownian force here has been noised-averaged over times long compared to particle momentum relaxation time. Substituting Eq. (B.9) into

Eq. (B.8) gives

$$\begin{aligned}
\boldsymbol{S}_1^H = \; & -\boldsymbol{R}_{11}^{SU} \cdot (\boldsymbol{M}_{11}^{UF} \cdot \boldsymbol{F}_1^{ext} + \boldsymbol{M}_{12}^{UF} \cdot \boldsymbol{F}_2^{ext}) - \boldsymbol{R}_{12}^{SU} \cdot (\boldsymbol{M}_{21}^{UF} \cdot \boldsymbol{F}_1^{ext} + \boldsymbol{M}_{22}^{UF} \cdot \boldsymbol{F}_2^{ext}) \\
& -\boldsymbol{R}_{11}^{SU} \cdot (\boldsymbol{M}_{11}^{UF} \cdot \overline{\boldsymbol{F}_1^B} - \boldsymbol{M}_{12}^{UF} \cdot \overline{\boldsymbol{F}_2^B}) - \boldsymbol{R}_{12}^{SU} \cdot (\boldsymbol{M}_{21}^{UF} \cdot \overline{\boldsymbol{F}_1^B} + \boldsymbol{M}_{22}^{UF} \cdot \overline{\boldsymbol{F}_2^B}) \\
& -\boldsymbol{R}_{11}^{SU} \cdot (\boldsymbol{M}_{11}^{UF} \cdot \boldsymbol{F}_1^P + \boldsymbol{M}_{12}^{UF} \cdot \boldsymbol{F}_2^P) - \boldsymbol{R}_{12}^{SU} \cdot (\boldsymbol{M}_{21}^{UF} \cdot \boldsymbol{F}_1^P + \boldsymbol{M}_{22}^{UF} \cdot \boldsymbol{F}_2^P) \\
& -\boldsymbol{R}_{11}^{S\Omega} \cdot (\boldsymbol{M}_{11}^{\Omega F} \cdot \boldsymbol{F}_1^{ext} + \boldsymbol{M}_{12}^{\Omega F} \cdot \boldsymbol{F}_2^{ext}) - \boldsymbol{R}_{12}^{S\Omega} \cdot (\boldsymbol{M}_{21}^{\Omega F} \cdot \boldsymbol{F}_1^{ext} + \boldsymbol{M}_{22}^{\Omega F} \cdot \boldsymbol{F}_2^{ext}) \\
& -\boldsymbol{R}_{11}^{S\Omega} \cdot (\boldsymbol{M}_{11}^{\Omega F} \cdot \overline{\boldsymbol{F}_1^B} + \boldsymbol{M}_{12}^{\Omega F} \cdot \overline{\boldsymbol{F}_2^B}) - \boldsymbol{R}_{12}^{S\Omega} \cdot (\boldsymbol{M}_{21}^{\Omega F} \cdot \overline{\boldsymbol{F}_1^B} + \boldsymbol{M}_{22}^{\Omega F} \cdot \overline{\boldsymbol{F}_2^B}) \\
& -\boldsymbol{R}_{11}^{S\Omega} \cdot (\boldsymbol{M}_{11}^{\Omega F} \cdot \boldsymbol{F}_1^P + \boldsymbol{M}_{12}^{\Omega F} \cdot \boldsymbol{F}_2^P) - \boldsymbol{R}_{12}^{S\Omega} \cdot (\boldsymbol{M}_{21}^{\Omega F} \cdot \boldsymbol{F}_1^P + \boldsymbol{M}_{22}^{\Omega F} \cdot \boldsymbol{F}_2^P),
\end{aligned} \tag{B.10}$$

where terms inside brackets in Eq. (B.10) are the translational and rotational velocities induced by the external, Brownian and interparticle forces. This can be shown using the linearity statement between the translational velocity and the microscopic forces

$$\begin{pmatrix} \boldsymbol{U}_1 \\ \boldsymbol{U}_2 \end{pmatrix} = -\begin{pmatrix} \boldsymbol{M}_{11}^{UF} & \boldsymbol{M}_{12}^{UF} \\ \boldsymbol{M}_{21}^{UF} & \boldsymbol{M}_{22}^{UF} \end{pmatrix} \cdot \begin{pmatrix} \boldsymbol{F}_1^H \\ \boldsymbol{F}_2^H \end{pmatrix} = \begin{pmatrix} \boldsymbol{M}_{11}^{UF} & \boldsymbol{M}_{12}^{UF} \\ \boldsymbol{M}_{21}^{UF} & \boldsymbol{M}_{22}^{UF} \end{pmatrix} \cdot \begin{pmatrix} \boldsymbol{F}_1^{ext} + \boldsymbol{F}_1^B + \boldsymbol{F}_1^P \\ \boldsymbol{F}_2^{ext} + \boldsymbol{F}_2^B + \boldsymbol{F}_2^P \end{pmatrix}, \tag{B.11}$$

from which we get

$$\begin{aligned}
\boldsymbol{U}_1 = \; & (\boldsymbol{M}_{11}^{UF} \cdot \boldsymbol{F}_1^{ext} + \boldsymbol{M}_{12}^{UF} \cdot \boldsymbol{F}_2^{ext}) + (\boldsymbol{M}_{11}^{UF} \cdot \overline{\boldsymbol{F}_1^B} + \boldsymbol{M}_{12}^{UF} \cdot \overline{\boldsymbol{F}_2^B}) + (\boldsymbol{M}_{11}^{UF} \cdot \boldsymbol{F}_1^P + \boldsymbol{M}_{12}^{UF} \cdot \boldsymbol{F}_2^P) \\
= \; & \boldsymbol{U}_1^{ext} + \boldsymbol{U}_1^B + \boldsymbol{U}_1^P.
\end{aligned} \tag{B.12}$$

Similarly, the linearity statement between the rotational velocity and the microscopic forces gives

$$\boldsymbol{\Omega}_1 = \boldsymbol{\Omega}_1^{ext} + \boldsymbol{\Omega}_1^B + \boldsymbol{\Omega}_1^P. \tag{B.13}$$

Substituting Eqs. (B.12) and (B.13) into Eq. (B.10) gives

$$\begin{aligned}
\boldsymbol{S}_1^H = \; & -\boldsymbol{R}_{11}^{SU} \cdot (\boldsymbol{U}_1^{ext} + \boldsymbol{U}_1^B + \boldsymbol{U}_1^P) - \boldsymbol{R}_{12}^{SU} \cdot (\boldsymbol{U}_2^{ext} + \boldsymbol{U}_2^B + \boldsymbol{U}_2^P) \\
& -\boldsymbol{R}_{11}^{S\Omega} \cdot (\boldsymbol{\Omega}_1^{ext} + \boldsymbol{\Omega}_1^B + \boldsymbol{\Omega}_1^P) - \boldsymbol{R}_{12}^{S\Omega} \cdot (\boldsymbol{\Omega}_2^{ext} + \boldsymbol{\Omega}_2^B + \boldsymbol{\Omega}_2^P) \\
= \; & -\boldsymbol{R}_{11}^{SU} \cdot \boldsymbol{U}_1 - \boldsymbol{R}_{12}^{SU} \cdot \boldsymbol{U}_2 - \boldsymbol{R}_{11}^{S\Omega} \cdot \boldsymbol{\Omega}_1 - \boldsymbol{R}_{12}^{S\Omega} \cdot \boldsymbol{\Omega}_2,
\end{aligned} \tag{B.14}$$

recovering the expressions for the external force-induced, Brownian and dissipative interparticle stresslet presented in Sec. 2.3.2.

In fact, Eq. (B.14) is the expression that one will obtain from the resistance formulation for computing the hydrodynamic stresslet $\boldsymbol{S}_1^H$ [79]

$$\begin{pmatrix} \boldsymbol{F}_1^H \\ \boldsymbol{F}_2^H \\ \boldsymbol{L}_1^H \\ \boldsymbol{L}_2^H \\ \boldsymbol{S}_1^H \\ \boldsymbol{S}_2^H \end{pmatrix} = - \begin{pmatrix} \boldsymbol{R}_{11}^{FU} & \boldsymbol{R}_{12}^{FU} & \boldsymbol{R}_{11}^{F\Omega} & \boldsymbol{R}_{12}^{F\Omega} & \boldsymbol{R}_{11}^{FE} & \boldsymbol{R}_{12}^{FE} \\ \boldsymbol{R}_{21}^{FU} & \boldsymbol{R}_{22}^{FU} & \boldsymbol{R}_{21}^{F\Omega} & \boldsymbol{R}_{22}^{F\Omega} & \boldsymbol{R}_{21}^{FE} & \boldsymbol{R}_{22}^{FE} \\ \boldsymbol{R}_{11}^{LU} & \boldsymbol{R}_{12}^{LU} & \boldsymbol{R}_{11}^{L\Omega} & \boldsymbol{R}_{12}^{L\Omega} & \boldsymbol{R}_{11}^{LE} & \boldsymbol{R}_{12}^{LE} \\ \boldsymbol{R}_{21}^{LU} & \boldsymbol{R}_{22}^{LU} & \boldsymbol{R}_{21}^{L\Omega} & \boldsymbol{R}_{22}^{L\Omega} & \boldsymbol{R}_{21}^{LE} & \boldsymbol{R}_{22}^{LE} \\ \boldsymbol{R}_{11}^{SU} & \boldsymbol{R}_{12}^{SU} & \boldsymbol{R}_{11}^{S\Omega} & \boldsymbol{R}_{12}^{S\Omega} & \boldsymbol{R}_{11}^{SE} & \boldsymbol{R}_{12}^{SE} \\ \boldsymbol{R}_{21}^{SU} & \boldsymbol{R}_{22}^{SU} & \boldsymbol{R}_{21}^{S\Omega} & \boldsymbol{R}_{22}^{S\Omega} & \boldsymbol{R}_{21}^{SE} & \boldsymbol{R}_{22}^{SE} \end{pmatrix} \cdot \begin{pmatrix} \boldsymbol{U}_1 - \boldsymbol{U}^\infty(\boldsymbol{x}_1) \\ \boldsymbol{U}_2 - \boldsymbol{U}^\infty(\boldsymbol{x}_2) \\ \boldsymbol{\Omega}_1 - \boldsymbol{\Omega}^\infty(\boldsymbol{x}_1) \\ \boldsymbol{\Omega}_2 - \boldsymbol{\Omega}^\infty(\boldsymbol{x}_2) \\ -\boldsymbol{E}^\infty \\ -\boldsymbol{E}^\infty \end{pmatrix}. \tag{B.15}$$

In other words, rather than the mobility formulation Eq. (B.1), one can use the equivalent resistance formulation to find the particle stresslet, provided that the unknown velocities and straining motion on the right-hand side of Eq. (B.15) are first determined from the mobility formulation. We adopted this approach in deriving the hydrodynamic stresslet in Sec. 2.3.2.

Up to this point, we have presented the derivation of the hydrodynamic stresslet. To obtain the total stresslet, we recall that it comprises two other contributions from equilibrium thermal energy and a non-hydrodynamic stresslet $\boldsymbol{xF}^P$. In the literature, some authors combined the linearity statement Eq. (B.15) with the non-hydrodynamic stresslet to give a compact matrix representation of the total stresslet [20, 8]

$$\begin{pmatrix} \boldsymbol{F}_\alpha^{Tot} \\ \boldsymbol{S}_\alpha^{Tot} \end{pmatrix} = - \begin{pmatrix} \boldsymbol{R}^{FU} & \boldsymbol{R}^{FE} \\ \boldsymbol{R}^{SU} & \boldsymbol{R}^{SE} \end{pmatrix} \cdot \begin{pmatrix} \boldsymbol{U}_\alpha - \boldsymbol{U}^\infty(\boldsymbol{x}_\alpha) \\ -\boldsymbol{E}^\infty \end{pmatrix} + \begin{pmatrix} \boldsymbol{F}_\alpha^{ext} + \overline{\boldsymbol{F}_\alpha^B} + \boldsymbol{F}_\alpha^P \\ -\boldsymbol{xF}_\alpha^P \end{pmatrix}, \tag{B.16}$$

where $\boldsymbol{F}_\alpha^{Tot}$ is a compact notation for the vector representing the total force and torque vector acting on particle α, $\boldsymbol{U}_\alpha$ is for the vector representing the total translational and rotational velocity of particle α, and $\boldsymbol{R}$ is block matrix defined using these compact notations. It is straightforward to show the validity of this

matrx representation. Let us first consider the first row of the matrix corresponding to the total force/torque. For our present model where there is no net total force on a particle, we get

$$0 = -\boldsymbol{R}^{FU} \cdot \boldsymbol{U}_\alpha + \boldsymbol{F}_\alpha^{ext} + \overline{\boldsymbol{F}_\alpha^B} + \boldsymbol{F}_\alpha^p, \tag{B.17}$$

where we recognize that $-\boldsymbol{R}^{FU} \cdot \boldsymbol{U}_\alpha$ is the hydrodynamic force $\boldsymbol{F}_\alpha^H$:

$$\boldsymbol{F}_\alpha^H = -\boldsymbol{R}^{FU} \cdot \boldsymbol{U}_\alpha. \tag{B.18}$$

We remark that Eq. (B.18) is not a trivial statement of Stokes' drag law. This states that there is a configuration-dependent hydrodynamic force that arises on particles' surfaces as a result of their motion through the suspension, where this motion experiences the solvent drag, drag from no-slip surfaces, drag from a deformed microstructure, microstructural gradients that produce Brownian drift drag, and interparticle drag. Thus, this total drag force on a particle relates strictly to the net motion of the probe. Readers are referred to Appendix D and [104] for connections to an effective Stokes' drag law defining the suspension microviscosity.

Substituting Eq. (B.18) into Eq. (B.17) recovers a force/torque balance in Stokes flow.

Further, the second row of the matrix gives the total stresslet as

$$\boldsymbol{S}_\alpha^{Tot} = -\boldsymbol{R}^{SU} \cdot \boldsymbol{U}_\alpha - \boldsymbol{x}\boldsymbol{F}_\alpha^P, \tag{B.19}$$

where imposed straining motion is absent in our model, and we recognize that $-\boldsymbol{R}^{SU} \cdot \boldsymbol{U}_\alpha$ is the hydrodynamic stresslet $\boldsymbol{S}_\alpha^H$:

$$\boldsymbol{S}_\alpha^H = -\boldsymbol{R}^{SU} \cdot \boldsymbol{U}_\alpha = -\boldsymbol{R}^{SU} \cdot (\boldsymbol{U}_\alpha^{ext} + \boldsymbol{U}_\alpha^B + \boldsymbol{U}_\alpha^P). \tag{B.20}$$

Substituting Eq. (B.20) into Eq. (B.19) gives

$$\boldsymbol{S}_{\alpha}^{Tot} = -\boldsymbol{R}^{SU} \cdot \boldsymbol{U}_{\alpha}^{ext} - \boldsymbol{R}^{SU} \cdot \boldsymbol{U}_{\alpha}^{B} - (\boldsymbol{R}^{SU} \cdot \boldsymbol{U}_{\alpha}^{P} + \boldsymbol{x}\boldsymbol{F}^{P}), \tag{B.21}$$

recovering the expressions for the total stresslet presented in Sec. 2.3.2.

APPENDIX C

COEFFICIENTS OF THE LOW- AND HIGH-*PE* ASYMPTOTES OF THE NORMAL STRESSES, FIRST NORMAL STRESS DIFFERENCE AND PARTICLE OSMOTIC PRESSURE

In this section, the coefficients comprise the expressions of the low- and high-*Pe* asymptotes of the nonequilibrium normal stresses, first normal stress difference and the osmotic pressure in Chapter 2 and 3 are presented. The coefficients in the low-*Pe* asymptotes are composed of hydrodynamics functions, and thus only have radial dependence. With reference to Eqs. (2.25)–(2.27), (2.39)–(2.41), (3.11)–(3.13) and (3.27)–(3.29), the coefficients associated with the low-*Pe* asymptotes read,

$$\begin{aligned}\mathcal{A}^{H,ext} = & -\frac{16}{45(1+\kappa)}\Big[X^G_{11}(\kappa r)x^A_{11}(\kappa r) + X^G_{12}(\kappa r)x^A_{12}(\kappa r) \\ & +3\left(Y^G_{11}(\kappa r)y^A_{11}(\kappa r) + Y^G_{12}(\kappa r)y^A_{12}(\kappa r)\right)\Big] \\ & +\frac{16}{5(1+\kappa)}\Big[Y^H_{11}(\kappa r)y^B_{11}(\kappa r) - Y^H_{12}(\kappa r)y^B_{12}(\kappa r)\Big],\end{aligned} \tag{C.1}$$

$$\mathcal{B}^{H,ext} = -\frac{4}{9(1+\kappa)}\Big[X^P_{11}(\kappa r)x^A_{11}(\kappa r) + X^P_{12}(\kappa r)x^A_{12}(\kappa r)\Big], \tag{C.2}$$

$$\begin{aligned}\mathcal{A}^{B} = & \frac{8}{45(1+\kappa)}\left[\frac{1}{r^2}\frac{d}{dr}\left[r^2\left(X^G_{11}(\kappa r) - X^G_{12}(\kappa r)\right)G(\kappa r)\right]\right. \\ & \left.-\frac{6}{r}\left(Y^G_{11}(\kappa r) - Y^G_{12}(\kappa r)\right)H(\kappa r)\right] \\ & -\frac{16}{5(1+\kappa)r}\Big[Y^H_{11}(\kappa r) - Y^H_{12}(\kappa r)\Big]\left(y^B_{11}(\kappa r) - y^B_{12}(\kappa r)\right),\end{aligned} \tag{C.3}$$

$$\mathcal{B}^{B} = \frac{2}{9(1+\kappa)r^2}\frac{d}{dr}\left[r^2\left(X^P_{11}(\kappa r) - X^P_{12}(\kappa r)\right)G(\kappa r)\right], \tag{C.4}$$

$$\mathcal{A}^{P} = \frac{32}{45(1+\kappa)}\Big[X^G_{11}(2(1+\kappa)) - X^G_{12}(2(1+\kappa))\Big]G(2(1+\kappa)), \tag{C.5}$$

$$\mathcal{B}^P = \frac{8}{9(1+\kappa)}\left[X_{11}^P(2(1+\kappa)) - X_{12}^P(2(1+\kappa))\right]G(2(1+\kappa)), \tag{C.6}$$

$$\mathcal{C}^P = -\frac{12}{5}, \tag{C.7}$$

$$\mathcal{G}^P = -\frac{4}{5}, \tag{C.8}$$

$$\mathcal{J}^P = \frac{4}{3}, \tag{C.9}$$

where $\mathcal{A}$'s and $\mathcal{B}$'s are associated with the traceless and isotropic parts of the stress respectively, and $\mathcal{C}$, $\mathcal{G}$ and $\mathcal{J}$ correspond to the elastic stresslet $\langle \boldsymbol{r}\boldsymbol{F}^P \rangle$.

The coefficients in the high-*Pe* asymptotes are form the lubrication forms of the hydrodynamics functions, and they are constants with no radial and angular dependence. With reference to Eqs. (2.31)–(2.33), (2.45)–(2.47), (3.17)–(3.19) and (3.33)–(3.35), the coefficients associated with the high-*Pe* asymptotes read,

$$\mathcal{D}^{H,ext} = -\frac{16}{(1+\kappa)}g_2^{YG}\left(a_{11}^{(1)} - a_{12}^{(1)}\right) + \frac{48}{(1+\kappa)}\left(g_2^{YH}b_{11}^{(1)} - g_5^{YH}b_{12}^{(1)}\right), \tag{C.10}$$

$$\begin{aligned}\mathcal{E}^{H,ext} = \; & \frac{16}{3(1+\kappa)}\left[g_1^{XG}\left(d_{11}^{(2)} - d_{12}^{(2)}\right) + G_{11}^X d_{11}^{(1)} + G_{12}^X d_{12}^{(1)}\right] \\ & + \frac{48}{(1+\kappa)}\left[g_2^{YH}\left(b_{11}^{(2)} - b_{11}^{(1)}e^{(1)}\right) - g_5^{YH}\left(b_{12}^{(2)} - b_{12}^{(1)}e^{(1)}\right) + H_{11}^Y b_{11}^{(1)} - H_{12}^Y b_{12}^{(1)}\right],\end{aligned} \tag{C.11}$$

$$\mathcal{F}^{H,ext} = \frac{8}{3(1+\kappa)}\left[g_1^{XP}\left(d_{11}^{(2)} - d_{12}^{(2)}\right) + P_{11}^X d_{11}^{(1)} + P_{12}^X d_{12}^{(1)}\right], \tag{C.12}$$

$$\begin{aligned}\mathcal{D}^B = \; & \frac{8}{(1+\kappa)}\left[g_2^{XG}\left(d_{11}^{(2)} - d_{12}^{(2)}\right) - g_1^{XG}\left(d_{11}^{(3)} - d_{12}^{(3)}\right) - \frac{3}{2}g_2^{YG}\left(a_{11}^{(1)} - a_{12}^{(1)}\right)\right] \\ & - \frac{36}{(1+\kappa)}\left(g_2^{YH} + g_5^{YH}\right)\left(b_{11}^{(1)} - b_{12}^{(1)}\right),\end{aligned} \tag{C.13}$$

$$\mathcal{F}^B = \frac{4}{3(1+\kappa)}\left[g_2^{XP}\left(d_{11}^{(2)} - d_{12}^{(2)}\right) - g_1^{XP}\left(d_{11}^{(3)} - d_{12}^{(3)}\right)\right], \tag{C.14}$$

$$\mathcal{D}^P = \frac{8}{(1+\kappa)}\left(d_{11}^{(2)} - d_{12}^{(2)}\right) g_1^{XG}, \tag{C.15}$$

$$\mathcal{F}^P = \frac{4}{3(1+\kappa)}\left(d_{11}^{(2)} - d_{12}^{(2)}\right) g_1^{XP}, \tag{C.16}$$

$$\mathcal{H}^P = -6, \tag{C.17}$$

$$\mathcal{I}^P = -3, \tag{C.18}$$

$$\mathcal{K}^P = 2, \tag{C.19}$$

where $\mathcal{D}$'s and $\mathcal{E}$ are associated with the traceless part of the stress, $\mathcal{F}$'s with the isotropic part, and $\mathcal{H}$, $\mathcal{I}$ and $\mathcal{K}$ correspond to the elastic stresslet. In Eqs. (C.10)–(C.19), $a_{ij}^{(k)}$, $b_{ij}^{(k)}$, $d_{ij}^{(k)}$, $e^{(1)}$, g_k^{lm}, G_{ij}^X, P_{ij}^X are the coefficients of the lubrication expressions of the hydrodynamic functions defined in *e.g.*, [75, 79, 73, 74], where $i, j = (1, 2)$ with "11" representing single-particle (self) interaction and "12" representing two-particle (probe-bath particle) interaction; $k = (1, 2, 3, 5)$ indicates the order of the coefficient in the lubrication expressions; $l = (X, Y)$, indicates the longitudinal or the transverse component of a hydrodynamic function; $m = (G, H, P)$ are the notations of the hydrodynamic resistance functions defined in Chapter 2 and 3.

APPENDIX D

SUMMARY OF MICROVISCOSITY THEORY

In this section, we summarize the micromechanical theories and key results of the microviscosity from prior studies [124, 78, 131].

The presence of microstructure hinders the probe's motion and its deformation to the suspension, giving rise to an effective suspension viscosity higher than the solvent viscosity. This effective viscosity changes with the degree of microstructural distortion which, in turn, depends on the dimensionless force Pe, describing the strength of the probe forcing, F_0, relative to the Brownian restoring force, $2kT/a_{th}$. Squires and Brady [124] and Khair and Brady [78] related the reduction in the mean velocity of the probe, $\langle \boldsymbol{U} \rangle$, to the effective viscosity, η^{eff}, via the Stokes' drag law,

$$\boldsymbol{F}^{\text{ext}} = 6\pi\eta a \frac{\eta^{eff}}{\eta} \langle \boldsymbol{U} \rangle, \tag{D.1}$$

and the effective viscosity is given by

$$\eta^{eff} = \frac{F_0}{6\pi a \langle \boldsymbol{U} \rangle \cdot \hat{\boldsymbol{F}}^{\text{ext}}}, \tag{D.2}$$

where $\hat{\boldsymbol{F}}^{\text{ext}} = \boldsymbol{F}^{\text{ext}}/F_0$ is the unit vector pointing in the direction of the external probe force. In the dilute limit, $\phi_b \ll 1$, the effective viscosity can be Taylor-expanded as,

$$\frac{\eta^{eff}}{\eta} = 1 + \eta^{micro}\phi_b + O(\phi_b^2). \tag{D.3}$$

The microviscosity comprises contributions from the hydrodynamic, Brownian and interparticle forces, $\eta^{micro} = \eta^H + \eta^B + \eta^P$.

In fixed-force active microrheology, the probe is driven by a constant external force induced by, *e.g.* magnetic field [61], and experiences fluctuating motion.

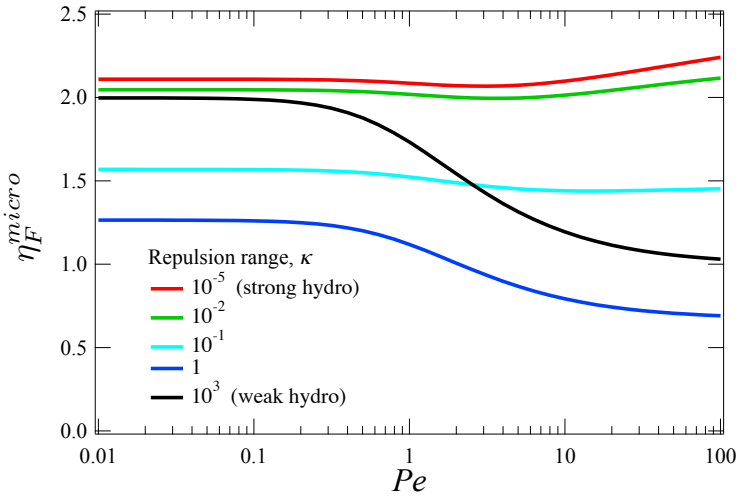

Figure D.1: Evolution of the total fixed-force microviscosity, η_F^{micro}, as a function of flow strength Pe for various strength of hydrodynamic interactions κ.

Squires and Brady [124] and Khair and Brady [78] derived the microviscosities as

$$\begin{aligned}\eta_F^H &= -\int_2^\infty \left[x_{11}^a(\kappa r) + 2y_{11}^a(\kappa r) - 3\right] r^2 dr \\ &\quad -\frac{3}{4\pi}\hat{\boldsymbol{F}}^{\text{ext}}\hat{\boldsymbol{F}}^{\text{ext}} : \int_{r\geq 2}\left[x_{11}^a(\kappa r)\hat{\boldsymbol{r}}\hat{\boldsymbol{r}} + y_{11}^a(\kappa r)(\boldsymbol{I} - \hat{\boldsymbol{r}}\hat{\boldsymbol{r}}) - \boldsymbol{I}\right] f(\boldsymbol{r}) d\boldsymbol{r},\end{aligned} \tag{D.4}$$

$$\eta_F^B = \frac{3}{4\pi}\frac{1}{Pe}\hat{\boldsymbol{F}}^{\text{ext}} \cdot \int_{r\geq 2}\left[\frac{G(\kappa r) - H(\kappa r)}{r} + \frac{1}{2}\frac{dG(\kappa r)}{dr}\right] f(\boldsymbol{r})\hat{\boldsymbol{r}} d\boldsymbol{r}, \tag{D.5}$$

$$\eta_F^P = \frac{3}{2\pi}\frac{G(2(1+\kappa))}{Pe}\hat{\boldsymbol{F}}^{\text{ext}} \cdot \oint_{r=2} f(\boldsymbol{r})\hat{\boldsymbol{r}} d\Omega, \tag{D.6}$$

where the components of the hydrodynamic mobility functions $x_{\alpha\beta}$, $y_{\alpha\beta}$, G, and H are defined following the conventional notations [13, 75, 80, 79]. They depend only on the relative separation between a pair of particles, r, and the dimensionless repulsion range, κ. The nonequilibrium distortion $f(r)$ of the microstructure is defined as $g(\boldsymbol{r}) = g^{eq}(1 + f(\boldsymbol{r}))$, where the pair distribution function, $g(\boldsymbol{r})$ describes the spatial distribution of bath particles with reference to a probe particle, and g^{eq} is the equilibrium microstructure and is equal to unity in a dilute dispersion. Both $g(\boldsymbol{r})$ and $f(r)$ have been studied for the full range of flow strength

Pe and hydrodynamic interactions κ in previous studies [124, 78, 153, 34]. Figure D.1 shows the evolution of the total fixed-force microviscosity η_F^{micro} with Pe for various κ.

Active microrheology can also be operated in the fixed-velocity mode: the probe is held fixed in an optical trap and moved past the bath at a constant velocity [102, 126]. Fixed-velocity microviscosity can be deduced analogously following Eqs. (D.1)-(D.3) with the external-velocity being held fixed and the external-force being the fluctuating quantity. The hydrodynamic, Brownian, and interparticle microviscosities were derived by Swan and Zia [131] as

$$\begin{aligned}\eta_U^H &= \int_2^\infty \left[\frac{1}{x_{11}^a(\kappa r)} + \frac{1}{2y_{11}^a(\kappa r)} - 3\right] r^2 dr \\ &+ \frac{3}{4\pi}\hat{\boldsymbol{U}}_{\mathbf{1}}\hat{\boldsymbol{U}}_{\mathbf{1}} : \int_{r\geq 2}\left[\frac{\hat{\boldsymbol{r}}\hat{\boldsymbol{r}}}{x_{11}^a(\kappa r)} + \frac{\boldsymbol{I}-\hat{\boldsymbol{r}}\hat{\boldsymbol{r}}}{y_{11}^a(\kappa r)} - \boldsymbol{I}\right] f(\boldsymbol{r})d\boldsymbol{r},\end{aligned} \tag{D.7}$$

$$\eta_U^B = \frac{3}{8\pi}\frac{1}{Pe}\hat{\boldsymbol{U}}_{\mathbf{1}} \cdot \int_{r\geq 2}\left\{\frac{1}{r}\left[\frac{G(\kappa r)}{x_{11}^a(\kappa r)} - \frac{H(\kappa r)}{y_{11}^a(\kappa r)}\right] + \frac{1}{2}\frac{d}{dr}\left[\frac{G(\kappa r)}{x_{11}^a(\kappa r)}\right]\right\} f(\boldsymbol{r})\hat{\boldsymbol{r}}d\boldsymbol{r}, \tag{D.8}$$

$$\eta_U^P = \frac{3}{\pi}\frac{G(2(1+\kappa))}{x_{11}^a(2(1+\kappa))}\frac{1}{Pe}\hat{\boldsymbol{U}}_{\mathbf{1}} \cdot \oint_{r=2} f(\boldsymbol{r})\hat{\boldsymbol{r}}d\Omega, \tag{D.9}$$

where $\hat{\boldsymbol{U}}_{\mathbf{1}} = \boldsymbol{U}_1/U_1$ is the unit vector pointing in the direction of the imposed probe velocity, and evaluation of the nonequilibrium distortion $f(r)$ was given in [131]. We note that a factor of two was missing in the original results in [131], and we corrected them in Eqs. (D.8) and (D.9) above.

Here, we summarize the behavior of the microviscosity in the limits of asymptotically weak and strong probe forcing and hydrodynamic interactions. In both fixed-force and fixed-velocity active microrheology, the deviation of hydrodynamic, Brownian and interparticle microviscosities from their equilibrium values were found to scale as Pe^2 at asymptotically small Pe, $Pe \ll 1$, regardless

of the strength of hydrodynamics:

$$(\eta^H_{F,U} - \eta^H_{0\,F,U})\ ,\ (\eta^B_{F,U} - \eta^B_{0\,F,U})\ ,\ (\eta^P_{F,U} - \eta^P_{0\,F,U}) \sim Pe^2 \qquad \text{for} \quad Pe \ll 1, \tag{D.10}$$

where η_0 is the equilibrium values of the microviscosities.

In the opposite limit of asymptotically large Pe, $Pe \gg 1$, fixing external-force or velocity leads to qualitatively different microstructural deformation, giving rise to distinct scalings of the microviscosities. In the fixed-force mode, the hydrodynamic, Brownian and interparticle microviscosities scale as

$$\eta^H_F \sim C_1 + C_2 Pe^{\delta-1}\ ,\ \eta^B_F \sim Pe^{\delta-2}\ ,\ \eta^P_F \sim Pe^{\delta-1} \qquad \text{for} \quad Pe \gg 1, \tag{D.11}$$

where $1 \geq \delta \geq 0.799$ as the influence of hydrodynamics evolves from weak ($\kappa \gg 1$, $\delta = 1$) to strong ($\kappa \ll 1$, $\delta = 0.799$), and C_1 and C_2 are obtained by extrapolating the high-Pe results to the limit $Pe \gg 1$ [78]. In the fixed-velocity mode, the Pe-dependence of the three microviscosities have the same functional form as the fixed-force counterparts,

$$\eta^H_U \sim C_3 + C_4 Pe^{\zeta-1}\ ,\ \eta^B_U \sim Pe^{\zeta-2}\ ,\ \eta^P_U \sim Pe^{\zeta-1} \qquad \text{for} \quad Pe \gg 1, \tag{D.12}$$

but with new extrapolating parameters C_3 and C_4, and δ replaced by ζ, which varies between $\zeta \in [1, 0.825]$ as the strength of hydrodynamics changes from weak to strong [131].

APPENDIX E

SUMMARY OF FLOW-INDUCED DIFFUSIVITY THEORY

In this section, we summarize the micromechanical theories and key results of the microviscosity from prior studies [153, 68, 69].

In addition to causing reduction in the mean velocity of the probe, probe/bath encounters also deflect the probe from its mean path. Flow-induced diffusion (microdiffusivity) is defined as the change in the effective diffusivity of the probe, $\boldsymbol{D}^{eff}$, given rise by these interactions [153]. To focus on this nonequilibrium fluctuation, flow-induced diffusivity, $\boldsymbol{D}^{flow}$, was defined as [69]

$$\boldsymbol{D}^{eff} = \boldsymbol{D}^{eq} + \boldsymbol{D}^{flow}, \tag{E.1}$$

where the first term, $\boldsymbol{D}^{eq}$ is the equilibrium value in the absence of external force, and the second term, $\boldsymbol{D}^{flow}$, corresponds to the $O(\phi_b)$ departure from equilibrium arising from the external force.

While determination of the microviscosity requires the pair distribution function, $g(\boldsymbol{r})$, to describe the likelihood finding a bath particle reference to the probe, evaluation of the flow-induced diffusivity requires the fluctuation field, $\boldsymbol{d}(\boldsymbol{r})$, which details the strength and direction of probe/bath encounters. Akin to microviscosity, flow-induced diffusivity comprises contribution from the hydrodynamic, Brownian and interparticle forces. Zia and Brady [153] and Hoh and Zia [69] derived these contributions as

$$\frac{\boldsymbol{D}^{flow,H}}{D_a\phi_b} = \frac{3}{4\pi}Pe\int_{r\geq 2}[x_{11}^a(\kappa r)\hat{\boldsymbol{r}}\hat{\boldsymbol{r}} + y_{11}^a(\kappa r)(\boldsymbol{I}-\hat{\boldsymbol{r}}\hat{\boldsymbol{r}}) - \boldsymbol{I}]\cdot\left(\frac{1}{Pe}f(\boldsymbol{r})\boldsymbol{I} - 2\hat{\boldsymbol{F}}^{\text{ext}}\boldsymbol{d}^{neq}\right)d\boldsymbol{r}, \tag{E.2}$$

$$\frac{\boldsymbol{D}^{flow,B}}{D_a\phi_b} = \frac{3}{2\pi}\int_{r\geq 2}\left[\frac{G(\kappa r)-H(\kappa r)}{r} + \frac{1}{2}\frac{dG(\kappa r)}{dr}\right]\hat{\boldsymbol{r}}\boldsymbol{d}^{neq}d\boldsymbol{r}, \tag{E.3}$$

$$\frac{\boldsymbol{D}^{flow,P}}{D_a\phi_b} = \frac{3}{\pi}G(2(1+\kappa))\oint_{r=2}\hat{\boldsymbol{r}}\boldsymbol{d}^{neq}d\Omega, \tag{E.4}$$

where $D_a = kT/6\pi\eta a$ is the bare diffusivity of a colloid of hydrodynamic size a, and $\boldsymbol{d}^{neq}(\boldsymbol{r})$ is the nonequilibrium part of the fluctuation field associated with the change in the probe's diffusivity under external force.

The flow-induced diffusivity tensor is anisotropic in general. To characterize this anisotropy, flow-induced diffusivity parallel and perpendicular to the line of the external force, $D_{\parallel}^{flow}$ and $D_{\perp}^{flow}$, are obtained by projecting the tensor in the corresponding directions,

$$D_{\parallel}^{flow} = \boldsymbol{D}^{flow} : \boldsymbol{e}_z\boldsymbol{e}_z, \tag{E.5}$$

$$D_{\perp}^{flow} = \boldsymbol{D}^{flow} : \boldsymbol{e}_y\boldsymbol{e}_y, \tag{E.6}$$

where $\boldsymbol{e}_z$ and $\boldsymbol{e}_y$ are the unit vectors in the direction parallel and perpendicular to the external force, respectively. We note that diffusivity in the two perpendicular directions, x and y, are the same owing to axisymmetry of the external flow, and thus $D_{\perp}^{flow} \equiv D_{yy}^{flow} = D_{xx}^{flow}$. Figure E.1 shows the evolution of the parallel $D_{\parallel}^{flow}$ and perpendicular flow-induced diffusivity $D_{\perp}^{flow}$, and $\alpha_{\parallel}$ and $\alpha_{\perp}$ in Eq. (4.18), with Pe and κ.

Here, we summarize the behavior of the flow-induced diffusivity in the limits of asymptotically weak and strong probe forcing and hydrodynamic interactions. In the limit of weak hydrodynamic interactions, $\kappa \gg 1$, Zia and Brady [153] found that both parallel and perpendicular diffusivities grow as Pe^2 under weak forcing,

$$D_{\parallel}^{flow}, D_{\perp}^{flow} \sim Pe^2 \qquad \text{for} \quad \kappa \gg 1\ ,\ Pe \ll 1, \tag{E.7}$$

whereas they grow linearly in Pe under strong forcing

$$D_{\parallel}^{flow}, D_{\perp}^{flow} \sim Pe \qquad \text{for} \quad \kappa \gg 1\ ,\ Pe \gg 1. \tag{E.8}$$

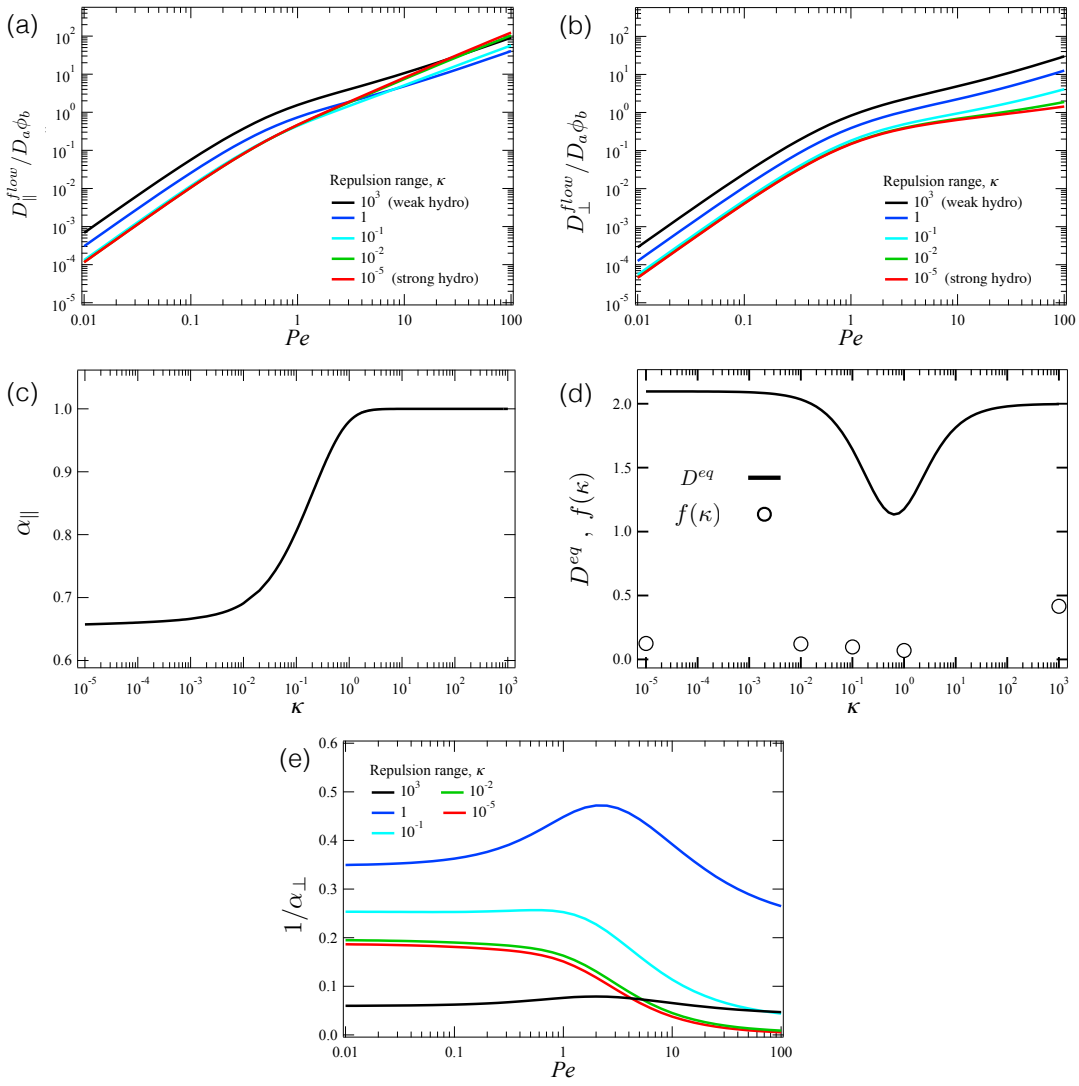

Figure E.1: Evolution of the (a) parallel $D_{\parallel}^{flow}$ and (b) perpendicular flow-induced diffusivity $D_{\perp}^{flow}$, as a function of flow strength Pe for various strength of hydrodynamic interactions κ. Evolution of (c) $\alpha_{\parallel}$ and (d) D^{eq} and $f(\kappa)$ in Eq. (4.18), as a function of κ. Noted that $f(\kappa) = D^{eq}(\kappa)/16.8$, except in the limit of weak hydrodynamics where $f(10^3)$ is taken as 0.416. (e) Evolution of $\alpha_{\perp}$ in Eq. (4.18), as a function of Pe for various κ.

In the limit of strong hydrodynamic interactions, $\kappa \ll 1$, Hoh and Zia [69] found that the low-Pe scalings of the two diffusivities remain unchanged

$$D_{\parallel}^{flow}, D_{\perp}^{flow} \sim Pe^2 \qquad \text{for} \quad \kappa \ll 1\ ,\ Pe \ll 1. \tag{E.9}$$

As flow strength increases, the scaling of both diffusivities changes qualitatively

$$D_{\parallel}^{flow} \sim Pe, \qquad D_{\perp}^{flow} = 0 \qquad \text{for} \quad \kappa \ll 1 \ , \ Pe \gg 1, \tag{E.10}$$

recovering the result of Hoh and Zia [68] in the strong-flow, pure-hydrodynamic limit.

BIBLIOGRAPHY

[1] A. Acrivos, R. Mauri, and X. Fan. Shear-induced resuspension in a Couette device. *Intl J. Multiphase Flow*, 19:797–802, 1993.

[2] B. Alberts, D. Bray, J. Lewis, M. Raff, K. Roberts, and J. D. Watson. *Molecular Biology of the Cell*. Garland Science, New York, NY, 1994.

[3] Y. Almog and H. Brenner. Non-continuum anomalies in the apparent viscosity experienced by a test sphere moving through an otherwise quiescent suspension. *Phys. Fluid*, 9:16–22, 1997.

[4] Y. Almog and I. Frankel. The rotary motion of dipolar axisymmetric particle in homogeneous shear flow. *J. Fluid Mech.*, 289:243–261, 1995.

[5] Y. Almog and I. Frankel. Rheology of a dilute suspension of dipolar axisymmetric Brownian particles in homogeneous shear flow. *J. Fluid Mech.*, 366:289–310, 1998.

[6] M. Anand and K. R. Rajagopal. A shear-thinning viscoelastic fluid model for describing the flow of blood. *Int. J. Cardiovasc. Med. Sci.*, 4:59–68, 2004.

[7] R. A. Bagnold. Experiments on a gravity-free dispersion of large solid spheres in a Newtonian fluid under shear. *Proc. R. Soc. London*, 225:49–63, 1954.

[8] A. J. Banchio and J. F. Brady. Accelerated Stokesian dynamics: Brownian motion. *J. Chem. Phys.*, 118:10323–10332, 2003.

[9] D. J. Barber and I. C. Freestone. An investigation of the origin of the colour of the lycurgus cup by analytical transmission electron microscopy. *Archarometry*, 32:33–45, 1990.

[10] H. A. Barnes. Shear-thickening ("dilatancy") in suspensions of nonaggregating solid particles dispersed in Newtonian liquids. *J. Rheol.*, 33, 1989.

[11] G. K. Batchelor. The stress system in a suspension of force-free particles. *J. Fluid Mech.*, 41:545–570, 1970.

[12] G. K. Batchelor. Sedimentation in a dilute dispersion of spheres. *J. Fluid Mech.*, 52:245–268, 1972.

[13] G. K. Batchelor. Brownian diffusion of particles with hydrodynamic interaction. *J. Fluid Mech.*, 74:1–29, 1976.

[14] G. K. Batchelor. The effect of Brownian motion on the bulk stress in a suspension of spherical particles. *J. Fluid Mech.*, 83:97–117, 1977.

[15] G. K. Batchelor. Sedimentation in a dilute polydisperse system of interacting spheres. Part 1. General theory. *J. Fluid Mech.*, 119:379–408, 1982.

[16] G. K. Batchelor and J. T. Green. The determination of the bulk stress in a suspension of spherical particles to order c^2. *J. Fluid Mech.*, 56:401–427, 1972.

[17] G. K. Batchelor and J. T. Green. The hydrodynamic interaction of two small freely-moving spheres in a linear flow field. *J. Fluid Mech.*, 56:375–400, 1972.

[18] G. K. Batchelor and C. S. Wen. Sedimentation in a dilute polydisperse system of interacting spheres. Part 2. Numerical results. *J. Fluid Mech.*, 124:495–528, 1982.

[19] J. Bergenholtz, J. F. Brady, and M. Vicic. The non-Newtonian rheology of dilute colloidal suspensions. *J. Fluid Mech.*, 456:239–275, 2002.

[20] G. Bossis and J. F. Brady. The rheology of Brownian suspensions. *J. Chem. Phys.*, 91:1866–1874, 1989.

[21] F. Boyer, O. Pouliquen, and E. Guazzelli. Dense suspensions in rotating-rod flows: normal stresses and particle migration. *J. Fluid Mech.*, 686:5–25, 2011.

[22] J. F. Brady. Stokesian dynamics. *Annu. Rev. Fluid Mech.*, 20:111–157, 1988.

[23] J. F. Brady. Brownian motion, hydrodynamics, and the osmotic pressure. *J. Chem. Phys.*, 98:3335–3341, 1993.

[24] J. F. Brady. The rheological behavior of concentrated colloidal dispersions. *J. Chem. Phys.*, 99:567–581, 1993.

[25] J. F. Brady and G. Bossis. The rheology of concentrated suspensions of spheres in simple shear flow by numerical simulation. *J. Fluid Mech.*, 155:105–129, 1985.

[26] J. F. Brady and J. F. Morris. Microstructure of strongly sheared suspensions and its impact on rheology and diffusion. *J. Fluid Mech.*, 348:103–139, 1997.

[27] J. F. Brady and M. Vicic. Normal stresses in colloidal dispersions. *J. Rheol.*, 39, 1995.

[28] H. Brenner and M. H. Weissman. Rheology of a dilute suspension of dipolar spherical particles in an external field. II. Effect of rotary Brownian motion. *J. Colloid Interface Sci.*, 41, 1972.

[29] R. Brown. A brief account of microscopical observations made in the months of june, july and august 1827, on the particles contained in the pollen of plants; and on the general existence of active molecules in organic and inorganic bodies. *Philos. Mag.*, 4, 1827.

[30] H. B. Callen and T. A. Welton. Irreversibility and generalized noise. *Phys. Rev.*, 83:34–40, 1951.

[31] C. F. Carnahan and K. E. Starling. Equation of state for nonattracting rigid spheres. *J. Chem. Phys.*, 51:635–636, 1969.

[32] S. B. Chen and D. L. Koch. Rheology of dilute suspensions of charged fibers. *Phys. Fluid*, 8:2792–2807, 1996.

[33] S. B. Chen and D. L. Koch. Rheology of highly aligned nematic liquid crystals. *J. Non-Newtonian Fluids*, 69:273–292, 1997.

[34] H. C. W. Chu and R. N. Zia. Active microrheology of hydrodynamically interacting colloids: normal stresses and entropic energy density. *J. Rheol.*, 60, 2016.

[35] H. C. W. Chu and R. N. Zia. The non-Newtonian rheology of hydrodynamically interacting colloids via active, nonlinear microrheology. *J. Rheol.*, 61, 2017.

[36] I. L. Claeys and J. F. Brady. Suspensions of prolate spheroids in Stokes flow. Part 1. Dynamics of a finite number of particles in an unbounded fluid. *J. Fluid Mech.*, 251:411–442, 1993.

[37] I. L. Claeys and J. F. Brady. Suspensions of prolate spheroids in Stokes

flow. Part 2. Statistically homogeneous dispersions. *J. Fluid Mech.*, 251:443–477, 1993.

[38] I. L. Claeys and J. F. Brady. Suspensions of prolate spheroids in Stokes flow. Part 3. Hydrodynamic transport properties of crystalline dispersions. *J. Fluid Mech.*, 251:479–500, 1993.

[39] F. R. Cunha and E. J. Hinch. Shear-induced dispersion in a dilute suspension of rough spheres. *J. Fluid Mech.*, 309:211–223, 1996.

[40] R. H. Davis and N. A. Hill. Hydrodynamic diffusion of a sphere sedimenting through a dilute suspension of neutrally buoyant spheres. *J. Fluid Mech.*, 236:513–533, 1992.

[41] R. H. Davis, Y. Zhao, K. P. Galvin, and H. J. Wilson. Solid-solid contacts due to surface roughness and their effects on suspension behaviour. *Phil. Trans. R. Soc. Lond. A*, 361:871–894, 2003.

[42] G. Drazer, J. Koplik, B. Khusid, and A. Acrivos. Microstructure and velocity fluctuations in sheared suspensions. *J. Fluid Mech.*, 511, 2002.

[43] L. Durlofsky, J. F. Brady, and G. Bossis. Dynamic simulation of hydrodynamically interacting particles. *J. Fluid Mech.*, 180:21–49, 1987.

[44] A. Einstein. On the theory of the Brownian movement. *Ann. Phys.*, 324:371–381, 1906.

[45] D. L. Ermak and J. A. McCammon. Brownian dynamics with hydrodynamic interactions. *J. Chem. Phys.*, 69:1352–1360, 1978.

[46] H. Faxen. Der widerstand gegen die bewegung einer starren kugel in einer zhen flssigkeit, die zwischen zwei parallelen ebenen wnden eingeschlossen ist. *Arkiv fur Matematik*, 18, 1924.

[47] M. Fixman. Simulation of polymer dynamics. i. General theory. *J. Chem. Phys.*, 69:1527–1537, 1978.

[48] D. R. Foss. *Rheological behavior of colloidal suspensions: the effects of hydrodynamic interactions*. PhD thesis, California Institute of Technology, 1999.

[49] D. R. Foss and J. F. Brady. Self-diffusion in sheared suspensions by dynamic simulation. *J. Fluid Mech.*, 401:243–274, 1999.

[50] D. R. Foss and J. F. Brady. Structure, diffusion and rheology of Brownian suspensions by Stokesian dynamics simulation. *J. Fluid Mech.*, 407:167–200, 2000.

[51] E. M. Furst. Applications of laser tweezers in complex fluid rheology. *Curr. Opin. Coll. Surf. Sci.*, 10:79–86, 2005.

[52] F. Gadala-Maria. *The rheology of concentrated suspensions*. PhD thesis, Stanford University, 1979.

[53] F. Gadala-Maria and A. Acrivos. Shear-induced structure in a concentrated suspension of solid spheres. *J. Rheol.*, 24:799–814, 1980.

[54] C. Gamonpilas, J. F. Morris, and M. M. Denn. Shear and normal stress measurements in non-Brownian monodisperse and bidisperse suspensions. *J. Rheol.*, 60, 2016.

[55] C. Gao, S. D. Kulkarni, J. F. Morris, and J. F. Gilchrist. Direct investigation of anisotropic suspension structure in pressure-driven flow. *Phys. Rev. E*, 81, 2010.

[56] S. Garland, G. Gauthier, J. Martin, and J. F. Morris. Normal stress measurements in sheared non-Brownian suspensions. *J. Rheol.*, 57, 2013.

[57] T. Gisler and D. A. Weitz. Tracer microrheology in complex fluids. *Curr. Opin. Colloid Interface Sci.*, 3:586–592, 1998.

[58] T. Gisler and D. A. Weitz. Scaling of the microrheology of semidilute f-actin solutions. *Phy. Rev. Lett.*, 82:1606–1610, 1999.

[59] T. Graham. Liquid diffusion applied to analysis. *Phil. Trans. R. Soc. Lond.*, 151:183–224, 1861.

[60] E. Guazzelli and J. F. Morris. *A physical introduction to suspension dynamics*. Cambridge University Press, Cambridge, UK, 2012.

[61] P. Habdas, D. Schaar, A. C. Levitt, and E. R. Weeks. Forced motion of a probe particle near the colloidal glass transition. *Europhys. Lett.*, 67:477–483, 2004.

[62] J. Happel and H. Brenner. *Low Reynolds number hydrodynamics*. Martinus Nijhoff, Leiden, 1965.

[63] H. Hasimoto. On the periodic fundamental solutions of the Stokes equations and their application to viscous flow past a cubic array of spheres. *J. Fluid Mech.*, 5:317–328, 1959.

[64] I. A. Hasnain and A. M. Donald. Microrheological characterization of anisotropic materials. *Phy. Rev. E*, 73:031901, 2006.

[65] M. Haw. *Middle world - The restless heart of matter and life*. Macmillan, 2007.

[66] E. J. Hinch. Application of the langevin equation to fluid suspensions. *J. Fluid Mech.*, 72:499–511, 1975.

[67] N. J. Hoh. *Effects of particle size ratio on single particle motion in colloidal dispersions*. PhD thesis, California Institute of Technology, 2013.

[68] N. J. Hoh and R. N. Zia. Hydrodynamic diffusion in active microrheology of non-colloidal suspensions: the role of interparticle forces. *J. Fluid Mech.*, 785, 2015.

[69] N. J. Hoh and R. N. Zia. Force-induced diffusion in suspensions of hydrodynamically-interacting colloidals. *J. Fluid Mech.*, 795, 2016.

[70] N. J. Hoh and R. N. Zia. The impact of probe size on measurements of diffusion in active microrheology. *Lab Chip*, 16, 2016.

[71] H. A. Houghton. *Microstructural studies of clay dispersions and gels*. PhD thesis, University of Cambridge, 2007.

[72] D. M. Husband and F. Gadala-Maria. Anisotropic particle distribution in dilute suspensions of solid spheres in cylindrical Couette flow. *J. Rheol.*, 31:95–110, 1987.

[73] D. J. Jeffrey. The calculation of the low Reynolds number resistance functions for two unequal spheres. *Phys. Fluids*, 4, 1992.

[74] D. J. Jeffrey, J. F. Morris, and J. F. Brady. The pressure moments for two rigid spheres in low-Reynolds-number flow. *Phys. Fluids*, 5, 1993.

[75] D. J. Jeffrey and Y. Onishi. Calculation of the resistance and mobility functions for two unequal rigid spheres in low-Reynolds-number flow. *J. Fluid Mech.*, 139, 1984.

[76] I. M. Jnosi, T. Tl, D. E. Wolf, and J. A. C. Gallas. Chaotic particle dynamics in viscous flows: the three-particle stokeslet problem. *Phy. Rev. E*, 56:2858–2868, 1997.

[77] L. C. Johnson, B. J. Landrum, and R. N. Zia. Transient yield of reversible colloidal gels via dynamic simulation. 2017. in review.

[78] A. S. Khair and J. F. Brady. Single particle motion in colloidal dispersions: a simple model for active and nonlinear microrheology. *J. Fluid Mech.*, 557:73–117, 2006.

[79] S. Kim and S. J. Karrila. *Microhydrodynamics: Principles and Selected Applications*. Butterworth-Heinemann, Boston, MA, 1991.

[80] S. Kim and R. T. Mifflin. The resistance and mobility functions of two equal spheres in low-Reynolds-number flow. *Phys. Fluids*, 28, 1985.

[81] G. Kirchoff. *Vorlesungen ber mathematische Physik: Mechanik*. Teubner, Leipzig, 1876.

[82] I. M. Krieger and T. J. Dougherty. A mechanism for non-Newonian flow in suspension of rigid spheres. *Trans. Soc. Rheol.*, 3, 1959.

[83] R. Kubo. The fluctuation-dissipation theorem. *Rep. Prog. Phys.*, 29:255–284, 1966.

[84] A. Kumar, R. G. Henriquez Rivera, and M. D. Graham. Flow-induced segregation in confined multicomponent suspensions: effects of particle size and rigidity. *J. Fluid Mech.*, 738, 2014.

[85] H. Lamb. *Fluid mechanics*. Dover Publications, New York, NY, 1932.

[86] B. J. Landrum, R. N. Zia, and W. B. Russel. Delayed yield in colloidal gels via dynamic simulation. *J. Rheol.*, 2016. in review.

[87] P. Langevin. Sur la thorie du mouvement Brownien. *C. R. Acad. Sci.*, 146, 1908.

[88] D. Leighton and A. Acrivos. Viscous resuspension. *Chem. Engng Sci.*, 41:1377–1384, 1986.

[89] D. Leighton and A. Acrivos. Measurement of self-diffusion in concentrated suspensions of spheres. *J. Fluid Mech.*, 177:109–131, 1987.

[90] D. Leighton and A. Acrivos. The shear-induced migration of particles in concentrated suspensions. *J. Fluid Mech.*, 181:415–439, 1987.

[91] N. Y. C. Lin, J. H. McCoy, X. Cheng, B. Leahy, J. N. Israelachvili, and I. Cohen. A multi-axis confocal rheoscope for studying shear flow of structured fluids. *Rev. Sci. Instrum.*, 85:033905, 2014.

[92] R. A. Lionberger and W. B. Russel. Effectiveness of non-equilibrium closures for the many-body forces in concentrated colloidal dispersions. *J. Chem. Phys.*, 106:402–416, 1997.

[93] R. A. Lionberger and W. B. Russel. A smoluchoski theory with simple approximations for hydrodynamic interactions in concentrated dispersions. *J. Rheol.*, 41:399–425, 1997.

[94] H. A. Lorentz. A general theorem concerning the motion of a viscous fluid and a few consequences derived from it. *Zittingsverslag. Akad. Wet. Amsterdam*, 5, 1896.

[95] H. A. Lorentz. Ein allgemeiner satz, die bewegung einer reibenden flssigkeit betreffend, nebsteinigen anwendungen desselben. *Abhand. Theor. Phys.*, 1, 1907.

[96] M. B. Mackaplow and E. S. Shaqfeh. A numerical study of the sedimentation of fibre suspensions. *J. Fluid Mech.*, 376:149–182, 1998.

[97] F. MacKintosh, J. Ks, and P. A. Janmey. Elasticity of semiflexible biopolymer networks. *Phys. Rev. Lett.*, 75:4425–4428, 1995.

[98] R. K. Mallavajula, L. A. Archer, and D. L. Koch. The average stress in a suspension of cube-shaped magnetic particles subject to shear and magnetic fields. *Phys. Fluids*, 27:093101, 2015.

[99] M. Marchioro and A. Acrivos. Shear-induced particle diffusivities from numerical simulations. *J. Fluid Mech.*, 443, 2001.

[100] T. G. Mason and D. A. Weitz. Optical measurements of frequency-dependent linear viscoelastic moduli of complex fluids. *Phys. Rev. Lett.*, 74:1250–1253, 1995.

[101] J. Mewis and N. J. Wagner. *Colloidal suspension rheology*. Cambridge University Press, Edinburgh, UK, 2012.

[102] A. Meyer, A. Marshall, B. G. Bush, and E. M. Furst. Laser tweezer microrheology of a colloidal suspension. *J. Rheol.*, 50:77–92, 2006.

[103] W. J. Miliken, M. Gottlieb, A. L. Graham, L. A. Mondy, and R. L. Powell. The viscosity volume fraction relation for suspensions of rod-like particles by falling ball rheometry. *J. Fluid Mech.*, 202:217–232, 1989.

[104] R. P. Mohanty. *The effect of hydrodynamic interactions on structural and rheological evolution during flow startup and relaxation upon flow cessation: Transient nonlinear microrheology*. PhD thesis, Cornell University, 2018.

[105] R. P. Mohanty and R. N. Zia. The impact of hydrodynamics on viscosity evolution in colloidal dispersions: Transient, nonlinear microrheology. *J. Fluid Mech.*, 2017. in review.

[106] A. Mohraz and M. J. Solomon. Orientation and rupture of fractal colloidal gels during start-up of steady shear flow. *J. Rheol.*, 49, 2005.

[107] G. Ngele and J. Bergenholtz. Linear viscoelasticity of colloidal mixtures. *J. Chem. Phys.*, 108:9893–9904, 1998.

[108] H. Nyquist. Thermal agitation of electric charge in conductors. *Phys. Rev.*, 32:110–113, 1928.

[109] J. Oldroyd. On the formulation of rheological equations of state. *Proc. R. Soc. A*, 200:523–541, 1950.

[110] W. Ostwald. Ueber die rechnerische darstellung des strukturgebietes der viskositt. *Kolloid-Zeitschrift*, 47:176–187, 1929.

[111] F. Parsi and F. Gadala-Maria. Fore-and-aft asymmetry in a concentrated suspension of solids spheres. *J. Rheol.*, 31:725–732, 1987.

[112] J. K. Percus and G. J. Yevick. Analysis of classical statiscal mechanics by means of collective coordinates. *Phys. Rev.*, 110:1–13, 1958.

[113] J-. B. Perrin. Mouvement Brownian et ralit molculaire (Brownian motion and the molecular reality). *Ann. Chim. Phys.*, 18:5–114, 1909.

[114] R. J. Philips, R. C. Armstrong, R. A. Brown, A. L. Graham, and J. L. Abbott. A constitutive equation for concentrated suspensions that accounts for shear-induced particle migration. *Phys. Fluids A*, 4, 1992.

[115] D. J. Pine, J. P. Gollub, J. F. Brady, and A. M. leshansky. Chaos and threshold for irreversibility in sheared suspensions. *Nature*, 438:997–1000, 2005.

[116] I. Rampall, J. R. Smart, and D. T. Leighton. The influence of surface roughness on the particle-pair distribution function of dilute suspensions of non-colloidal spheres in simple shear flow. *J. Fluid Mech.*, 339:1–24, 1997.

[117] M. Reiner. The deborah number. *Phys. Today*, 17:62, 1964.

[118] W. B. Russel. The Huggins coefficient as a means for characterizing suspended particles. *J. Chem. Soc., Faraday Trans. 2*, 80:31–41, 1984.

[119] W. B. Russel and A. P. Gast. Nonequilibrium statistical mechanics of concentrated colloidal dispersions: Hard spheres in weak flows. *J. Chem. Phys.*, 84:1815–1826, 1986.

[120] M. I. Shliomis. Effective viscosity of magnetic suspensions. *J. Exp. Theor. Phys.*, 34:1291–1294, 1972.

[121] A. Sierou and J. F. Brady. Accelerated Stokesian dynamics simulations. *J. Fluid Mech.*, 448, 2001.

[122] A. Singh and P. R. Nott. Experimental measurements of the normal stresses in sheared Stokesian suspensions. *J. Fluid Mech.*, 490:293–320, 2003.

[123] M. Smoluchowski. Zur kinetischen theorie der brownschen molekularbewegung und der suspensionen. *Ann. Phys.*, 21:756–780, 1906.

[124] T. M. Squires and J. F. Brady. A simple paradigm for active and nonlinear microrheology. *Phys. Fluids*, 17:073101, 2005.

[125] T. M. Squires and T. G. Mason. Fluid mechanics of microrheology. *Annu. Rev. Fluid Mech.*, 42:413–438, 2010.

[126] I. Sriram, R. DePuit, T. M. Squires, and E. M. Furst. Small amplitude active oscillatory microrheology of a colloidal suspension. *J. Rheol.*, 53:357–381, 2009.

[127] S. R. Strand and S. Kim. Dynamics and rheology of a dilute suspension of dipolar nonspherical particles in an external field: Part 1. Steady shear flows. *Rheol. Acta*, 31:94–117, 1992.

[128] Y. Su, H. C. W. Chu, and R. N. Zia. Microviscosity, normal stress and osmotic pressure of brownian suspensions by accelerated stokesian dynamics simulation. *Soft Matter*, 2017. in review.

[129] G. Subramanian and D. L. Koch. Inertial effects on fibre motion in simple shear flow. *J. Fluid Mech.*, 535:383–414, 2005.

[130] G. Subramanian and D. L. Koch. Inertial effects on the orientation of nearly spherical particles in simple shear flow. *J. Fluid Mech.*, 557:257–296, 2006.

[131] J. W. Swan and R. N. Zia. Active microrheology: Fixed-velocity versus fixed-force. *Phys. Fluids*, 25:083303, 2013.

[132] G. J. Tangelder, H. C. Teirlinck, D. W. Slaaf, and R. S. Reneman. Distribution of blood platelets flowing in arterioles. *Am. J. Physiol. Heart Circ. Physiol.*, 248, 1985.

[133] M. T. Valentine, P. D. Kaplan, D. Thota, J. C. Crocker, T. Gisler, R. K. Prud'homme, M. Beck, and D. A. Weitz. Investigating the microenvironments of inhomogeneous soft materials with multiple particle tracking. *Phys. Rev. E*, 64:061506, 2001.

[134] P. Varadan and M. J. Solomon. Shear-induced microstructural evolution of a thermoreversible colloidal gel. *Langmuir*, 17:2918–2929, 2001.

[135] N. J. Wagner and J. F. Brady. Shear thickening in colloidal dispersions. *Phys. Today*, 62:27–32, 2009.

[136] N. J. Wagner and W. B. Russel. Nonequilibrium statistical mechanics of concentrated colloidal dispersions: Hard spheres in weak flows with many-body thermodynamic interactions. *Physica A*, 155:475–518, 1989.

[137] N. J. Wagner and A. T. J. M. Woutersen. The viscosity of binary and polydisperse suspensions of hard spheres in the dilute limit. *J. Fluid Mech.*, 278:267–287, 1994.

[138] T. A. Waigh. Microrheology of complex fluids. *Rep. Prog. Phys.*, 68:685–742, 2005.

[139] D. Weihs, T. G. Mason, and M. A. Teitell. Bio-microrheology: A frontier in microrheology. *Biophys. J.*, 91:4296–4305, 2006.

[140] K. Weissenberg. A continuum theory of rheological phenomena. *Nature*, 159:310–311, 1947.

[141] H. J. Wilson. An analytic form for the pair distribution function and rheology of a dilute suspension of rough spheres in plane strain flow. *J. Fluid Mech.*, 534, 2005.

[142] H. J. Wilson and R. H. Davis. The viscosity of a dilute suspension of rough spheres. *J. Fluid Mech.*, 421, 2000.

[143] H. J. Wilson and R. H. Davis. Shear stress of a monolayer of rough spheres. *J. Fluid Mech.*, 452, 2002.

[144] L. G. Wilson, A. W. Harrison, A. B. Schofield, J. Arlt, and W. C. K. Poon. Passive and active microrheology of hard-sphere colloids. *J. Phys. Chem. B*, 113:3806–3812, 2009.

[145] D. Wirtz. Particle tracking microrheology of living cells: principles and applications. *Annu. Rev. Biophys.*, 38:301–326, 209.

[146] B. Xu and J. F. Gilchrist. Microstructure of sheared monosized colloidal suspensions resulting from hydrodynamic and electrostatic interactions. *J. Chem. Phys.*, 140:204903, 2014.

[147] Y. Yurkovetsky and J. F. Morris. Particle pressure in sheared Brownian suspensions. *J. Rheol.*, 52, 2008.

[148] Z. Zapryanov and S. Tabakova. *Dynamics of bubbles, drops and rigid particles*. Kluwer Academic Publishers, Dordrecht, The Netherlands, 1999.

[149] I. E. Zarraga, D. A. Hill, and D. T. Leighton. The characterization of the total stress of concentrated suspensions of noncolloidal spheres in newtonian fluids. *J. Rheol.*, 44, 2000.

[150] K. Zhang and A. Acrivos. Viscous resuspension in fully developed laminar pipe flows. *Intl J. Multiphase Flow*, 20:579–591, 1994.

[151] R. N. Zia. *Individual particle motion in colloids: Microviscosity, microdiffusivity, and normal stresses*. PhD thesis, California Institute of Technology, 2011.

[152] R. N. Zia. Active and passive microrheology: Theory and simulation. *Annu. Rev. Fluid Mech.*, 2018. in review.

[153] R. N. Zia and J. F. Brady. Single particle motion in colloids: force-induced diffusion. *J. Fluid Mech.*, 658, 2010.

[154] R. N. Zia and J. F. Brady. Microviscosity, microdiffusivity, ad normal stresses in colloidal dispersions. *J. Rheol.*, 56, 2012.

[155] R. N. Zia and J. F. Brady. Stress development, relaxation, and memory in colloidal dispersions: Transient nonlinear microrheology. *J. Rheol.*, 57, 2013.

[156] R. N. Zia, B. J. Landrum, and W. B. Russel. A micro-mechanical study of coarsening and rheology of colloidal gels: Cage building, cage hopping, and smoluchowski's ratchet. *J. Rheol.*, 58, 2014.

[157] R. N. Zia, J. W. Swan, and Y. Su. Pair mobility functions for rigid spheres in concentrated colloidal dispersions: Force, torque, translation, and rotation. *J. Chem. Phys.*, 143:224901, 2015.